3D Tracking of Motile Microorganisms

An Experimental Investigation of the Kinematics and Interactions of C. Reinhardtii

Mehmood, J.

DOI
10.4233/uuid:1ae2f7c4-b4b8-4ec8-a64b-9be8e1189983

Publication date
2024

Document Version
Final published version

Citation (APA)
Mehmood, J. (2024). *3D Tracking of Motile Microorganisms: An Experimental Investigation of the Kinematics and Interactions of C. Reinhardtii*. [Dissertation (TU Delft), Delft University of Technology]. https://doi.org/10.4233/uuid:1ae2f7c4-b4b8-4ec8-a64b-9be8e1189983

3D Tracking of Motile Microorganisms

An Experimental Investigation of the Kinematics and Interactions of C. Reinhardtii

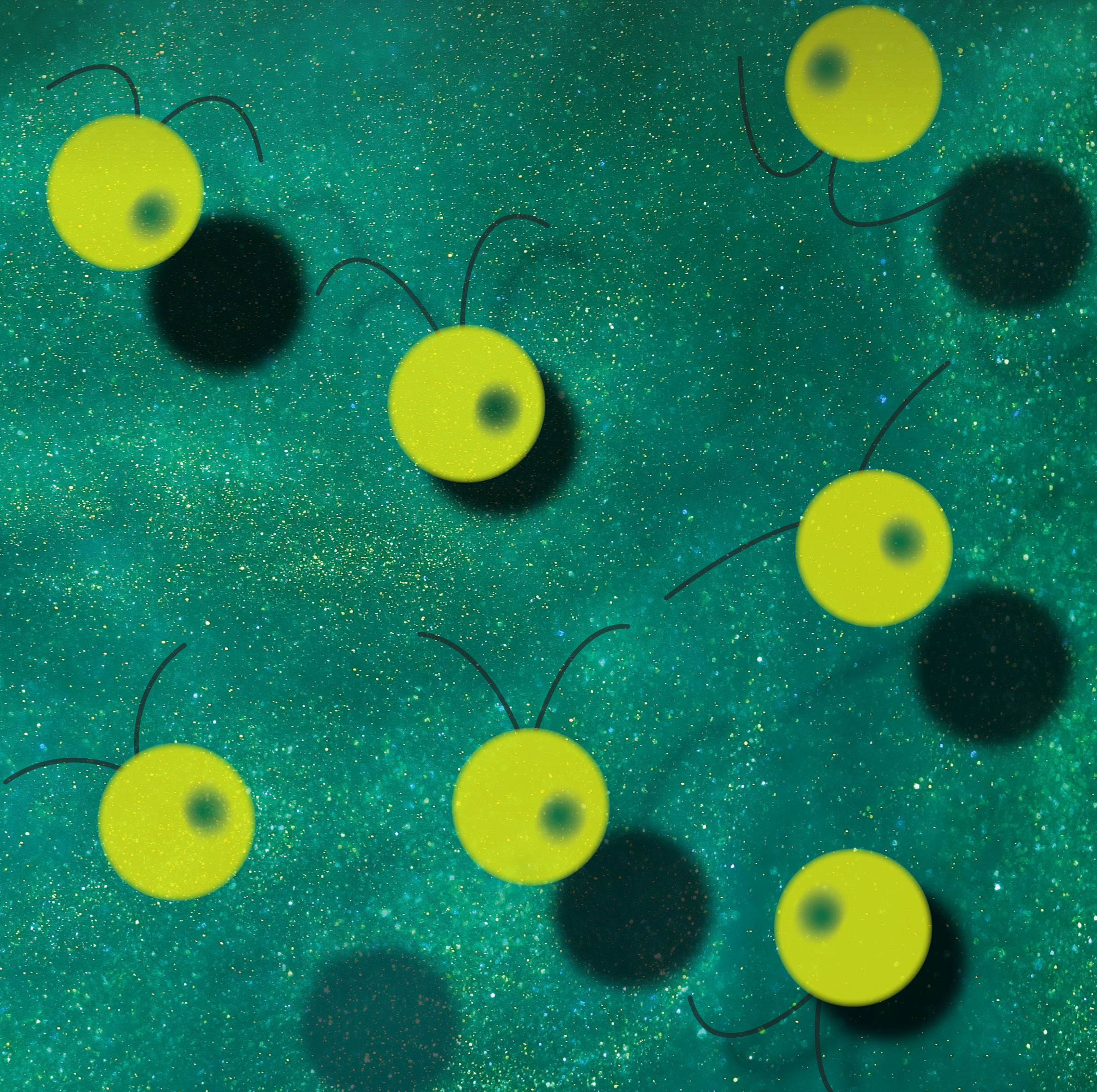

Junaid Mehmood

3D TRACKING OF MOTILE MICROORGANISMS

AN EXPERIMENTAL INVESTIGATION OF THE KINEMATICS AND INTERACTIONS OF C. REINHARDTII

3D TRACKING OF MOTILE MICROORGANISMS

AN EXPERIMENTAL INVESTIGATION OF THE KINEMATICS AND INTERACTIONS OF C. REINHARDTII

Dissertation

for the purpose of obtaining the degree of doctor
at Delft University of Technology,
by the authority of Rector Magnificus prof. dr. ir. T.H.J.J. van der Hagen,
Chair of the Board for Doctorates,
to be defended publicly on
Thursday 21 November 2024 at 12.30 o'clock

by

Junaid MEHMOOD

Master of Science in Chemical Engineering,
Delft University of Technology, Delft, The Netherlands,
born in Vehari, Pakistan.

This dissertation has been approved by the promoters.

Composition of the doctoral committee:

Rector Magnificus,	chairperson
Dr. D. S. W. Tam,	Delft University of Technology, promotor
Dr. A. J. L. L. Buchner,	Delft University of Technology, copromotor
Independent Members:	
Prof. dr. ir. J. T. Padding	Delft University of Technology, The Netherlands
Prof. dr. V. Garbin	Delft University of Technology, The Netherlands
Dr. H. Gadelha,	University of Bristol, England
Dr. G. J. Amador,	Wageningen University & Research, The Netherlands
Dr. ir. G. E. Elsinga,	Delft University of Technology, *reserve member*

This research was funded through European Research Council project no. 716712.

Keywords: Microorganisms, Motility, Chlamydomonas Reinhardtii, 3D Tracking, Multi-camera microscopy, Low Reynolds number, Kinematics, Cell-cell interactions, Non-Newtonian, Viscoelasticity, Surface interactions

Printed by: Gildeprint - Enschede

Cover design: Junaid Mehmood

ISBN: 978-94-6384-673-8

An electronic version of this dissertation is available at
`http://repository.tudelft.nl/`.

The most exciting phrase to hear in science, the one that heralds new discoveries, is not ‘Eureka!’ but ‘That’s funny…’

Isaac Asimov

CONTENTS

SUMMARY

Despite significant advancements in microscopy, studying microorganism locomotion has been limited by either low resolution or low accuracy. Two-dimensional techniques fail to capture the nuances of three-dimensional movement, while three-dimensional techniques often lack higher resolution. This thesis introduces a novel 3D tracking system and methods to improve the understanding of microorganism motility within their three-dimensional complex fluid environments. The new imaging techniques developed allow for a more detailed exploration of microorganism kinematics and interactions, addressing limitations of previous methods, and improving both accuracy and resolution.

The dissertation is organized into five chapters. Chapter 1 discusses the importance of studying microorganisms, focusing on their motility and locomotion at low Reynolds numbers. It reviews previous work, highlights open questions in the field, and discusses the need for better 3D imaging techniques.

Chapter 2 showcases the multi-camera microscopy system designed for 3D tracking of microswimmers, featuring a single objective, a light source, and four sCMOS cameras. Advanced calibration and tracking algorithms based on projective geometry enable tracking microorganisms with higher accuracy. This system captures significantly denser image data and reveals new insights into the helical swimming patterns and diffusive behavior of the unicellular green alga, *C. reinhardtii*.

Chapter 3 focuses on the pair-wise interactions of *C. reinhardtii*, utilizing the capabilities of the multi-camera system to observe over half a million 3D trajectories. The findings indicate asymmetrical scattering behaviors and avoidance of permanent bound states during interactions, challenging previous theoretical models. This analysis underscores the importance of real-world dynamics in understanding cell-cell interactions, facilitated by a robust tracking system and enhanced by numerical simulations using a spring-bead model.

Chapter 4 explores the effects of non-Newtonian fluid rheology on the kinematics and surface interactions of *C. reinhardtii*. It contrasts the behaviors of cells in Newtonian and viscoelastic fluids, noting differences in flagellar beating frequency, swimming speed, and helical path characteristics. The study highlights how the viscosity and elasticity of the medium influence the motility and surface interaction patterns of microorganisms. This work shows that cells in viscoelastic fluids have higher reorientation times and different scattering dynamics compared to Newtonian fluids.

Chapter 5 provides an outlook on the future directions and potential impact of this work. It discusses how the novel 3D tracking system and methodologies developed in this thesis can advance our understanding of microorganism motility and interactions. The insights gained from this research have broad implications for various fields, including biological research, medical diagnostics, and environmental science.

SAMENVATTING

Ondanks significante vooruitgangen in microscopie is het bestuderen van de voortbeweging van micro-organismen beperkt gebleven door ofwel lage resolutie ofwel lage nauwkeurigheid. Tweedimensionale technieken kunnen de nuances van driedimensionale beweging niet vastleggen, terwijl driedimensionale technieken vaak een hogere resolutie missen. Deze thesis introduceert een nieuw 3D-tracksysteem en methoden om het begrip van de motiliteit van micro-organismen in hun driedimensionale complexe vloeistofomgevingen te verbeteren. De nieuw ontwikkelde beeldvormingstechnieken maken een meer gedetailleerde verkenning van de kinematica en interacties van micro-organismen mogelijk, waarbij de beperkingen van eerdere methoden worden aangepakt en zowel de nauwkeurigheid als de resolutie worden verbeterd.

Het proefschrift is onderverdeeld in vijf hoofdstukken. Hoofdstuk 1 bespreekt het belang van het bestuderen van micro-organismen, met de nadruk op hun motiliteit en voortbeweging bij lage Reynolds-getallen. Het bespreekt eerder werk, belicht open vragen in het veld en bespreekt de behoefte aan verbeterde 3D-beeldvormingstechnieken.

Hoofdstuk 2 toont het multi-camera microscopie systeem dat is ontworpen voor 3D-tracking van microswimmers, met een enkele objectief, een lichtbron en vier sCMOS-camera's. Geavanceerde kalibratie- en trackingsalgoritmen gebaseerd op projectieve geometrie maken het mogelijk om micro-organismen met hogere nauwkeurigheid te volgen. Dit systeem vangt aanzienlijk dichtere beeldgegevens op en onthult nieuwe inzichten in de helixvormige zwempatronen en diffusief gedrag van de eencellige groene alg, *C. reinhardtii*.

Hoofdstuk 3 richt zich op de pareninteracties van *C. reinhardtii*, waarbij gebruik wordt gemaakt van de mogelijkheden van het multi-camera systeem om meer dan een half miljoen 3D-trajecten te observeren. De bevindingen wijzen op asymmetrisch verstrooiingsgedrag en het vermijden van permanente gebonden toestanden tijdens interacties, wat eerdere theoretische modellen uitdaagt. Deze analyse benadrukt het belang van real-world dynamiek bij het begrijpen van cel-cel interacties, gefaciliteerd door een robuust volg systeem en verbeterd door numerieke simulaties met een veer-kraal model.

Hoofdstuk 4 onderzoekt de effecten van niet-Newtoniaanse vloeistofreologie op de kinematica en oppervlakte-interacties van *C. reinhardtii*. Het vergelijkt het gedrag van cellen in Newtoniaanse en visco-elastische vloeistoffen, waarbij verschillen in flagellabeatsfrequentie, zwemsnelheid en spiraalvormige padkenmerken worden opgemerkt. De studie benadrukt hoe de viscositeit en elasticiteit van het medium de beweeglijkheid en oppervlakte-interactiepatronen van micro-organismen beïnvloeden, waarbij visco-elastische vloeistoffen heroriëntatietijden verlengen en verstrooiingsdynamiek veranderen in vergelijking met Newtoniaanse vloeistoffen.

Hoofdstuk 5 geeft een vooruitblik op toekomstige richtingen en de potentiële impact van dit werk. Het bespreekt hoe het nieuwe 3D-tracking systeem en de methodologieën ontwikkeld in dit proefschrift ons begrip van de beweeglijkheid en interacties van micro-organismen kunnen verbeteren. De inzichten verkregen uit dit onderzoek hebben brede implicaties voor verschillende velden, waaronder biologisch onderzoek, medische diagnostiek en milieuwetenschappen.

خلاصہ

خوردبینی کے شعبے میں نمایاں پیش رفت کے باوجود، خوردبینی جانداروں کی حرکت کا مطالعہ اکثر کم ریزولیوشن یا درستگی کی کمی کی وجہ سے محدود رہتا ہے۔ دو جہتی تراکیب تین جہتی حرکت کی باریکیوں کو مکمل طور پر نہیں سمجھ پاتیں، جبکہ تین جہتی تکنیکیں عموماً زیادہ ریزولیوشن فراہم نہیں کرتیں۔ اس مقالے میں ایک نیا تین جہتی ٹریکنگ سسٹم اور اس سے متعلقہ طریقے متعارف کرائے گئے ہیں، جو پیچیدہ سیال ماحول میں خوردبینی جانداروں کی حرکت کو بہتر طور پر سمجھنے میں مدد دیتے ہیں۔ یہ نئی امیجنگ تکنیکیں زیادہ تفصیلی معائنہ ممکن بناتی ہیں اور پچھلے طریقوں کی خامیوں کو دور کرتے ہوئے ریزولیوشن اور درستگی دونوں میں بہتری فراہم کرتی ہیں۔

یہ مقالہ پانچ ابواب پر مشتمل ہے۔ باب اول خوردبینی جانداروں کی تحقیق کی اہمیت اور کم رینالڈز نمبروں کے تحت ان کی حرکت کے مطالعے پر روشنی ڈالتا ہے۔ اس باب میں پچھلی تحقیقات کا جائزہ لیا گیا ہے، موجودہ تحقیقی سوالات کو اجاگر کیا گیا ہے، اور بہتر تین جہتی امیجنگ تکنیکوں کی ضرورت پر زور دیا گیا ہے۔

باب دوم میں ملٹی کیمرہ مائیکروسکوپی سسٹم کا تعارف کرایا گیا ہے، جو خوردبینی جانداروں کی تین جہتی ٹریکنگ کے لیے بنایا گیا ہے۔ اس نظام میں ایک عدسہ، روشنی کا ذریعہ اور چار کیمرے شامل ہیں۔ پروجیکٹیو جیومیٹری پر مبنی جدید کیلیبریشن اور ٹریکنگ الگورتھمز کے ذریعے، یہ نظام خوردبینی جانداروں کی زیادہ درستگی سے ٹریکنگ کرتا ہے۔ اس سسٹم کی مدد سے زیادہ مفصل ڈیٹا حاصل کیا جا سکتا ہے، اور یک خلوی سبز الجی کی پیچیدہ حرکت کے نئے پہلو دریافت کیے جا سکتے ہیں۔

باب سوم میں یک خلوی سبز الجی کے جوڑوں کے تعاملات پر روشنی ڈالی گئی ہے۔ ملٹی کیمرہ سسٹم کی صلاحیتوں کو استعمال کرتے ہوئے، پانچ لاکھ سے زیادہ تین جہتی ٹریکنگ ڈیٹا کا تجزیہ کیا گیا ہے۔ نتائج سے ظاہر ہوتا ہے کہ یہ جاندار قریب آنے کے بعد غیر متناسب زاویوں پر بکھر جاتے ہیں اور مستقل جکڑاؤ میں نہیں پھنستے، جو کہ نظریاتی ماڈلز کے لیے ایک چیلنج ہیں۔ یہ تجزیہ خلیوں کے تعاملات کو سمجھنے میں حقیقی دنیا کی حرکیات کی اہمیت کو واضح کرتا ہے۔ اس مطالعے اور مشاہدے کی کامیابی کا سہرا اس بیان کردہ ٹریکنگ سسٹم اور اسپرنگ بیڈ ماڈل کے استعمال کو جاتا ہے۔

باب چہارم میں یک خلوی سبز الگا کی حرکیات اور سطحی تعاملات پر نان نیوٹنین مائعات کے ریالوجیکل اثرات کو تفصیل سے جانچا گیا ہے۔ اس باب میں نیوٹونین اور ویزکوئیلاسٹک مائعات میں خلیات کے رویے کا موازنہ کیا گیا ہے، جس میں فلیجلا کی بیٹنگ فریکوئنسی، تیراکی کی رفتار، اور پیچدار راستے کی خصوصیات کے درمیان فرق کو نمایاں کیا گیا ہے۔ یہ مطالعہ دکھاتا ہے کہ میڈیم کی چپچپاہٹ اور لچک خوردبینی جانداروں کی حرکت اور سطحی تعاملات کو کس طرح متاثر کرتی ہیں۔

باب پنجم اس تحقیق کے مستقبل کے امکانات اور اس کے اثرات پر روشنی ڈالتا ہے۔ اس باب میں، مقالے میں پیش کیے گئے نئے تین جہتی ٹریکنگ سسٹم اور طریقہ کار کی اہمیت پر بات کی گئی ہے اور یہ کہ یہ نظام خوردبینی جانداروں کی حرکت اور تعاملات کو سمجھنے میں کیسے مدد کر سکتا ہے۔ اس تحقیق سے حاصل ہونے والے نتائج مختلف شعبوں میں اہمیت رکھتے ہیں، جن میں حیاتیاتی تحقیق، طبّی تشخیص، اور ماحولیاتی سائنس شامل ہیں۔

1

INTRODUCTION

"Journey before destination is the ancient code of the Knights Radiant. Some may call it a simple platitude, but it's far more. A journey will have pain and failure. It is not only the steps forward that we must accept. It is the stumbles, the trials, the knowledge that we will fail and hurt those around us. But, if we choose to stop, if we accept the person we are when we fall, the journey ends, that failure becomes our destination. To love the journey is to accept no such end. I have found through painful experiences, that the most important step a person can take is always the next one."

Dalinar Kohlin in Oathbringer, Brandon Sanderson

And my journey begins here.

1.1. THE DANCE OF MICROORGANISMS

In the vast canvas of life on Earth, the complex dance of microorganisms often goes unnoticed. However, within this microscopic realm lies a fascinating world of motion, where bacteria, algae, and other microscopic life forms perform a ballet of survival, propagation, and interaction. Their ability to move independently, powered by metabolic energy, is a crucial component of the Earth's biological processes, impacting diverse areas from nutrient cycles to disease transmission [1].

Until about 350 years ago, this microscopic world remained largely unknown, hidden due to its small scale. This changed with the pioneering work of Antonie van Leeuwenhoek, a Dutch scientist in Delft, who, using basic microscopes he had built, discovered a world teeming with microscopic life. His observations provided initial insights into the movement, diversity, and environmental interactions of microorganisms [2, 3]. Previously invisible, these microorganisms are now recognized as vital to the health and diversity of the biosphere. The study of their dynamics has become crucial in the field of microbiology and biophysics, essential for understanding fundamental life processes and broadening comprehension of life.

The study of microorganism motility is highly relevant, with significant implications for environmental sustainability, biotechnology, health, agriculture, and even the understanding of climate change. For instance, in biotechnology, understanding the motility of microorganisms is essential for developing photobioreactors that sustainably convert algae biomass into bio-fuel [4, 5]. The efficiency of these reactors relies heavily on the microorganisms' ability to move and interact within a complex fluid environment, among many other factors [6]. Understanding the microorganisms' kinematics and interactions can inform advancements in reactor design, leading to more efficient biofuel production. In health and medicine, many pathogenic microorganisms are motile, and their locomotion can be critical to their virulence and colonization capabilities [7]. Studying their motility and interactions can provide valuable insights for developing new treatments and interventions [8, 9]. For instance, biofilms, communities of microorganisms that adhere to surfaces in an extracellular polymeric substance (EPS), are influenced by microbial motility and can cause serious issues in numerous industrial and clinical settings [10]. Understanding the motility and interactions of microorganisms can lead to better prediction and potentially controlling the biofilm formation [11]. In agriculture, motile bacteria are critical in soil health and nutrient cycling, directly affecting crop yields [12]. Furthermore, the movement of microorganisms, particularly in the ocean, has been recognized as an essential factor in Earth's biogeochemical cycles [13]. This has implications for understanding climate change and the design of mitigation strategies [14].

Investigating microorganism motility not only reveals a fascinating natural phenomenon but also opens the door to many practical applications. This dissertation aims to contribute to this burgeoning field by enhancing the understanding of microorganism motility and providing new insights that can support advancements toward a sustainable future.

1.2. PHYSICS OF MICROSWIMMER LOCOMOTION

One may wonder how microorganisms, as small as they are, navigate and survive in vastly different physical environments. To understand the intricacies of microorganism motility, it is crucial to step into their world and explore the governing physical principles. The incredible diversity of motile microorganisms presents a broad range of motility mechanisms, yet they all have one unifying feature: their interaction with the fluid environment. The mechanisms of their movement are dictated by their size and the properties of the fluids they inhabit. Their world is dominated by viscosity, as opposed to forces such as gravity and inertia that dictate our macroscopic world.

The microscopic world of these microorganisms is characterized by low Reynolds numbers. The Reynolds number, defined as the ratio of inertial forces to viscous forces in fluid flow, is expressed as $\mathrm{Re} = \rho LU/\eta$, where ρ is the fluid's density, L is the organism's characteristic length, U is the characteristic velocity, and η is the fluid's viscosity. Inertial forces, which are influenced by the fluid's density, the organism's velocity, and size, reflect the fluid's tendency to maintain its motion due to momentum. Viscous forces, conversely, represent the fluid's internal resistance to flow changes, resisting variation in speed or direction, and are governed by the fluid's viscosity. The value of the Reynolds number distinguishes between different swimming regimes, indicating whether inertial or viscous forces dominate. For $\mathrm{Re} \ll 1$, locomotion occurs in the Low Reynolds number regime, a typical characteristic of microorganism swimming. For example, in the case of *Chlamydomonas Reinhardtii*, an alga, with $L = 10\mu\mathrm{m}$ and $U = 100\mu\mathrm{m/s}$ while navigating in water, the Reynolds number is at $O(10^{-3})$. In such a regime, the effect of viscous dissipation far surpasses that of inertial forces. This reality is eloquently captured by Purcell [15]:

> *"For these animals, inertia is totally irrelevant. We know that $F = ma$, but they could scarcely care less."*

In environments where the Reynolds number is relatively high, the flow dynamics are primarily governed by inertial forces. This regime is typical for organisms like fish, birds, and insects [16, 17]. These organisms use locomotion strategies that leverage inertia and would be largely ineffective at low Reynolds numbers due to the influence of viscous forces. Consequently, microorganisms have evolved to devise strategies that proficiently circumvent and exploit the viscous drag to move and interact in the fluid environments they inhabit.

1.3. SWIMMING OF MICROORGANISMS

Microorganisms have adopted various swimming strategies, many of which rely on whip-like appendages called flagella. Fig. 1.1 presents different microorganisms and their motility strategies.

The bacterium *Salmonella typhimurium* (Fig. 1.1A) propels itself forward using a bundle [21] of multiple flagella. The flagella rotate collectively in a counter-clockwise direction, propelling the bacterium in a straight ‘run’ When one or more flagella change their rotation to a clockwise direction, the bundle disassembles, causing the bacterium to ‘tumble’ and change direction for the subsequent ’run’ [22, 23] as shown in Fig. 1.1B.

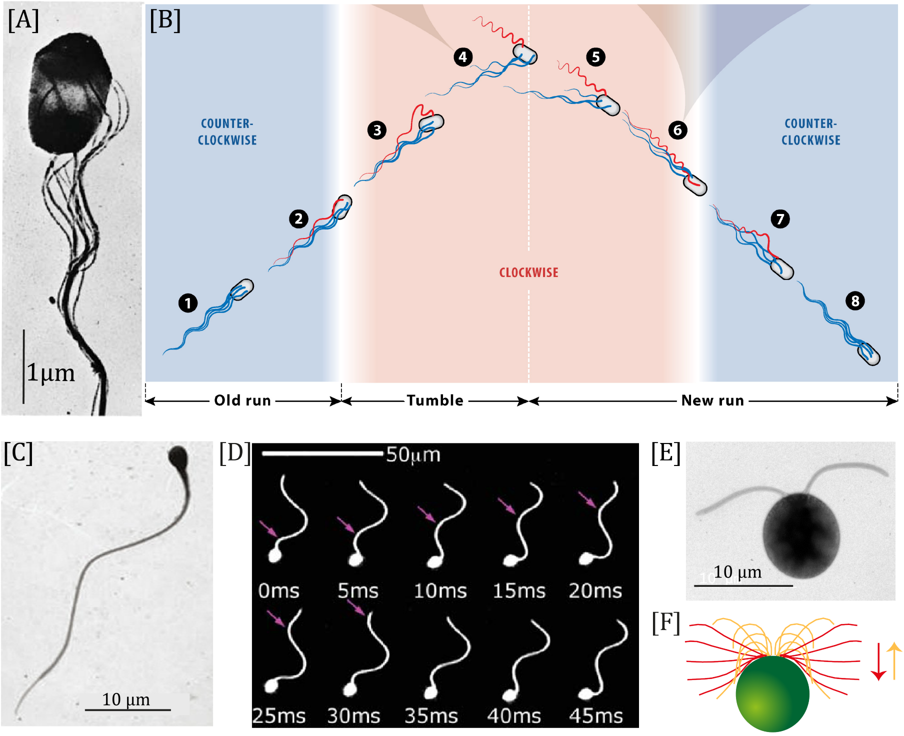

Figure 1.1: Various motility strategies observed in microorganisms. [A] *Salmonella typhimurium* bacteria with a bundle of rotating flagella. Adapted from [3]. [B] 'Run and tumble' motion of bacteria: Counter-clockwise rotation of the whole flagella bundle during a run (blue) and clockwise rotation of at least one flagellum causing a tumble (red), resulting in changes in flagellar form and cell direction. Adapted from [18]. [C] Human sperm cell and its single, wave-like moving flagellum. Adapted from [19]. [D] The flagellar motion of sperm cells: a sinusoidal wave propagating from the head to the tip. Adapted from [3]. [E] *Chlamydomonas Reinhardtii*, a unicellular alga with two flagella. Adapted from [20]. [F] 'Breaststroke' motion of *C. reinhardtii*'s flagella: The flagella move in opposing directions during power (red) and recovery (yellow) strokes, propelling the cell body forward and backward as indicated by yellow and red arrows, respectively.

This 'run and tumble' motion is characteristic of many bacteria and enables efficient exploration of their environment [3]. Sperm cells exhibit a different variation of flagellar locomotion (Fig. 1.1C). Here, a single flagellum beats in a wave-like fashion, driving the sperm cell forward. The undulating wave starts at the base of the flagellum near the cell body and travels towards the tip (Fig. 1.1D). The shape and amplitude of this wave motion are different on one side of the flagellum compared to the other as the wave travels from the base to the tip. This asymmetric waveform, combined with the bending flexibility of the flagellum, generates a net forward motion [21]. The green alga *Chlamydomonas reinhardtii* (Fig. 1.1E), a eukaryotic microorganism, employs two flagella for movement. These flagella beat in a coordinated, symmetrical pattern akin to a ‘breaststroke’ motion [24]. The simultaneous motion of the two flagella propels the alga forward in a direction opposite to the stroke (Fig. 1.1F). These highlighted examples of bacteria, spermatozoa, and green algae represent only a small fraction of the diverse locomotion strategies exhibited by microorganisms. Other examples, like the spinning motion of dinoflagellates [25] or the coordinated flagellar movement in Volvox colonies [3], further enrich this diversity. The range of these strategies has evolved in response to the unique ecological environments these microorganisms inhabit, highlighting the complexity and adaptability of life at microscopic scales.

So far, we have explored the diverse strategies that microorganisms use to navigate their environments. The reasons behind their motility are equally diverse. Microorganisms display directed motility, known as ‘taxis’, to move towards or away from specific stimuli, such as chemical concentration (chemotaxis) [22, 26], light (phototaxis) [24, 27, 28], and gravity (gravitaxis) [29]. These responses play a significant role in the survival and proliferation of microorganisms. For example, chemotaxis, a well-studied form of taxis, is crucial for bacteria to find nutrients and avoid toxins in their environment [30]. Phototaxis influences the behavior of algae, such as *Euglena* and *Chlamydomonas*, with movement towards or away from light sources to optimize their photosynthetic activity [31].

Beyond the motility of individual cells, microorganisms exhibit collective behaviors. These behaviors result from inter-cellular interactions [32], enabling them to form larger, more complex structures and dynamic patterns beyond the sum of their individual components [33]. Biofilms are a classic example of microbial collective behavior. These are colonies of bacteria embedded within a self-produced matrix of extracellular polymeric substances, allowing bacterial communities to protect themselves from environmental stressors, antibiotics, and the host immune response [34]. In fluid environments, dense suspensions of bacteria like *Bacillus subtilis* exhibit collective swimming, resulting in micro-scale turbulence [35, 36]. This turbulent behavior is reminiscent of high Reynolds number turbulence, and the energy spectrum for both classic and bacterial turbulence follows a power law [35]. Sperm cells also display collective behavior, which varies between different species. For example, mass motility is observed for bull and ram semen, where cells self-organize and show features similar to bacterial turbulence [37, 38]. For rodent species, sperm trains are formed where sperm cells aggregate and link with each other due to hydrodynamic interactions, resulting in increased velocity for the group, compared to the individual [39]

Both individual and collective behaviors of microorganisms are significantly affected by the complex environments they inhabit. These are typically not just simple aqueous solutions but complex fluids, including solid particles and polymeric molecules, exhibiting non-Newtonian rheology. These environments range from the mucus layers within an animal’s body and biofilms to the soil and sediments in aquatic and terrestrial ecosystems. The complex nature of these fluids presents challenges for swimming microorganisms. The non-Newtonian properties, such as shear-thinning or thickening behavior and elasticity, can significantly alter the swimming dynamics compared to a Newtonian fluid [40, 41]. The effect of the rheological properties of these complex fluids on the swimming strategies of individual microorganisms is multifaceted. For example, spermatozoa show changes in their swimming paths in response to the rheological properties of the surrounding fluid. Sperm cells swim on straighter paths in mucus, which exhibits viscoelastic properties, compared to semen [42]. Similarly, bacterial species like *E. coli* also experience changes in their swimming dynamics in response to the non-Newtonian nature of their surroundings. The swimming velocity of bacteria significantly reduces in non-Newtonian fluids with both shear-thinning and viscoelastic properties compared to Newtonian ones [43, 44]. In addition, eukaryotic microorganisms like *C. reinhardtii* display alterations in their flagellar beating frequency in response to the rheological properties of their environment. When these organisms encounter more viscous environments, the beating frequency of their flagella reduces. However, elasticity changes this behavior, and cells beat at higher frequencies than pure viscous environments [45].

Apart from individual responses, the non-Newtonian rheology of complex fluids also influences the collective behaviors of microorganisms. For example, spermatozoa display collective behaviors affected by the rheological properties of the medium, with viscoelasticity resulting in enhanced clustering [46]. *Escherichia coli* exhibits a vortex swimming pattern at high concentrations with only a counter-clockwise swimming direction. In large polymer concentrations, the direction of the vortex reverses and oscillates between clockwise and counter-clockwise patterns [47]. Moreover, for *Bacillus subtilis*, the velocity correlation for their collective motion increases with the concentration of viscoelastic media. In contrast, the variations in the concentration of Newtonian media do not affect the velocity correlation [48]. This suggests that the collective behavior of *B. subtilis* is primarily influenced by fluid elasticity.

In light of these observations, it is evident that the dynamics of microorganisms' locomotion are influenced by the interaction with their diverse and complex environments. The movements of microorganisms, whether alone or in groups, are closely linked to their environment's physical and rheological characteristics. This section has provided an overview of microorganism locomotion, yet the topic's complexity goes beyond this summary. For a deeper understanding, comprehensive reviews by Lauga and Powers [2], Elgeti *et al.* [3], and Spagnolie and Underhill [49] are recommended.

1.4. TECHNOLOGICAL LIMITATIONS AND UNCHARTED FRONTIERS

Despite considerable progress in understanding microorganism locomotion, numerous open questions invite further exploration. These questions arise from the limited understanding of microorganism motility in a three-dimensional (3D) context. Microorganisms naturally move and interact in three-dimensions, and studying them in an environment that mimics their habitats is essential. Traditional two-dimensional (2D) studies have provided valuable insights but offer only a partial view, missing the full complexity of 3D motion. To address this need, promising 3D tracking technologies have emerged such as tracking microscopy [22, 50], defocused particle tracking [51, 52], and holographic microscopy [53, 54]. These techniques have advanced the study of microorganism trajectories and behaviors in 3D environments. However, they come with limitations, including but not limited to resolution constraints [55, 56] and the complexity of tracking multiple organisms simultaneously [57], particularly in densely populated suspensions.

The limitations of existing technologies have left several important areas of research unexplored. Understanding short- and long-range hydrodynamic interactions and their influence on the collective behavior of microorganisms remains a significant challenge [58]. Despite investigations into individual behavior [2, 3] and some aspects of collective dynamics [33, 59], the specific characteristics and effects of these interactions are still elusive. The ongoing debate on whether collective behavior stems from short or long-range interactions [60–62] necessitates more advanced 3D imaging and tracking techniques.

Another important question in the study of microorganism locomotion is how non-Newtonian fluid properties affect their 3D motility. Most current understanding is derived from studies in simple, Newtonian fluids, which fail to mimic the complex environments where microorganisms typically exist. A few experimental studies in non-Newtonian fluids have shown the complex interplay between rheological properties and locomotion of microswimmers. These studies predominantly utilize two-dimensional microscopy. However, microorganism motility is inherently three-dimensional. Therefore, a comprehensive understanding of motility in such environments requires detailed three-dimensional investigations that can accurately capture critical behaviors such as helical trajectories, cell orientation, and tactic responses. Bridging this gap could have far-reaching implications, including optimizing bio-remediation processes and advancing drug delivery systems.

Advancing 3D microscopic tracking techniques is necessary to allow for more detailed exploration of key research areas. For instance, 3D imaging can improve our understanding of microorganism morphology and how physical structure influences motility. Investigating responses to stimuli, such as chemical gradients or light, can benefit from 3D tracking, offering a more detailed understanding of tactic behaviors and how microorganisms navigate their complex environments. Furthermore, 3D techniques can enhance the study of microbial interactions with their abiotic environment, revealing new aspects of their behavior and survival strategies.

1.5. OBJECTIVE AND OUTLINE OF THE DISSERTATION

This dissertation advances our understanding of microorganism motility by introducing a novel 3D imaging technique. Specifically, we explore 3D kinematics and interactions between microorganisms and their navigation in complex fluids. The thesis is structured into three main chapters addressing distinct but interrelated research questions. While each chapter can be read individually, they collectively form a comprehensive exploration of microorganism motility in 3D environments.

1. **Three-dimensional Microscopy of Microorganisms (Chapter 2):** This chapter introduces our three-dimensional tracking system, designed to image the movement of microswimmers, focusing on the green alga, *C. reinhardtii*. We first detail our experimental setup and the calibration processes. The performance of our system is evaluated through tracking *C. reinhardtii* at various concentrations. This system offers improvements over previous methods, notably its capability to track at higher

image densities of 0.06 particles per pixel. We record trajectories and shed light on the 3D dynamics of these organisms and their interactions with surfaces. Our analysis reveals that *C. reinhardtii* cells predominantly move in helical patterns, with a left-handed chirality. We also examine the diffusive behaviors of these cells and show that 3D tracking is necessary to accurately determine their diffusive characteristics. Additionally, our findings demonstrate the effect of hydrodynamic forces on cellular interactions with surfaces.

2. **Pair-wise interactions of *Chlamydomonas reinhardtii* (Chapter 3):** This chapter explores the pair-wise interactions of microorganisms and their effects on kinematics and trajectories. Using our multi-camera microscope setup and in-house tracking algorithm, we capture three-dimensional trajectories of unicellular alga *C. reinhardtii*. We find asymmetry in the scattering of pairs and highlight the roles of the approach angle and minimal approach distance between cells. The stochasticity in the cell dynamics due to biological noise leads to changes in the swimming direction, competing with those induced by pair interactions. Numerical simulations provide further insight into these interactions. Our experimental and numerical results qualitatively agree and indicate that cells scatter more strongly at short distances with nearly parallel approach angles.

3. **Kinematics & Surface Interactions of *Chlamydomonas reinhardtii* in Complex Fluids (Chapter 4):** This chapter addresses the relatively unexplored area of 3D swimming behaviors of microorganisms in complex fluids. We examine the effects of non-Newtonian rheology on the kinematics and surface interactions of *C. reinhardtii* cells. By leveraging two primary imaging techniques, 2D tracking with an inverted microscope and 3D tracking with our multi-camera microscope setup, we investigate how these cells navigate and adapt to their environment. Our investigations reveal the influence of fluid properties on swimming behaviors, surface interactions, and adaptation strategies to improve phototaxis. In viscoelastic solutions, *C. reinhardtii* cells display an increased beating frequency but no related increase in swimming speed. We also find that irrespective of the medium, *C. reinhardtii* cells adapt their swimming to maintain a constant rotational velocity along their helical trajectory. We also show that in viscoelastic fluids, cells swim closer to the surface, resulting in higher cell accumulations near surfaces than Newtonian fluids.

2

THREE DIMENSIONAL TRACKING OF MICROSWIMMERS

Understanding the locomotion of microorganisms is essential for insights into microbial ecology, infection, and colonization processes. Two-dimensional microscopy has remained an essential tool in acquiring this understanding, yet it fails to capture the full scope of microswimmers' three-dimensional (3D) motility. Recent advances in three-dimensional imaging techniques like Defocused Particle Tracking, Holographic Tracking Velocimetry, and Stereo-microscopy have improved the detail and precision of observations. However, these methods still face challenges with resolution at high particle densities and tracking multiple particles simultaneously. This chapter introduces a unique multi-camera microscopy system that significantly improves the accuracy of tracking microswimmers in three dimensions. This system uses four sCMOS cameras to image microorganisms in the same volume of approximately 2.5 × 2.5 × 2 mm^3*. We evaluate the performance of our microscopy system by tracking a population of the unicellular motile algae Chlamydomonas reinhardtii. An in-house tracking algorithm based on the projective geometry framework facilitates tracking with reprojection errors of 0.3 body lengths. Our system allows imaging and tracking image densities of 0.06 particles per pixel, one order of magnitude higher than other 3D microscopy techniques. Analysis of C. reinhardtii trajectories in 3D revealed predominantly left-handed chirality and helical swimming patterns. Moreover, our three-dimensional tracking data yielded translational and rotational diffusion coefficients that differed from those obtained via traditional two-dimensional methods. This highlights the limitations of previous approaches and the need for three-dimensional data to characterize microswimmer motility appropriately.*

Part of this chapter has contributed to "J. Mehmood, K. Muller, S. Kumar, A.J. Buchner, and D.S.W. Tam, “Three dimensional tracking of microswimmers”, Experiments in Fluids, 2024, [Submitted]"

2.1. INTRODUCTION

The study of microbial ecology, colonization, and infection requires a fundamental understanding of the interactions between microorganisms and their physical environment, including surface interactions, accumulations, cell-cell interactions, and collective behavior. Tracking the motion and orientation of these microorganisms is, therefore, crucial to gain insights into their behavior and how they navigate through complex environments and respond to external stimuli such as light [28, 63], gravity [64], chemical gradients [65, 66] or physical barriers [67, 68]. Moreover, tracking microswimmers also has practical applications, including optimizing the design of bioreactors [69, 70], developing more effective strategies for the treatment of infections [8, 9], and monitoring the formation and dispersal of biofilms [11].

Microswimmers display a wide range of motility patterns, which are three-dimensional in nature. For instance, bacteria navigate complex 3D environments through stochastic patterns of linear movements and sudden reorientations [3, 71]. Protists, such as *Chlamydomonas Reinhadtii*, display inherently three-dimensional helical swimming behavior [24, 28, 72]. Most studies focusing on microorganism locomotion have relied on two-dimensional optical microscopy as a main tool for live imaging of microswimmers [24, 73–81]. However, two-dimensional microscopy does not capture the full range of the kinematics of microswimmers [82]. Furthermore, more complex trajectory parameters, e.g., curvature and torsion, which underlie microswimmer motion, are lost or have higher signal-to-noise ratios. Therefore, to fully understand microswimmer locomotion, it is essential to use three-dimensional trajectory data, which enables a more accurate and detailed representation of their motile behavior.

An early experimental technique, developed to obtain three-dimensional motility data of microswimmers, was designed to track the bacterium *Escherischia coli* [50]. In this method, the microorganism was kept in focus by physically moving the microscope stage using feedback control, and the three-dimensional motion was deduced from the displacements of the stage. Such tracking microscopes have been used to characterize different aspects of bacterial motility, such as chemotaxis [22], rheotaxis [83], and coupled motion of the cell body and flagellum [84]. This method is limited to tracking one object at a time, resulting in a low throughput of acquired trajectories that limit the characterization of the population behavior. Additionally, microorganisms with the size ranging from 10 μm (*C. reinhardtii*) to 100 μm (*Volvox*) require a larger flow chamber to inhibit surface effects. Tracking microscopy for these larger flow chambers induces uncontrolled background flow inside the chamber. To address these limitations, several imaging techniques have been developed in recent years that enable the tracking of multiple microswimmers simultaneously, resulting in higher throughput of acquired trajectories and more comprehensive characterization of individual and population behavior. These methods include defocused particle tracking (DPT) [51, 52, 82, 85], holographic tracking velocimetry (HTV) [53, 54, 86–89], and stereo-microscopy [90–94], among others.

In Defocused Particle Tracking (DPT), the three-dimensional positions of particles are tracked using the image characteristics they exhibit. These characteristics arise due to the spherical aberrations of the microscopic objective [51, 82]. When a particle is at the focal plane, its image appears as a sharp point. However, any displacement from this plane results in defocused images. This defocus presents itself in the form of rings arising due to both diffraction and the spherical aberrations of the lens system. The diameter of these rings is directly proportional to the particle's distance from the focal plane, and this relationship is used to determine the three-dimensional position of the particle [95]. DPT facilitates a depth of field that varies from 30 μm [85] to 200 μm [82]. This technique has proven instrumental in examining the collective dynamics of *E. coli* [52], discerning bacterial species' variations in run and tumble behaviors [82], and to measure the flow field of *Euglena gracilis* [85]. DPT has the main advantage of being easy to use, with simple optical setup requirements and multi-particle tracking. However, defocusing methods face limitations at higher particle densities and are sensitive to low signal-to-noise ratio [57].

In Holographic Tracking Velocimetry (HTV), a particle's three-dimensional position is determined from its hologram, a recorded interference pattern, using digital holography. While various methods exist to create this hologram, single beam in-line holography is used for microscopic applications [57]. In this particular method, the hologram is produced by the combination of the wave scattered by the particle (object beam) and the unscattered portion of the illumination beam (reference beam). This interference pattern provides the necessary data regarding phase and amplitude for numerical algorithms to reconstruct the particle's position in three dimensions. HTV has been used to study the motility of various species, such as copepod *nauplius* [96], dinoflagellates (*Pfiesteria piscicida, Karlodinium veneficum, Prorocentrum minimum*) [54, 87], spermatozoa [86] and different bacterial species (*E. coli, Agrobacterium tumefaciens, Pseudomonas aeruginosa*) [88, 89]. HTV offers higher accuracy and a larger depth of field ($\sim 100-1000\mu m$) than tracking microscopy and DPT. However, it still faces challenges in reconstructing overlapping holograms, limiting its resolution [56] and has a larger uncertainty of one to two particle diameters along the optical axis [55].

Stereoscopic microscopy utilizes two distinct optical paths, each with its respective camera system, to image particles from different viewing directions. Particle images are first identified and matched across both camera views. The three-dimensional positions of the particles are then determined by computing the points of intersection of the lines of sight corresponding to the particle images from each camera view. The depth of field for these microscopes is primarily influenced by the geometry of the optical path and the characteristics of the objective lens, enabling stereo microscopy to achieve a depth of field of 2000 μm [92]. Stereo-microscopy has been used to study the three-dimensional trajectories of sea urchin larvae *Clypeaster japonicus* [90], and green algae *C. reinhardtii* [91–93]. Compared to DFT and HTV, stereoscopic microscopy is advantageous as it offers a greater depth of field and relies on simpler computational algorithms [93] for particle position reconstruction. However, it is limited by the use of low particle densities to avoid false particle identifications and overlapping images [97]. Moreover, in practice, the lines of sight from the two cameras never really intersect, compromising calibration precision and thereby diminishing the technique's overall efficacy.

The methods discussed above have provided important insights into the three-dimensional locomotion of different microswimmers. However, tracking multiple cells leads to high occlusion rates and results in low tracking certainty. The development of an experimental technique to accurately track multiple microswimmers is of great interest to the study of many outstanding questions in biophysics, e.g., population behavior in a complex 3D environment like that encountered in nature, and the description of cell-cell interactions.

Here, we present a unique multi-camera microscopy system to track microswimmers in three dimensions with high tracking accuracy at low to medium particle densities. Our tracking system uses four sCMOS cameras to image the same volume of $2.5 \times 2.5 \times 2\ \mathrm{mm}^3$. We use a custom-made tracking algorithm based on the projective geometry framework to track microorganisms. By tracking green algae *C. reinhardtii* at varying concentrations, we evaluate the performance and limitations of our tracking system and algorithm. We demonstrate a significant improvement over previous work by achieving accurate and reliable tracking at higher image densities of 0.06 particles per pixel, with a low reprojection error of 0.3 body length. Our approach supports the accurate reconstruction of the kinematics of cell trajectories and cell surface interaction analysis. Our experimental results reveal that *C. reinhardtii* cells exhibit predominantly left-handed chirality and swim in elongated helices with larger pitch and shorter radii. Furthermore, we show that helical angular velocity varies from 1 to 2 Hz across the population. We also calculate the population's persistence length and diffusive coefficients, providing insights into their diffusive behavior and showcasing that 3D data is necessary to characterize the diffusion behavior correctly.

This chapter is organized into four sections. In section 2.2, we describe the experimental setup, the calibration procedure, and the tracking experiments for *C. reinhardtii* and the tracking algorithm. In section 2.3, we present performance parameters that characterize our setup and tracking algorithm. In section 2.4, we present the tracking results of our experiments with *C. reinhardtii* and characterize the kinematic properties of the extracted trajectories. Our microscopy setup has also enabled us to investigate *C. reinhardtii* surface interactions, revealing phenomena such as bi-modal interaction kinematics (steric & hydrodynamic) and trajectory hopping behavior near the surface, which have been extensively discussed in Buchner *et al.* [98]. In this section, we briefly summarize these findings. Finally, in section 2.5, we conclude this chapter by discussing the scope and limitations of our setup.

2.2. THREE DIMENSIONAL TRACKING SETUP

In this section, we first describe the details of our microscopy system and calibration procedure. We then present the details of the tracking experiments for *C. reinhardtii*, including cell culturing and flow chamber design. We also discuss the tracking algorithm and post-processing steps used for *C. reinhardtii* tracking experiments to extract 3D trajectory data.

2.2.1. MULTI-CAMERA MICROSCOPY SETUP

We track a suspension of microswimmers using a multi-camera microscope (Fig. 2.1). Our three-dimensional tracking setup is designed around a single common objective and includes a light source, four sCMOS cameras, and a flow chamber (see Fig. 2.1B for schematics of the setup). Similar optical configurations have previously been utilized for Tomo-PIV and particle tracking in thin immersion droplets [99, 100].

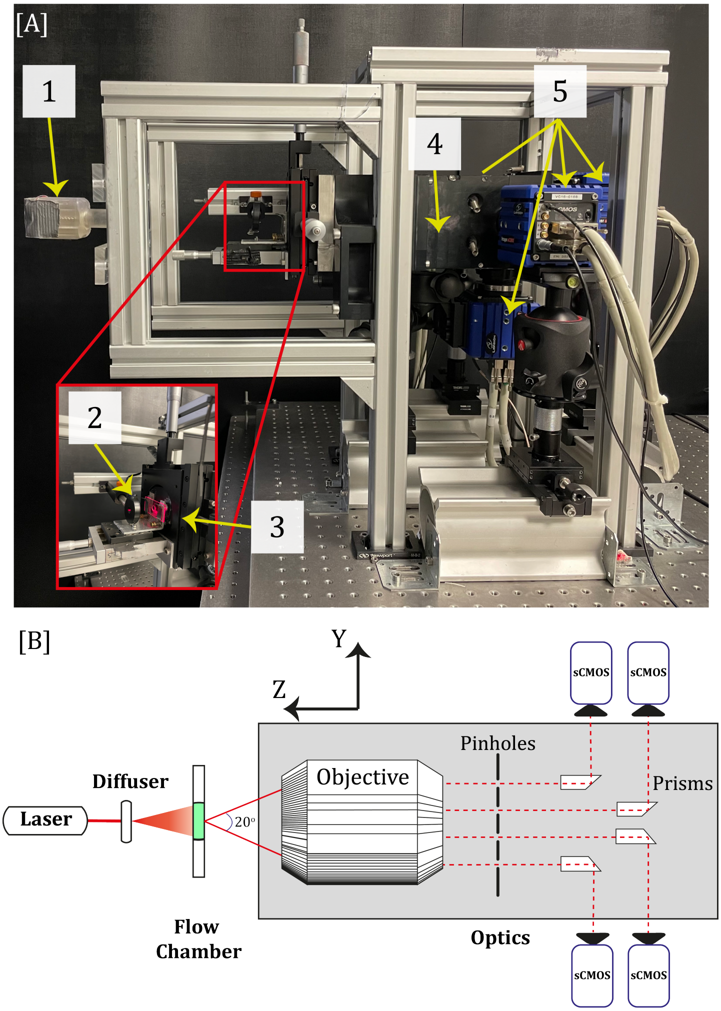

Figure 2.1: [A] The experimental setup: (1) Laser, (2) light diffuser, (3) Flow chamber & mechanical stage, (4) Objective & optics, (5) Cameras. [B] Schematic of the experimental setup. Dashed red lines show the optical path. The laser light passes through the diffuser and illuminates the microswimmers inside the flow chamber. An objective of magnification $M = 1.5$ and focal length $f = 30$mm collects the scattered light. The scattered light then passes through small pinholes, leading to a large depth of field. Prisms are used to guide the optical rays to the four sCMOS cameras.

We illuminate the sample with a laser and place a light diffuser (Optotune; LSR300) between the illumination source and the sample to reduce undesired speckles and provide uniform illumination by expanding the laser beam. The illumination intensity is modulated by the alignment of the diffuser on the optical rail. Our system supports both lasers and LEDs of different wavelengths. For our *C. reinhardtii* tracking experiments, we use green and red lasers with wavelengths of 500 nm and 650 nm, respectively.

The flow chamber containing the microswimmer suspension is fixed to a 3-axis mechanical stage inside the illumination volume. The positioning of the flow chamber is controlled with 10 μm accuracy by mechanical micrometers. Our imaging system can be used with different flow chamber designs. It is versatile and supports a broad range of experiments, such as three-dimensional parameter estimation, and can be used to study the effect of shear rate and temperature on microswimmer locomotion.

We use four cameras to image the sample through a single common objective (Zeiss; $M = 1.5$, $f = 30mm$), each camera collecting the light passing through a pinhole of diameter D_h. This results in the cameras viewing the sample at an angle of 20° from the optical axis [99]. Therefore, the optical path of each camera is off-axis, such that no transmitted light reaches the cameras, and the cameras only collect forward scattered light by the cells. Our imaging system is, therefore, similar to dark field microscopy, and cells appear as bright spots against a dark background. The cameras used are imager sCMOS, which have a resolution of 2560 × 2160 pixels, a 16-bit dynamic range, and a maximum frame rate of 50 fps. The pixel size of the cameras is 6.5 μm^2.

The depth of field (Δz_o) of the system can be adjusted by varying the diameter of the pinholes[99]:

$$\Delta z_o = 4\left[1+\frac{1}{M}\right]^2\left[\frac{f}{D_h}\right]^2\lambda \tag{2.1}$$

In this equation, D_h is the pinhole diameter, and λ is the light wavelength. D_h can be varied between 1 mm and 7 mm. For red light illumination at 650 nm, this range of pinhole diameters yields a depth of field varying between 6 mm and approximately 200 μm. Although it is possible to decrease the pinhole size to less than 1 mm, this leads to lower image quality.

Cell images appear as bright dots of diameter D_I in our recordings. An estimate for the particle image diameter can be calculated as:

$$D_I = \sqrt{[MD_s]^2 + D_L^2} \tag{2.2}$$

Here, D_s is the diameter of the cell ($D_s \approx 10\mu\text{m}$), M is the objective magnification, and D_L is the diffraction-limited object diameter. Considering the low magnification of our objective, the size of the cell image in our recordings is determined by the diffraction limit. D_L is affected by the aperture size and the wavelength of light and can be calculated using the following equation:

$$D_L = 2.44\lambda\,[1+M]\,\frac{f}{D_h} \tag{2.3}$$

Decreasing the pinhole diameter (D_h) results in an increase in image diameter (D_I) for a constant swimmer size, as shown in Fig. 2.2 A. Choosing the appropriate pinhole diameter depends on several factors, such as the wavelength of light, the size of the swimmer, and the required depth of field. For our tracking experiments of *C. reinhardtii*, we use a 2 mm pinhole size. This pinhole size leads to 9-pixel sized cell images (Fig. 2.2 B.) and induces a depth of field of 2mm, such that the entire flow cell remains in focus and cells can be tracked throughout the entire chamber's depth.

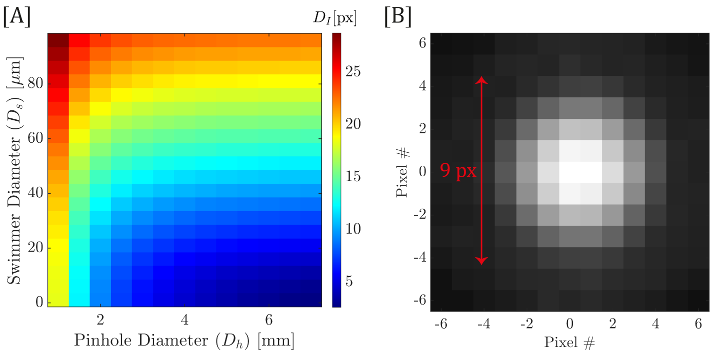

Figure 2.2: [A] Effect of pinhole diameter (D_h) on the swimmer image diameter (D_I) as a function of swimmer size (D_s) for the light wavelength $\lambda = 650$ nm. [B] An example image of a *C. reinhardtii* cell with a pinhole diameter of 2mm under $\lambda = 650$nm laser light illumination.

2.2.2. CALIBRATION PROCEDURE

We calibrate our tracking system with a custom-made calibration procedure, which uses the DaVis 8.4 calibration module as a starting point and rewrites the mapping function in the projective geometry framework commonly used in computer vision [101]. Recasting the mapping function is necessary because our tracking algorithm uses the framework of projective geometry, which supports fast and computationally efficient linear ray tracing. We describe the camera calibration procedure for the *C. Reinhardtii* tracking experiments below.

We used a calibration target containing a regularly spaced 100 μm dotted pattern (see Fig 2.3A). The calibration target was positioned at the exact location as the measurement volume of the flow chamber. To align and focus the cameras, we first increased the pinhole diameter to 7 mm, such that we imaged the target with a shallow depth of field of 200 μm. Once all of the cameras were focused and positioned to observe the same view volume, the pinhole diameter was decreased to 2 mm to achieve a 2 mm depth of field. We acquired 13 images for each camera, moving the target through the measurement volume with 200 μm increments. This resulted in a calibrated measurement volume of 2.4mm depth in the optical axis. The sweep can be extended/shortened depending on the depth of field of the experiment. We used the DaVis 8.4 calibration module to acquire both the coordinates of the images of the dotted pattern in the camera image planes of each camera and the corresponding world coordinates in the measurement volume, as shown in Fig. 2.3B. These coordinates were then used to construct the calibration model. Below, we describe the mathematical structure of the calibration mapping function we use in this study. A more complete description can be found in Muller *et* *al.* [102], describing a recently developed calibration procedure. It bears emphasis that the calibration method described in Muller *et al.* [102] is fundamentally different from the one used here since the calibration mapping function is determined solely from images of a free calibration target without knowledge of its position and orientation in the measurement volume. This is not the case here, where the displacements of the target are imposed and its position is known. Though the calibration procedure is different, the mathematical structure of the mapping function in this study is identical to Muller *et al.* [102].

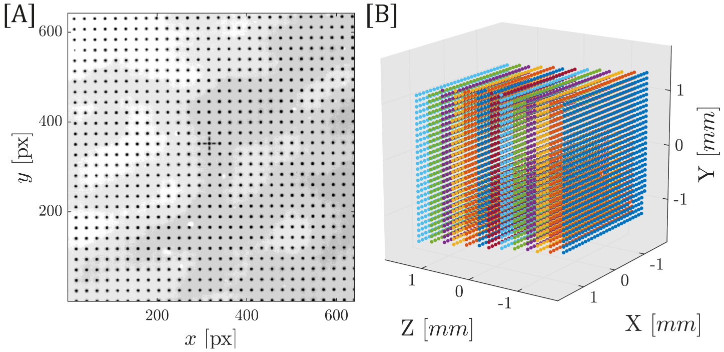

Figure 2.3: [A] An image of the calibration grid. Black grid points are 100 μm apart in each direction in the object domain. [B] Location of the grid points in the object domain. Images were taken of the calibration grid at 13 xy-planes by traversing the calibration grid by 200 μm, each represented by a different color in the Z direction, covering the full range of depth of field of 2 mm.

The camera mapping function has two components: a linear part, which models the geometry of the optical setup and supports linear ray tracing, and a non-linear part, which corrects for optical distortions. We first correct for optical distortions by computing a distortion correction map m that dewarps the calibration images to produce the distortion-corrected image. This step yields a function $\hat{\mathbf{x}} = m(\mathbf{x})$, which maps the coordinates in the camera image plane $\mathbf{x} = \begin{bmatrix} x & y \end{bmatrix}^T$ to distortion corrected images $\hat{\mathbf{x}} = \begin{bmatrix} \hat{x} & \hat{y} \end{bmatrix}^T$. We then determine a mapping function $\hat{\mathbf{x}} = F(\mathbf{X})$ to map the coordinates $\mathbf{X} = \begin{bmatrix} X & Y & Z \end{bmatrix}^T$ of a point in the three-dimensional object domain to the dewarped projected image $\hat{\mathbf{x}}$. This function F is a linear function formulated within the projective geometry framework.

In this framework, augmented vectors facilitate the representation of points in both the image plane and the object domain. Specifically, in the dewarped image plane, coordinates are augmented into the ray-tracing vector $\tilde{\mathbf{x}} = \begin{bmatrix} k\hat{x} & k\hat{y} & k \end{bmatrix}^T$, where k is a scaling parameter representing a coordinate along the principal optical axis. An inverse mapping $p(\tilde{\mathbf{x}})$ inverts this transformation, resulting in $\hat{\mathbf{x}} = p(\tilde{\mathbf{x}}) = \begin{bmatrix} \tilde{x}/k & \tilde{y}/k \end{bmatrix}$. Similarly, world coordinates $\mathbf{X}$ are augmented to obtain a homogeneous vector $\tilde{\mathbf{X}} = \begin{bmatrix} X & Y & Z & 1 \end{bmatrix}^T$, simplifying geometric transformations in the calibration procedure. Fig. 2.4 illustrates the relationship between these coordinate systems, showing the camera, the world coordinate system, and the dewarped image plane.

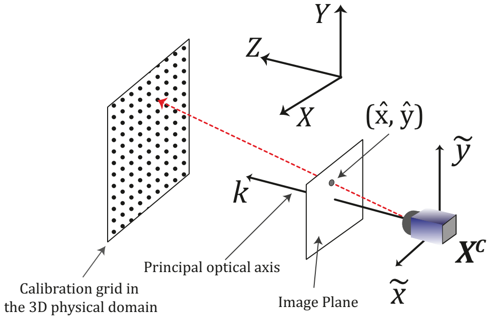

Figure 2.4: Illustration of the optical path geometry in the calibration process. The optical ray, represented by the solid red line, extends from the camera center $\mathbf{X^c}$ to a grid point location on the calibration grid in the three-dimensional object domain ($\mathbf{X} = \begin{bmatrix} X & Y & Z \end{bmatrix}$). The camera's coordinate system is denoted as $\tilde{\mathbf{x}} = \begin{bmatrix} \tilde{x} & \tilde{y} & k \end{bmatrix}$. The intersection of the optical ray with the dewarped image plane yields the coordinates $\hat{\mathbf{x}} = \begin{bmatrix} \hat{x} & \hat{y} \end{bmatrix}$.

For each camera, the mapping function F models both extrinsic camera properties, *i.e.* the position and orientation of the camera, as well as intrinsic properties, *i.e.* optical properties and sensor properties. The extrinsic properties are represented by a rotation and translation $\begin{bmatrix} \mathcal{R} & \mathcal{T} \end{bmatrix}$, which represent the transformation from the world coordinates system to the camera coordinates system. Here, $\mathcal{R}$ is a 3×3 rotation matrix, $\mathcal{T}$ is a 3×1 translation vector. The intrinsic properties are represented by a 3×3 camera matrix $\mathcal{K}$ of the following form:

$$\mathcal{K} = \begin{bmatrix} f r_x & \mathcal{S} & p_x \\ 0 & f r_y & p_y \\ 0 & 0 & 1 \end{bmatrix} \tag{2.4}$$

where f is the focal length of the lens in mm, r_x and r_y are the pixel pitch of the sCMOS sensor (px/mm), $\mathcal{S}$ is the pixel skew, and p_x and p_y are the coordinates of a point at the intersection of the principal optical axis and the dewarped image plane. With these notations, the mapping F can be written in the following form [101]:

$$\hat{\mathbf{x}} = F(\mathbf{X}) = p\left(\mathcal{K}\begin{bmatrix} \mathcal{R} & \mathcal{T} \end{bmatrix}\tilde{\mathbf{X}}\right) \tag{2.5}$$

The calibration procedure determines, for each camera, the matrices $\mathcal{K}$, $\mathcal{R}$, and $\mathcal{T}$, represented as a projection matrix $\mathcal{P} = \mathcal{K}\begin{bmatrix} \mathcal{R} & \mathcal{T} \end{bmatrix}$, which is a 3×4 matrix with 12 elements. The four projection matrices $\mathcal{P}^c$ are deduced by solving for each a least squares problem, using the positions in the object domain of the dots on the calibration target $\tilde{\mathbf{X}}_{\mathbf{j}}$ and the augmented coordinates of their images on the four camera image plane $\tilde{\mathbf{x}}^{\mathbf{c}}_{\mathbf{j}}$:

$$\min_{\mathcal{P}^c} \sum_j \left\| \tilde{\mathbf{x}}^{\mathbf{c}}_{\mathbf{j}} - \mathcal{P}^c \tilde{\mathbf{X}}_{\mathbf{j}} \right\|^2 \tag{2.6}$$

Superscript c is for cameras, and the subscript j denotes the calibration grid point number and includes all 13 positions of the target. Finally, an RQ decomposition is used to determine $\mathcal{K}$, $\mathcal{R}$, and $\mathcal{T}$ from the optimized projection matrices.

ACCURACY OF THE CAMERA CALIBRATION

We follow the approach described in Muller *et al.* [102] to assess the spatial accuracy of our calibration. Images of a dot from the calibration target on the camera's image planes are associated with four optical rays using projective geometry. For a perfect calibration, the optical rays from all cameras should intersect at one point in the object domain. However, in practice, camera optical rays are skew lines and do not intersect at one point. We characterize the accuracy of the camera calibration by computing the skewness between the optical rays. The skewness is evaluated by first triangulating the location of each grid point in the object domain and then computing the average distance of this point from the camera optical rays (see Muller *et al.* [102] for more details). For each of the 13 positions of the calibration target, we average the skewness corresponding to each dot on the target, and present in Fig. 2.5 the average skewness as a function of the depth position Z. Our calibration procedure resulted in low triangulation error, characterized by low skewness values. The minimum value was 0.3 μm at the center of the flow chamber, while the maximum value was 0.7 μm near the lower and upper surfaces of the viewing volume. These skewness values are an order of magnitude smaller than the diameter of the *C. reinhardtii* cell, indicating a high level of accuracy for our calibration.

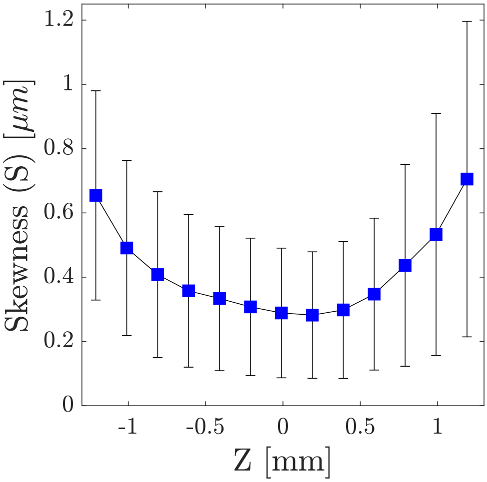

Figure 2.5: Accuracy of camera calibration characterized by average skewness for all grid points for four cameras along the Z-axis (optical axis). The error bars represent the standard deviation of the mean.

For our *C. Reinhardtii* tracking experiments, calibration was performed using a calibration target in ambient air. However, our experiments are performed when the cells swim in the aqueous tris solution. The higher index of refraction of the aqueous solution results in a small shortening of the optical direction. The distortion induced by changes in the index of refraction is corrected in the final step after the cells in the experiments have been tracked in the object domain by multiplying the Z-coordinates with a refraction correction factor. The definition of this correction factor is described in a later section.

2.2.3. C. REINHARDTII TRACKING EXPERIMENTS

This study focuses on the tracking of unicellular motile algae *C. reinhardtii*. Here, we provide the details of our cell culturing protocol, the design of our flow chamber, and the cell imaging.

Cell Culture

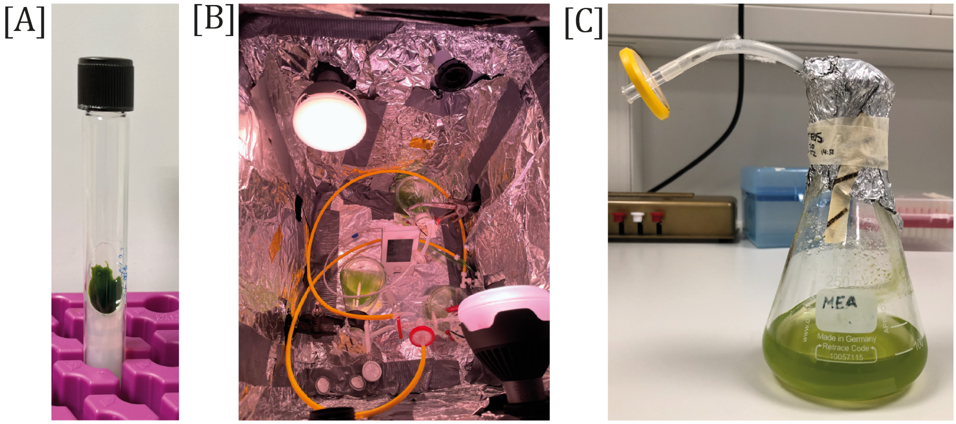

Figure 2.6: [A] Tube containing agar slant upon which a culture of quiescent algae cells was maintained. [B] Liquid growth chamber with two light bulbs. Silicone tubes allow air bubbles into the liquid culture. An air filter of pore size 0.2 μm was connected to the silicone tubes to filter the air being transferred to the culture. [C] 250ml conical flask containing cell culture of density 1×10^6 cells/ml four days post-inoculation.

In this work, we performed tracking experiments on green algae *C. reinhardtii*. Quiescent cells of wild-type CC125 were obtained from the Chlamydomonas Resource Center and transferred to agar slants (see Fig. 2.6A). Once transferred, algae slants were kept under constant illumination of broad-spectrum light with low intensity of 25 μmol/m^{2}s. New slants were re-streaked every two months to prevent the aging of the slants.

Liquid cultures were started by transferring a small number of cells from agar slants into 250 ml conical flasks containing 100 ml of Tris minimal medium. Cells were grown phototrophically in liquid cultures under constant air bubbling, and the flasks were maintained in a custom-made growth chamber at 24-26°C, using two Philips Green Power LED bulbs for illumination (see Fig. 2.6B). Cells were exposed to a 14/10-hour light/dark cycle with a light intensity of 150 μ mol/m^{2}s. Cells were harvested during the exponential growth phase when the cell density reached 1×10^6 cells/ml (Fig. 2.6 C). We achieved experimental concentrations ranging from 5×10^4 to 5×10^5 cells/ml via dilution with Tris minimal medium. The protocols listed above are the same as those used by Quaranta *et al.* [103] to study *C. Reinhardtii* flagellar hydrodynamics.

FLOW CHAMBER: DESIGN, CHARACTERIZATION, AND CLEANING PROCEDURES

We performed our tracking experiments using a simple reservoir flow chamber. Flow chambers were fabricated from a 2 mm thick transparent acrylic sheet with dimensions of 60 mm × 26 mm (Fig. 2.7). A hole was laser-cut in the middle of the sheet to create the chamber for algae suspension. Two glass coverslips (VWR; 631-1572) were then used to seal the reservoir using Norland optical glue (Thorlabs; NOA81).

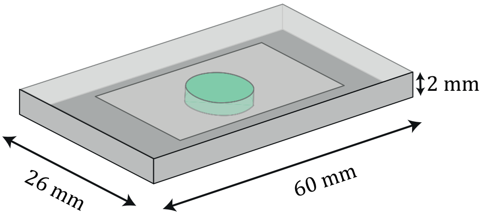

Figure 2.7: A schematic of the flow chamber used for *C. Reinhardtii* tracking experiments. The cover slip is shown with a light gray color, which encloses the reservoir from both sides. The reservoir is represented by a green cylinder in the middle of the flow cell.

The coverslips were cleaned and treated before use to minimize flagellar adhesion [104] and remove dirt particles that can significantly lower the quality of the images. First, ultrasonic cleaning was performed for 25 minutes in a surfactant (Sigma-Aldrich; Z805939-1EA) solution. Next, the coverslips were rinsed with de-ionized water and placed in a sonic bath for 25 minutes in de-ionized water only. After cleaning, the coverslips were immersed in 1% bovine serum albumin (Sigma-Aldrich; A7906-50G)/phosphate buffer solution (Sigma-Aldrich; P4417-50TA) for more than 24 hours at 4°C. After that, coverslips were rinsed with de-ionized water and dried with pressurized air. The coverslips were stored in a dust-free container before the tracking experiments.

The acrylic chambers were cleaned with 70% alcohol and de-ionized water to remove any residue from the laser cutting procedure. Before each experiment, we transferred approximately 100 μl of algae solution using a micro-pipette and placed the flow chamber on the multi-camera microscope stage. We waited for 15 minutes before starting the recording to ensure that the cells acclimated to the environment in the flow chambers.

CELL IMAGING

The algae suspension inside the 8mm diameter flow chamber was illuminated with red laser light (PICOTRONIC; D1650), with a wavelength (λ) of 650nm, to prevent the phototactic response [27, 105]. As mentioned before, we used a 2mm pinhole, resulting in a depth of field of 2mm and a particle image diameter of 9 pixels. The camera sensors were cropped to 640 × 640 pixels to reduce the image size, resulting in a total viewing volume of 2.5 × 2.5 × 2 mm^3. Images were acquired via a commercial PIV software, DaVis 10, at 20 fps with an exposure time of 42ms. The recording time for one experiment was set to 5 minutes, corresponding to a total recording of 6000 frames. Tracking experiments were performed for cell concentrations ranging from 5×10^4 to 5×10^5 cells/ml to characterize the performance of the setup. Fig. 2.8 shows a typical image for an algae suspension of 5×10^4 cells/ml for all four cameras.

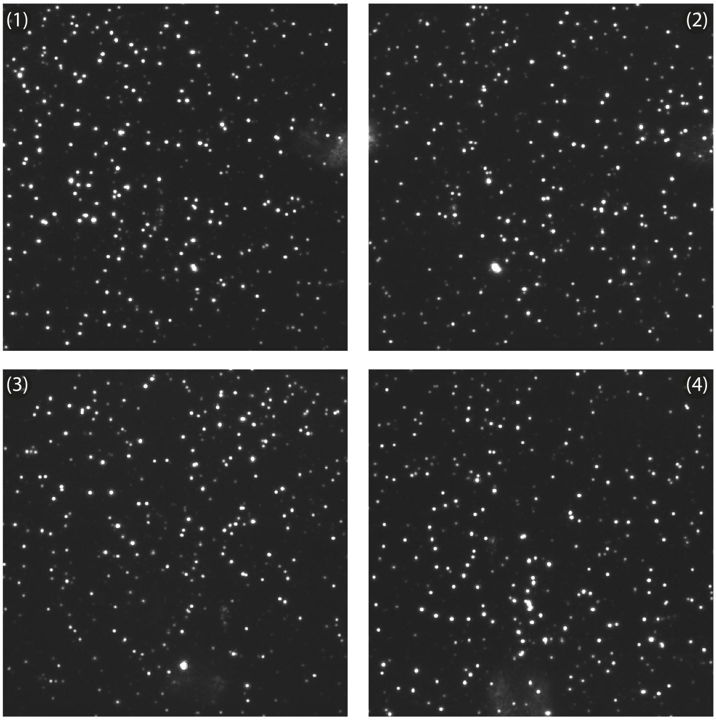

Figure 2.8: The four camera views imaging an algae suspension of 5×10^4 cells/ml concentration. Bright dots represent the scattered light from individual illuminated cells. The number on each image corresponds to a specific camera.

2.2.4. LAGRANGIAN PARTICLE TRACKING

In our experiments, we record the movement of cells using a setup of four cameras, and the resulting dataset consists of a sequence of images. We utilize a custom-made particle tracking algorithm based on the projective geometry framework [101] to obtain accurate three-dimensional trajectories of the cells. With projective geometry, we leverage the accuracy of our calibration and use linear ray tracing, leading to linear mathematical operations throughout the tracking process, which optimizes performance and reduces computational complexity. A detailed description of the algorithm can be found in Muller [106]; here, we provide an overview of the algorithm's important steps that are relevant to the subsequent part of this thesis. The Lagrangian particle tracking (LPT) algorithm is subdivided into five steps: particle identification, image tracking, coordinate matching & triangulation, time-resolved tracking & optimization, and post-processing.

STEP 1: PARTICLE IDENTIFICATION

The first step in our tracking algorithm is particle detection, which involves identifying the positions of cells in the camera image planes at each time step. We first dewarp the camera images by applying the distortion correction obtained from the calibration procedure (see section 2.2.2). Next, we apply a convolution filter with a Mexican hat shape to enhance the contrast of the image. We use a custom-made peak-finding algorithm to identify the ellipsoidal shape of algae cells in each camera view. This method uses the projective geometry framework to identify cell images as conics [101]. In this way, algae images can be easily manipulated and projected onto all camera views using computationally efficient linear ray tracing in subsequent steps. Within this framework, the outer contour of each alga is represented in terms of homogeneous coordinates as:

$$\mathbf{\hat{x}}^{\mathbf{T}}\mathbf{C}\mathbf{\hat{x}} = \begin{bmatrix} \hat{x} & \hat{y} & 1 \end{bmatrix} \begin{bmatrix} C_1 & C_2/2 & C_4/2 \\ C_2/2 & C_3 & C_5/2 \\ C_4/2 & C_5/2 & C_6 \end{bmatrix} \begin{bmatrix} \hat{x} \\ \hat{y} \\ 1 \end{bmatrix} = 0 \tag{2.7}$$

Here, $\mathbf{\hat{x}}$ is a vector of homogeneous coordinates, and $\mathbf{C}$ is a 3x3 symmetric matrix that defines the conic in the image plane. The values of the coefficients C_i are determined by using a characteristic kernel size corresponding to the size of the cell image [107]. We then calculate the midpoints of the conics to track the position of each algae cell as follows:

$$\begin{bmatrix} \hat{x}_o^j \\ \hat{y}_o^j \end{bmatrix} = -\begin{bmatrix} 2C_1 & C_2 \\ C_2 & 2C_3 \end{bmatrix}^{-1} \begin{bmatrix} C_4 \\ C_5 \end{bmatrix} \tag{2.8}$$

Here, $\hat{x}_o^j$ and $\hat{y}_o^j$ represent the x and y coordinates of the midpoint of the j-th conic in the dewarped image plane. These midpoints are the initial positions for tracking the algae cells from one frame to another.

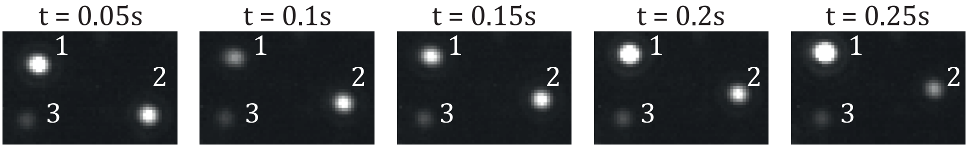

Figure 2.9: Images of three algae cells at different time steps showing variation in their image size due to the cell movement across the depth of field. Moreover, the cell blinking effect is visible for algae 1 & 2, where the intensity of the bright spot changes from one time step to the next due to cell rotation.

In all our experiments, the algae images are characterized by strong time fluctuations in both the size of the cell image and the light intensity, as seen in Fig. 2.9. These strong fluctuations are caused by the three-dimensional motion of the cells. *C. reinhardtii* does not scatter the incident light isotropically, and the rotation of the algae cells leads to quasi-periodic variations in the intensity values of the cell images throughout the recording sequence. This effect is significant and causes the cells to appear as blinking dots. This blinking of the algae cells impacts the performance of the peak detection algorithm. To address this issue, we utilize a multi-kernel approach for outer contour detection, using three kernel sizes of 5 × 5, 7 × 7, and 9 × 9, and derive three outer contours for each algae image. The unique coefficients C_i that define the outer contour of the algae cells are determined through a voting criterion based on the average intensity value within each kernel size.

Fig. 2.10A shows a typical image, the detected cells, and their midpoints. The inset, Fig. 2.10B, corresponds to the same algae as those from Fig. 2.9. Fig. 2.10 C demonstrates the robustness of our algorithm, where images of two overlapping algae are detected separately.

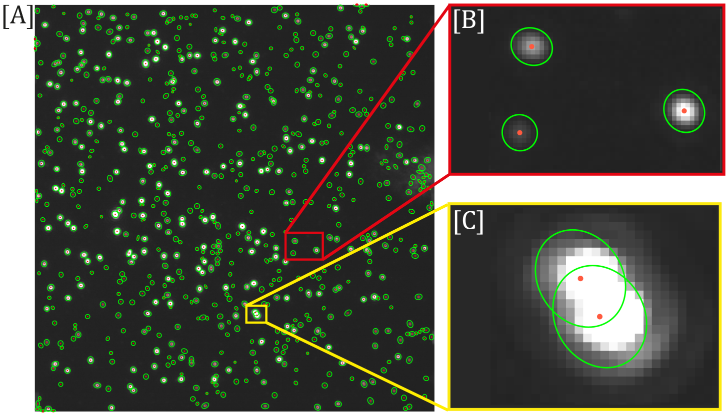

Figure 2.10: [A] Camera image with detected algae cells represented by green conics. Red dots show the midpoints of the conics. [B] A close-up of detected algae cells for the same cell images from Fig. 2.9. [C] Identification of the cells for overlapping cell images.

STEP 2: IMAGE TRACKING

In the second step of our Lagrangian tracking algorithm, we track the movement of algae cells, referred to as particles, in each camera view. Our approach involves identifying particle images in frame $n+1$ that are within a distance of one body length from those in frame n, which enables us to establish a two-dimensional track for each particle. To accomplish this, we compute the distance between the midpoints of particle images using the following equation:

$$L_p = \sqrt{\left| 1 - \frac{\hat{\mathbf{x}}_{\mathbf{o,n+1}}^T \, \mathbf{C}_n \, \hat{\mathbf{x}}_{\mathbf{o,n+1}}}{\hat{\mathbf{x}}_{\mathbf{o,n}}^T \, \mathbf{C}_n \, \hat{\mathbf{x}}_{\mathbf{o,n}}} \right|} \tag{2.9}$$

Here, L_p is the distance between two particle images' midpoints, $\hat{\mathbf{x}}_{\mathbf{o,n}}$ and $\hat{\mathbf{x}}_{\mathbf{o,n+1}}$, in frame n and $n+1$, respectively, normalized by the conic size of the particle image in frame n.

We use the computed distance L_p to determine whether the particle in frame $n+1$ is part of the track in frame n. If L_p is less than 1, the particle in frame $n+1$ lies within the conic in frame n, and is considered part of the track for that specific conic. Conversely, if L_p is greater than 1, that particle is not considered part of that track. Occlusions may result in one detected particle becoming part of two tracks. In such instances, instead of maintaining a single, uninterrupted track for a particle, the track splits at the point of overlap. Specifically, while non-overlapping particles continue to be tracked with their unique indices, any overlap prompts the initiation of a new track segment from that moment onward. As a result, a single particle is tracked by multiple track segments. Single tracks are recovered for each particle during an optimization step, which we will discuss later.

The image tracking step results in an indexed list of two-dimensional tracks, including particle conic and midpoint information for each particle for all cameras. Fig. 2.11 demonstrates the effectiveness of the image tracking algorithm in accurately capturing the motion of algae cells in a 50-frame sequence for one of the cameras. The figure highlights that most trajectories correspond to real particles and effectively track their motion. A few short tracks are also reconstructed that do not correspond to actual particles because of image noise. These false particle identifications and trajectories are later removed in the post-processing step.

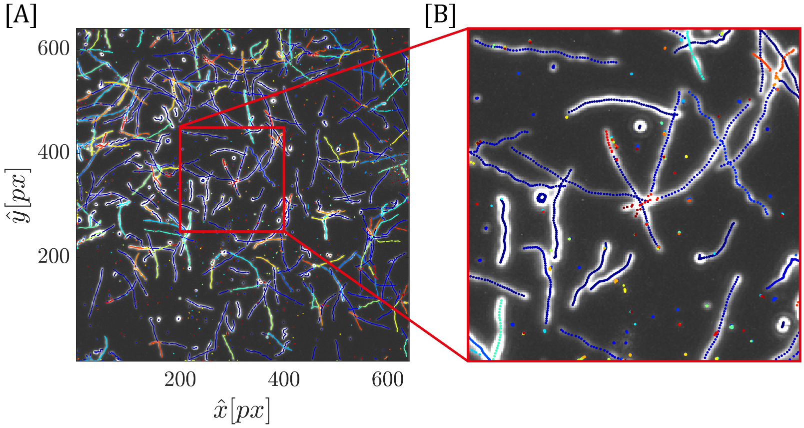

Figure 2.11: Visualization of two-dimensional image tracking. [A] An average image created from 50 individual camera images, temporally spaced from one another by Δt =0.05 seconds, forming a time series, displaying particle motion as streaks with 2D tracks of each particle overlaid in distinct colors. [B] A zoomed-in view of the particle motion as streaks and their corresponding 2D tracks, including short tracks resulting from false particle identifications due to image noise.

STEP 3: CORRESPONDENCE MATCHING & TRIANGULATION

The next step in our tracking algorithm is to match particle images between the different cameras. We establish camera correspondences by using epipolar geometry [101]. This technique utilizes the geometric relationship between the image planes of two calibrated cameras. Specifically, when the image of a given particle is known in one camera, its image in a second camera lies along the epipolar line. This line corresponds to the projection of the optical ray passing through a particle in the object domain and the center of camera 1 onto the image plane of camera 2 (see Fig. 2.12A).

The epipolar line plays a crucial role in establishing correspondences between particle images in both camera views. Using the particle's image from camera 1, we determine its associated epipolar line in camera 2. We then compute the distance between the epipolar line and all particle images in camera 2. Ideally, a particle image in camera 2 would align perfectly with the epipolar line, resulting in a distance of zero. However, due to image noise and calibration errors, the distance may not always be zero; hence, we set a threshold of one body length for match consideration. If the distance between the epipolar line and the particle's image in camera 2 is less than one body length, we consider the images in both cameras to represent the same particle and thus establish a correspondence.

The projective geometry framework is ideally suited to the fast computation of epipolar lines and the distance between epipolar lines and particle images. For particle locations $\tilde{\mathbf{x}}^{\mathbf{1}}_{\mathbf{j}}$ in camera 1, the epipolar line ($\boldsymbol{l}_{12}$) from camera 1 to camera 2 can be computed as a single linear operation, as follows:

$$\boldsymbol{l}_{12} = \left[\mathcal{P}^2\mathbf{X}^{\mathbf{1}}\right]_\times \mathcal{P}^2\mathcal{P}^{1^+}\tilde{\mathbf{x}}^{\mathbf{1}}_{\mathbf{j}} \tag{2.10}$$

Here, $\mathcal{P}^1$ and $\mathcal{P}^2$ represent the projection matrices for Camera 1 and Camera 2, respectively, and $[]_\times$ denotes the skew-symmetric matrix. $\mathcal{P}^+$ is the pseudo-inverse of the projection matrix $\mathcal{P}^1$, and $\mathbf{X}^{\mathbf{1}}$ is the location of Camera 1 in the three-dimensional domain. This framework enables the computation of epipolar lines through linear matrix operations. For more details on this computation and the calculation of the distance between the epipolar lines and particle images, we refer to Muller [106].

Establishing a reliable correspondence between two particle images in two different camera views requires that the particle image in each camera lies within one body length of the epipolar line associated with the other corresponding particle image in the other camera. When this bi-directional condition is satisfied, we consider the two particle images to be matched and refer to this as a stereoscopic correspondence. In our four-camera setup, multiple combinations of epipolar lines are possible, as shown in Fig. 2.12B. Trifocal correspondences between three particle images in three camera views imply that a stereoscopic correspondence is established for each of the three combinations involving two particle images. Quad-focal correspondences extend this principle to all four cameras. This implies that, for four particle images in four different cameras, stereoscopic correspondence is established for any of the six combinations involving two out of the four particle images.

We exclude stereoscopic correspondences and only process particles with trifocal and quad-focal correspondences, as these correspondences provide a higher level of geometric constraint. This helps to limit the number of false correspondences, including ghost particles that may appear due to image noise, occlusion, or errors in the camera calibration.

Our tracking algorithm allows one particle image to be matched with more than one image in another camera. This can occur because of particle occlusions, where one particle moves in front of another particle, and their particle images can no longer be distinguished in one of the camera views. By allowing for multiple matches, we capture the entire trajectory of the particle and avoid losing tracks because of occlusions. However, during the optimization step later in the algorithm, we establish unique correspondences for each particle image by selecting the best match among the multiple candidates based on the re-projection error.

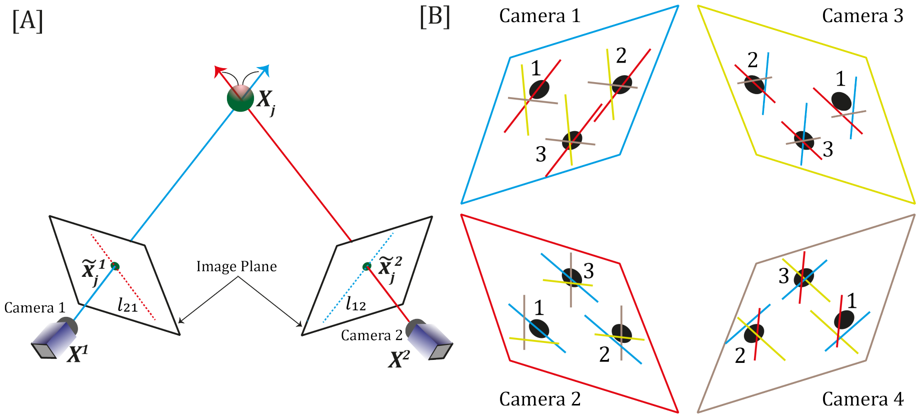

Figure 2.12: [A] Epipolar geometry setup. Two cameras (camera 1 and camera 2) image a particle "j" at location $\mathbf{X_j}$ in the object domain. The solid blue and red lines represent the rays from the camera centers ($\mathbf{X^1}$ and $\mathbf{X^2}$) intersecting with the particle. The green circles in the image planes are the location of the particle in each image plane, represented by homogeneous coordinates $\tilde{x}^1_j$ and $\tilde{x}^2_j$. Epipolar lines ($\boldsymbol{l}_{21}$ and $\boldsymbol{l}_{12}$) corresponding to the particle are represented by dashed lines and projected onto the image planes of camera 1 and camera 2, respectively. [B] Illustration of various camera correspondences for a multi-camera system. Images of each camera are represented by a unique color, with their corresponding epipolar lines matching these colors. The image of particle 1 shows stereoscopic correspondence between two cameras (camera 1 & camera 2), while images of particle 2 and particle 3 demonstrate tri-focal and quad-focal correspondences among three and all four cameras, respectively.

After matching particle images, we use triangulation to locate the particles in the three-dimensional object domain. We use matched particle images $\hat{\mathbf{x}}^{\mathbf{c}}$ in the different camera views to triangulate the location of the corresponding particle in the three-dimensional object domain. The location of the particle in the object domain is triangulated as the three-dimensional point $\mathbf{X}$, minimizing the sum of the squared point-line distances between $\mathbf{X}$ and the optical rays from each camera associated with the particle images $\hat{\mathbf{x}}^{\mathbf{c}}$:

$$\min_{\mathbf{X}} \sum_{c} \left\| d\left(\mathbf{X}, \boldsymbol{l}(\hat{\mathbf{x}}^{\mathbf{c}})\right) \right\|^2 \tag{2.11}$$

In the equation, $d\left(\mathbf{X}, \boldsymbol{l}(\hat{\mathbf{x}}^{\mathbf{c}})\right)$ is the distance between the particle location in the object domain $\mathbf{X}$ and the optical ray, denoted as $\boldsymbol{l}(\hat{\mathbf{x}}^{\mathbf{c}})$, associated with the particle image $\hat{\mathbf{x}}^{\mathbf{c}}$ in camera c.

STEP 4: TIME RESOLVED TRACKING & OPTIMIZATION

The previous steps described how particles are tracked in two dimensions and how triangulation is performed after establishing camera correspondences between particle images. These steps are independent of each other. In this step, we combine the two-dimensional tracking and the particle image correspondences to obtain continuous trajectories in three dimensions.

In the first recorded frame, we initiate three-dimensional trajectories from each particle location obtained from the triangulated locations of particle image correspondences. The trajectories are then continuously extended using two-dimensional camera tracking information. For each trajectory, we model its path with a polynomial function in the image plane, enabling us to predict the particle's position in the next frame. This modeling aids in resolving uncertainties that emerge from image processing and tracking.

Using the polynomial fit, we predict the position in the next frame for all trajectories. Based on this prediction, we find the particle image within one body length of the predicted particle image position in the next frame. This prediction step is particularly beneficial in instances of image occlusion, allowing us to find the particle image even when occlusion occurs. This action compensates for inconsistencies in camera tracking. If no image identification is available in the subsequent frames within one body length, we extrapolate the image position for an existing trajectory based on our fit. This extrapolation helps us track the particle, especially if its image is out of view of one camera but is present in the other cameras.

As we progress through frames, new particle images are identified and appended to their corresponding trajectories. For each of these images, we triangulate their location in three-dimensions using image correspondences and subsequently calculate the re-projection error. Particle locations with an average re-projection error (evaluated across all cameras) that is less than one body length get incorporated into the three-dimensional trajectories. Conversely, trajectories that display a re-projection error exceeding one body length are terminated at that specific frame. This iterative approach continues for all frames, appending trajectories accordingly.

These steps result in a set of feasible trajectories for all particle images, where one particle might still be part of more than one trajectory due to occlusions and imperfect correspondences arising from calibration errors. We devise a cost-function solution strategy that rewards longer trajectories, matched number of image identifications (tri-focal and quad-focal), and low re-projection error. We employ a divide and conquer strategy inspired by Attanasi *et al.* [108] to find a solution that best fits simultaneous tracking in the object and image domains. This algorithm aims to reduce computational time and complexity arising from multiple camera images, the total number of frames, and the number of particles in each camera image. Once the optimization is complete, we obtain unique indices for each trajectory and their respective image and three-dimensional locations.

Fig. 2.13A illustrates the result of our tracking algorithm after step 4, tracking cells over 50 frames at 5×10^4 cells/ml concentration. For 6000 frames, which corresponds to

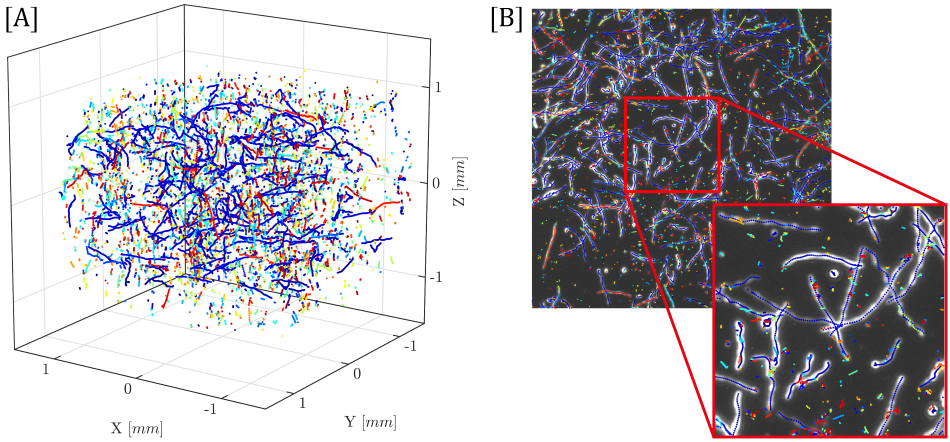

Figure 2.13: [A] Triangulated positions in the object domain for 50 frames of recording at a cell density of 5×10^4 cells/ml. Longer trajectories can be observed in the middle, corresponding to the viewing volume location, given the 2mm flow chamber length along the optical axis. Shorter trajectories inside and outside the viewing volume are predominantly ghost trajectories. [B] An image created by averaging the intensity of the same 50 frames used for triangulation in [A]. Overlaid on this average intensity image are color-coded 2D projections of the algae trajectories. The inset displays a close-up of the region highlighted by the red rectangle. The colored markers indicate the image plane locations where each three-dimensional trajectory projects, accurately following each cell image streak. Some trajectory locations appear clustered around a single position in the image plane; these short trajectories mostly belong to ghost particles and false algae identifications.

5 minutes of recording, we obtain approximately 0.8 million trajectories with an average track length of 10 frames. Many of these trajectories are ghost tracks or associated with spurious identifications (see Fig. 2.13B). We filter out these trajectories in the post-processing step, as discussed below.

STEP 5: POST PROCESSING

The robust and thorough nature of our tracking algorithm ensures that no data is lost during tracking. However, this results in a high number of unphysical trajectories, such as ghost particle trajectories (see Fig. 2.13B). To address this, we remove spurious trajectories in a post-processing step. First, we reduce the tracking data size by filtering trajectories based on length. Tracks shorter than 20 frames are discarded. This step effectively removes most ghost trajectories, which are typically short. Next, we remove tracks corresponding to immobile cells, which correspond, for example, to cells stuck on solid surfaces. These tracks are identified by computing the standard deviation of positions along the tracks. Tracks with a standard deviation smaller than 20 μm are removed. Finally, we eliminate tracks belonging to particles moving faster than 250 μm/s since the average swimming speed of algae cells is 100 μm/s [72].

The remaining trajectories are filtered in order to reduce the noise resulting from calibration errors, occlusions, and inaccuracies in the triangulated position due to cell

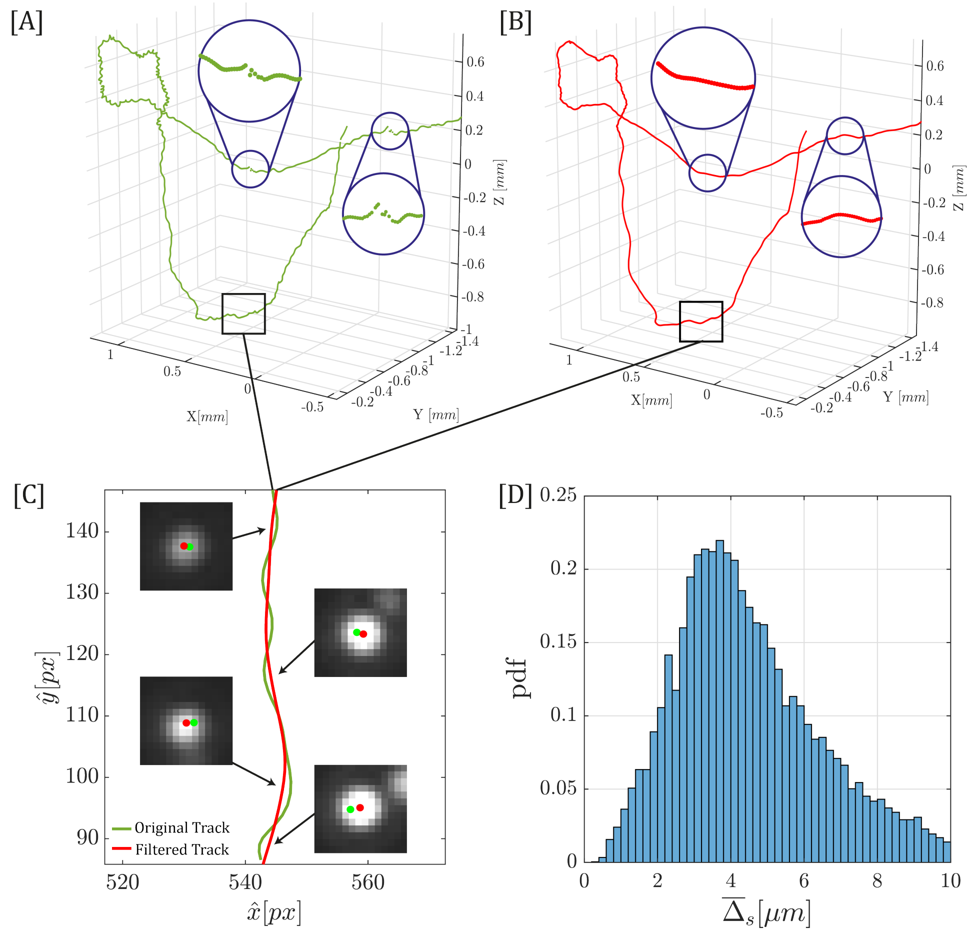

Figure 2.14: [A] A characteristic cell trajectory in three dimensions. Circular insets show the discontinuous nature of the trajectory due to occlusions and imperfect matching. The rectangle shows the part of the trajectory re-projected on one of the camera images in panle [C]. [B] Trajectory filtered by the Savitzky-Golay filter of kernel length 25 and order 3. Circular insets show the correction of discontinuities due to the smoothing filter. The rectangle represents the part of the filtered trajectory re-projected on the camera image in panel [C]. [C] Two-dimensional trajectories of the re-projected positions from the original and the filtered trajectories. Insets show the re-projected positions of the original and filtered trajectories on the particle image at different time steps. [D] Distribution of the time averaged difference $\overline{\Delta}_s$ between original and filtered trajectory locations in object space for all of the trajectories.

blinking in at least one camera view. Fig. 2.14A displays a representative cell trajectory illustrating these artifacts. The position triangulated in step 3 is influenced by minor differences in midpoints across various cameras caused by the blinking effect, leading to a shift in the triangulated position from one frame to another and generating an apparent high-frequency helical motion. This can be seen when inspecting a portion of the track (indicated by a rectangle) projected onto the image plane (Fig. 2.14C). Camera images are also presented in the inset at different points along the track. The reconstructed cell trajectory is marked with green dots in Fig. 2.14 and can be seen to oscillate from one side of the particle image to the other. It is clear that this oscillation is not physical. The re-projected position oscillates from one side of the algae image to the other because of the cell blinking effect in another camera view. Another artifact is the discontinuity of the trajectory, denoted by circles in Fig. 2.14A, which arises from occlusions and imperfect matching at these positions. To correct for this noise, we use a Savitzky-Golay filter with a kernel length of 25 and an order of 3. The filtered track is represented in Fig. 2.14B, and its re-projected location is displayed in Fig. 2.14C with a red line and red dots on the camera images. Fig. 2.14C shows that the re-projection of the filtered trajectory aligns with the particle's image center, thereby validating our filtering approach. We characterize the difference between the filtered track and the original track by computing a time-averaged difference as $\overline{\Delta}_s = \frac{1}{N}\sum_{t=1}^{N}\left|\mathbf{X}_t - \mathbf{X}_t^s\right|$, where $\mathbf{X}_t^s$ represents the filtered track position. Fig. 2.14D displays the distribution of average differences for all trajectories. The mean value for the $\overline{\Delta}_s$ distance is 4.5 ± 1.9 μm, which is on the order of the algae cell's radius. This indicates that the filtering does not affect the trajectory's helicity but mainly corrects errors due to blinking effects and other artifacts.

Finally, we describe the last post-processing step, which rescales the depth of the flow chamber. As mentioned earlier, the change in the index of refraction between the calibration procedure and the experiments results in a shortened distance along the optical axis. We address this issue by applying a linear correction to the position in the Z direction. To perform this correction, we first identify the locations of the upper ($\mathcal{Z}_u$) and lower ($\mathcal{Z}_l$) surfaces in the shortened frame of reference. These locations are determined by identifying cells stuck to the surfaces of the top and bottom coverslips. Cells remaining on the surfaces exhibit minimal movement (V <20 μm/s) compared to cells in bulk. We fit a plane through these cells to find the upper and lower surface locations. Once the surface locations are known in the shortened frame of reference, we perform the correction as follows:

$$Z_{corrected} = \mathcal{Z}_L + \underbrace{\left(\frac{\mathcal{Z}_U - \mathcal{Z}_L}{\mathcal{Z}_u - \mathcal{Z}_l}\right)}_{\text{rcf}}(Z - \mathcal{Z}_l) \tag{2.12}$$

where $\mathcal{Z}_U$ and $\mathcal{Z}_L$ define the true upper and lower surface location and takes the value of 1 and -1, respectively.

Fig. 2.15A shows the filtered three-dimensional trajectories in the corrected frame of reference for cell density of 5×10^4 cells/ml. For clarity, we only display 266 trajectories for 2.5 seconds (50 frames), but we acquired ~ 7000 trajectories for five minutes of recording time (6000 frames) with an average track length of 200 frames. We have successfully removed trajectories belonging to ghost and immobile cells (see Fig. 2.15B).

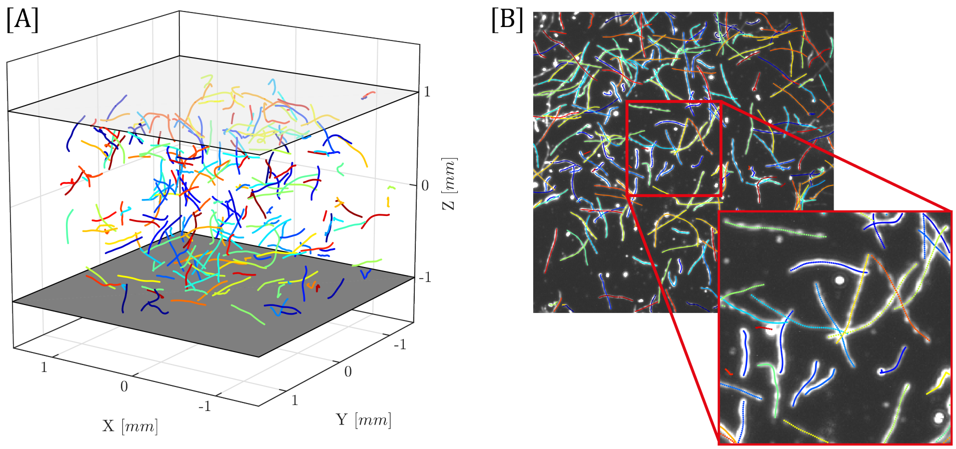

Figure 2.15: [A] Cleaned and filtered trajectories from a time series of 50 recorded frames for cell density of 5×10^4 cells/ml. Light and dark gray planes indicate the locations of upper and lower surfaces of the flow chamber in the object domain. [B] An image created by averaging the intensity of the same 50 frames used for triangulation in [A], overlaid with three-dimensional trajectory locations, re-projected into the image plane. Bright spots without projected tracks represent the locations of dust particles on the surface and immobile algae cells that exhibit no motion. Inset shows a close-up at the same location as in Fig. 2.13. Unphysical trajectories have been removed, leaving only the tracks that follow the cell motion.

2.3. Validation of the experimental approach

We validate the experimental approach by first looking at the transport of passive tracers to characterize the recirculation within the flow cells. Subsequently, we quantify the tracking performance and determine the maximum number of cells that can be tracked simultaneously.

2.3.1. Characterization of background flow

The recirculation within the flow chamber forms a background flow that can influence the behavior and motion of microswimmers [93]. This is especially true for *C. reinhardtii*, where a shear rate exceeding 1 s^{-1} has been shown to affect the motility and population behavior of the algae cells [78].

In our experimental setup, the background flow arises from small temperature differences across the chamber due to heating from the illumination source, leading to a buoyancy-driven flow. The reservoir size directly influences the magnitude of the background flow, with buoyancy-driven convection resulting from the temperature difference and gravity increasing the background flow's magnitude. An increased flow leads to passive/immotile cells to be transported with higher velocity magnitudes, which can no longer be distinguished from the swimming velocities of active particles. Thus, careful consideration of these factors informs our choice of reservoir size, ensuring that the background flow remains moderate and does not unduly influence our observations and analyses.

To characterize this, we conducted experiments with passive tracer particles of size 10 μm in flow chambers of varying sizes, ranging from 8mm to 12mm in diameter. The flow field was reconstructed using tomo-PIV. Fig. 2.16 displays the flow fields of background flow in reservoir chambers of 8mm and 10mm diameters for tomo-PIV experiments. Despite the consistent flow profile across different chamber sizes, we observed a significant difference in the magnitude of the background flow. As the size of the flow chamber increases from 8mm to 10mm, the background flow also increases considerably - from an average of 20 μm/s to 50 μm/s in the center of the reservoir.

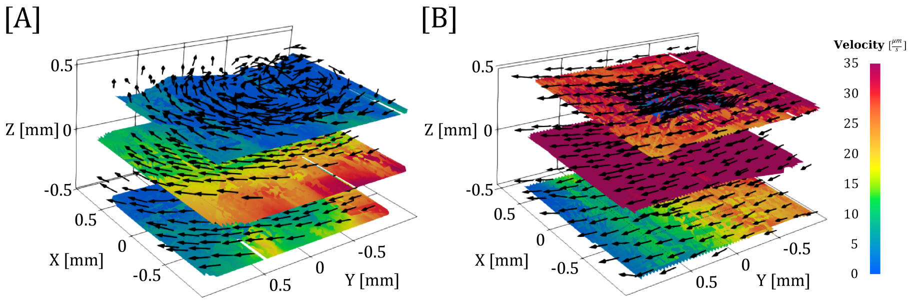

Figure 2.16: Eulerian flow field representing background flow inside [A] 8mm and [B] 10mm diameter reservoir.

We performed additional numerical simulations using COMSOL multiphysics software to determine the origin of the observed background flow. Details of the experiments and simulations can be found in Appendix A.2. Our simulations revealed that the increase in background flow is due to a small temperature difference of 1°C across the sides of the reservoir. This finding highlights the influence of the chamber size on the background flow and, consequently, on the shear rate experienced by the microswimmers.

Based on these findings, we chose an 8mm diameter flow chamber for our experiments. Given that the height of the flow chamber is 2mm, this setup results in an average shear rate of 0.02 s^{-1}, significantly lower than the 1 s^{-1} threshold that could influence the motility and population behavior of *C. reinhardtii*. Furthermore, this setup minimizes the background flow, facilitating the detection of immobile cells drifting within the flow.

2.3.2. TRACKING PERFORMANCE

To assess the accuracy and reliability of our three-dimensional tracking setup and algorithm, we computed the reprojection errors and the lengths of the tracks for various concentrations of *C. Reinhardtii* cells. Our aim was to evaluate how our system performed as the number of particles increased. Fig. 2.17 shows the variation in the number of particles in the images for different concentrations.

We quantified the increase in the number of particles with increasing cell concentration by computing the image density (N_I), a widely used metric in particle tracking experiments [109]. N_I represents the density of particles in each image in particles per pixel. To compute N_I, we divide the number of detected particles in an image ($N_{\hat{x}}$) by the area of the image (A_I) and a normalization factor of $(2.5/9)^2$. This factor accounts for the larger particle size in our experiments (9 pixels) compared to typical PIV and PTV applications ($2-3$ pixels) [109]. We found that our object detection algorithm accurately detected particles up to a concentration of 2×10^5 cell/ml (see Fig. 2.17). However, some particles went undetected beyond this concentration due to overlapping particle images, which is a common challenge in experiments with a high density of particles [110]. Table 2.1 presents our experiments' concentration, the average number of detected particles, and image densities.

No.	Concentration ($\frac{cells}{ml}$)	Detected Particles (#)	N_I (ppp)
I	5×10^4	705	0.022
II	1×10^5	1176	0.037
III	2×10^5	2082	0.065
IV	5×10^5	4340	0.137

Table 2.1: Number of detected particles and image density averaged over all four cameras across all frames for four different cell culture concentrations.

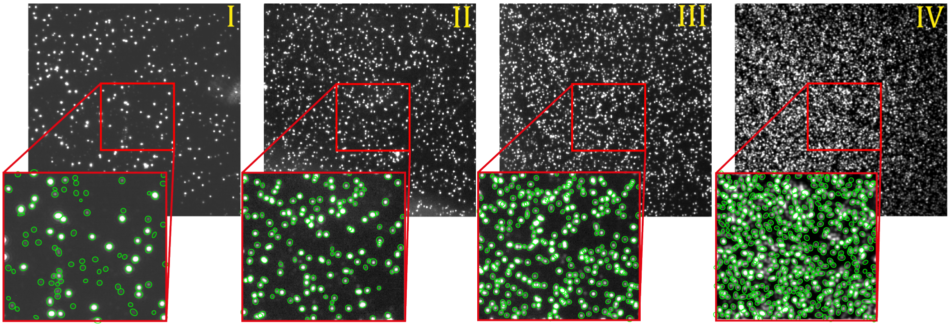

Figure 2.17: Sample camera images for varying cell concentrations: I. 5×10^4 cells/ml, II. 1×10^5 cells/ml, III. 2×10^5 cells/ml, IV. 5×10^5 cells/ml. Close-ups show the detected cells in part of each image.

To assess the reprojection error (ε_r), we reprojected the triangulated position in three dimensions onto each of the camera images (see Fig. 2.18A). Theoretically, the reprojected position should match the center of the detected particle image. However, in practice, the reprojected location differs due to the skewness of the camera rays. We normalize the distance from the particle center to the reprojected location with the size of the particle image. Thus, the reprojection error ranges from 0 to 1, with a higher value indicating more uncertainty in the location of the three-dimensional position. For each trajectory, we report the time-averaged reprojection error in Fig. 2.18B for increasing image densities.

The reprojection error exhibits a bimodal distribution for all densities except the highest at $N_I = 0.14$ ppp, with the first peak around 0.15 representing correctly reconstructed particles. The second peak, located at a higher reprojection error (0.5), corresponds to particles with overlapping images or tri-focal correspondences instead of quad-focal. As the image density increases, the number of particles with larger reprojection errors also increases. This indicates that the increased occurrence of particle image overlap at higher particle concentrations leads to less reliable reconstruction. The results also indicate that an image density of $N_I = 0.14$ ppp results in a lower than 0.5 reprojection error for most of the trajectories and indicates an accurate reconstruction of the particle trajectories. However, due to the high density, particles quickly lose correspondence. Consequently, most of the trajectories were shorter than ten frames and removed during post-processing. This was because of challenges in distinguishing between real and ghost particle tracks. As a result, the number of tracked particles was lower than in lower-density data sets, as shown in Figure 2.18A-IV.

We find that the density of particles in the image affects the accuracy and reliability of our tracking setup and algorithm. While a higher density leads to an increase in the number of tracks, it also increases the number of overlapping particles, leading to poor reconstruction and tracking performance. The average reprojection error increased from 0.15 to 0.3, with an increase in image density from 0.02 to 0.06 ppp. In the context of our *C. reinhardtii* tracking experiments, such a reprojection error translates to a positional uncertainty of up to 3 μm. This compares favorably with particle location uncertainties of 1 to 2 cell diameter from holographic tracking techniques imaging particles ranging from 40 to 270 μm in size [55].

We also analyzed the variation in track length as a function of image density (see Fig. 2.18C). At the lowest density of 0.02 ppp, the average track length was around 200 frames or 10 seconds. However, the average track length decreased as we increased the image density. For example, for an image density of 0.14 ppp, the average track length was only 2 seconds. This reduction in track length is mainly due to higher occlusion rates at higher image densities, which create ambiguities in unique correspondences and particle detection. Nonetheless, we obtained trajectories at least 5 seconds long for image densities up to 0.06 ppp, sufficient for performing kinematics and population behavior analysis.

Our performance assessment shows that we can reliably track active swimmers for image densities of 0.06 ppp corresponding to particle concentration of 2×10^5 particles/ml. This is one order of magnitude higher when compared to prior studies that tracked particles at image densities of 0.006 ppp [82] and particle concentrations ranging from $1.3 - 1.7 \times 10^4$ particles/ml [111], allowing us to track microswimmers at higher concentrations. Moreover, our tracking algorithm results in high throughput of long trajectories with low reprojection error, which provides the basis of our analysis of cell kinematics, cell-cell interaction, and the effect of non-Newtonian fluids on cell behavior throughout this thesis.

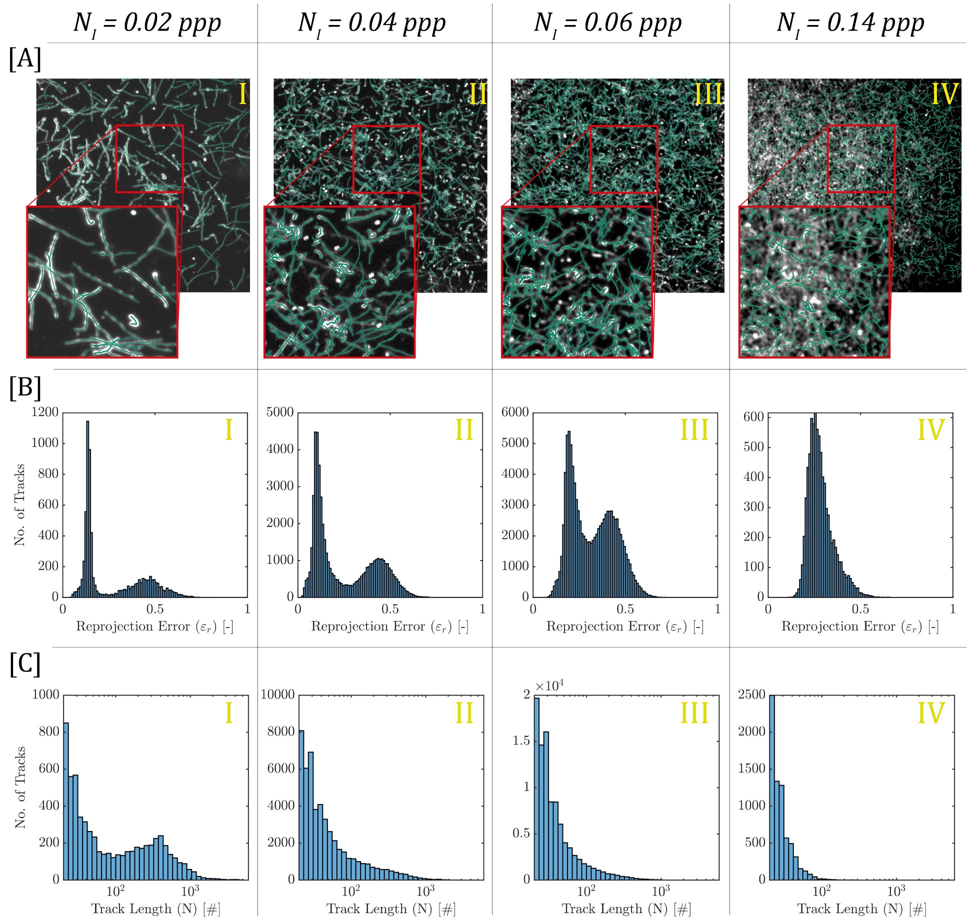

Figure 2.18: Tracking performance for varying cell concentrations: I. 5 × 10^4 cell/ml ($N_I \approx 0.02$), II. 1 × 10^5 cells/ml ($N_I \approx 0.04$), III. 2 × 10^5 cells/ml ($N_I \approx 0.06$), IV. 5 × 10^5 cells/ml ($N_I \approx 0.14$). [A] Composite camera image for 50 frames, overlayed with the re-projected three-dimensional position. Insets show the close-up views of a subsection of each image composite, for clarity. [B] Distributions of time-averaged reprojection error for different cell concentrations. [C] Distributions of track length in terms of number of frames, for each cell concentration.

2.4. APPLICATION OF MULTI-CAMERA MICROSCOPE TO CELL TRACKING

In this section, we present the results of our *C. reinhardtii* tracking experiments conducted with a concentration of 5 × 10^4 cells/ml, focusing on characterizing cell kinematics through various parameters. These parameters include velocity, radius, pitch, angular velocity, and diffusion coefficients. In addition, we investigated the cell-surface interactions using the same setup, details of which can be found in Buchner *et* *al.* [98] but only briefly summarized at the end of this section.

2.4.1. THREE DIMENSIONAL TRACKING OF *C. reinhardtii*

The methodology described in section 2.2 is ideally suited to investigate the three-dimensional motility of *C. reinhardtii*. In our study, we obtained ~45000 trajectories at a concentration of 5×10^4 cells/ml, providing a substantial dataset for analyzing the trajectory kinematics of *C. reinhardtii*. Fig. 2.19 shows examples of three-dimensional trajectories for freely swimming microalgae. Cells display helical motion, which can vary significantly from one cell to another. The majority of the cells move along elongated helices, forming a straightened trajectory, similar to trajectories 1 to 4 in Fig. 2.19. In addition, we observed a few trajectories similar to 5 and 6, characterized by tight helices with short radii and pitch. Our trajectory dataset also highlights a distinct 'hopping' behavior near surfaces, represented by trajectory 3. Here, cells display a series of bouncing motions against the surface before moving away. This hopping behavior emerges as a prevalent feature for surface interactions of the microalgae.

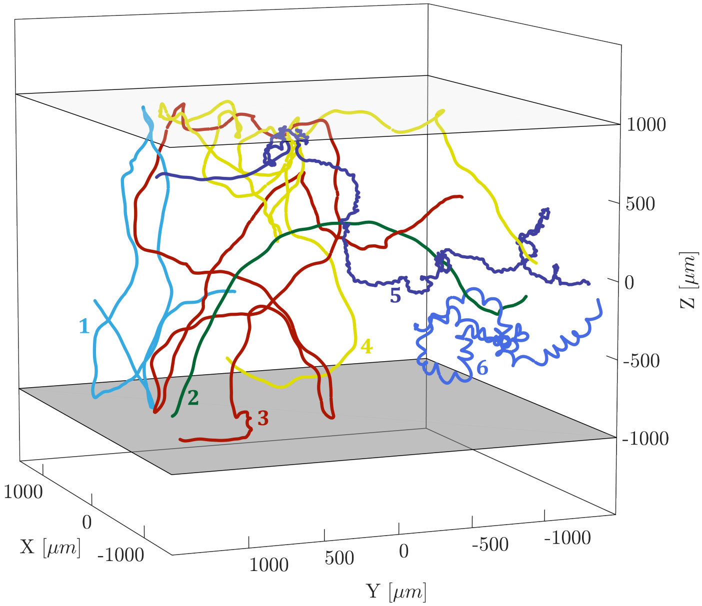

Figure 2.19: Six example three dimensional trajectories of *C. Reinhardtii* cells. Light and dark gray shaded regions represent the glass surfaces enclosing the flow chamber.

2.4.2. EXTRACTION OF HELICAL PARAMETERS

The three-dimensional motion analysis requires estimating parameters such as velocity, curvature, torsion, and others [72]. These parameters are computed by using the Frenet-Serret framework, which is applied to a time-parameterized curve $\mathbf{X}(t) = \begin{bmatrix} X(t) & Y(t) & Z(t) \end{bmatrix}$ [112]. The Frenet-Serret framework, also known as the **TNB** reference frame system, defines a local coordinate system where **T** is the unit tangent vector to the curve $\mathbf{X}(t)$, **N** is the normal unit vector and **B** is the unit bi-normal vector, see Fig. 2.20. **T**, **N**, and **B** vectors form the orthonormal basis for the Frenet-Serret framework.

To derive the Frenet-Serret reference frame, we define the arc length as the distance $s(t)$ along the trajectory $\mathbf{X}(t)$ up to time t:

$$s(t) = \int_0^t \left\| \mathbf{X}'(t) \right\| dt \tag{2.13}$$

For a curve $\mathbf{X}(s)$, parametrized by its arc length, we can write:

$$\mathbf{T}(s) = \frac{\mathrm{d}\mathbf{X}(s)}{\mathrm{d}s}, \quad \mathbf{N}(s) = \frac{\frac{\mathrm{d}\mathbf{T}(\mathbf{s})}{\mathrm{d}s}}{\left\| \frac{\mathrm{d}\mathbf{T}(\mathbf{s})}{\mathrm{d}s} \right\|}, \quad \mathbf{B}(s) = \mathbf{T}(s) \times \mathbf{N}(s) \tag{2.14}$$

The curvature κ of a curve is defined as the magnitude of the rate of change of the tangential vector with respect to arc length, expressed as $\kappa = \left\| \frac{\mathrm{d}\mathbf{T}(\mathbf{s})}{\mathrm{d}s} \right\|$. Torsion quantifies the deviation of a curve from being planar at a given arc length and is associated with the rate of change of the binormal vector **B**. The behavior of the particle along the path $s(t)$ is governed by the following equations:

$$\frac{\mathrm{d}\mathbf{T}}{\mathrm{d}s} = \kappa \mathbf{N} \tag{2.15}$$

$$\frac{\mathrm{d}\mathbf{N}}{\mathrm{d}s} = -\kappa \mathbf{T} + \tau \mathbf{B} \tag{2.16}$$

$$\frac{\mathrm{d}\mathbf{B}}{\mathrm{d}s} = -\tau \mathbf{N} \tag{2.17}$$

Our trajectories are more naturally parameterized with time, and we use the chain rule to compute the velocity (**V**), the curvature (κ), and the torsion (τ) as functions of time:

$$\mathbf{V}(t) = \mathbf{X}'(t) \tag{2.18}$$

$$\kappa(t) = \frac{\left\| \mathbf{X}'(t) \times \mathbf{X}''(t) \right\|}{\left\| \mathbf{X}'(t) \right\|^3} \tag{2.19}$$

$$\tau(t) = \frac{\left[\mathbf{X}'(t) \times \mathbf{X}''(t) \right] \cdot \mathbf{X}'''(t)}{\left\| \mathbf{X}'(t) \times \mathbf{X}''(t) \right\|^2} \tag{2.20}$$

From the formulation discussed above, it is evident that the complete definition of the Frenet-Serret framework requires second-order time derivatives. While this poses no issue for continuous curves, for our discrete curve in the form $\mathbf{X}(t) = \begin{bmatrix} X(t) & Y(t) & Z(t) \end{bmatrix}$, numerical differentiation techniques can be employed to approximate the necessary parameters. This technique, introduced by Crenshaw *et al.* [72], was initially used to analyze the three-dimensional tracks of *C. reinhardtii* and

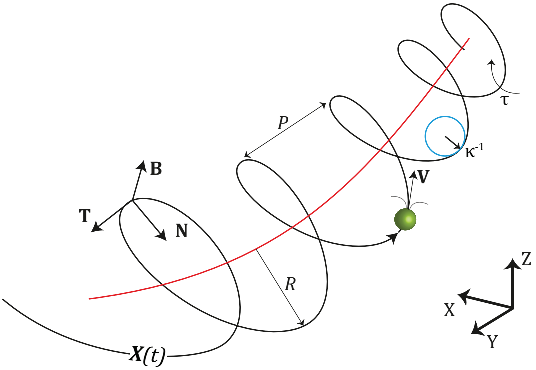

Figure 2.20: Frenet-Serret frame of reference, represented as **TNB**, in relation to a fixed Cartesian reference, **XYZ** for an alga navigating along a three-dimensional curve, denoted as $\mathbf{X}(t)$, with a velocity $\mathbf{V}(t)$, and characterized by a curvature $\kappa(t)$ and a torsion $\tau(t)$. The osculating circle, represented in blue, best defines the curve at that specific point. The radius of this circle is the reciprocal of the curvature (κ). The helix's central axis, depicted by a solid red line, establishes the radius (R) of the helical trajectory. The helix's pitch (P) is the distance covered along the curve for one complete revolution.

sea urchin spermatozoa. However, calculating second-order derivatives numerically on our 20 fps tracking data tends to amplify noise and introduce instability, leading to unreliable velocity and acceleration estimates essential for our analysis. Additionally, numerical differentiation results depend on the choice of the differentiation time step and finite difference method (forward, backward, or central), which can introduce variability and inconsistency in the derivative estimates. To overcome these limitations, in our study, we express the trajectories $\mathbf{X}(t)$ as a continuous vector function that is analytically differentiable, yielding exact solutions. For this, we use piece-wise Legendre polynomials and perform a least square fit to find $\mathbf{X}(t)$. Our piecewise Legendre fitting approach fits all data points within each individual track simultaneously, preventing local artifacts and minimizing the risk of introducing non-physical attributes. The mathematical formulation of the curve fitting problem is discussed in Appendix A.1.

Fig. 2.21 A-D illustrates the accuracy of our curve-fitting algorithm for the given trajectory. Each sub-figure (A, B, and C) represents the X, Y, and Z components of the curve, respectively, while Fig. D showcases the track in three dimensions. The fitted curve, represented by solid black lines, accurately follows the trajectory. Curve fitting was performed using a spline length of 10 and a polynomial order of 6. To assess the quality of the fit, the fitting error was computed using the formula $\varepsilon_f = \frac{1}{N}\sum_{t=1}^{N}\left|\mathbf{X}(t)-\mathbf{X}_t^s\right|$. For the particular trajectory shown in Fig. 2.21D, the fitting error ε_f is measured to be 0.2 μm. Figure 2.21E presents the distribution of fitting errors for all the trajectories. Notably, the total fitting error remains consistently well below $1\mu m$, indicating the high accuracy of the curve fitting for all trajectories.

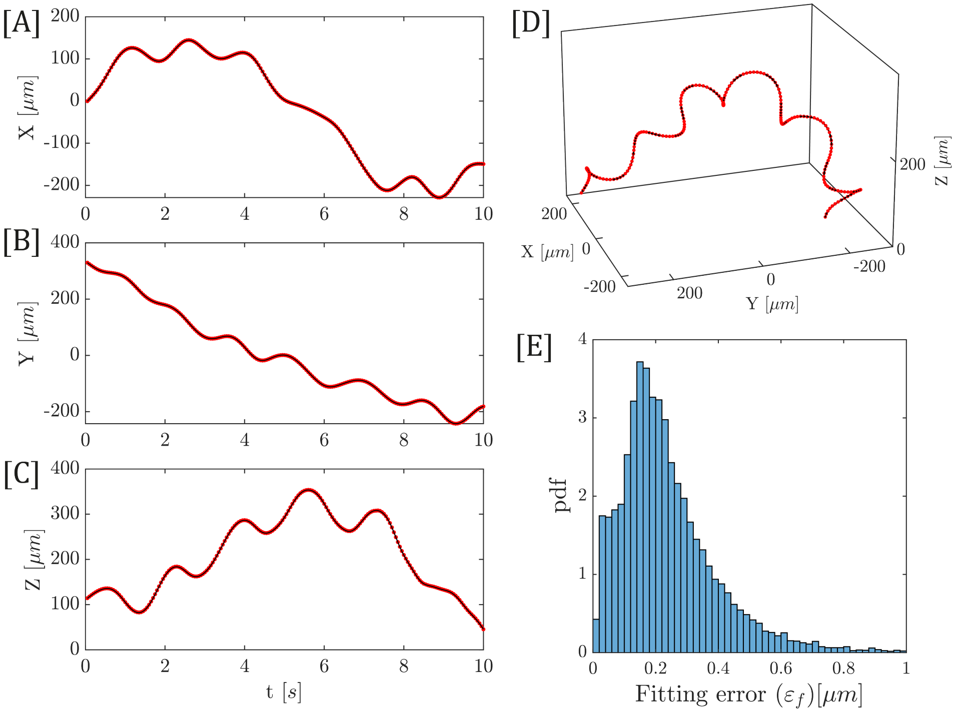

Figure 2.21: [A-C] The X, Y, and Z components of an example trajectory, represented by red dots, with the fitted curve $\mathbf{X}(t) = \begin{bmatrix} X(t) & Y(t) & Z(t) \end{bmatrix}$, shown as a solid black line. [D] Three-dimensional view of the trajectory (red dots) with the fitted curve (solid black line). [E] The distribution of fitting error ε_f between fitted trajectory $\mathbf{X}(t)$ and the filtered trajectory $\mathbf{X}_t^s$ for all of the trajectories.

2.4.3. CHARACTERIZATION OF HELICAL PARAMETERS OF *C. reinhardtii* TRAJECTORIES

We first characterized the helical parameters of these trajectories, specifically, velocity (V), pitch (P), and radius (R). The pitch (P) refers to the distance between consecutive turns of the helix, representing the vertical displacement of one full revolution, and the radius (R) defines the distance from the helix's central axis to the outer edge of its spiral (see Fig. 2.20). We calculated these parameters using analytic differentiation of the curve of the form, $\mathbf{X}(t) = \begin{bmatrix} X(t) & Y(t) & Z(t) \end{bmatrix}$, as follows:

$$V(t) = \|\mathbf{X}^{'}(t)\|\,, \quad P(t) = \frac{2\pi\tau(t)}{\kappa(t)^2 + \tau(t)^2}\,, \quad R(t) = \frac{\kappa(t)}{\kappa(t)^2 + \tau(t)^2}$$

where, $\kappa(t)$ and $\tau(t)$ were computed using Eq. 2.19 and Eq. 2.20, respectively. We then computed time-averaged values for all of the parameters, resulting in one value for each trajectory. Fig. 2.22A presents the distribution of time-averaged velocities ($\overline{V}$) for all trajectories. The distribution is characterized as tri-modal, with modes centered approximately at 20 μm/s, 90 μm/s, and 160 μm/s. The first mode corresponds to non-motile algae cells drifting in the background flow. The magnitude of this background flow agrees with observations from passive tracer particles, and the cells exhibit similar circular motion (see Appendix A.2 for additional details).

Excluding the non-motile cells, the remaining distribution is predominantly bimodal, showing the behavior of the motile and healthy cells. For our subsequent analysis and discussion, we focus on these cells, specifically those with $\overline{V} \geq 30$ μm/s. The average swimming velocity of *C. Reinhardtii* in our experiments was 137 ± 42 μm/s, higher than the average velocities reported by Barry *et al.* [78], yet similar to the velocity range of $80-160\mu$m/s reported by Jin *et al.* [79]. The lower average velocities of 58 ± 24 μm/s from Barry *et al.* [78] can be attributed to differences in growth conditions, as *C. Reinhardtii*'s motility behavior varies depending on these conditions [105].

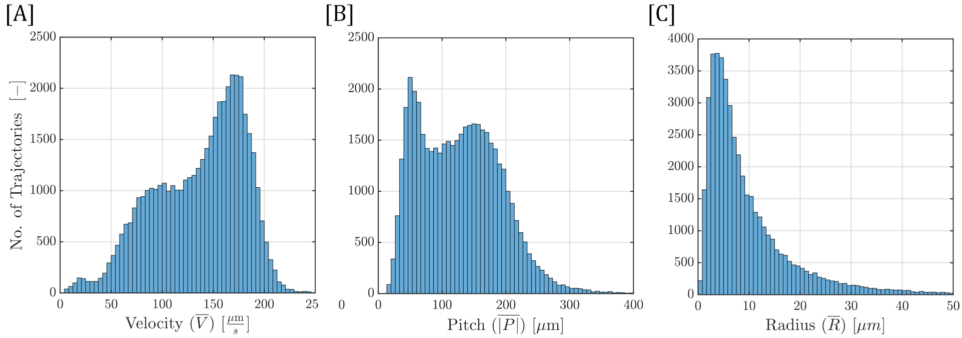

Figure 2.22: The distributions of time-averaged helical parameters across all trajectories. [A] velocities ($\overline{V}$) [B] Pitch ($\overline{|P|}$) and [C] Radius ($\overline{R}$)

Fig. 2.22 B and C present the distribution of time-averaged absolute pitch ($\overline{|P|}$) and radius ($\overline{R}$) for all trajectories, respectively. We consider the absolute value of the pitch ($|P|$) as we are interested in the scale of the pitch. The average pitch across all trajectories was $137 \pm 64\mu$m, and the average radius was measured as $8 \pm 7\mu$m. These measurements confirm that *C. reinhardtii* cells predominantly follow straighter trajectories, as denoted by the higher average pitch and low average radius values. Such trajectories are similar to the trajectories 1-4 in Fig. 2.19. However, the significant standard deviations in pitch and radius measurements indicate considerable variability in the motility patterns across the cell population.

We also consider the joint distributions of helical parameters. Fig. 2.23 presents the 2D joint density plot for the helix parameters velocity ($\overline{V}$), pitch ($\overline{P}$), and radius ($\overline{R}$). The joint density plot for velocity and radius (Fig. 2.23A) shows that with an increase in velocity up to approximately 130 μm/s, the radius slightly increases from 2 to 5 μm. Beyond this velocity, the radius is independent of velocity, suggesting that the relationship between these variables is not strong across all velocity values. To further quantify this non-linear relationship, we calculated the Spearman's rank correlation coefficient for these parameters, which yielded a value of 0.55. This moderate positive correlation indicates that, although an association exists between the two parameters, it remains relatively weak. On the other hand, the distribution of velocity and pitch shows a strong relationship between the two parameters, where cells swim with smaller pitch values at low velocities and with higher pitch values as the velocity increases. The Spearman's rank correlation coefficient reinforces this observation with a value of 0.85, underscoring the strong relationship between the two parameters. Moreover, our findings show that approximately 70% of the algae swim with left-handed chirality, as depicted by negative pitch values in Fig. 2.23B, consistent with previous studies [72].

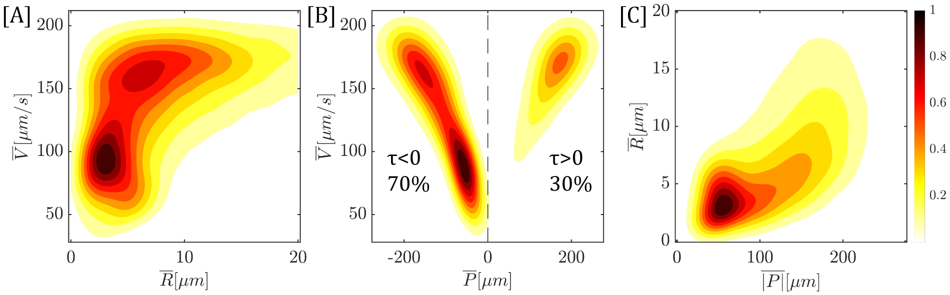

Figure 2.23: 2D joint density plots for time-averaged helix parameters for *C. reinhardtii* trajectories. [A] Velocity vs. Radius [B] Velocity vs. Pitch [C] Pitch vs. Radius. The color bar represents the relative density.

An important feature of *C. reinhardtii* swimming is the rotation of the cell body around its axis, previously measured at a rate of 1.4 - 2 Hz [24]. This rotation is due to the beating asymmetry between the cis and trans flagellum, which, together with the three-dimensional flagellar beating pattern, leads to the characteristic helical motion [24, 113]. Notably, one cell rotation corresponds to one helical turn [24]. Thus, we calculate helical angular velocity to consider variations in cell rotation speeds. Our trajectory data facilitates the computation of this helical angular velocity using the following equation based on trajectory parameters:

$$\Omega(t) = \frac{V(t)}{\sqrt{P(t)^2 + R(t)^2}} \tag{2.21}$$

The distribution of time-averaged helical angular velocity ($\overline{\Omega}$) for all trajectories in our study is illustrated in Fig. 2.24. The helical angular velocity ranges from 0.5 to 2.5 Hz, with an average of 1.23 ± 0.36 Hz. As rotation speed directly influences the helical trajectory, a lower rotation speed would result in straighter trajectories, as observed in our experimental data. Furthermore, the spread of angular velocities indicates that not all cells rotate at the same speed but experience different rotation velocities. This could be due to the differences in force asymmetries that each algal cell experiences. Angular velocity in our experiments is slightly lower than the previously measured rotation speed from Rüffer and Nultsch [24]. The *C. reinhardtii* strain used in their study differed from ours, which could explain the difference in the values.

The motility of C. reinhardtii cells has been shown to exhibit a certain level of stochasticity, which varies with environmental conditions [92, 114]. The asynchronous flagellar beating pattern causes stochastic sharp turns during the cell's motion and is

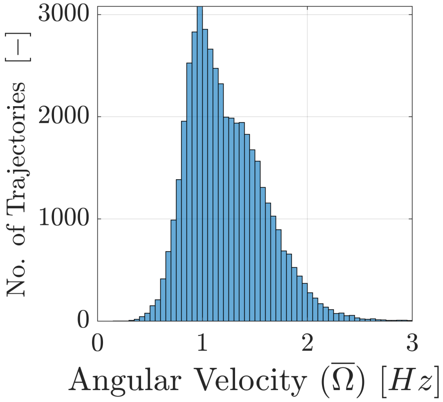

Figure 2.24: The distribution of time-averaged angular velocity ($\overline{\Omega}$) for all of the trajectories .

responsible for a run-and-tumble random walk [92], which leads to a diffusive behavior on longer time scales. We computed the reorientation time and persistence length of the cell's motion using our extensive trajectory data set to characterize this behavior. The reorientation time reflects the time scale at which the cell changes direction, while the persistence length, calculated directly from the reorientation time, shows the length scale at which the trajectory strays from a straight line. Additionally, we calculated the translational and rotational diffusion coefficients to further describe the diffusive behavior of the cell motion.

To calculate the reorientation time (τ_P), we derive an expression for the mean squared displacement (MSD) of a cell, assuming the correlation function of the swimming direction decays exponentially with a characteristic timescale τ_P. This timescale marks the crossover from ballistic to diffusive regimes. In the ballistic regime, applicable at short timescales where $t \ll \tau_P$, the MSD scales as Δt^2. Conversely, at longer timescales where $t \gg \tau_P$, the motion transitions to a diffusive regime, and the MSD scales linearly with Δt.

The MSD is expressed by the equation:

$$\mathrm{MSD}(\Delta t) = 2\langle V^2\rangle \Delta t \tau_p \left[1 - \frac{\tau_p}{\Delta t}\left(1 - e^{-\frac{\Delta t}{\tau_P}}\right)\right] \tag{2.22}$$

Here, $\langle V^2\rangle$ is the mean squared velocity of the cell. A detailed description of our model is provided in Appendix A.3. We compute the MSD for all trajectories in our experiments as $\mathrm{MSD}(\Delta t) = \langle|\mathbf{X}(\Delta t + t_\circ) - \mathbf{X}(t_\circ)|\rangle$, and τ_p is determined by fitting Eq. 2.22 to our data as illustrated in Fig. 2.25. Following this, we computed the persistence length translational and rotational diffusion coefficients as follows:

$$L_P = \sqrt{\langle V^2\rangle}\tau_P, \quad D_T = \frac{L_P^2}{3\tau_P}, \quad D_R = \frac{1}{2\tau_P}$$

Table 2.2 presents the diffusion parameters investigated in this study. Our findings regarding these parameters are consistent with previous research, indicating

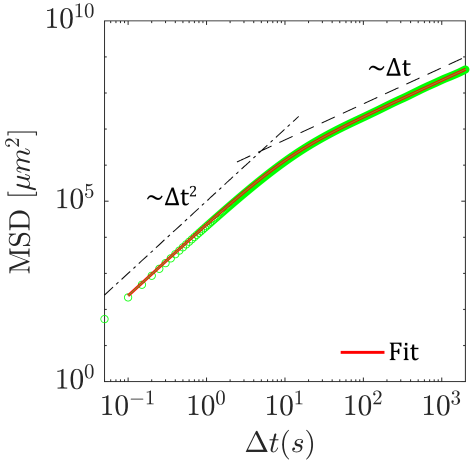

Figure 2.25: Mean square displacement (MSD) for *C. reinhardtii* three-dimensional trajectories as a function of Δt. The solid red line shows the fit used to determine reorientation time (τ_P)

Parameter	Present Work	Previous Studies
Re-orientation time (τ_P) [s]	4.7	11.2 [92], 10.8 [80]
Persistence length (L_P) [μm]	729	-
Translational diffusion coefficient (D_T) [μm^2/s]	3.77×10^4	4.7×10^4 [92], 5.56×10^3 [78]
Rotational diffusion coefficient (D_R) [rad^2/s]	0.106	0.15 [61, 78]

Table 2.2: Diffusive characteristics of *C. reinhardtii* cells swimming in Tris medium at 5×10^4 cells/ml concentration.

the reliability of our measurements. The observed average persistence length of approximately 729 μm suggests that *C. reinhardtii* cells move along relatively straight paths. Furthermore, our study emphasizes the importance of considering dimensions when making measurements, as evidenced by the contrasting translational diffusion coefficients obtained from 2D and 3D studies. Specifically, our measurement yielded a translational diffusion coefficient of 3.77×10^4 μ m^2/s, which is higher than the 5.56×10^3 μ m^2/s reported in a 2D measurement by Barry *et al.* [78]. However, our translational diffusion coefficient closely aligns with the value reported in a 3D study conducted by Polin *et al.* [92]. These findings highlight the importance of accounting for the three-dimensional motion of motile cells, as relying solely on a 2D approach may lead to an incomplete understanding of cell diffusive behavior.

2.4.4. *C. reinhardtii* CELL SURFACE INTERACTIONS

In addition to studying the trajectory kinematics of *C. reinhardtii* cells, we have used our tracking setup to investigate their interactions with solid surfaces. Our study has investigated the mechanisms underlying the accumulation of motile microswimmers at solid interfaces, which is a critical process for surface colonization and biofilm formation [115, 116]. To achieve this, we have employed our multi-camera microscope to track the swimming behavior of *C. reinhardtii* cells in a relatively unconstrained three-dimensional (3D) domain, including cell-surface encounters with a planar wall. We use our large sample of 3D trajectories to study both near-wall and long-range surface interactions. We summarize the main results here and refer the reader to Buchner *et al.* [98] for more details.

In the near-wall region, we have identified a bimodality in the cell scattering mechanisms, which corresponds to contact and non-contact interactions. Contact interactions exhibit a consistent departure angle that is independent of the approach angle, supporting the notion that geometric considerations determine the critical departure angle during contact. While contact scattering occurs more frequently, we also observe frequent non-contact scattering with planar walls, characterized by symmetrical trajectories reflecting the time reversibility of the Stokes equations.

Away from the wall, cells swimming toward the surface rotate toward it, consistent with long-range hydrodynamic interactions for puller-type microswimmers. Conversely, cells moving away from the surface display a bias towards surface-directed rotation, leading to hopping trajectories characterized by periodic surface interactions. We have implemented Markov chain Monte Carlo (MCMC) simulations to establish a clear link between micro-scale motility near interfaces and cell distribution on a macro-scale, confirming that long-range interactions play a more significant role in surface cell accumulation than near-wall scattering dynamics.

Our study highlights the importance of long-range hydrodynamic interactions in determining the surface accumulation of *C. reinhardtii* cells. Therefore, efforts to modulate cell-surface adhesion and biofilm growth through surface topography design should consider both long-range interactions and near-wall scattering dynamics.

2.5. CONCLUSION

This chapter presents a three-dimensional tracking setup and algorithm that accurately and reliably tracks the motion of microswimmers, specifically the unicellular green alga *C. reinhardtii*. Our system represents a significant advancement over previous microswimmer tracking methods, achieving reliable tracking even at higher image densities of 0.06 particles per pixel (ppp), compared to 0.006 ppp for de-focused particle tracing appraoch [82]. Our algorithm generates long trajectories with low reprojection error, enabling detailed analysis of trajectory kinematics and cell surface interactions.

Analysis of our tracking data reveals that *C. reinhardtii* cells exhibit helical swimming patterns with varying radii and pitch, as illustrated in Fig.2.19. Most cells swim in elongated helices with larger pitches and shorter radii. Additionally, we find that approximately 70% of the algae swim with left-handed chirality, consistent with previous studies. We also determine the helical angular velocity, with an average value of 1.23 ± 0.36 Hz. Lower rotation speeds result in more linear trajectories, and variations in rotation speeds among cells suggest individual differences in flagellar force asymmetries.

We characterize the diffusive behavior of *C. reinhardtii* cells by calculating parameters such as reorientation time, persistence length, translational diffusion coefficients, and rotational diffusion coefficients. Our investigation of diffusion parameters reaffirms the consistency of our measurements with previous research. Importantly, we highlight the significance of considering dimensions when quantifying diffusion. Specifically, our 3D measurement yields a translational diffusion coefficient one order of magnitude higher than that previously reported in 2D measurements by Barry *et al.* [78]. These findings underscore the necessity of accounting for the three-dimensional nature of cell motion, as relying solely on a 2D approach may limit our understanding of cell diffusion behavior.

Our investigation of *C. reinhardtii* cell surface interactions using our tracking setup provide valuable insights into the mechanisms governing the accumulation of motile microswimmers at solid interfaces. We differentiate between contact and non-contact interactions in the near-wall region, observing consistent departure angles during contact and symmetrical trajectories during non-contact scattering with planar walls. Away from the wall, cells swimming toward the surface exhibit surface-directed rotation, while those moving away from the surface display a bias towards surface-directed rotation, resulting in hopping trajectories with periodic surface interactions. Our findings demonstrate the significance of long-range hydrodynamic interactions in surface cell accumulation, emphasizing the need to consider these interactions in efforts to modulate cell-surface adhesion and biofilm growth through surface topography design alongside near-wall scattering dynamics.

Overall, the results of our study demonstrate the effectiveness and versatility of our tracking setup, which is a powerful tool for investigating the motile behavior of microorganisms with high accuracy. In addition, our system can be utilized to study the impact of environmental factors, such as light, gravity, and nutrient availability, on the motility of various microorganisms. These investigations hold significant implications for microbiology, ecology, and biotechnology.

3

PAIR-WISE INTERACTIONS OF CHLAMYDOMONAS REINHARDTII

Microorganisms exhibit collective behaviors, such as biofilm formation, bioconvection, and bacterial turbulence. The origins of these behaviors, whether they arise from short-range, long-range, or a combination of both types of interactions, are not well understood. This uncertainty stems from the fact that the nature of pairwise interactions and their impact on microorganism trajectories has predominantly been explored through numerical simulations, with only a limited number of experimental studies. To address this gap, this chapter experimentally investigates the pairwise interactions of C. reinhardtii cells to better understand how pairwise interactions between cells influence the trajectories of microswimmers. Utilizing a unique multi-camera microscopy system, we captured over 552,000 three-dimensional trajectories within the same volume of 2.5 × 2.5 × 2 mm^3*. These trajectories are reconstructed using an in-house tracking algorithm based on projective geometry, allowing for the analysis of 35,135 algal pairs with interaction distances ranging from 10 µm to 100 µm. Numerical simulations are also performed using the spring-bead model to gain insights into our experimental observations. Our analysis focused on both geometric and kinematic parameters of cell motion, investigating cell scattering and acceleration during interactions. The results revealed significant variability in scattering behavior, with small dependence on the distance between cells or incoming angle. In contrast, simulated trajectories showed a clear dependence on these factors, with scattering angles notably smaller than those observed experimentally. This difference suggests that hydrodynamic forces alone cannot explain the observed behaviors; instead, inherent motility factors such as variations in cell velocity and flagellar dynamics play a critical role. Further analysis of tangential acceleration during interactions identified distinct patterns of 'hard' and 'soft' collisions. We observed more instances of 'soft' collisions, where variations in acceleration were negligible during cell-cell interactions. Overall, our findings suggest that although hydrodynamic interactions influence cell trajectories, biological noise plays a more significant role.*

3.1. INTRODUCTION

Understanding the nature of pair-wise interactions is the first step towards unraveling the collective behavior arising from microorganisms' interactions. Collective behaviors on the small scale, such as bioconvection [117], biofilm formation [116], and bacterial turbulence [118], are reminiscent of macro-scale phenomena like bird flocking and fish schooling and hint at the universal nature of such patterns [33]. Questions naturally emerge regarding the origins and characteristics of collective phenomena in microswimmers. A central question is to identify the nature of pair-wise interactions and the relative importance of close and long-range interactions on these observed collective behaviors [60–62]. Pair-wise interactions are the building blocks of collective behavior and lead to the scattering of microorganisms [119–122], which, in turn, significantly affect the overall behavior of the population [123–125]. Therefore, investigating pair-wise interactions can provide critical insights into the mechanisms driving larger-scale phenomena.

Numerical and analytical studies have been conducted to discern the nature of interactions among microswimmers [119–133]. These interactions are influenced by several factors, including the type of microorganism [119–122], whether the swimmer can be characterized as extensile or contractile, and its shape[134]. Furthermore, interactions between microswimmers can be broadly categorized into two types based on the distance between the organisms: long-range (far-field) and short-range (near-field) interactions. Long-range interactions are primarily driven by the hydrodynamic forces generated by the microswimmers, which significantly influence the flow patterns and hydrodynamic fields surrounding the microorganisms [121]. On the other hand, short-range interactions are predominantly a result of direct collisions and hydrodynamic forces, such as lubrication forces [61].

Early investigations into the interactions of microswimmers primarily focused on hydrodynamic interactions in both the close-range and long-range [119, 120, 123, 126]. These studies are based on analytical representations of the swimmers, including the squirmer model [135] and the three-bead swimmer model [136], which are used in numerical simulations to predict the effects of hydrodynamic interactions by determining swimmer trajectories. The studies demonstrate that these interactions can be repulsive, attractive, or a combination of both, depending on factors like swimmer type (extensile or contractile) and relative orientation. Additionally, hydrodynamic interactions are most significant at close distances, where swimmer scattering is more prominent, and become negligible at distances exceeding ten body lengths.

Recent studies have investigated the factors affecting interactions between microswimmers, especially at close range. Using the squirmer model, Darveniza *et al.* [122] showed that the angle at which swimmers approach each other can result in different scattering states. These states include a permanent bound state, an orbiting state (more common among extensile swimmers), a scattering state where swimmers scatter in various directions, and a parallel swimming state where cells swim parallel to each other while maintaining a constant distance. Similarly, Ziegler *et al.* [121] applied the spring-bead model and found that the incoming angle also influenced the resulting

---

Part of this chapter has contributed to "J. Mehmood, K.Muller, and D. Tam, “Pair-wise interactions of Chlamydomonas Reinhardtii”, Physical Review Fluids, 2024, In preparation".

scattering behaviors, which ranged from orbiting to pair-wise swimming.

Together, these results highlight the complex nature of interactions between microswimmers, leading to changes in motility that can be understood by examining cell kinematics. However, translating these theoretical results to biological swimmers in natural environments poses challenges. The analytical and numerical models rely on assumptions such as steady-state modeling, identical velocities for both swimmers and simplified flagellar shapes, which may affect the accuracy of interaction predictions. The simplicity of these models limits their ability to capture the complexity of the interactions between microswimmers. For example, *C. reinhardtii* cells swim with an unsteady flow field where the stresslet sign changes with each power and recovery stroke [137]. Furthermore, recent measurements indicate that the unsteady flow component is equally important as the steady component within a few body lengths [138]. Therefore, incorporating unsteady flow is essential in studying hydrodynamic interactions. Additionally, motility is subject to biological noise, which leads to microswimmers changing their swimming direction randomly and influences the movement of microorganisms [3]. For example, biological noise in the motility of bacteria and *C. reinhardtii* lead to a diffusive behavior that can be stronger than the effect of long-range hydrodynamic interactions [61]. These important factors are often overlooked in many analytical and numerical studies. Experimental studies are crucially needed to elucidate pair-wise interaction between biological swimmers, but such experiments are challenging, and only a few studies have attempted to characterize pair-wise interactions, including a study of *E. coli* bacteria [139] and a study of protist *Paramecium caudatum* [140].

The first experimental study of *E. coli* used a two-dimensional epifluorescent microscopy technique to track the movements of the bacteria [139]. This study measured the velocity correlations between individual cells and characterized the correlation decay as a function of the inter-swimmer distances. The results suggested that these bacteria interact with each other through the force-quadruple component of the flow fields. The interaction mode was further investigated in an analytical study [141]. This work proposed that the observed decay in velocity correlation, attributed to the quadruple moment in Liao *et al.* [139], was instead predominantly influenced by orientation correlations associated with a dipole moment, a factor not accounted for in the experimental study of Liao *et al.* [139]. The second experimental investigation focused specifically on interactions between *Paramecium caudatum* [140]. This organism is significantly larger than *E. coli* and other microorganisms like *C. reinhardtii*. The study revealed the existence of both close and long-range interactions between two cells, highly dependent on the initial orientation of the cells. It is important to note that the experimental design, which included a flow device with a small chamber between two flat plates, inherently restricted the motion of the microswimmer. Consequently, surface interactions were also an influence on the observed phenomenon.

Direct experimental observations of cell-cell interactions are challenging, and few such studies have been attempted. An experimental setup to investigate pair-wise interactions requires a high tracking accuracy to resolve small distances, an unconstrained flow geometry to eliminate surface effects, and freely swimming cells.

Meeting these conditions is challenging for conventional three-dimensional imaging techniques, as discussed in chapter 2. Here, we use our unique multi-camera microscope to investigate the pair-wise interactions of *C. reinhardtii*, a puller-type microorganism. We image the same volume of 2.5 × 2.5 × 2 mm^3 with four sCMOS cameras recording from four different viewing angles. Three-dimensional trajectories of microswimmers are reconstructed using an in-house tracking algorithm based on the projective geometry framework. First, we focus on the scattering behavior of the cells, examining the angles at which cells scatter when in close proximity. Our findings indicate an asymmetry of scattering behavior, with one cell in each pair scattering at a smaller angle compared to the other. Through comparison with numerical simulations of scattering angles, we observe that biological noise, the inherent variability in the swimming motion of microorganisms, influences these scattering behaviors. We then explore the effects of interactions on the instantaneous motion of the cells by analyzing trajectory curvature. Our numerical simulations demonstrate how the distance between cells and their approach angle influence trajectory deflections due to hydrodynamic interactions. Our experimental data is in qualitative agreement with the simulations for cells coming within 15 μm of each other and approaching each other with parallel incoming angles. Additionally, we investigate the variations in tangential acceleration during close-range interactions, distinguishing between 'hard' and 'soft' collisions. In 'hard' collisions, at least one cell comes to a complete stop before continuing forward, while 'soft' collisions exhibit no noticeable effect on cell acceleration. We observe more instances of 'soft' collisions than 'hard' ones. Together, our findings show the effect of hydrodynamic interaction on cell-cell interaction and highlight the need for theoretical models to include biological noise as a critical factor to capture the complex dynamics of these interactions accurately.

Below, we first describe our experimental methodology. Next, we discuss cell-cell scattering in detail before examining the instantaneous effects of interactions on three-dimensional trajectories, using both numerical simulations and our experimental data. We then highlight the impact of pair-wise interactions on tangential acceleration. Finally, we conclude this chapter by summarizing our findings and discussing their implications.

3.2. METHODOLOGY

This section describes the methodology used in our study of pair-wise interactions of *C. reinhardtii*. We begin by describing the tracking experiments conducted to capture the movement and behavior of the microorganisms, including the algorithm used to extract three-dimensional trajectories from the recorded images. We also describe the curve-fitting algorithm used to compute relevant trajectory parameters for our analysis. As our focus lies on understanding pair-wise interactions, we describe how we identify trajectories corresponding to pair data within the tracking data and the methodology employed to characterize these pairs. Finally, we outline the numerical model used in conjunction with 3D tracking experiments to study pairwise interactions.

3.2.1. CELL IMAGING AND 3D TRACKING

We performed cell imaging of a dilute suspension of *C. reinhardtii* with a concentration of 5×10^4 cells per ml. The cells were loaded into a flow chamber made from an acrylic sheet by laser cutting a hole with dimensions of 8 mm in diameter and 2 mm in height. The chamber was sealed with two parallel glass coverslips and treated with BSA to prevent cell adhesion to the surfaces. To capture the three-dimensional behavior of the microorganisms, we used our unique multi-camera microscopy system, consisting of four sCMOS cameras simultaneously imaging the same volume of $2.5 \times 2.5 \times 2\ \mathrm{mm}^3$. Red laser light with a wavelength of 650 nm was used for illumination, which does not trigger the phototactic response [27, 105]. Thirty-eight recordings were taken, each recorded at 20 frames per second, resulting in a dataset of 2.28×10^5 images per camera and a cumulative recording time of 190 minutes.

Tracking was performed using our in-house algorithm based on the framework of projective geometry. The algorithm involved initial cell detection using a peak finding algorithm, followed by tracking within individual frames. Cell images in the different camera views are matched in the projective geometry framework, enabling triangulation in three dimensions. Subsequently, three-dimensional trajectories are obtained using an iterative optimization algorithm. Data segmentation and filtration were performed to remove the ghost tracks and artifacts due to algae blinking and poor reconstructions. With this methodology, we extracted 5.52×10^5 trajectories, with an average track length of 5 ± 1 seconds and an average re-projection error of $1.8 \pm 0.4\ \mu$m. Details of the cell culturing, microscopy setup, and tracking algorithm can be found in chapter 2.

3.2.2. CURVE FITTING

Following the precise tracking of cell pairs, we use a curve-fitting procedure on the recorded trajectories. This step is important for three reasons. First, curve fitting allows us to represent cell trajectories as continuously parameterized curves of the form, $\mathbf{X}(t) = \begin{bmatrix} X(t) & Y(t) & Z(t) \end{bmatrix}$. This parametric representation can be analytically differentiated to extract the relevant trajectory parameters, such as acceleration and curvature. Second, this method reduces tracking-associated noise, which is inevitable due to false identification and correspondences, as well as the effect of algae blinking (see section 2.2.4 and 2.4.2). Lastly, the curve fitting procedure smooths the helical characteristics of the cell trajectories. This helps distinguish between orientation changes due to pair-wise interactions and periodic orientation changes resulting from helical swimming patterns. Details of the curve fitting procedure are described below.

We begin from the trajectory parameterization based on piece-wise Legendre polynomials as described in chapter 2.4.2. This yields continuous trajectories with an average fitting error of less than 0.2 μm. Next, we use a least-square minimization technique to approximate and smooth the curve by minimizing an energy function. This energy minimization technique, specially designed for smoothing three-dimensional curves, incorporates stretching, bending, and twisting energies, calculated as follows [142]:

$$E_{\text{stretch}} = \int \left|\mathbf{X}'(t)\right| dt\,, \quad E_{\text{bend}} = \int \kappa^2(t) \left|\mathbf{X}'(t)\right| dt\,, \quad E_{\text{twist}} = \int \left|\tau^2(t)\mathbf{X}'(t)\right| dt \tag{3.1}$$

Here, κ and τ represent the curvature and torsion of the curve, respectively. The stretching energy represents the length of the curve while bending and twisting energies depend on the curvature and torsion.

For our trajectories, we only minimized the stretching energy, as minimizing bending and twisting energies resulted in excessive smoothing of the trajectories. To solve this nonlinear optimization problem associated with the minimization of stretch energy (E_{stretch}) as described in Eq. 3.1, we use a quadratic energy function [142]:

$$E_{\text{stretch}} = \int \left|\mathbf{X}^{'}(t)\right|^{2} dt \tag{3.2}$$

This quadratic formulation was chosen because it transforms the energy function into a smooth and continuously differentiable form, simplifying the computation of derivatives and the overall optimization process. Unlike the linear form, which involves the integral of the norm and can lead to non-differentiability issues at points where $\mathbf{X}^{'}(t) = 0$, the quadratic form ensures that the gradient can be computed uniformly across all points. Furthermore, the quadratic energy function naturally leads to linear equations during optimization, enhancing computational efficiency and stability.

The objective function of our minimization problem combines the stretching energy and least squares fitting error between the trajectory parametrization and the measured position along the trajectory. This formulation differs from the method described in section 2.4.2 due to the inclusion of the term for minimizing stretching energy, which may lead to variations in the re-projected positions on the image. The complete formulation is presented below:

$$\min_{\beta} \sum_{i=0}^{N} \left|\mathbf{X}(t_i,\beta) - \mathbf{X}_i\right|^{2} + \gamma \int_{0}^{N} \left|\mathbf{X}^{'}(t_i,\beta)\right|^{2} dt \tag{3.3}$$

Here, γ is a weighting parameter, N represents the time steps along the trajectory, and $\mathbf{X}(t,\beta)$ defines our parameterized trajectory. The weighting parameter γ is critical to our optimization problem and is calculated using $N\bar{R}/L$, where $\bar{R}$ represents the average trajectory radius, and L is the trajectory length. Details of the solution to this optimization problem are described in Appendix B.2.

Fig. 3.1 shows how a parameterized trajectory is fitted to a pair of cell trajectories. In Fig., 3.1 A, the green and red dots represent the trajectories directly obtained from the triangulated points directly obtained from the three-dimensional tracking algorithm. The solid black lines illustrate the parameterized trajectories obtained from our curve-fitting algorithm. Our approach regularizes the periodic helical movements inherent in the cell trajectories. It bears emphasis that the regularization applied by our curve-fitting algorithm does not change the overall direction of cell movement, which is still preserved. In Fig. 3.1B, the dots represent the curvatures (κ) computed from the original trajectories and the solid lines the curvature deduced from the parameterized trajectories for the same tracks a and b in Fig. 3.1A. The original trajectory data contain significant noise, which is effectively reduced in the parameterized trajectories.

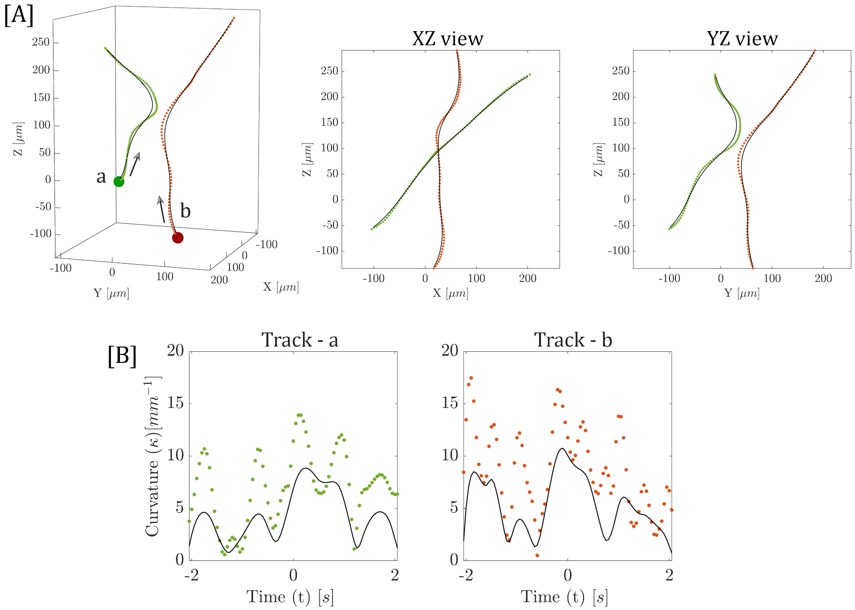

Figure 3.1: [A] Three different views of the trajectories of two algae cells, denoted as (a) and (b), in three-dimensional space. Green and red dots represent the cells' trajectories. The first plot presents a three-dimensional perspective, while the second and third plots show the XZ and YZ plane views, respectively. The solid black lines in each plot illustrate the parameterized trajectories obtained from the curve-fitting algorithm. [B] Curvature of the original and smoothed trajectories for cell (a) (left) and cell (b) (right). The solid black lines correspond to the curvature of the smoothed trajectories. The dots represent the curvature of the unsmoothed trajectories, highlighting the original noise level.

3.2.3. DEFINITION AND TRACKING OF PAIR INTERACTIONS

In this study, we identify pair interactions as events where two algae cells first swim towards each other, then come within a distance of at most 100 μm, and subsequently move away from each other. The distance between two cells is determined at each time from the three-dimensional trajectories of each cell. Fig. 3.2 is a representative illustration of the tracking of a pair interaction. Each image row in Fig. 3.2 A displays the sequence of cell images captured by one of the cameras, overlaid with the cells detected using our peak finding algorithm (see section 2.2.4 for more details). The image sequence extends from $t = -0.25s$ to $t = 0.25s$, with $t = 0$ defined as the time step when two cells are at a minimal distance.

At the time step $t = -0.25$ s, both cells are detected separately in each of the four cameras. As the cells approach each other and their images begin to overlap, the two cells are no longer individually detected in all four cameras. For the pair tracked in Fig. 3.2 A, the two cells are not separately detected at some point during the sequence in each camera view. These occlusions can lead to uncertainties in cell detections and cell matching across the different camera views and lead to unreliable tracking. Our multi-camera setup is advantageous for tracking these close interactions because, in most cases, at a given time steps, cells can be separately detected in at least one of the four camera views. The separate identification of cells in at least one of the cameras allowed our three-dimensional tracking algorithm to successfully reconstruct the positions of the algal cells, as demonstrated in Fig. 3.2 B and C. In this pair interaction, the cells pass each other at a minimum distance of 1.6 body lengths. Fig. 3.2 D displays the re-projected trajectories in each camera plane, illustrating the accurate tracking of algae cells.

In some cases, the cell image overlapped for over 0.5 seconds in at least two cameras. Although the cells were detected separately in at least one camera, this overlap could lead to uncertainties in tracking. These uncertainties lead, in some cases, to cell images switching from one track to the other and being assigned to the wrong trajectory before and after the point of the nearest approach. This issue was detected through manual inspection focused on cell pairs with a minimum distance of less than 30 μm, where cell images can overlap. The re-projected positions of these pairs were reviewed in a video sequence from $t = -1$s to $t = 1$s. The velocities of the trajectories were also checked for consistency before and after the point of minimum distance, as cells are expected to have a similar velocity pattern before and after passing each other. Trajectory switching was found in about 5% of the inspected pairs. A correction procedure was implemented to resolve this. Further details about the trajectory switching and the correction procedure are provided in Appendix B.1.

3.2.4. PAIR SELECTION AND CHARACTERIZATION

For our analysis, we focus on pairs that meet the following criteria. First, both cells in a pair must exhibit an average velocity greater than 50 μm/s, ensuring that we only consider motile swimming cells. We only considered trajectories that include at least one second of tracking data before and after the closest approach. This selection criterion ensures that we have sufficient trajectory information to examine the behavior of the pairs over time. Finally, we only kept pairs where the two cells are the closest cells to each other at each time step. This temporal restriction allows us to investigate the immediate interaction between the cells without the influence of any third cell close by.

Pair interactions are defined using two key parameters: the approach angle ϑ and the cell-cell distance at the point of nearest approach $d_{\min}$. We define the incoming angle, ϑ, as the angle between the two unit vectors ($\hat{\boldsymbol{T}}_a$ and $\hat{\boldsymbol{T}}_b$) tangent to the trajectories of two swimmers, "a" and "b", as they approach each other. The unit vectors ($\hat{\boldsymbol{T}}_a$ and $\hat{\boldsymbol{T}}_b$) are obtained by fitting a parameterized line to the respective trajectories from $t = -1$s to $t = -0.5$s. This is illustrated in Fig. 3.3, where $t = 0$ marks the time of closest approach and $d_{\min}$ is the minimum distance between the swimmers. These two parameters have been used previously in studies considering cell-cell scattering and interaction dynamics [119, 121, 122].

Our dataset samples the full range of ϑ and $d_{\min}$. Fig. 3.4A presents the joint distribution of minimum distances and incoming angles for all the algae pairs recorded in this investigation. We acquired 35,135 algae pairs with a cell-cell distance at the nearest approach $d_{\min}$ ranging from 10 μm to 100 μm. The number of pairs in our dataset increases with $d_{\min}$, see Fig. 3.4A. Fig. 3.4B shows the distribution of incoming angles ϑ in our dataset. While most pair interactions have an incoming angle close

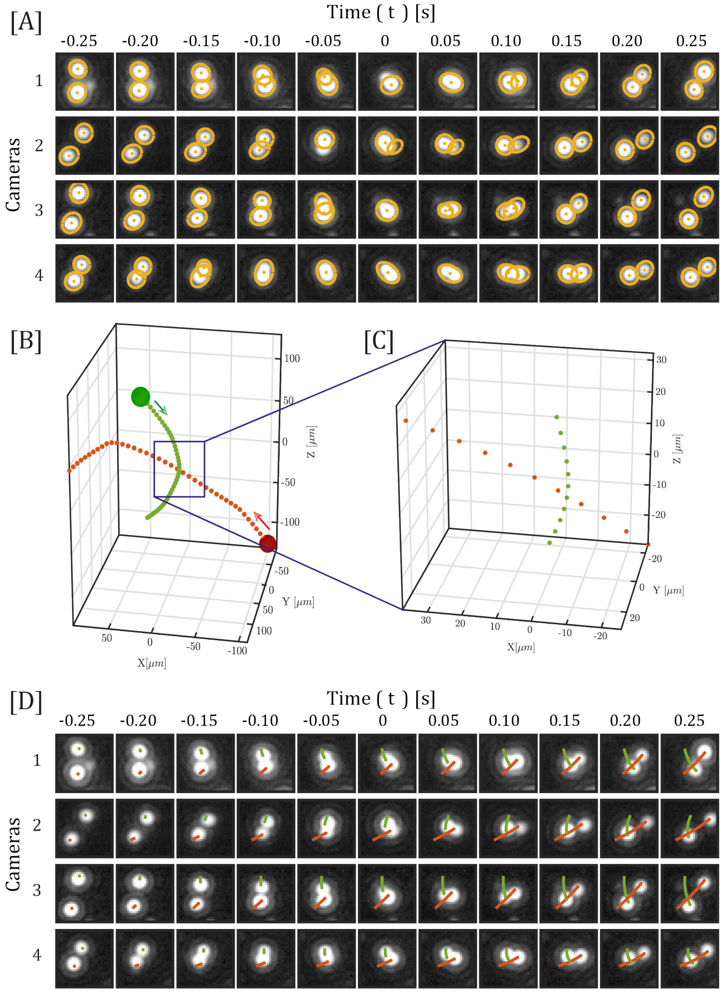

Figure 3.2: Tracking of algae cells during close interactions. [A] Series of image frames captured for each of the four cameras, showing detected algae and their midpoints, for successive time steps. The negative time steps depict the approach phase of the cells, while positive time steps show the cells moving away from each other. At $t = 0$, the cells are at their minimum separation distance in physical space, and their images overlap in each camera view. [B] The three-dimensional positions of both algal cells, triangulated using the detections from multiple cameras. Arrows indicate the direction of motion. [C] A detailed, zoomed-in view of the triangulated positions during the closest approach phase, demonstrating the precision with which the positions are determined despite overlapping images. [D] The re-projection of the three-dimensional tracks onto the camera plane effectively illustrates the accurate tracking of algal cells through various stages of their interaction and validates the robustness of the tracking algorithm during close encounters. Note that the minimum separation distance between the cells during this interaction is 1.6 body lengths.

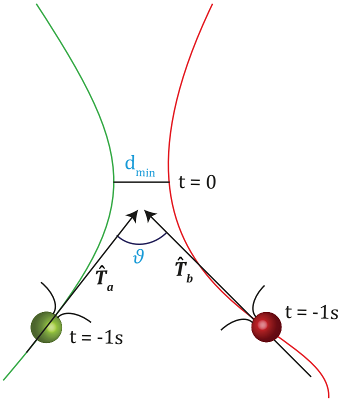

Figure 3.3: The relative geometry for the trajectories of swimmer *a* (green) and swimmer *b* (red). $t = 0$ represents the time of the closest approach, d_{min} denotes the distance at the closest approach, and $\hat{\boldsymbol{T}}_a$ and $\hat{\boldsymbol{T}}_b$ are the unit direction vectors obtained by fitting a parameterized line from $t = -1s$ to $t = -0.5s$. Incoming angle, denoted by ϑ, represents the angle between $\hat{\boldsymbol{T}}_a$ and $\hat{\boldsymbol{T}}_b$.

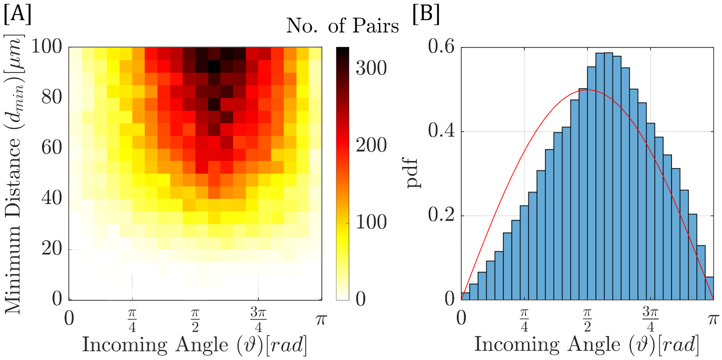

Figure 3.4: [A] Joint distribution of minimum distance (d_{min}) and incoming angle (ϑ) for all the algae pairs. [B] The probability density function (pdf) of incoming angle (ϑ) for all the algae pairs. The solid red lines show the theoretical distribution, $\sin(\vartheta)/2$, of the incoming angle (ϑ) between two particles moving randomly in three dimensions.

to $\pi/2$, we observed a slight under-representation of angles between 0 and $\pi/2$ and a slight over-representation between $\pi/2$ and π compared to the theoretical isotropic distribution (solid red line in Figure 3.4B). The Wasserstein distance between the two distributions is only about 11°, indicating that the deviation from isotropic behavior is minimal. The difference between the theoretical and measured distributions arises from our sampling method, which preferentially selects pairs of cells that are approaching each other. This results in an inherent bias towards interactions at angles between $\pi/2$ and π. This bias is due to the similar velocities of the cells, which make encounters from the front more probable than from behind. Despite this bias, the observed distribution closely resembles the isotropic distribution, suggesting that in our experiment, cells swim mostly without a preferred direction.

3.2.5. NUMERICAL SIMULATIONS

This section outlines the approach used in the numerical simulations we performed to gain insight into our 3D study of pair-wise interactions. These simulations provide a theoretical framework to compare with our experimental results and to help in understanding the influence of ϑ and d_{min} on the scattering behavior during cell-cell interactions of *C. reinhardtii*.

We use the same spring-bead model used by Lushi *et al.* [143] to study surface scattering of *C. reinhardtii*. This model was originally introduced to study the dynamics of confined suspensions [144, 145]. The spring-bead model is a simple model that captures the dynamics of the microswimmers' motion and has been applied in various contexts, including cell-surface scattering [143], investigating the effects of swimmer size and shape [146], and analyzing pair-wise interactions [121]. In this model, each *C. reinhardtii* cell is represented as a three-bead system comprising a body bead and two smaller beads representing the flagella, each with half the radius of the body bead. The three beads are linked to each other with linear springs. The motion of the bead is deduced from a force balance on each bead. The forces applied on each one of them include: (i) the elastic forces, due to the linear springs connecting the beads (ii) the hydrodynamic drag forces (iii) a propulsion force, which acts only on the flagellum beads. The swimming velocity is deduced from the condition that the entire swimmer is force and torque-free. The hydrodynamic drag force on each bead is computed using a generalized Stokes' law, which depends on the velocity of the beads and on the background flow velocity generated by the motion of the other beads. The flow field generated by each bead is modelled with a regularized Stokeslet at each bead location. For simulations involving interactions between two swimmers, we account for hydrodynamic interactions by updating the fluid velocities at each bead's location at every time step, reflecting the influences of all beads from both swimmers. A complete description and validation of this model is provided in appendix B.3.

To investigate pair-wise interactions in our study, we consider two three-bead swimmers, "a" and "b", as shown in Fig. 3.5. The positions of each swimmer are described using spherical coordinates, with r the radial distance from the origin, θ the polar angle, and ϕ the azimuthal angle. θ is measured from the positive Z-axis and ranges from 0 to π, and ϕ is measured from the positive X-axis in the XY plane towards the projection of the radial line $\mathbf{r}$ and ranges from 0 to 2π. The distance between two swimmers, d,

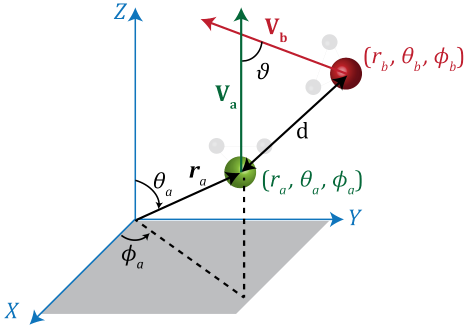

Figure 3.5: Schematic illustration of the spherical coordinate system used to define the positions and motions of two three-bead swimmers, labeled as swimmer a and swimmer b. The coordinates (r, θ, ϕ) describe the position of each swimmer, where r is the radial distance from the origin, θ is the polar angle measured from the positive Z-axis, and ϕ is the azimuthal angle measured from the positive X-axis on the XY plane. The distance d between the swimmers is represented by the magnitude of the vector difference between their positions, and ϑ represents the angle between their velocity vectors $\mathbf{V}_a$ and $\mathbf{V}_b$.

corresponds to $|\mathbf{r}_b - \mathbf{r}_a|$, where $\mathbf{r}_b$ and $\mathbf{r}_a$ are the position vectors of each swimmer. Additionally, the approach angle ϑ is defined as the angle between the initial velocity vectors of each swimmer $\mathbf{V}_a$ and $\mathbf{V}_b$ at $t = 0$.

To simulate hydrodynamic interactions between two three-bead swimmers, “a” and “b”, we initialize the positions, velocities, and directions of motion at $t = 0$. Swimmer “a” is located at $r_a = 200\ \mu$m, $\theta_a = \pi$, and $\phi_a = 0$, moving in the positive Z-direction with a velocity of V_a. The starting coordinates of swimmer “b”, r_b, θ_b, and ϕ_b, are chosen within specific ranges: r_b from 200 μm to 400 μm, θ_b from 0 to π, and ϕ_b from 0 to $\pi/4$. The direction of motion for swimmer “b” is adjusted by varying $\mathbf{V}_b$. The propulsion force for each swimmer is adjusted to achieve specific velocities: swimmer “a” moves at $V_a = 100\mu$m/s, and swimmer “b” at $V_b = 112\mu$m/s. These velocities are the typical swimming speed of *C. reinhardtii*, with the relative speed of 12 μm/s accounting for scenarios where one swimmer approaches the other from behind when ϑ is approaching zero. The swimmers’ trajectories are then computed at each time step and take into account hydrodynamic interactions as detailed in Appendix B.3. We perform 7500 simulations by varying r_b, θ_b, ϕ_b, and $\mathbf{V}_b$ for each simulation. These simulations yield a range of d_{min} and ϑ, and the distribution of d_{min} and ϑ are represented in Fig. 3.6 similar to to the representation for our experiments Fig. 3.4.

Fig. 3.7 A presents the trajectories of three pairs of simulated swimmers to illustrate the numerical approach used in our simulations. The larger spheres represent the body, and the smaller spheres represent the flagella. Swimmer a in each pair starts at the same location, swimming at 100 μm/s in the positive Z direction. Swimmer b moves with a velocity of 112 μm/s, and the initial position of this swimmer is different in each of the three examples, creating different incoming angles: Pair I with an angle (ϑ) of $\pi/10$ and

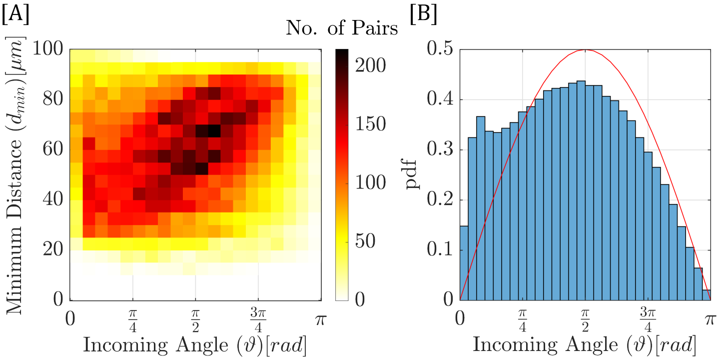

Figure 3.6: [A] Joint distribution of minimum distance (d_{min}) and incoming angle (ϑ) for all the simulated pairs. [B] The probability density function (pdf) of incoming angle (ϑ) for all the algae pairs. The solid red line shows the theoretical distribution, $\sin(\vartheta)/2$, of the incoming angle (ϑ) between two swimmers moving randomly in three dimensions.

a minimum distance (d_{min}) of 18 μm; Pair II with $\vartheta = \pi/3$ and $d_{\text{min}} = 14\mu$m; and Pair III with $\vartheta = 5\pi/6$ and $d_{\text{min}} = 18\mu$m.

In the absence of hydrodynamic interactions, these swimmers would travel along straight trajectories. Here, each swimmer influences the swimming velocity of the other through hydrodynamic interactions, and we can characterize this scattering by quantifying the changes in direction. The scattering is stronger for Pairs I and II compared to pair III, even though for each pair, the cells came within a similar minimal distance d_{min} to each other. We observe that the scattering of the swimming direction begins before the swimmers reach the point of minimum distance, see in particular Pair I. These preliminary observations motivate a more detailed exploration in the results section, where we will expand our examination to cover the full parameter space using this simulation setup.

3.3. CELL-CELL SCATTERING DYNAMICS

3.3.1. 3D TRAJECTORIES AND SCATTERING BEHAVIOR: ANALYSIS OF EXAMPLE PAIRS

We begin by presenting nine examples of pairs approaching each other at different approach angles ϑ to illustrate the nature of our dataset. For these nine pairs, the minimum approach distance between the cells ranges from $d_{\text{min}} = 9\mu$m to 29 μm. Fig. 3.8 represents the reconstructed trajectories of these pairs, which are divided into three distinct categories based on their incoming angles: parallel ($\vartheta \approx 0$), perpendicular ($\vartheta \approx \pi/2$), and anti-parallel ($\vartheta \approx \pi$). For each category, we present the trajectories associated with three pairs. The solid colored lines correspond to the three-dimensional trajectories, and the dotted colored lines are the projections of the trajectory in the best-fitting 2D plane. The length of the corresponding directional arrow indicates the velocity of each swimmer. Fig. 3.9 presents the original camera images associated with these

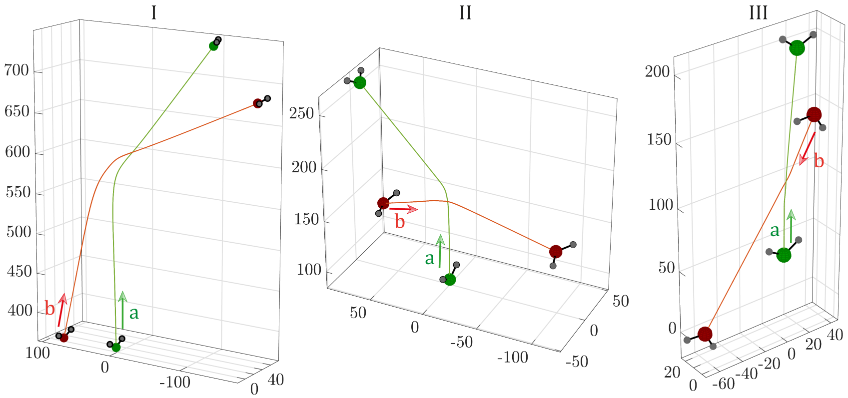

Figure 3.7: Example three-dimensional trajectories of the three-bead model simulation for pair interactions: I) $\vartheta = \pi/10$, $d_{\text{min}} = 18\mu$m, II) $\vartheta = \pi/3$, $d_{\text{min}} = 14\mu$m, III) $\vartheta = 5\pi/6$, $d_{\text{min}} = 18\mu$m. The larger sphere represents the body bead, while the smaller spheres represent the flagellar beads. The velocities of swimmer a and swimmer b are 100 and 112 μm/s, respectively.

nine pair interactions together with the reprojected trajectories on the camera plane. For each pair, the cell images overlap in at least one camera view, which indicates that the cells come within a small distance of each other.

To quantify the observed changes in trajectories, we define the scattering angles α for all trajectories displayed in Fig. 3.8. The scattering angle quantifies the extent of directional changes in a cell's trajectory resulting from an interaction with another cell. We compute this angle from the change in the direction of the tangential vector to the cell's trajectory before and after reaching the point of closest approach (see Appendix B.4 for more details). The computed scattering angles for each trajectory are shown in Fig. 3.10. For Pair I, IV, and VII, the scattering angles α are below $\pi/6$ for both trajectories, indicating only minor deflections from the initial paths. Pair II, V, and VIII scatter asymmetrically , with one cell deviating considerably from its path with $\alpha \sim \pi/3$ while the other continues with minimal directional change $\alpha \leq \pi/6$. Lastly, Pairs III, VI, and IX exhibit larger scattering angles for both cells with $\alpha \geq \pi/6$. Our dataset includes three distinct scattering behaviors: i) no deflection for both cells, ii) significant deflection of only one of the two cells, and iii) both cells scattering at high angles. All three of these scattering behaviors can be observed for different values of the approaching angle ϑ.

3.3.2. SCATTERING BEHAVIOR OF MICROSWIMMERS: THE INFLUENCE OF BIOLOGICAL NOISE

In this section, we examine the scattering dynamics of 1065 experimental pair interactions coming within a minimal distance of at most $d_{\text{min}} \leq 30\mu$m. In characterizing the nine example pairs, we observed asymmetry in the scattering for several pairs. Consequently, we designate the cell associated with the lower scattering angle in each pair as 'Cell a' and the one with the higher scattering angle as 'Cell b'. First, we consider the results of our 3D tracking experiments. The distribution of α_a,

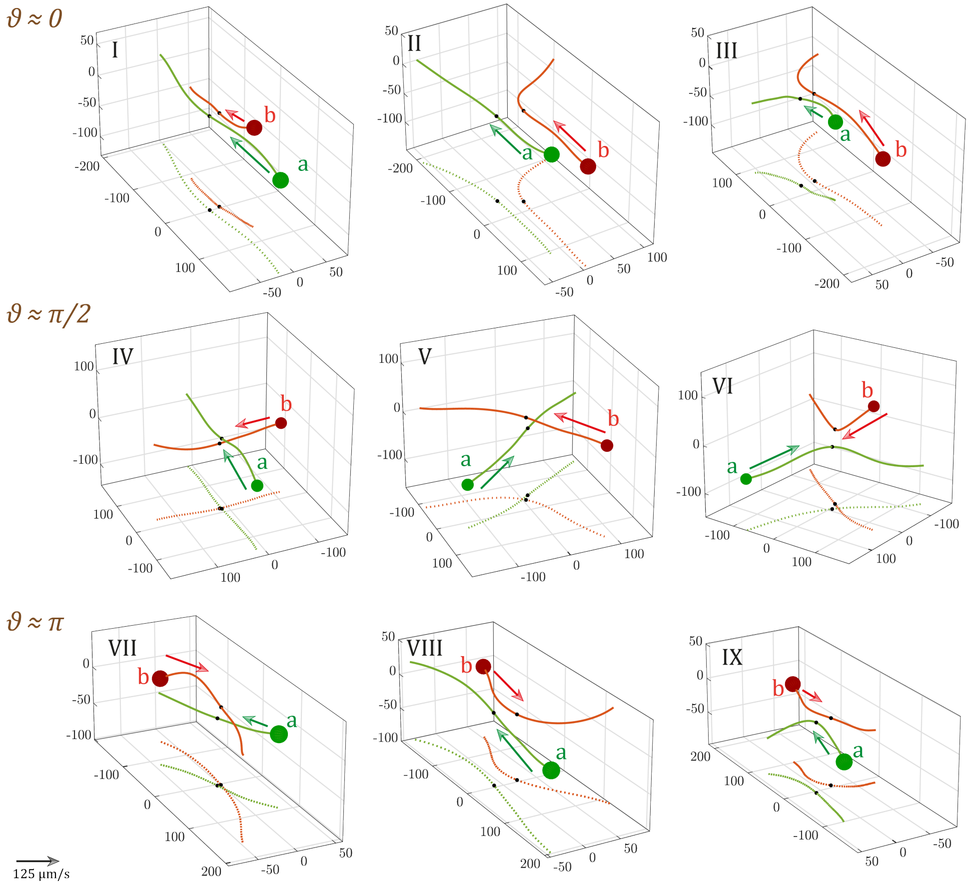

Figure 3.8: Three-dimensional trajectories from experiments for pairs under different incoming angles (ϑ), $\vartheta \approx 0$ (top row, pairs I-III), $\vartheta \approx \pi/2$ (middle row, pairs IV-VI), $\vartheta \approx \pi$ (bottom row, pairs VII-IX), with the closest approach distances (d_{min}) of I) 20 μm, II) 29 μm, III) 17 μm, IV) 9 μm, V) 27 μm, VI) 21 μm, VII) 12 μm, VIII) 28 μm, IX) 27 μm. The solid lines represent the 3D trajectories, while dotted lines represent 2D projections. The black marker indicates the point of minimum approach. The sphere at the start of each trajectory has a radius of 5 μm. Directional arrows are scaled to represent the swimmer's average velocity, with the reference arrow located at the bottom left of the figure. The axis units are in μm.

the scattering angles for 'Cell a', is shown in Fig. 3.11A. These cells, which exhibit lower scattering angles, predominantly scatter at an angle smaller than $\pi/4$, with a median of $\pi/11(17°)$. The scattering angles for 'Cell b', α_b in Fig. 3.11 B, exhibit a broader range of angles, extending from 0 to $\pi/2$ with a median of $\pi/5(36°)$. 'Cell b' can exhibit scattering angles exceeding $\pi/2$, indicative of significant directional change. For each pair, we compute the difference between α_a and α_b and present the distribution of this difference in Fig. 3.11C. For most pairs, the difference in scattering angle ranges

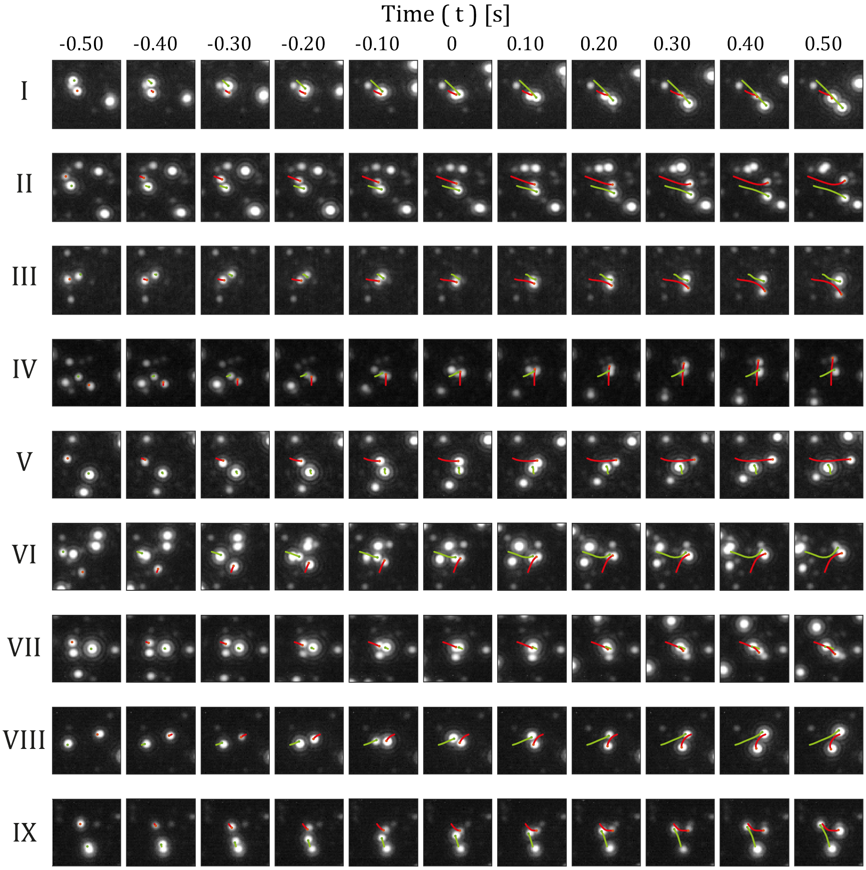

Figure 3.9: Cell images from one of the cameras for the trajectory pairs from Fig. 3.8. Solid lines represent the reprojected tracks in the image plane. The color of the lines is the same as the three-dimensional trajectory color from Fig. 3.8

between 0 to $\pi/4$, with a median value of $\pi/12(15^\circ)$. Only a few pairs have a difference in scattering angle of zero, corresponding to a symmetric scattering. For most pairs, the scattering is asymmetric and similar to the behavior of pairs II, V, and VIII illustrated in Fig. 3.10. This asymmetric scattering observed in our experiments is in contrast to the results from earlier analytical and theoretical studies [121, 122], which reported symmetric scattering for cell pairs. In these studies, the cells are identical to each other and have the same velocity. In our experimental study, the cells approach each other at different velocities and angles; the interactions between the flagella and the cell body depend on the phase of the flagellar beating stroke. The conditions under which pairwise interactions occur are complex and deviate from the often ideal initial conditions set in theoretical studies, resulting in the asymmetry of scattering angle observed in our experiments.

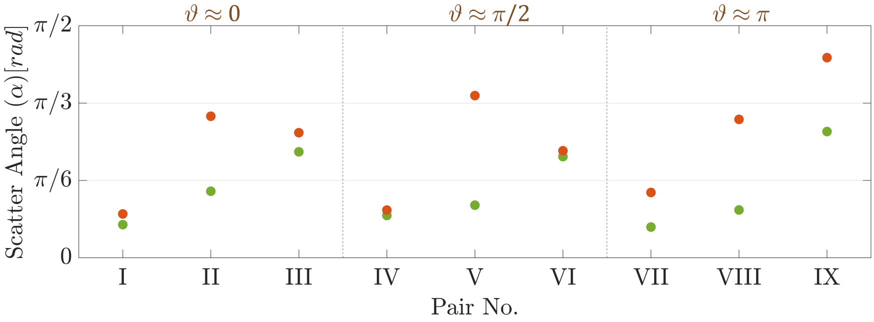

Figure 3.10: Scattering angle (α) for each cell in pairs shown in Fig. 3.8 for different incoming angle (ϑ). The color of the markers correspond to the trajectory color from Fig. 3.8.

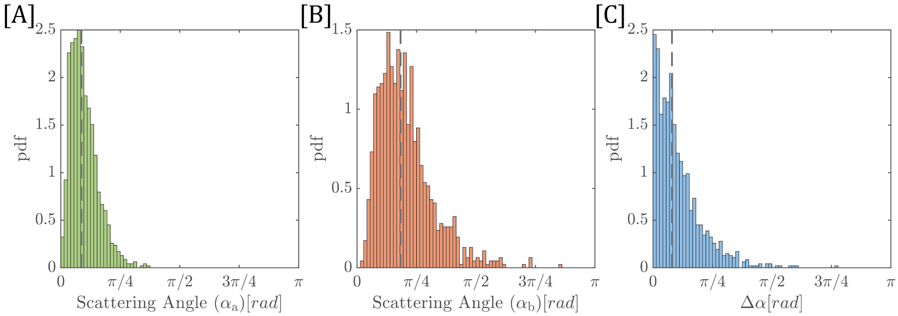

Figure 3.11: Distribution of scattering angles (α) of [A] cell a and [B] cell b in experimental cell pairs with $d_{\text{min}} \leq 30\mu$m. [C] The difference in scattering angles between cell a and b in the experiments. The dashed lines represent the median of each distribution.

We compare these results with our numerical simulations. These simulations, like our experiments, consider cell pairs coming within a minimum distance $d_{\text{min}} \leq 30\mu$m, and we use the same terminology for cells ‘a’ and ‘b’. In our methodology, we detailed the selection of initial conditions to account for variations in velocity and incoming angle (see Section 3.2.5), reflecting the non-symmetric nature of the cells and their interactions. Fig. 3.12 illustrates the distribution of scattering angles for ‘Cell a’ and ‘Cell b’ in the simulations. Here, ‘Cell a’ scatters with a median angle of $\pi/28$ (approximately 7°), and ’Cell b’ with a median angle of $\pi/17$ (approximately 10°). These values are noticeably lower than those observed in the experimental data. We find the difference in scattering angles between ‘Cell a’ and ‘Cell b’ as shown in Fig. 3.12C, we find an average difference of 2°.

Our numerical simulations show that when the initial conditions are not symmetric in terms of velocity and incoming angles, the resulting distribution of scattering angles is also asymmetric, with one cell scattering more than the other, qualitatively similar to the experimental data. The distributions of scattering angles in the experiments are much broader and have higher median values than those observed in the simulations.

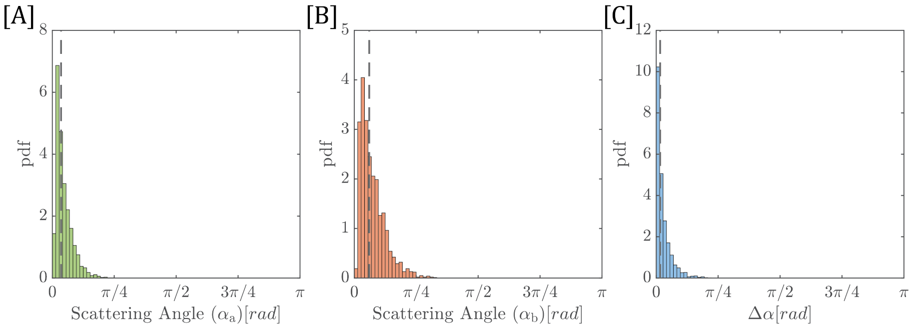

Figure 3.12: Distribution of scattering angles of [A] cell a and [B] cell b for numerical simulations of cell pairs within a 30 μm distance. [C] The difference in scattering angles between cell a and b in the simulation. The dashed lines represent the median of each distribution.

This broader distribution and higher median values in experiments are likely due to the stochasticity of the biological system inherent in real cellular interactions. To further investigate the underlying phenomenon contributing to these differences, we consider the scattering behavior of isolated cells from our experiments. Isolated cells provide a baseline to characterize the inherent stochasticity in the dynamics of *C. reinhardtii* in the absence of interaction with other cells. We define *isolated cells* as the cells for which the minimum approach distance to the nearest neighboring cell is no less than $d_{\text{min}} \geq 200\mu$m. At such distances, the effect of hydrodynamic forces is almost zero, and cells swim in isolation. This is supported by previous studies showing that at distances greater than 100 μm, both steady and unsteady velocity components fall below 1 μm/s, establishing a reference state for non-interacting cells [138, 147].

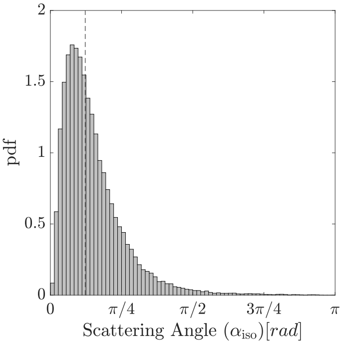

Figure 3.13: Distribution of scattering angles of isolated cells that swim at minimum distances greater than 200 μm from any other cell. The dashed line represents the median of the distribution.

Fig. 3.13 presents the distribution of scattering angles for isolated *C. reinhardtii* cells. These cells exhibit an average scattering angle of $\pi/8$ (approximately 22°). This measurement provides a baseline, indicating that the swimming direction of *C. reinhardtii* cells, deviates on average by 22° due to inherent biological noise. For the cells with $d_{\text{min}} \leq 30\mu$m (as shown in Fig. 3.11), particularly for cell "b", we observe a higher scattering angle, more than the baseline of isolated cells by about 14°. This increased deviation can be attributed to interactions between cells at close distances, which can involve both steric and hydrodynamic interactions.

Previous analytical studies have reported the existence of bound states for a pair of interacting microswimmers, leading to a permanent state of parallel or orbiting swimming [121, 122]. In our large set of experimental data, we did not record any instance of interaction where microswimmers become hydrodynamically entangled and remain trapped in each other's neighborhood. Our experimental data consists only of scattering events, where cells continue on their trajectories without forming any permanent bonds. The absence of such states can be attributed to two main factors. Firstly, permanent bound states necessitate cells to swim in the same direction at similar velocities. Given the variations in velocity, orientation, and beating frequency of cells in our experiment, the likelihood of this naturally occurring is low. Secondly, the stochastic motility inherent in our experimental data may result in changes in direction that disrupt potential bound states. This instability suggests that permanent bound states might not withstand such disruptions. The discrepancy between our observations and theoretical predictions underscores the need for theoretical models to incorporate the complex dynamics and behaviors microorganisms exhibit in natural environments.

3.3.3. SCATTERING ANGLES: INFLUENCE OF MINIMUM DISTANCE AND INCOMING ANGLE

We proceed by examining the influence of the incoming angle ϑ and the minimum cell-cell approach distance d_{min} on the scattering dynamics. We first consider the influence of ϑ and divide our dataset of pair interactions into three categories depending on whether the cells are initially swimming in: parallel directions with $\vartheta = 0 - \pi/3$, perpendicular directions with $\vartheta = \pi/3 - 2\pi/3$ and anti-parallel directions with $\vartheta = 2\pi/3 - \pi$. In the previous section, we have discussed how pair interactions are often asymmetric, with one cell scattering at a much larger angle than the other. We, therefore, characterize an interaction event by reporting the larger scattering angle of the pair, α_b. Fig. 3.14A&C presents our experimental measurements of scattering angles α_b for all three approach angle categories for both our experiments and simulations. In Fig. 3.14A&C, we represent the cumulative distribution function (CDF) of α_b instead of the distribution functions to allow a clearer and more straightforward comparison of the distributions for the three ϑ-categories on a single plot. The value of the cumulative distribution function CDF(α_b) represents the fraction of all interaction events for which the cell is scattered at an angle smaller or equal to α_b.

For the experiments, we observe no significant difference between the CDFs of α_b for perpendicular and anti-parallel approaches. We find a distinct, albeit small, difference between the CDF of α_b for parallel incoming angles compared to perpendicular and anti-parallel approach angles, where CDF(α_b) is lower for parallel compared to anti-parallel approaches. Surprisingly, this means that the cells scatter more for a parallel approach compared to a head-on anti-parallel approach. For example, CDF($\alpha_b = \pi/4$)=0.63 for a parallel approach, while it is 0.73 for the other two categories. This indicates that a higher proportion of cells scatters at more than $\pi/4$ for parallel approaches (37%) compared to anti-parallel and perpendicular approaches (27%). In our numerical simulations, we find a qualitatively similar behavior, where more cells scatter at higher angles during parallel approach compared to perpendicular and anti-parallel approaches, see Fig. 3.14C.

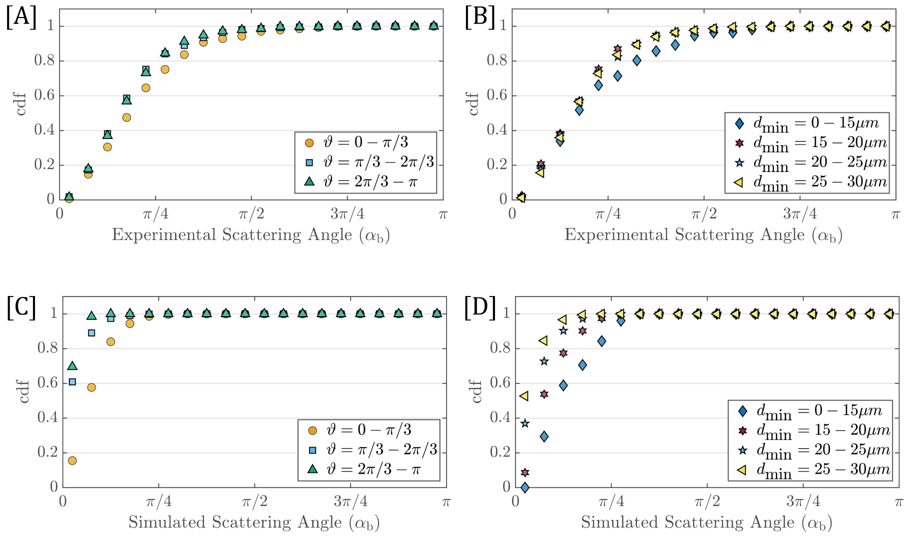

Figure 3.14: Cumulative density functions (CDFs) of scattering angles for cell "b" across different incoming angles categories for [A] Experiments, [C] Simulations, and minimum distances categories for [B] Experiments and [D] Simulations.

As mentioned before, our experimental dataset describes pair interactions involving two different biological cells with different velocities, leading to intrinsically asymmetric scattering. The parallel approaches at small ϑ involve two cells with different initial velocities, which are almost parallel. For these pairs, the faster cell slowly approaches the slower cell. These interactions are, therefore, characterized by lower relative velocities between the cells and interactions that last longer. The faster cell approaches the slower cell from behind, and the long interaction times imply that the orientation of both cells is more significantly affected by the flow field of the other. We then turn to our numerical model to understand why cells scatter at higher angles for parallel approaches. The velocity and vorticity fields of the three-bead swimmer model are represented in Fig. 3.15. For this model, the magnitude of the flow velocity behind the cells, $Z \leq 0$ in Fig. 3.15 A., is higher and extends over longer distances compared to the flow field in front of the cells. The flow fields are associated with a distribution of vorticity, represented in Fig. 3.15B, which induces a rotation of a neighboring swimming cell. The vorticity fields generated in the vicinity of the cell body associated with the longer interaction times of parallel approaches contribute to the significance of hydrodynamic interactions and lead to the increase in scattering angle for $\vartheta = 0 - \pi/3$, which is observed in our numerical simulations.

We now turn to the influence of the cell-cell distance on the interaction dynamics.

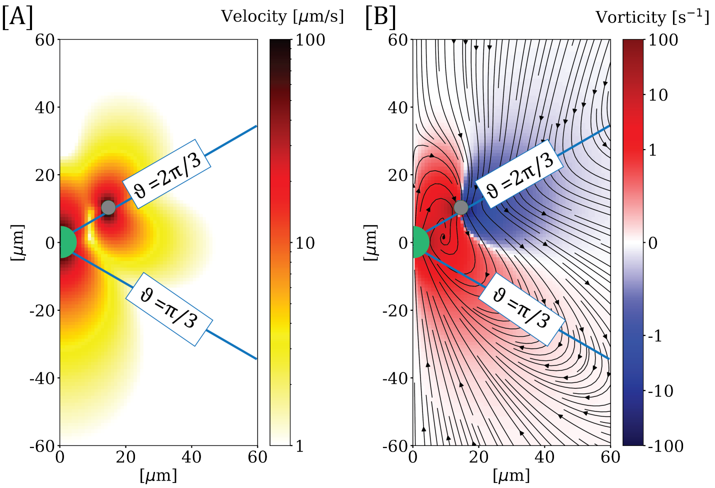

Figure 3.15: [A] Velocity field and [B] Vorticity field and flow streamlines induced by a three-bead swimmer model, presented in the plane containing the three beads. The green circle represents the location of the body bead, while the gray circle represents the flagellar bead. Solid blue lines define regions based on approach angles relative to the swimmer: parallel ($\vartheta = 0$ to $\pi/3$), perpendicular ($\vartheta = \pi/3$ to $2\pi/3$), and anti-parallel ($\vartheta = 2\pi/3$ to π).

We investigate the influence of the minimum cell-cell approach distance d_{min} and consider interactions for which cells come within a distance of $d_{\text{min}} = 0-15\mu$m, $15-20\mu$m, $20-25\mu$m and $25-30\mu$m. As previously, we report the CDF of α_b for each of these distances for both experiments and simulations as shown in Fig. 3.14 B & D. In our experiments, for the closest approaches $d_{\text{min}} = 0-15\mu$m, 33% of the cells scattered at angles greater than $\pi/4$, as CDF($\pi/4$) = 0.77 (Fig. 3.14B). In contrast, for distances greater than 15 μm, only about 18% of cells scattered at similar angles, CDF($\pi/4$) = 0.82, demonstrating small variations across different distance categories as shown by the overlapping CDF values (Fig. 3.14B). Fig. 3.14 D presents the corresponding results from the numerical simulations. For a given α_b, the value of the CDF is lower when the distance of minimal approach d_{min} is smaller. Hence, cells scatter on average at higher angles when they approach each other at smaller distances. This result is expected considering that the simulations only account for hydrodynamic interactions, which are stronger at smaller distances from the cell body, as can be seen in Fig. 3.15.

Both experimental and simulation data indicate that the scattering behavior of the cells is affected within the close range of $d_{\text{min}} \leq 15\mu$m. The gradual decrease in scattering angle at distances greater than 15 μm, characterized in simulations, is not present in the experimental data. Many biological factors and variations in the cell behavior are not accounted for in our simulations, such as stochastic motility or variations in flagellar position and phase. These behaviors contribute to the biological noise and to the stochasticity in our data, leading to random cell orientations. For interactions at larger cell-cell distances, these effects could be dominant and have a larger contribution to the cell scattering compared to the hydrodynamic forces, which decrease with cell-cell distance.

3.4. EFFECT OF CELL-CELL INTERACTION ON TRAJECTORY CURVATURE

In the previous sections, our analysis focused on the scattering of cells coming within a minimum distance of 30 μm. While the scattering angle provides a measure of deflection for the overall trajectory, it does not capture the instantaneous changes in cell orientation. To quantify these changes, we extend our investigation to examine the local changes in direction and consider the curvature κ along the trajectory. κ is computed using the Frenet-Serret frame of reference as:

$$\kappa(t) = \frac{\left|\mathbf{X}^{'}(t) \times \mathbf{X}^{''}(t)\right|}{\left|\mathbf{X}^{'}(t)\right|^{3}}. \tag{3.4}$$

Here, $\mathbf{X}^{'}(t)$ and $\mathbf{X}^{''}(t)$ represent the first and second-time derivatives of the parameterized continuous curve, respectively, see section 2.4.2 for more details. This analysis is not limited to pairs coming within 30 μm but includes all pair interactions from our 3D tracking experiments and simulations within an extended minimum distance ($d_{\min}$) of up to 100 μm. Specifically, we aim to quantify the changes in the local curvature of the trajectory, independent of how close the cells eventually approach each other. Our previous discussion on scattering angles highlighted the strong influence of biological noise in our experimental data, and we expect an equally strong influence on the measurements of local curvature. Therefore, we first analyze the results from our numerical simulations, which do not include the effects of biological noise.

3.4.1. NUMERICAL SIMULATIONS: EFFECT ON TRAJECTORY CURVATURE

We first present the results of numerical simulations for three specific pairs of swimmers corresponding to different approach angles ϑ, see Fig. 3.7A. The larger spheres represent the body of the swimmers, while the smaller ones represent the flagella. Swimmers “a” and “b” have a velocity of 100 and 112 μm/s, respectively. These pairwise interactions are characterized by: $\vartheta = \pi/10$ and $d_{\min} = 18\mu$m for pair I, $\vartheta = \pi/3$ and $d_{\min} = 14\mu$m for Pair II, and $\vartheta = 5\pi/6$ and $d_{\min} = 18\mu$m for Pair III. For Pairs I and II, which have comparatively lower incoming angles, we observe larger directional changes in the swimming direction. The cell direction begins to change and deviate from the original direction before the swimmers reach the minimum approach distance. This is especially clear when considering Pair I. In these simulations, the deviations are due to hydrodynamic interactions between the swimmers.

Fig. 3.7B and C present the relative distance between the swimmers and the curvature of each trajectory as a function of time through the interaction. For Pair I, the curvature κ of the trajectory for both cells is initially zero, indicating that cells are too far from each other for hydrodynamic interactions to affect the trajectory significantly. As the cells come within 50 μm of each other, κ begins to increase, see Fig. 3.7B and C. A similar increase in curvature is observed for Pair II as the cells approach each other, highlighting the effects of hydrodynamic interactions. In the case of Pair III, while κ also increases as the cells move closer, the values are lower than those for Pairs I and II. These smaller curvature values lead to smaller changes in the overall swimming direction for Pair III compared to Pairs I and II, as shown in Figure 3.7A. This demonstrates that κ provides a local measure of the magnitude of cell-cell interactions and significantly depends on the incoming angle ϑ. These results confirm our previous discussion that ϑ influences the duration over which the cells interact with each other's flow fields. For example, in Pair I, where cells approach each other in a parallel configuration, the relative velocity remains low, resulting in longer interaction times and significant changes in cell trajectories. Conversely, Pair III, with cells swimming in nearly anti-parallel directions, experiences shorter interaction periods, leading to less pronounced scattering effects and minimal changes in curvature.

We expand this discussion to include an analysis of all 7500 pairs from our simulations, including the full range of ϑ and d. Fig. 3.17 presents the distribution of curvature along the trajectory for the same three categories of trajectories introduced in section 3.3.3: [A] $\vartheta = 0 - \pi/3$ (parallel approach), [B] $\vartheta = \pi/3 - 2\pi/3$ (perpendicular approach), and [C] $\vartheta = 2\pi/3 - \pi$ (anti-parallel approach). The x-axis represents the distance d between cells and ranges from $d = 10 - 100\mu$m. For each value of d, the colormap represents the distribution of curvature κ_d. The insets in Fig. 3.17 reproduce the histogram of the distribution of curvatures within the smallest 10 to 20 μm distance bin. The curvature distributions κ_d are centered around lower values as the distance between the cells d increases. When cells are separated by more than $d \geq 80\mu$m, the curvature values approach zero, indicating that hydrodynamic forces have no effect on cell trajectories at such distances. This decrease in curvature is observed regardless of the incoming angle (ϑ), see categories Fig. 3.17A, B, C.

For small values of d, we find notable differences in the distribution of curvatures for different approach angles. From the insets in Fig. 3.17A, we can directly observe that the peak value of the curvature distributions is higher for parallel approaches ($\vartheta = 0 - \pi/3$ in Fig. 3.17A) compared to the distributions for perpendicular and anti-parallel approaches (Fig. 3.17B & C). These higher curvatures are found for cell-cell distance as high as $d = 40\mu$m. This observation is related to the results from section 3.3.3, where we reported larger scattering angles for parallel approaches.

To quantify the difference between the distributions of curvature, we compute the 1-Wasserstein distance [148]. This metric represents 'the work' required to transform one distribution into another and is suitable for our analysis involving 1-dimensional distributions of κ_d. We use the 1-Wasserstein distance to compare the curvature distribution κ_d at a given distance d to a reference distribution, which we choose to be the curvature distribution κ_∞ when the cell-cell distance is large and hydrodynamic interactions are small. The 1-Wasserstein distance is calculated as follows:

$$W(\kappa_d, \kappa_\infty) = \int_{\mathbb{R}} |\mathsf{F}_d(x) - \mathsf{F}_\infty(x)|\, dx \tag{3.5}$$

Here, F_d and F_∞ are the cumulative distribution functions(CDFs) of the distributions κ_d and κ_∞, respectively. This formulation computes the integral of the absolute differences of CDFs between these two distributions. κ_∞ is taken as the curvature distribution for $d = 90 - 100\mu$m. The value of W between different κ_d and κ_∞ measures

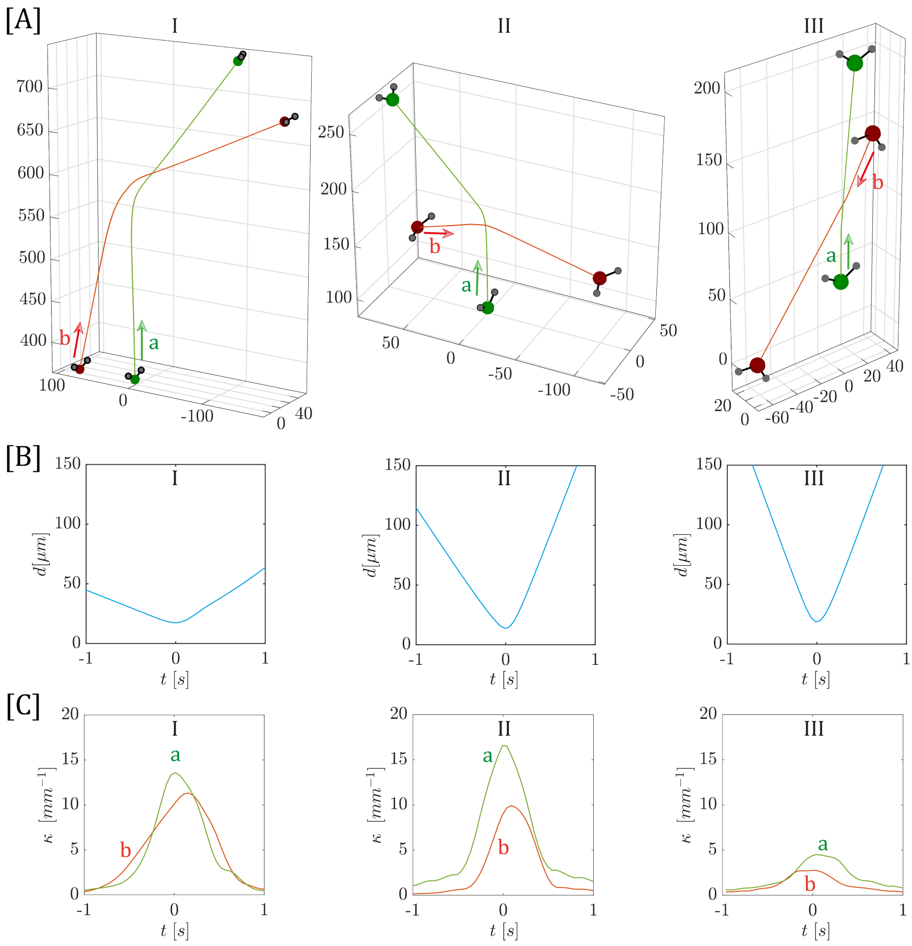

Figure 3.16: [A]Example three-dimensional trajectories from the three-bead model simulation for pair interactions: I) $\vartheta = \pi/10$, $d_{\text{min}} = 18\mu m$, II) $\vartheta = \pi/3$, $d_{\text{min}} = 14\mu m$, III) $\vartheta = 5\pi/6$, $d_{\text{min}} = 18\mu m$. The larger sphere represents the body bead, while the smaller spheres represent the flagellar beads. The velocities of swimmer “a” and swimmer “b” are 100 and 112 μm/s, respectively. [B] Relative distance of swimmers for each pair as a function of time, relative to the moment of closest approach, t_0=0. [C] Variations in trajectory curvature as a function of time, relative to the moment of closest approach t_0=0, for respective pairs.

the influence of hydrodynamic interactions within different distance ranges. These calculations are performed separately for each category of ϑ. W is expressed in units of κ (mm^{-1}), offering an interpretation as the average change in κ due to hydrodynamic interactions. For example, W of 2 mm^{-1} implies that, on average, the trajectory κ changes by this value due to hydrodynamic interactions compared to scenarios where cells are not interacting.

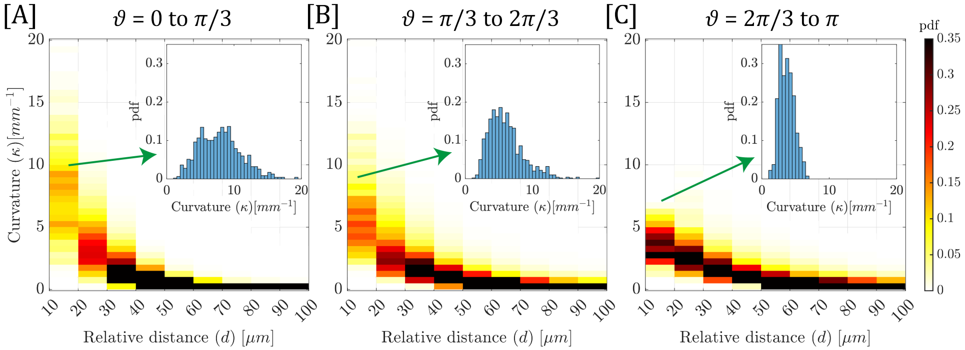

Figure 3.17: Conditional probability density functions of curvature (κ) for different relative distance (d) and incoming angle (ϑ) for pair-wise numerical simulations. Each panel corresponds to an incoming angle range: [A] 0 to $\pi/3$ (parallel), [B] $\pi/3$ to $2\pi/3$ (perpendicular), and [C] $2\pi/3$ to π (anti-parallel). Distance between swimmers (10 to 100 μm) is represented on the x-axis and binned into segments, while curvature values are depicted on the y-axis. The color-map signifies the likelihood (pdf) of a given curvature for the corresponding swimmer distance. Insets in each panel provide the the curvature distribution for a distance of 10 to 20 μm.

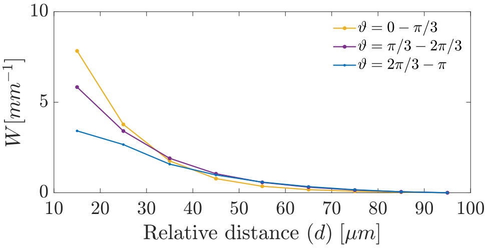

Figure 3.18: 1-Wasserstein distance between the curvature distributions κ_d at different relative distance and reference distribution of $\kappa(\infty)$ at distance of 90-100 μm for simulated trajectories. Solid lines represent different categories of incoming angles (ϑ).

Fig. 3.18 represents the value of $W(\kappa_d, \kappa_\infty)$ as a function of the cell-cell distances d for all three categories of ϑ. The ϑ categories are represented by three distinct solid lines. W is nearly zero at distances greater than 80 μm, indicating negligible variation in the distribution of κ beyond this range. $W(\kappa_d, \kappa_\infty)$ reaches its highest values at smaller distances for all ϑ categories. Specifically, at distances less than 30 μm, W remains high for parallel incoming angles of $\vartheta = 0$ to $\pi/3$, with a maximum value of 8.3 mm^{-1} for $d = 10-20\mu$m, indicative of a substantial average change in κ. For ϑ angles ranging from $\pi/3$ to $2\pi/3$, the maximum W is lower with $W = 6.4$mm^{-1} for the same range of d. For anti-parallel approaches with $\vartheta = 2\pi/3$ to π, the maximum W at a distance of 10–20 μm is the lowest, at 3.4 mm^{-1}, showing the least average change in trajectory κ.

The differences in W for different approach angles ϑ at shorter distances show the influence of ϑ on the change in swimming direction due to hydrodynamic interactions. The analysis using Wasserstein distance confirms our observations from Fig. 3.17 that both ϑ and d significantly influence hydrodynamic interactions. This also provides a quantitative basis for evaluating the impact of hydrodynamic forces on κ across different distances and incoming angles, which can be compared against experimental observations.

3.4.2. 3D TRACKING EXPERIMENTS: EFFECT ON TRAJECTORY CURVATURE

We now turn to our experimental data and use the same approach to investigate pairwise interactions, including the trajectories and the curvatures of 35,135 recorded cell pairs. Fig. 3.19 show the dependency of κ on ϑ on d using the same representation as the one used in Fig. 3.17 for the related simulation results. ϑ is categorized into three specific categories: [A] $\vartheta = 0 - \pi/3$ (parallel approach), [B] $\vartheta = \pi/3 - 2\pi/3$ (perpendicular approach), and [C] $\vartheta = 2\pi/3 - \pi$ (anti-parallel approach). Additionally, we present κ_d for three distance bins of 10-20, 50-60, and 90-100 μm in Fig. 3.19D, E and F for all three ϑ categories.

We observe distinct differences from the numerical simulations in our experimental results. The distribution of κ_d at large distances (d>70μm) is similar across all categories of ϑ. These distributions maintain an average curvature of approximately 5 mm^{-1}, showing no significant variation with either ϑ or d. This non-zero mean curvature at larger distances suggests a consistent deflection in the trajectories, which can be attributed to the biological noise inherent to cell trajectories from our experimental data. This agrees with the scattering results discussed earlier, which highlighted the influence of biological noise in changing the swimming direction in the absence of any interactions. At shorter distances (d<30μm), small differences in the distributions κ_d can be observed. For the parallel approach ($\vartheta = 0$ to $\pi/3$), the experimental data indicate a slightly higher median curvature compared to other ϑ categories.

Following the approach discussed to analyze the numerical simulations, we quantify the differences in the distributions κ_d for all the ϑ categories by using the Wasserstein distances (W). We use the 1-Wasserstein distance to compare each κ_d to the reference distribution κ_∞ at the 90-100 μm distance. These results are presented in Fig. 3.20. The W values increase slightly for swimmers at very close distances for all ϑ categories. This observation is consistent with our observation of κ_d discussed previously and similar to the observations in our numerical simulations (see Fig. 3.18), suggesting

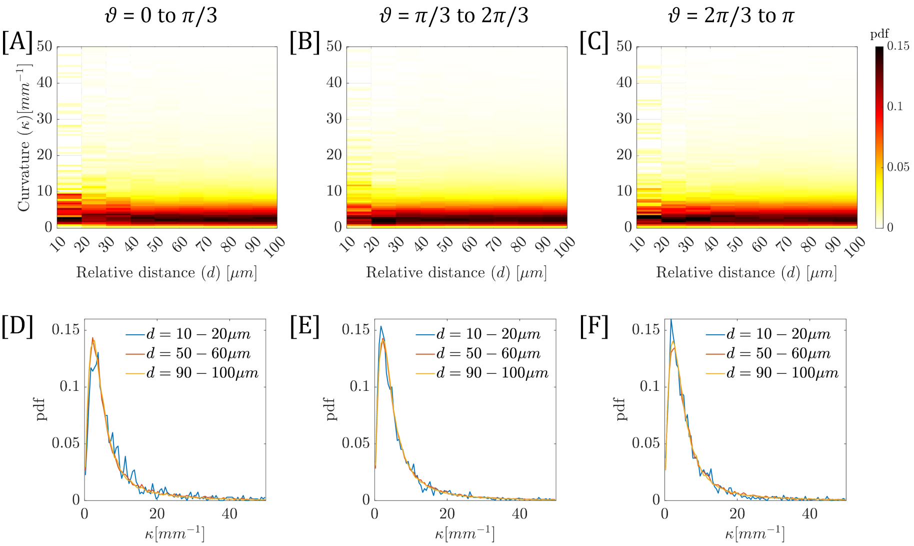

Figure 3.19: Conditional probability density functions and probability density functions (pdfs) illustrating the relationship between relative distance (d), curvature (κ), and incoming angle (ϑ) based on experimental data. Panels [A], [B], and [C] are conditional probability density functions corresponding to incoming angle ranges: 0 to $\pi/3$ (parallel), $\pi/3$ to $2\pi/3$ (perpendicular), and $2\pi/3$ to π (anti-parallel), respectively. Distance between swimmers (10 to 100 μm) is represented on the x-axis and binned into segments, while curvature values are depicted on the y-axis. The colormap signifies the likelihood (pdf) of a given curvature for the corresponding swimmer distance. Panels [D], [E], and [F] show the pdfs of curvature values for three specific distance ranges (10-20, 50-60, 90-100 μm) within each incoming angle range, offering an alternative visualization of the curvature distribution at these distances.

an influence of hydrodynamic interactions on trajectory κ at these shorter distances. For the parallel approach ($\vartheta = 0$ to $\pi/3$), W is higher compared to the other ϑ categories, with this slight difference between the distribution κ_d and κ_∞ becoming apparent for $d \leq 30\mu$m. This is qualitatively similar to the results from our numerical simulations, highlighting the influence of ϑ on cell scattering. The values of the 1-Wasserstein distance W remain below 1 mm^{-1}, indicating that the differences in the distributions are noticeable but modest. Considering Fig. 3.19, the dominant feature of the curvature distribution is the broad peak with an average κ of 5 mm^{-1}, corresponding to the presence of curvature in the trajectories due to biological noise. The presence of curvature due to stochastic effects masks, within the distributions, the potential effect of hydrodynamic interactions. Only when the cell-cell distance is small and the hydrodynamic interactions are stronger can we characterize a small difference in the distribution of curvature.

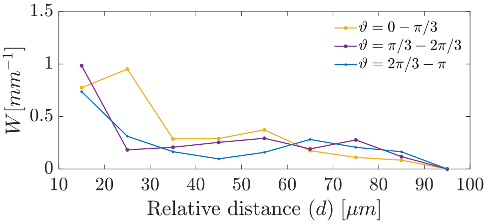

Figure 3.20: 1-Wasserstein distance between the curvature distributions κ_d at different relative distance and reference distribution of $\kappa_{(\infty)}$ at distance of 90-100 μm for experimental data. Solid lines represent different categories of incoming angles (ϑ).

3.5. Acceleration Effects: Investigating the Nature of Collisions

In the previous sections, we have characterized cell-cell interactions by considering changes in the orientation of the swimmers. We now consider the influence of cell-cell interactions on another quantity, characteristic of the cell dynamics, namely the cell velocity $V(t)$. We focus on cells coming in close proximity to each other, such that $d_{\min} \leq 30$ μm. Our previous work on cell-surface interactions [98] has highlighted the usefulness of considering the velocity fluctuations $\dot{V}(t)$ to identify the nature of the cell-surface interaction. For scattering events involving direct steric interactions, we found a distinct signature in the variations of $\dot{V}(t)$ consisting of deceleration followed by a re-acceleration. This distinct signature was absent from the scattering event, which only involved hydrodynamic interactions [98]. We, therefore, turn to the fluctuations in $\dot{V}(t)$ for cell-cell interaction to gain insight into the nature of the scattering events. Therefore, we compute the tangential acceleration using the continuous parameterization of $\mathbf{X}(t)$, as:

$$\dot{V}(t) = \frac{\mathrm{d}}{\mathrm{d}t}\left(\left|\frac{\mathrm{d}\mathbf{X}(t)}{\mathrm{d}t}\right|\right) \tag{3.6}$$

We follow [98] and non-dimensionalize $\dot{V}(t)$ using as characteristic length scale the cell diameter (D) and as characteristic velocity scale, the average cell velocity $(\overline{V})$.

Figure 3.21 A shows the fluctuations in the linear acceleration for three selected cell-cell interactions, which we have already considered earlier as Pairs II, V, and VI in Fig.3.8. For Pair II, a significant decrease in tangential acceleration in one cell (cell “b”) indicates that the cell stopped momentarily before scattering at an angle of $\pi/3$. Similarly, for Pair VI, both cells exhibit an initial decrease followed by an increase in acceleration near their point of closest approach. These dynamics are reminiscent of our findings from the study of cell-surface interactions, where changes in tangential acceleration indicated contact interactions with the wall.

We proceed by considering all pairs, for which the minimum cell-cell distance during the interaction is $d_{\min} \leq 30\mu$m, and represent the fluctuations of the tangential acceleration during the interactions. Fig. 3.21 C presents the distribution of $\dot{V}(t)$ for all cell pairs as a function of the time t, where t extends from $t = -1s$ to $t = 1s$, and $t = 0$ is defined as the time when two cells are closest to each other at $d_{\min}$. We

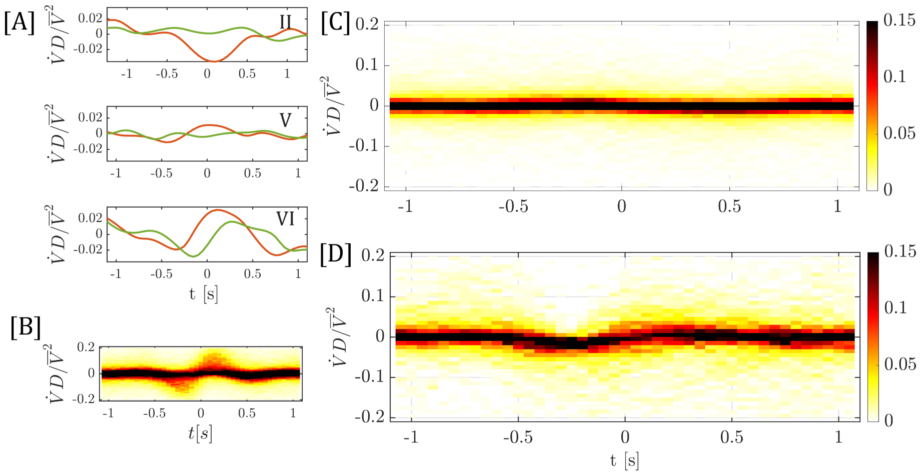

Figure 3.21: Analysis of tangential acceleration ($\dot{V}$) for cell-cell interactions for pairs with minimum distance (d_{min}) of 0-30 μm. [A] Sub-panels illustrate tangential acceleration of three specific cell pairs (Pairs II, V, and VI from Fig. 3.8), depicting temporal variations in $\dot{V}$. Green and red solid lines represent the trajectories of cell *a* and cell *b* from Fig. 3.8. [B] Evolution of the distribution of $\dot{V}(t)$ of tangential acceleration during cell-surface interactions, highlighting contact interactions as acceleration decreases and increases closer to the wall. We refer to our previous work Buchner *et al.* [98] for more details on this phenomenon. [C] Evolution of the distribution of $\dot{V}(t)$ for all cell pairs with trajectories lasting with length of 2 seconds or longer and minimum distances within 30 μm. [D] $\dot{V}(t)$ of selected trajectories with normalized tangential accelerations below -0.01 at $t = 0.25s$.

find that $\dot{V}(t)$ presents no significant fluctuations before or after the closest approach, maintaining a mean of 0 with a 0.01 standard deviation at all time steps. This is significantly different than the distribution of $\dot{V}(t)$ we have previously measured for cell-surface interaction [98], and represented for reference in Fig. 3.21 B. Fig. 3.21 B clearly indicates a deceleration before the cells reach their minimal distance to the surface and a subsequent acceleration after, for t>0. The absence of velocity fluctuations for cell-cell interactions in figure 3.21 C indicates that the cell velocity remains constant for most interacting pairs and that most cell-cell interactions do not involve abrupt kinematics, which can be expected when cells directly collide with each other. It bears emphasis, however, that for cell-surface interactions, the point of nearest approach to the wall provides a clear reference point to use to aggregate the data and compute the density distribution. For cell-cell interactions on the other hand, we use the time of closest cell-cell approach as the reference point. Because acceleration changes occur at different times for each pair relative to the time of closest approach, subtle variations in the acceleration do not change the overall aggregated data. We investigate the occurrence of pair interactions involving an abrupt deceleration characteristic of a collision. To isolate these, we consider trajectories where the normalized tangential acceleration falls below -0.01 at $t = -0.25s$. This threshold is based on our cell-surface interaction study [98]. We find only 20% of our trajectories meet this criterion. When we consider the distribution of $\dot{V}(t)$ only for these trajectories (Fig. 3.21 D), we still do not observe a significant kinematic akin to that seen in cell-surface interactions. Typically, in cell-surface interactions, cells decelerate as they approach the wall at t = 0s and then accelerate back to their normal velocity. However, for the selected trajectories, both deceleration and acceleration occur more rapidly and before the cells reach their minimum distance to each other, compared to cell-surface interactions.

We have found pair interactions in our data set, where abrupt fluctuations of the velocity clearly show that the cells came into direct contact during hard collisions; see, for example, pair II in fig.3.8. We find, however, that the majority of cell-cell pair interactions coming within a close range do not result in significant changes in the velocity. This suggests that, in most cases, cell-cell interactions at short distances remain soft in nature and are due to hydrodynamic interactions and soft interactions between the cell body of one microalgae and the flagella of the other.

3.6. Discussion

This study investigated the pairwise interactions of (C. reinhardtii) cells by capturing their three-dimensional motion using a unique multi-camera microscopy system. Using an in-house tracking algorithm based on the projective geometry, we tracked cells in 3D physical space, acquiring 5.52×10^5 trajectories for detailed analysis of pairwise interactions. A pair interaction was defined as two cells swimming towards each other, coming within 100 μm, and then moving apart. We characterized these pair interactions based on the closest approach distance (d_{min}) and the incoming angle (ϑ), identifying 35,135 algae pairs with d_{min} ranging from 10 μm to 100 μm. Most pairs exhibited an incoming angle of $\vartheta = \pi/2$, indicating an isotropic system with no preferred swimming direction. A Curve-fitting of the recorded trajectories yielded a continuous representation of the trajectories as parameterized curves, enabling extraction of interaction metrics, such as scattering angle (α), curvature (κ), and tangential acceleration ($\dot{V}$). We also performed numerical simulations using the spring-bead model [143] to get insights into the importance of hydrodynamic interactions in our experimental results.

First, we investigated the scattering behavior of (C. reinhardtii). Our primary focus was on cell pairs approaching each other within a d_{min} of 30 μm. We analyzed 3D trajectories and scattering behavior for nine pairs with different ϑ, as shown in Fig. 3.8. The analysis revealed a range of scattering patterns, from minor to significant trajectory deflections for one or both cells in each pair. Extending this to all 1065 pair interactions within d_{min} of 30 μm, we examined the distribution of α for each cell in a pair (Fig. 3.11). The scattering behavior varied significantly across cells in each pair. Typically, one cell in each pair deviated minimally, with a median α of $\pi/11$ (17°), while the other exhibited a broader range of scattering angles up to $\pi/2$ (90°), with a median of $\pi/5$ (36°). The difference in scattering angles between the cells varied from 0 to $\pi/4$ (Fig. 3.11C), indicating an asymmetry in scattering behavior, which contrasts with previous studies reporting symmetrical scattering for both cells [121, 122].

Our numerical simulations, in comparison to the experimental results, demonstrated a lower α for both cells (Fig. 3.12). This difference between experimental observations and simulation results suggests that hydrodynamic forces alone may not account for the scattering behaviors observed in the experiments. To identify the factors driving the scattering behavior of cells in our experiments, we compared the behavior of cells in close proximity (d_{min} <30 μm) to those swimming in isolation (Fig. 3.13). These isolated cells, swimming independently at distances greater than 200 μm from any other cell, exhibited an average α of $\pi/8$ (approximately 22°). The behavior of these isolated cells provided a baseline, indicating that the inherent motility of the cells, dependent on variations in cell velocity, flagellar beating frequency, and flagellar asynchrony, plays an important role in determining overall scattering behaviors.

Moreover, the observed scattering behavior of (C. reinhardtii) in our experiments involved only scattering states where cells approach each other, scatter, and continue on their trajectories without forming a permanent bond. This observation differs from earlier analytical predictions of permanent bound states [121, 122], suggesting that stochastic motility, whereby cells randomly change their orientation, may disrupt the stability of such states. The absence of predicted pairwise or orbiting swimming states in our experimental data underscores the need for theoretical models to consider more complex and dynamic behaviors exhibited by microorganisms in natural environments, including testing the stability of bound states to perturbations.

Furthermore, we observed that ϑ, categorized as parallel, perpendicular, and anti-parallel, had a minimal impact on the scattering dynamics (Fig. 3.14), except when cells interacted at a parallel incoming angle. The results from both experiments and simulations show that cells approaching from behind one another (parallel) undergo higher trajectory deflections compared to other approaches. Moreover, our experiments show that cells scatter with relatively high α at very close distances (0-15 μm), and beyond 15 μm, distance has no effect on scattering angles. In contrast, numerical simulations predict a steady decrease in α with increasing distance, reflecting the primary influence of hydrodynamic forces, which diminish over distance.

We also considered the effect of cell-cell interaction on instantaneous changes in cell trajectory. The analysis of trajectory curvature (κ), a metric for understanding instantaneous changes in cell orientation, was conducted using both 3D tracking experiments and numerical simulations. Our numerical simulations (Fig. 3.16 clearly demonstrate the influence of hydrodynamic interactions on κ. These interactions were most pronounced at closer distances, particularly under parallel incoming angles ($\vartheta = 0$ to $\pi/3$), with trajectory curvature showing notable changes when swimmers were within 10 to 40 μm of each other. The impact of these hydrodynamic forces diminished with increasing distance, becoming negligible beyond approximately 80 μm. This observation was quantitatively substantiated by the 1-Wasserstein distances (Fig. 3.18), which showed the average change in curvature due to hydrodynamic interactions, emphasizing the dependence of κ on both ϑ and relative distance (d) between swimmers. The results from our 3D tracking experiments presented a different picture (Fig. 3.19). Here, no clear trends emerged to indicate a significant effect of either ϑ or the d on κ except at very small d of 10-20 μm and when cells were approaching each other with parallel ϑ, where higher κ was recorded, compared to other approaches. The experimental data showed an average curvature value of approximately 5 mm^{-1} across all d for all ϑ, indicating a characteristic deflection in the trajectories of (C. reinhardtii) cells.

The dynamics of tangential acceleration during cell-cell interactions is another important finding of our study. A subset of cell pairs demonstrates a decrease in acceleration as they approach minimum distances, indicative of hard collisions, with velocity recovered post-collision. Conversely, for most of the cell pairs, acceleration does not change throughout the interaction demonstrating soft collisions.

Taken together, our findings suggest that while hydrodynamic interactions contribute to changes in cell trajectories, they are not the sole determinants. The asymmetric scattering patterns and higher scattering angles observed in our study are largely attributable to the inherent motility characteristics of these microorganisms. The stochastic nature of their movement, characterized by random changes in orientation and speed, emerges as a fundamental factor influencing cell interactions, overshadowing the effects of cellular interactions. Moreover, our study highlights the complexity of microorganism behavior and the challenges associated with predicting interactions based solely on theoretical models. The differences between simulation and experimental results underscore the importance of empirical data in understanding the dynamics of cell-cell interactions. In light of these insights, future research on microorganism interactions should incorporate the stochastic elements of cell motility into theoretical and computational models.

4

KINEMATICS & SURFACE INTERACTIONS OF *Chlamydomonas Reinhardtii* IN COMPLEX FLUIDS

Microorganisms propel themselves through a range of complex fluidic media, for example mucus or blood plasma, which exhibit non-Newtonian properties like viscoelasticity and shear-thinning. However, studies investigating microorganism motility in such environments are typically limited to either two-dimensional microscopy or theoretical and numerical analyses. This study investigates the effects of non-Newtonian rheological properties of the suspending fluid on the kinematics and surface interactions of Chlamydomonas reinhardtii cells within these complex fluids in three dimensions. Utilizing a multi-camera microscope, we captured the three-dimensional swimming behaviors of these microorganisms in the same volume of 2.5 × 2.5 × 2 mm^3*. We also performed 2D microscopy to analyze flagellar beating frequency. Our findings show that C. reinhardtii cells exhibit a higher flagellar beating frequency in viscoelastic media compared to Newtonian fluids of similar viscosities, yet swim slower due to an increase in cell velocity during recovery stroke. We also show that viscoelasticity significantly influences microswimmers' 3D locomotion due to changes in swimming speed, radius and pitch of their helical trajectories, and persistence length. Interestingly, the angular velocity along the helical path remained nearly constant across both Newtonian and viscoelastic media of different viscosities, suggesting an adaptive mechanism to maintain a constant environmental scanning rate for phototaxis. Additionally, our results demonstrate that viscoelastic media affect cell-surface interactions. Cells in viscoelastic fluids exhibit an increase in residence time and approach the surface at shallower angles compared to the cells in Newtonian media. Consequently, an increase in near-surface cell accumulation is observed for viscoelastic solutions.*

4.1. INTRODUCTION

Microorganisms often navigate complex environments and biological fluids with complex rheological properties. Bacteria such as *Pseudomonas aeruginosa* and *Escherichia coli* swim through the mucus of respiratory and gastrointestinal tracts, leading to diseases [149, 150]. Bacteria also reside within extracellular polymeric substances, forming biofilms [10, 151]. Similarly, mammalian spermatozoa move through cervical mucus [42, 152, 153], and the unicellular protozoan parasite *Plasmodium falciparum* swims in blood plasma to cause malaria [154]. Biological fluids, such as mucus, blood plasma, and biofilms, are non-Newtonian and exhibit viscoelastic and shear-thinning rheologies [46, 155–157]. By studying the movement and interactions of microorganisms within these non-Newtonian fluids, we can better understand their locomotion in such environments, leading to applications like improving fertilization processes [158], preventing biofouling [11], developing cell manipulation strategies [76], and designing artificial microswimmers [159].

Despite the ubiquity of non-Newtonian fluids in natural microbial environments, most work on the locomotion of microorganisms has focused on swimming in Newtonian fluids, and we refer the reader to recent texts for reviews [3, 160]. Only recently, the effects of non-Newtonian rheology on microorganism motility have drawn significant attention. This work has been predominantly theoretical [40, 41, 161–176] and numerical [177–187] with some early experimental investigations [43–45, 188–192]. Much of this work has investigated how viscoelasticity affects the swimming speed of microorganisms.

Early theoretical studies using Taylor's waving sheet model found that the velocity of a two-dimensional waving sheet decreases in a viscoelastic fluid, compared to a Newtonian fluid with similar viscosity [40, 163, 164]. This theoretical observation was confirmed by experimental studies of the swimming behavior of *Caenorhabditis elegans* in a viscoelastic medium [188]. Numerical simulations using the squirmer model have also shown a decrease in swimming speed for a pusher-type microswimmer in viscoelastic fluids [179]. Recent numerical studies have highlighted the complex interplay of kinematics, swimmer geometry, and elasticity in locomotion. For example, the swimming speed of a 2D waving sheet in a viscoelastic fluid can either increase or decrease based on fluid elasticity and the direction of the traveling wave [177, 183] and the swimming speed of a model pusher-type swimmers, made of two counter-rotating spheres, increases due to elastic properties [186]. Experimental investigations of *E. coli* in polymeric viscoelastic fluids have demonstrated an increase in swimming speed, which depends on the polymer concentration [43, 44]. The polymeric solutions used in this study exhibited both viscoelastic and shear-thinning behavior, and it remained unclear which non-Newtonian rheological property led to the velocity increase of *E. coli.* Three-dimensional tracking experiments of *E. coli* [193] have attributed the speed enhancement to shear-thinning properties, as the flagellum beats at a higher frequency and thus experiences less viscosity than the cell body, thereby leading to increased speed.

Part of this chapter has contributed to "J. Mehmood, A. J. Buchner, and D. Tam, “Kinematics & surface interactions of Chlamydomonas Reinhardtii in complex fluids”, Journal of the Royal Society Interface, 2024, In preparation".

The rheological properties of the surrounding fluid determine the stresses exerted by the fluid on microorganisms and, therefore, have a strong influence on the swimming gait exhibited by living organisms. For instance, the behavior of human sperm cells depends on the viscosity. At lower viscosities, the flagellum of a sperm cell functions as a puller during its beat cycle, but its time-averaged flow field exhibits characteristics similar to a pusher [194]. On the other hand, at higher viscosities, the swimming gait of human sperm changes, making both its instantaneous and time-averaged flow field resemble that of a pusher-type microswimmer [194].

Similarly, the flagellar cycle of *C. Reinhardtii* distinctly changes due to fluid properties [45]. In this work, Qin *et al.* used 2D microscopy to study the effects of viscosity and elasticity on the swimming kinematics of *C. reinhardtii*. Significant changes were observed in both the swimming velocity and the flagellar beating frequency of *C. reinhardtii* due to viscous and elastic effects. The increase in the viscosity of a Newtonian medium reduced the flagellar frequency and, consequently, the swimming speed. The behavior of cells in viscoelastic solutions showed distinct differences from those in Newtonian media of similar viscosity. Specifically, at high polymer concentrations, when viscosity (η) > 2.6, mPas.s, the flagellar beating frequency was higher compared to the one observed in a Newtonian medium of similar viscosity. This higher flagellar frequency in the viscoelastic media did not translate into a higher swimming speed. An analysis of the beating kinematics revealed that the rheology altered the flagellar gait, resulting in higher velocities in the recovery stroke, thereby decreasing the overall swimming speed [45]. This illustrates how the interactions between soft living microorganisms and the surrounding complex fluids lead to non-linear coupling, which strongly influences locomotion.

The interactions between microorganisms and solid substrates represent another important process in which the rheology of the medium has a significant influence. Biological examples of transport at physical boundaries involving complex fluids include the ciliary transport of mucus in the respiratory tract and the swimming of sperm cells in the oviduct. Recent work has been predominantly theoretical [167, 172, 173, 175, 176], and numerical [182, 184, 185] with few experimental observations [192]. These studies have provided insights into the effect of viscoelasticity on cell scattering and residence time near surfaces. Studies using a time-averaged 2D squirmer model for microswimmers combined with the Oldroyd-B fluid model showed an attraction layer near a no-slip boundary. This layer led to the entrapment of both pusher and puller-type swimmers near the surface [172]. For a 3D squirmer model swimming in a viscoelastic fluid defined by the Giesekus constitutive equation, entrapment was observed exclusively for pusher-type swimmers [182]. In both models, cells in viscoelastic media had longer residence times near surfaces than those in Newtonian media. Subsequent investigations using a 2D squirmer model, factoring in time-independent boundary conditions, highlighted the emergence of spiral trajectories for both pusher and puller-type swimmers, which were determined by the initial orientation towards the surface [173]. Additionally, the residence time near the surface depended on the approach angle and distance from the surface, irrespective of the swimmer type. For a more complex 3D squirmer model, the previously observed attraction layer was absent [175]. Consequently, neither pusher nor puller swimmers get permanently trapped near a no-slip boundary.

Finally, viscoelasticity has been suggested to influence the scattering from surfaces, resulting in a slight reduction in scattering angle [182, 184]. Residence time and scattering dynamics are critical in determining cell accumulation near surfaces and are relevant to biofilm formation. A 3D tracking study indicates that in viscoelastic media, *E. coli* accumulates less on surfaces compared to Newtonian solutions [192]. The observed difference is attributed to lift forces near surfaces in a viscoelastic medium caused by rotating flagella. These forces weaken hydrodynamic effects, leading to reduced surface accumulation.

These studies of microbial motility in complex fluids have yielded a complex picture of the effect of rheological properties on locomotion. Most of the previous experimental investigations have used two-dimensional microscopy, but microorganism motility is inherently three-dimensional. A comprehensive understanding of the motility and cell-surface interactions requires detailed three-dimensional studies to capture essential aspects like helical motion, cell reorientation, and tactic behavior, which are all inherently three-dimensional.

Here, we investigate the swimming kinematics and surface interactions of *C. reinhardtii* cells suspended in complex fluids. These cells were imaged using our unique multi-camera microscope in a $2.5 \times 2.5 \times 2\ mm^3$ viewing volume. An in-house tracking algorithm was used to track the algae cell. The resulting three-dimensional trajectories provide an extended data set to investigate the three-dimensional motility and cell-surface interactions. We also perform two-dimensional microscopy at higher magnification to measure the beating frequency and the velocities during the power and recovery strokes, similar to the work of Qin *et al.* [45]. We use different polymeric solutions to characterize the effect of increasing viscosity and viscoelasticity. We find that *C. reinhardtii* cells in viscoelastic fluids swim slower, despite a higher flagellar beating frequency, compared to cells in Newtonian fluids. This is due to the effect of fluid elasticity on their swimming strokes, especially during their recovery stroke. In addition, we find that the 3D swimming trajectories are strongly affected by the viscosity and elasticity of the fluid. Cells swim along tighter helices in more viscous and elastic fluids. Remarkably, despite the strong variations in the helical trajectories, we find that cells maintain a constant angular rotation velocity for all polymeric solutions tested, which allows them to scan their environment at a constant frequency. The rheological properties of the medium also have a strong influence on the persistence of the swimming direction. In more elastic fluids, the swimming trajectories are straighter, and the cells change their direction less frequently. Considering cell-surface interactions, we find that cells have a higher residence time in viscoelastic fluids, approach and depart at shallower angles, and show more spiraling trajectories near the surface than in Newtonian fluids. Finally, we find more cell accumulation near the surfaces in viscoelastic media compared to Newtonian media.

This chapter is divided into four sections. Experimental methods are described in section 4.2. The trajectory kinematics and cell surface interaction results are discussed in sections 4.3 and 4.4. The final section summarizes the main findings and the implications of these results for future research.

4.2. EXPERIMENTAL METHODOLOGY

In this section, we present our approach to study the effects of rheology on the motility of *C. reinhardtii* and scattering interactions with a solid surface. We first describe the different fluid media used in the study and their rheological characterization. We also present further details on the method used to image *C. reinhardtii* cells in polymeric solutions.

4.2.1. PREPARATION OF FLUIDS AND RHEOLOGICAL MEASUREMENTS

In this study, we use two different polymeric solutions: (1) Solutions of varying concentration of Ficoll400, which correspond to Newtonian fluids of varying viscosities, and (2) solutions of Polyacrylamide (PAAm) with a molecular weight (MW) of 1.8×10^7 g/mol, which have viscoelastic properties. We first obtained concentrated solutions of 13% (w/w) Ficoll in Tris minimal and 1000 ppm w/w PAAm in DI water. We then varied the polymer concentration through successive dilutions in Tris minimal buffer of the concentrated solution. Rheological measurements of solutions of both Ficoll400 and PAAm were conducted using the Anton Paar MCR302 rheometer with a 50 mm parallel plate tool. The measurements were performed at a controlled temperature of 25 $^\circ C$, corresponding to the temperature in our tracking experiments.

Our measurements of the effect of polymer concentrations on viscosity are presented in Fig. 4.1 A and B. The viscosity increases with the polymer concentration for both solutions. Ficoll solutions have a constant viscosity regardless of the shear rate (Fig. 4.1 B) corresponding to a Newtonian behavior, as previously reported [45, 193]. The PAAm solutions are slightly shear thinning within the range of shear rates investigated, in particular for concentrations exceeding 520ppm.

Our viscosity measurements for PAAm deviate from previously reported values that indicate a strong shear thinning behavior even at lower PAAm concentrations [45, 195]. This variation is due to the salt content (0.4 wt%) in our Tris-diluted solutions. It is well-established that salt concentrations, ranging from 0.05% [196] to 1% [195], alter PAAm's rheological properties, typically reducing its viscosity. To confirm this salt-induced deviation, we conducted additional viscosity measurements for PAAm in DI water. These findings aligned with earlier studies [45, 195], underscoring the influence of salt in our measurements.

In designing our methodology, we emulated the natural growth environment of the *C. reinhardtii* cells, grown in the Tris medium, while concurrently mitigating the effects of salt on PAAm's rheological behavior. To achieve this, we prepared the PAAm stock solution in DI water, which eliminated the immediate impact of salt. However, subsequent dilutions with the Tris minimal buffer ensured the solutions maintained the properties intrinsic to the Tris buffer. This approach was crucial, given that the physiological responses [197] and motility of *C. reinhardtii* are dependent on their environment. Our observations corroborate this, revealing marked differences in the swimming speeds of *C. reinhardtii* between Tris and Tap solutions, as discussed in Section 2.4.3.

Here, we use a polymeric solution of increasing Ficoll concentration to study the effect of increasing the viscosity of a Newtonian medium and solutions of increasing PAAm concentration to get insight into the effect of low viscoelasticity. To compare

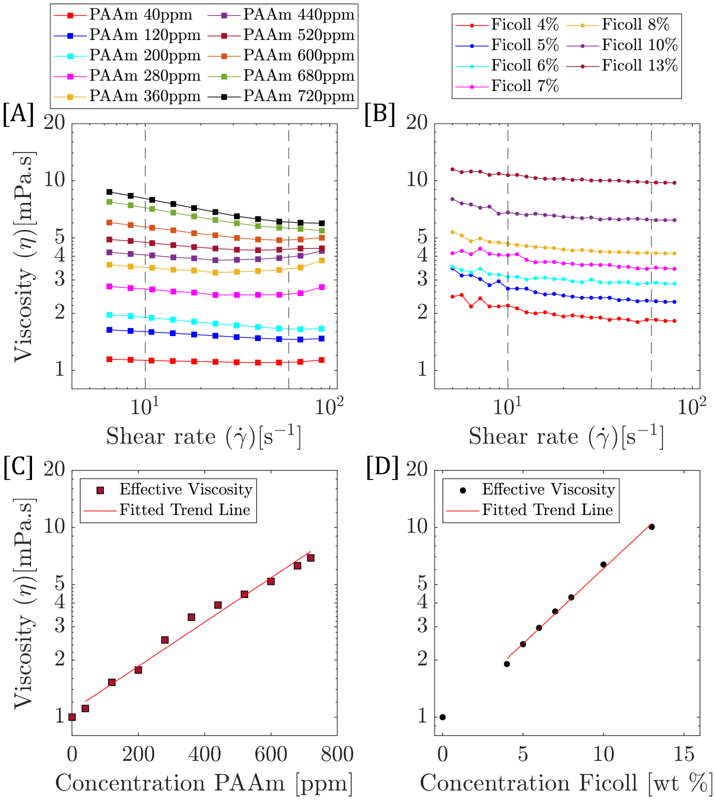

Figure 4.1: Viscosity Characterizations and effective viscosity calculations for PAAm and Ficoll solutions: Shear viscosity of [A] PAAm and [B] Ficoll solutions at various concentrations. The vertical dashed lines at shear rates of 10 and 60 s^{-1} indicate typical shear rates experienced by *C. reinhardtii*. Effective viscosity of [C] PAAm and [D] Ficoll solutions as a function of concentration, calculated by averaging viscosity values between the indicated shear rates.

the results of our experiments for Ficoll and PAAm at different concentrations, we compute an effective viscosity (η) for both solutions. This way, we can compare the swimming properties in Newtonian and viscoelastic fluids with similar viscosity values. The effective viscosity is determined by averaging the viscosity values within the shear rates of 10 to 60 s^{-1}. This range corresponds to the typical shear rates experienced by a *C. reinhardtii* cell, which has a radius of $R = 5\mu$m, swimming at a speed $V = 100\mu$m/s and exhibits a flagellar beat frequency of $f = 60$ Hz. Fig. 4.1 C and D show how the effective viscosity increases with concentration. We use the measurements in Fig. 4.1 C and D to deduce the effective viscosity in each tracking experiment.

Table 4.1 lists all the concentrations and their corresponding effective viscosity values used in this study. The viscosity of Tris minimal buffer alone was measured to be ~1 mPa.s, serving as a baseline Newtonian solution. Henceforth, we will generally identify Ficoll and PAAm solutions by their effective viscosity; table 4.1 and Fig. 4.1 can then be used to trace back the polymer concentration. This approach is consistent with the study of Qin *et al.* [45], which have used the same polymers, Ficoll400 and PAAm. It should be noted that [45] report the viscosities of PAAm dissolved in DI water, which are significantly higher than the viscosities of PAAm in salt solutions [195, 196]. We have chosen to report the viscosities in salt solutions to be consistent with our motility experiments, in which we always add a fixed volume of *C. reinhardtii* in salt-rich growth medium to the concentrated PAAm solution.

PAAm (ppm w/w)	Viscosity (mPa.s)	Ficcol (wt %)	Viscosity (mPa.s)
40	1.20	4	2.03
80	1.34	5.5	2.67
120	1.49	6.6	3.27
160	1.67	7.5	3.85
200	1.86	8.4	4.53
240	2.07	9	5.06
280	2.31	10.4	6.53
320	2.57	11.5	7.98
360	2.87		
400	3.20		
440	3.57		
480	3.97		
520	4.43		
560	4.94		
600	5.51		
640	6.14		
680	6.84		
720	7.63		

Table 4.1: Effective viscosity for various PAAm and Ficoll concentrations used in this study.

In our discussion thus far, we have primarily focused on the measurement of the viscous properties of the polymeric solutions. We now shift our focus to the characterization of the elastic properties of PAAm solutions. The measurement of elastic properties requires the estimation of the storage modulus ($G^{'}$) and the loss modulus ($G^{''}$). For PAAm above 2500 ppm concentration, these quantities have been extensively characterized [198]. However, determining these properties for lower concentrations, such as those used in our experiments, proves challenging. This is due to the limitations of commercially available rheometers, like the Anton Paar MCR302, which we used in our research. While there are non-conventional methods available, such as optical tweezers [195] and microfluidic rheometers [199], they necessitate customized experimental setups which were not feasible for our study.

PAAm has demonstrated viscoelastic properties even at these lower concentrations, where the relaxation time has been observed to increase with concentration [45, 195]. An increase in relaxation time corresponds to an increase in the elasticity of the solution. For the purposes of our research, an exact relaxation time value was not crucial. We were able to discern the elastic effects by comparing solutions with similar viscosities.

4.2.2. CELL IMAGING

3D TRACKING EXPERIMENTS

C. Reinhardtii cells of the CC-125 strain were cultured in Tris minimal medium and harvested during their exponential growth phase when the cell concentration reached $\mathcal{O}(10^6)$ cells/ml. Cell culturing and harvesting procedures are detailed in section 2.2.3. We use the cell concentration of 5×10^4 cells/ml for our tracking experiments. This concentration was achieved by mixing the algae culture with different Newtonian and viscoelastic solution concentrations as listed in table 4.1.

Approximately 100 μl of each solution containing algae cells was loaded into an acrylic flow chamber. The 2 mm deep chamber is made by laser-cutting an 8 mm hole and sealing it with two BSA-treated glass slides to form a flow chamber. The chamber was then positioned on our multi-camera microscope, composed of 4 Imager sCMOS cameras, a common objective of 1.5x magnification, and red laser light (650 nm wavelength) illumination, a wavelength that does not trigger a phototactic response in *C. reinhardtii* [27, 105]. This system can capture the microorganisms' three-dimensional behavior within a measurement volume of $2.5 \times 2.5 \times 2$ mm^3. Experimental recordings started an hour after the solution preparation to allow the cells to acclimate to the polymeric medium. For all solutions, a minimum of 10 minutes of data was recorded at a frame rate of 20 fps.

Trajectories are reconstructed in three dimensions from the recordings, using our custom-made three-dimensional Lagrangian tracking algorithm, detailed in section 2.2.4. The algorithm uses a peak-finding approach for initial cell detection, followed by frame-wise tracking. Cell images from the multiple camera views are matched and triangulated using linear ray tracing in the projective geometry framework. Data segmentation and filtration were used to remove ghost tracks, the periodic blinking of algae due to their 3D trajectories, and poor reconstructions. Following this, the curve fitting algorithm, as discussed in section 2.4.2, was used to obtain a continuous representation of three-dimensional trajectories. We obtained approximately 5000 trajectories to analyze for each recorded concentration.

2D MICROSCOPY

3D tracking experiments offer detailed insights into cell trajectories but are insufficient to extract the cell beating frequency f and the velocity during the power and recovery stroke. Measurement of these parameters is crucial when investigating the effect of viscoelasticity on *C. reinhardtii* motility. The core limitation is the frame rate of the 3D microscopic setup. The maximum frame rate of 50 Hz is too low to accurately capture the *C. reinhardtii* beating frequency, which is also around 50 Hz [45, 137]. Consequently, even at the highest frame rate, the aliasing requirement of $f_{\text{sampling}} \geq 2f_{\text{experiment}}$ is not satisfied. Hence, we adopted a 2D experimental approach to measure the beating frequency and velocities during the power and recovery strokes. We used an inverted microscope equipped with a single sCMOS camera with a smaller image size (2560 × 402) to record at a high frame rate of 500 fps. Imaging was performed for Newtonian and viscoelastic solutions by dispensing a droplet on a glass slide and recording under white light. Each recording lasted 30 seconds and was conducted at a 15x magnification. Fig. 4.2 A presents a representative example of a recorded image from the Tris minimal solution. We adapted our Lagrangian tracking algorithm for two-dimensional tracking.

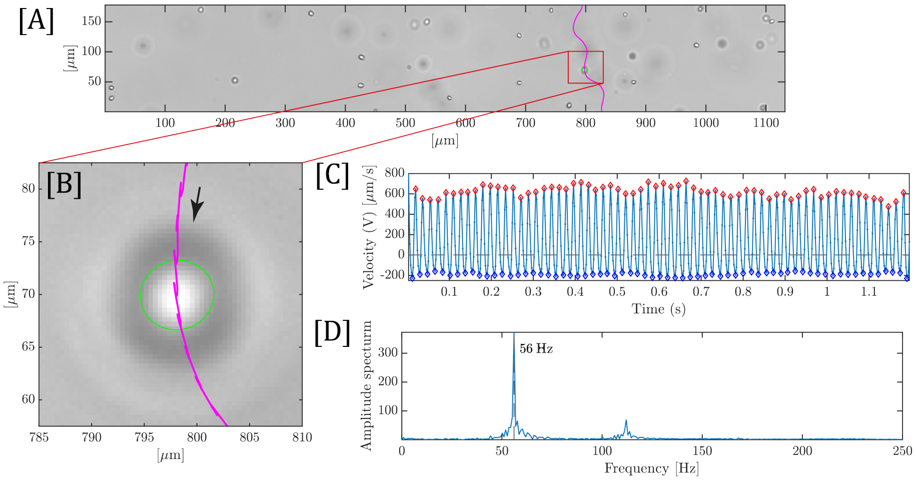

Figure 4.2: [A] Representative image captured with a 15x magnified inverted microscope, depicting swimming algae cells in Tris medium solution. The solid magenta line indicates the two-dimensional trajectory of the cell enclosed by the green circle. [B] Enlarged image of a detected algae cell, with the arrow indicating its mean travel direction. [C] Time-dependent variation in velocity, with forward (red markers) and backward (blue markers) peak velocities. [D] Amplitude spectrum of velocity signal from panel [C], obtained using the Fast Fourier Transform (FFT). The dominant frequency, marked by the vertical dashed line at 56 Hz, corresponds to the flagellar beating frequency.

The generated trajectories were manually inspected for all tracked cells. We selected for analysis the trajectories in which the cell remained in focus for at least 1 second, identified by their brighter appearance compared to cells that moved out of focus. Fig. 4.2 B represents one such cell and its corresponding trajectory. The cell exhibits forward and backward motion due to the power and recovery stroke.

To extract the velocities during power and recovery strokes, we plotted the directional velocity against time (see Fig. 4.2 C). Peaks in the direction of the average motion of the cells represent forward velocity, while those in the opposite direction indicate backward velocity (see Fig. 4.2 C). We derived each cell's forward and backward velocities from the mean value of these peaks. For the particular cell shown in Fig. 4.2 B, the forward velocity (V_+) was 503 $\mu m/s$ and the backward velocity (V_-) was 198 $\mu m/s$. The cell beating frequency f was deduced from the discrete Fourier transform of the velocity signal, which is computed with fast Fourier transform (FFT). The amplitude spectrum of the velocity signal is shown in Fig. 4.2 D, where the dominant frequency represents the cell beating frequency. For the example cell, the frequency was 56 Hz. This procedure was applied to extract forward and backward velocities and beating frequencies for cells suspended in Newtonian and viscoelastic solutions. We gathered an average of 15 data points for all solutions, except those with viscosity exceeding 5 mPa.s, where only 4 to 7 cell trajectories could be further analyzed.

4.3. CELL KINEMATICS

We analyzed the swimming kinematics of *C. reinhardtii* cells in both two and three dimensions to provide a comprehensive understanding of cell motility. We performed two-dimensional (2D) microscopy experiments to examine the effects of viscosity and viscoelasticity on the details of the cell's motion. Specifically, we characterized forward and backward velocities during the power and recovery strokes of the flagella and measured the flagella beating frequencies. In our three-dimensional (3D) analysis, we focused on the complex, helical trajectories of the cells. In particular, we investigated how the rheology of the fluid influences these trajectories, specifically the helical parameters and diffusive behavior.

4.3.1. BEATING FREQUENCY AND VELOCITIES DURING POWER & RECOVERY STROKE

We used our 2D microscopy data to examine the effects of polymer concentration on cell beating frequencies f and average swimming speed V in both Newtonian (Ficoll solutions) and viscoelastic (PAAm solutions) media (Fig 4.3), following a similar approach to Qin *et al.* [45]. At low polymeric concentrations, the viscosity of both media is $\eta \approx 1-2$mPa.s, comparable to that of the tris growth medium, and the beating frequency is $f \approx 60$ Hz, close to the value recorded in tris-medium. For increasing concentrations of ficoll, f monotonically decreases from 60 Hz to 30 Hz, at viscosities around $\eta \approx 8$mPa.s corresponding to 11.5% Ficoll. These results are in agreement with previous studies [200, 201]. In contrast, the beating frequency f remains nearly constant at a high value of $f \approx 55-60$ Hz, for PAAm concentration up to 720 ppm and $\eta \approx 8$mPa.s, see Fig. 4.3 A. Our results agree with the study from Qin *et al.* [45], reporting that flagella maintain a high beating frequency in a viscoelastic medium.

The swimming velocity V decreases with the concentration of both ficoll and PAAm (Fig. 4.3B). For Newtoninan solution of Ficoll, V decreases monotonically from $V = 120\mu\text{m.s}^{-1}$ to very low speeds of $7\mu\text{m.s}^{-1}$ at the highest Ficoll concentration of 11.5% ($\eta \approx 8$mPa.s). For viscoelastic PAAm solution, the decrease in V is much stronger at lower polymer concentration, leading to lower swimming velocities for PAAm solution of viscosities between $1-5$mPa.s compared to the Ficoll solution of equivalent viscosities. For effective viscosities beyond 5 mPa.s, the swimming velocity in the PAAm solution is constant with a value of $V \approx 20\mu\text{m.s}^{-1}$. Only at the highest polymer concentration, corresponding to an effective viscosity $\eta \approx 8$ mPa.s, do cells swim faster in PAAm solutions compared to ficoll solutions. Our findings on average velocity across both viscoelastic and Newtonian media are consistent with the results reported by Qin *et al.* [45].

The higher beating frequency f, together with the lower swimming velocity V in viscoelastic solutions, imply that the net displacement of the microswimmer per beating stroke is significantly smaller in the viscoelastic solutions compared to the Newtonian ones. The net displacement of *C. reinhardtii* per stroke depends on the

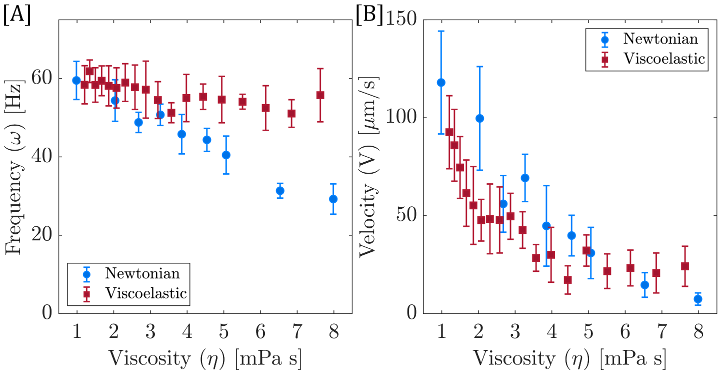

Figure 4.3: [A] Mean swimming speed and [B] Mean beating frequency for algae cells in Newtonian and viscoelastic fluids at different viscosity. Error bars represent the standard deviation across all measured cells.

relative magnitude of the forward and backward motion during the power and recovery strokes of the flagella. Therefore, we separately report the swimming speeds of the cells during the power (V_+) and recovery strokes (V_-), see Fig. 4.4. Forward velocities during the power stroke decrease with polymer concentration for both polymeric solutions. This decrease in V_+ is stronger in ficoll compared to PAAm solutions, for which V_+ reaches a constant value for the highest effective viscosities, see Fig. 4.4A. This disparity can be quantified by normalizing V_+ with the cell forward velocity in Tris solution (Fig. 4.4C). In Newtonian fluids, V_+ decreases by 80% at the highest concentration ($\eta \approx 8$ mPa.s), while for viscoelastic fluids, V_+ decreases by 30% for PAAm concentration of 560 ppm ($\eta = 5$ mPa.s) with no significant decrease beyond this concentration. The backward velocities V_- during the recovery stroke are reported in Fig. 4.4B. In Newtonian ficoll solutions, V_- decreases with ficoll concentration up to 60% at the highest concentration ($\eta \approx 8$ mPa.s), see Fig. 4.4D. In viscoelastic PAAm solutions, we observe the opposite and find the backward velocity in the recovery stroke to increase with polymer concentration. Fig. 4.4 D shows an increase in V_- in viscoelastic fluids of $\sim 20\%$ even for low concentrations of PAAm ($\eta \leq 2$ mPa.s) and remains at these higher values for the largest PAAm concentration of 720 ppm ($\eta \approx 8$ mPa.s).

The average swimming velocity V is directly influenced by the forward V_+ and backward V_- velocities during the power and recovery strokes. For Newtonian ficoll solutions, both the power and recovery stroke velocities continuously decrease with viscosity, though the decrease in V_- is not as strong as the decrease in V_+. This leads to an overall decrease in the swimming speed. For the viscoelastic medium, the sharp decrease in swimming velocity observed at low polymer concentrations is due to the decrease in forward velocity V_+ and also to the surprising increase in backward velocity during the recovery stroke. Given that f is independent of PAAm concentration, this increase in the backward velocity suggests that viscoelasticity increases the backward displacement during the recovery stroke. These results obtained from our study are in agreement with the prior experimental work by Qin *et al.* [45]. Specifically, Qin

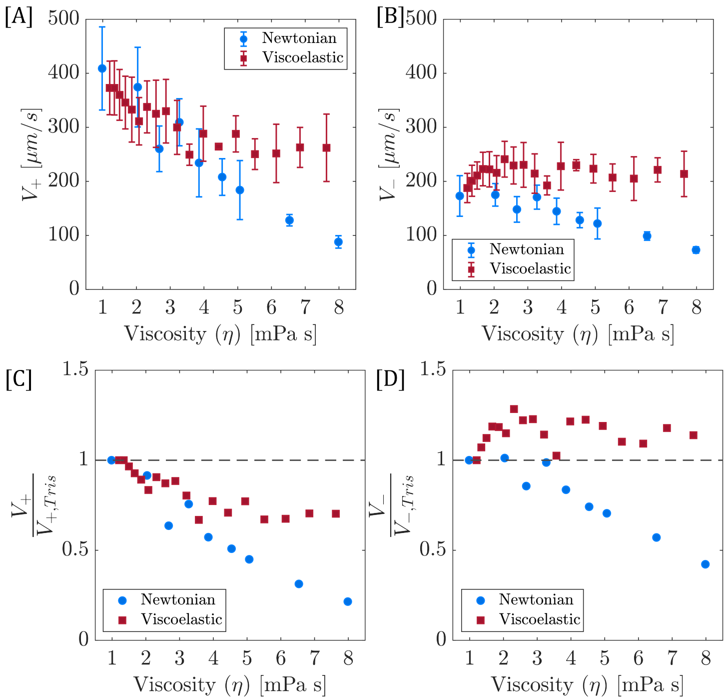

Figure 4.4: The effect of viscosity on mean velocity during [A] power stroke and [B] recovery stroke for algae cells in Newtonian and viscoelastic fluids. Error bars represent the standard deviation across all measured cells. The tris normalized velocity values for [C] power stroke and [D] recovery stroke as a function of viscosity.

et al. [45] emphasized the influence of elasticity on the kinematics of the flagellar deformations during both power and recovery strokes. Our findings corroborate their results, particularly in terms of the elastic effect on swimmer velocity. Additionally, we explored the polymer concentrations resulting in viscosities exceeding 5 mPa.s. This analysis extends on the research of Qin *et al.* [45]. We show that at such high viscosities, the presence of elasticity enables the organism to maintain constant power and recovery stroke velocities, resulting in constant swimming speed.

4.3.2. 3D TRAJECTORIES OF *C. reinhardtii* IN NEWTONIAN & VISCOELASTIC FLUIDS

We extend our analysis from two-dimensional velocity measurements to 3D measurements. Here, we characterize the 3D kinematics of *C. reinhardtii*, considering all cell trajectories from our experiments in Newtonian and viscoelastic fluids. We present our 3D measurements for polymer concentrations corresponding to viscosities up to 5 mPa.s. We do not present data for higher polymer concentration (viscosities ranging from 5 to 8 mPa.s) because the 3D-motility of the cells is inconsistent in these solutions, and the swimming velocity is very low (see Fig. 4.3 B).

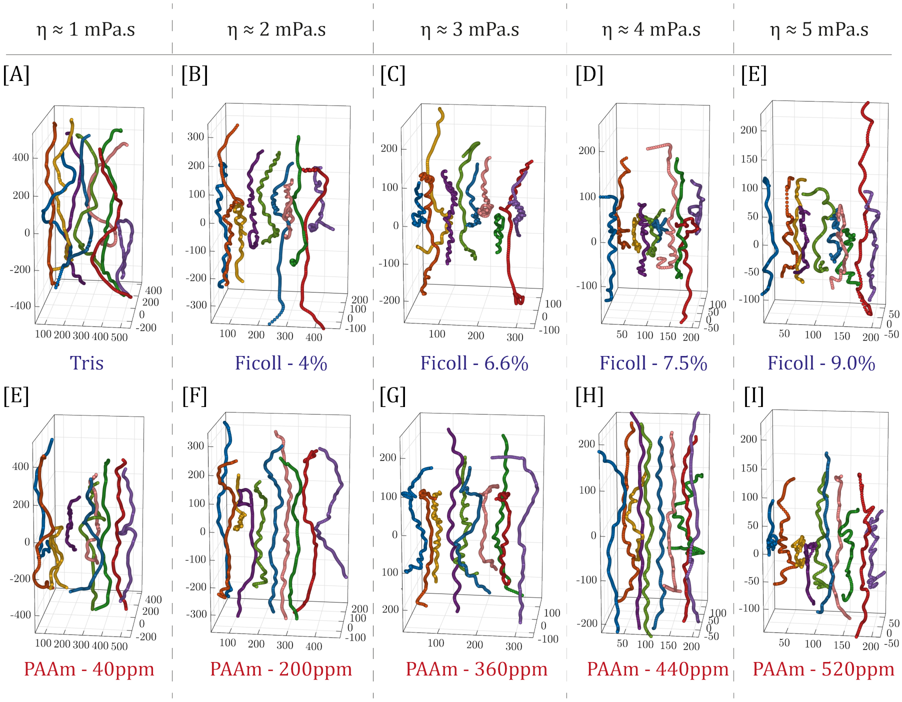

Figure 4.5: Sample trajectories for various [A-E] Newtonian and [F-I] viscoelastic fluids. Polymer concentrations correspond to viscosity ranging from 1 to 5 mPa.s. The axis scale is consistent for the same viscosity value.

Figure 4.5 presents a representative sample of 10-second long trajectories of *C. reinhardtii* in both Ficoll and PAAm solutions of different concentrations, with effective viscosities ranging from 1 to 5 mPa.s. The trajectories are helical for all solutions, which is characteristic of *C. reinhardtii*'s swimming behavior. Increasing the polymer concentration leads to cells swimming in tighter helices for both solutions. Cell trajectories in the Newtonian solutions of Ficoll concentrations larger than 4% display sharper turns and frequent abrupt changes in the swimming direction (see Fig. 4.5 C-E). In comparison, cell trajectories in viscoelastic solutions are straighter with less frequent changes in direction for PAAm concentration up to 440ppm (Fig. 4.5 F-H). In Fig. 4.5, This difference is clear when comparing trajectories at similar viscosity of 4 mPa.s corresponding to Ficoll 7.5% (Fig. 4.5D) and PAAm 440ppm (Fig. 4.5H). At the highest polymer concentration for $\eta \approx$ 5mPa.s (Fig. 4.5 E & I), cells turn at a higher rate in tighter helices and are qualitatively similar in both fluids. Qualitatively, we observe that cells maintain their swimming direction for longer periods and change direction at a lower rate, resulting in straighter trajectories in viscoelastic solutions compared to Newtonian solutions. The following section quantifies these effects by examining velocity, radius, pitch, and helical angular velocity.

4.3.3. EFFECT OF FLUID PROPERTIES ON HELICAL SWIMMING PARAMETERS

We now consider the effect of fluid properties on the helical parameters of 3D trajectories, specifically, the velocity V, the radius R, the pitch P, and the angular velocity Ω, for both Newtonian and viscoelastic solutions. These parameters are computed by analytic differentiation of the position vector, $\mathbf{X}(t) = \begin{bmatrix} X(t) & Y(t) & Z(t) \end{bmatrix}$, as follows:

$$V(t) = |\mathbf{X}^{'}(t)|, \quad R(t) = \frac{\kappa(t)}{\kappa(t)^2 + \tau(t)^2}, \quad P(t) = \frac{2\pi\tau(t)}{\kappa(t)^2 + \tau(t)^2}$$

where $\kappa(t)$ and $\tau(t)$ represent the curvature and torsion of the curve, respectively, calculated in the Frenet-Serret frame of reference (see Section 2.4.2 for more details). These geometric parameters are computed at each time step for all 3D trajectories. For our analysis, we compute the time-averaged values for velocity, radius, and pitch represented by $\overline{V}$, $\overline{R}$, and $\overline{P}$, respectively.

Our experimental results are presented in Fig. 4.6, which provides joint distributions of the trajectory parameters $\overline{V}$, $\overline{R}$, $\overline{P}$, and Fig. 4.7, which focuses on the dependence of $\overline{V}$, $\overline{R}$, $\overline{P}$ on polymer concentration. Fig. 4.6A.-F. presents the joint distribution of $\overline{V}$ and $\overline{R}$ and shows that the swimming velocity decreases with increasing concentration of Ficoll (Fig. 4.6A.,C.,E.) and PAAm (Fig. 4.6B.,D.,F.). In addition, a comparison between the distribution of $\overline{V}$ for the Ficoll and PAAm solutions of equivalent viscosity shows that the cells swim faster in the Newtonian medium compared to the viscoelastic medium. These observations are summarized in Fig. 4.7A, which encompasses all concentrations studied for both types of solutions.

We verify the consistency of our measurements by comparing the velocity measurements obtained with our 3D microscope to those from our previous measurement (see Section 4.3.1) using two-dimensional microscopy. This comparison is depicted in the inset of Fig. 4.7A, illustrating the swimming velocity ($\overline{V}$) obtained from 3D microscopy plotted against that from 2D microscopy across all concentrations for both types of polymer solutions. The values fall on the first bisector and demonstrate the consistency of the 2D and 3D measurements.

We now focus on the chirality and geometric parameters defining each trajectory. Figure 4.6G.-L. presents the joint distribution of $\overline{P}$ and $\overline{V}$, used to characterize the helicity of 3-dimensional trajectories [54, 87]. These joint distributions are given for both Newtonian and viscoelastic solutions at increasing polymer concentrations. In all our experiments, we find that the sign of the pitch is always predominantly negative. This signifies that *C. Reinhardtii* cells swim in left-handed helices regardless of the rheology of the fluid medium. Helical trajectories allow algae cells to navigate and adjust their orientation in response to light stimuli [202, 203]. This shows that the kinematics of the flagellar beat of *C. Reinhardtii* robustly supports the chirality of the helical swimming pattern in media of different rheologies.

While the overall helical nature and chirality of the trajectories are preserved in the different media, the geometric parameters $\overline{R}$ and $\overline{P}$ are strongly influenced by the rheology and polymer concentration. The radius of the helices remains small for the trajectories in all media and remains within the range of $2-5\mu$m in all experiments. $\overline{R}$ decreases moderately with polymer concentration from 5 μm to 3 μm in Ficoll solutions

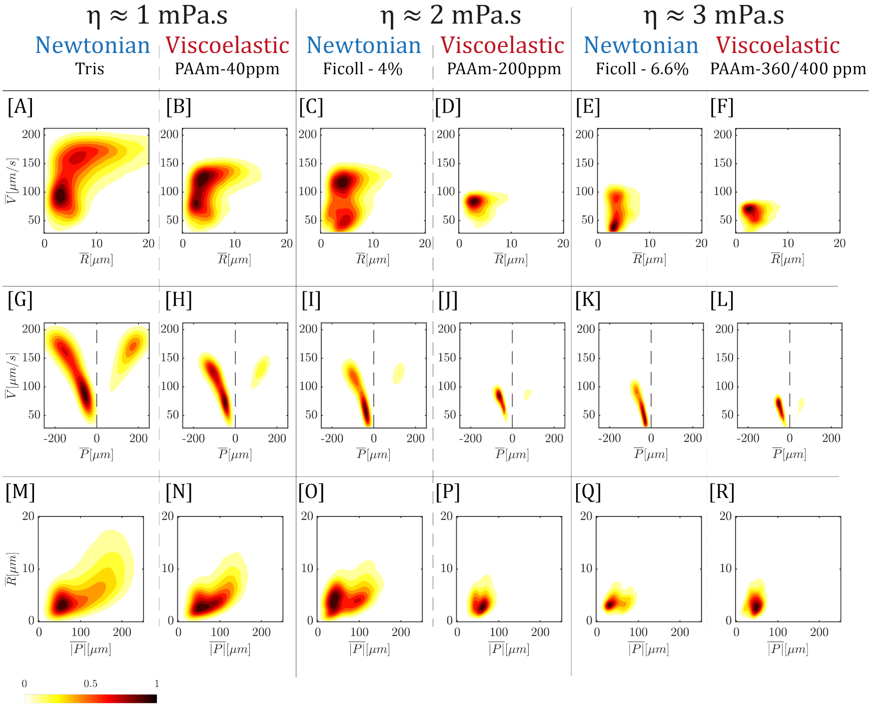

Figure 4.6: Joint distributions of trajectory behavior characterized by time-averaged velocity ($\overline{V}$), radius ($\overline{R}$), and pitch ($\overline{P}$) for Newtonian and viscoelastic fluids at the viscosity of 1, 2, and 3 mPa.s [A-F] Velocity vs. radius. [G-L] Velocity vs. Pitch [M-R] Pitch vs. radius. The color bar represents the relative density.

of 0 to 9% and from 4.6 μm at 1.2 mPa.s to approximately 2 μm in PAAm solutions of 40 to 560 ppm (see Fig. 4.7B). In addition, we find the cells swim with smaller radii in viscoelastic solutions compared to Newtonian fluids of similar viscosities, though the differences are moderate (see Fig. 4.7B).

The pitch $\overline{P}$ corresponds to the height of one complete revolution of the helix and decreases with polymer concentration in a qualitatively similar fashion as $\overline{R}$. In Newtonian Ficoll solutions, $\overline{P}$ decreases from about 98 μm (0% ficoll) to 27 μm (9%); in viscoelastic PAAm solutions, $\overline{P}$ decreases from 65 μm (40ppm) to about 20 μm (560ppm). Similar to the radius $\overline{R}$, the pitch values $\overline{P}$ are lower, corresponding to tighter helices, in viscoelastic solutions compared to Newtonian solutions of equivalent viscosity (see Fig. 4.7C).

The decrease in the helical geometric parameters $\overline{R}$ and $\overline{P}$ for Newtonian fluids implies that the stroke kinematics of the flagella is not constant and that it depends on the hydrodynamic forces experienced. Such variations in the stroke patterns due to changes in the rheology or due to changes in external hydrodynamic loads have been previously reported through direct microscopic observations of the flagella [45, 204]. The decrease in the geometric parameters of the helix $\overline{R}$ and $\overline{P}$ are indicative of a decrease in the stroke amplitude of the flagella with increasing polymer concentration and effective viscosity.

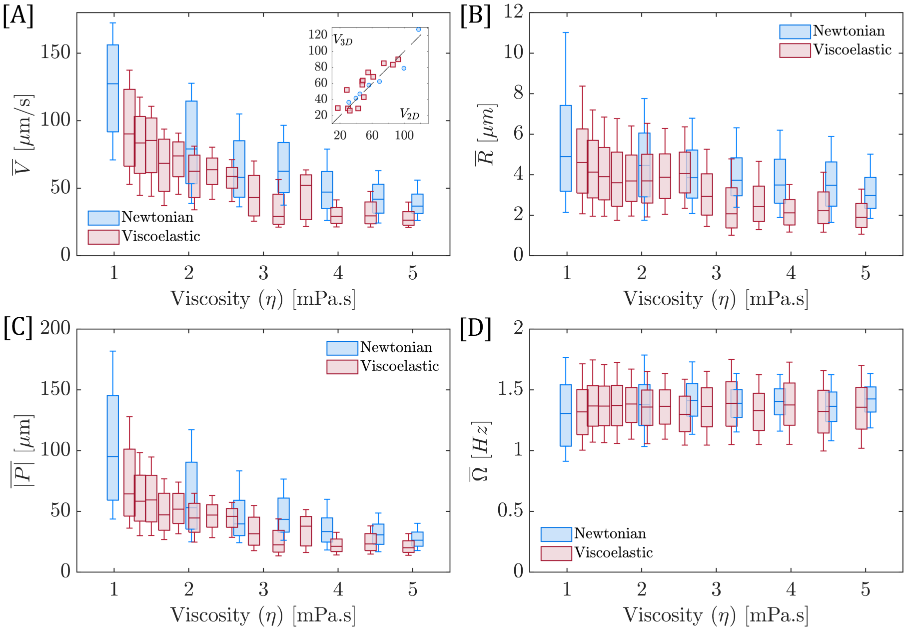

Figure 4.7: Box plots of time-averaged velocity ($\overline{V}$), radius ($\overline{R}$), pitch ($\overline{P}$), and helical angular velocity ($\overline{\Omega}$) of 3D trajectories in different Newtonian and viscoelastic solutions. The median value is represented by the central bar in each box, with the lower and upper bounds of the box indicating the 25th and 75th percentiles, respectively, forming the interquartile range. The top and bottom whiskers represent the 10th and 90th percentiles. The inset in [A] shows the agreement between 2D and 3D velocity measurements, with circle markers representing the velocity in Newtonian solutions and squares in viscoelastic solutions.

A striking characteristic of the overall distributions of $\overline{V}$, $\overline{R}$, and $\overline{P}$ is how broad the distributions are, particularly the distributions in Newtonian Ficoll solutions. This can be seen from the larger whiskers in Fig. 4.7 A.-C. and the broader peaks in Fig. 4.6 G.-R. for the Newtonian Ficoll solutions compared to the viscoelastic PAAm solution of comparable viscosity. Close inspection reveals a bimodal distribution in the joint distribution of $\overline{V}$ and $\overline{R}$ in Fig. 4.6 A-C-E as well as in the distribution of $\overline{V}$ and $\overline{P}$ in Fig. 4.6 G-I-K. The two peaks correspond to two different modes with different swimming speeds, one faster than the other. In low viscosity Tris medium, the faster swimming mode corresponds to the weaker peak with swimming velocities $\overline{V} \approx 150\mu\text{m.s}^{-1}$ and the slower swimming mode corresponds to the main peak with $\overline{V} \approx 80-90\mu\text{m.s}^{-1}$. This bimodality is conserved for Newtonian fluids of increased viscosity at higher Ficoll concentration, Fig. 4.6 A-C-E. Remarkably, this bimodal distribution is significantly altered by viscoelasticity. At the lower PAAm concentration in fig 4.6 B, the medium is weakly viscoelastic, and the predominance of the two swimming modes is reversed, with the faster swimming mode being prevalent. Upon increasing the PAAm concentration in fig 4.6 D-F, the slower mode disappears, and only the faster swimming mode remains. *C. Reinhardtii* cells have been reported previously to swim in two gears, in an eukaryotic equivalent of a run-and-tumble motion [92]. The "run"-mode corresponds to the cell swimming with its two flagella synchronized and is characterized by fast swimming, while in the "tumble"-mode the two flagella beat asynchronously, inducing a reorientation of the swimming direction and slower swimming velocity. We can, therefore, assume that the two modes identified in our distributions Fig. 4.6 A-C-E correspond to two sub-populations of cells, characterized by their swimming modes: the faster mode corresponds to fast swimming cells whose flagella remain mostly synchronized, and the slower mode corresponds to cells with a higher incidence of asynchronous beating, leading to cell reorientation and slower swimming velocities. This characterization of the two swimming modes agrees with our earlier qualitative description of the trajectories, see Fig. 4.5. First, the prevalence of the slower swimming mode in the Newtonian medium implies that the cells have a higher incidence of tumbles, agreeing with the observation of trajectories with a higher rate of sharp turns. Second, the prevalence of the faster swimming mode and disappearance of the slower swimming mode in viscoelastic flow indicate that cells swim in a "run"-mode for most of the time, agreeing with our recording of trajectories, which are significantly straighter in a viscoelastic medium. Together, our result strongly suggests that the viscoelastic rheology of the fluid modulates the flagellar synchronization, with increased elasticity promoting robust synchrony. Recent work has demonstrated that the synchronization between the two flagella of *C. Reinhardtii* is due to internal elastic stresses in the fibrous structures connecting the two flagella as opposed to viscous stresses acting through the fluid [103, 205, 206]. This new result points to the fundamental role of elasticity in promoting synchrony, both through structural elasticity and through fluid viscoelasticity.

We conclude this section by considering the correlations between $\overline{V}$, $\overline{R}$, and $\overline{P}$. The joint distributions between $\overline{V}$ and $\overline{R}$, and between $\overline{R}$ and $\overline{P}$, show weak correlations for all of the polymer solutions, with Spearman's rank correlation coefficients ranging from 0.2 to 0.5 and 0.3 to 0.5, respectively (see Fig. 4.6A.-F. and M.-R.). On the other hand, the joint distribution of $\overline{V}$ and $\overline{P}$ clusters around a straight line through the origin, indicative of a linear relation between the geometric parameter $\overline{P}$ and the kinematic parameter $\overline{V}$, see Fig. 4.6 G.-L. We find an extremely strong correlation with Spearman's rank correlation coefficients varying between 0.8 and 0.9 for different solutions between the swimming velocity $\overline{V}$ and the helical pitch $\overline{P}$. This strong correlation has a few outstanding features. First, in comparison to the significant variability and broad distributions of $\overline{R}$, $\overline{P}$, and $\overline{V}$ as shown in Fig. 4.7, the correlation between $\overline{V}$ and $\overline{P}$ is surprisingly strong and the joint distribution narrow. Also, the two peaks corresponding to the faster "run"-dominated mode and the slower "tumble"-dominated mode in the joint distribution fall along the same line, see 4.6 G-H-I, such that the linear relation between velocity and pitch holds for both modes. Finally, the robustness of this linear correlation to changes in the rheology is remarkable. Cells swimming in the Newtonian solution of increased viscosity exhibit the same linear correlation between velocity and pitch, with the joint distribution clustering along a line with the slope of ~0.85, see

Fig. 4.6 G-I-K. The same observation holds for the viscoelastic solutions at all PAAm concentrations, see Fig. 4.6 H-J-L. The fact that the slope of the velocity/pitch correlation remains the same for all the tested polymeric solutions is all the more unexpected, considering our earlier discussion that rheology strongly affects the kinematics of the flagellar stroke, the geometry of the trajectories, the beating frequency, and swimming velocity.

The slope of the linear correlation is the ratio between $\overline{V}$ and $\overline{P}$ and corresponds to the inverse of the characteristic time required for the cell to swim over the distance between two consecutive turns of the helix. Since the radius of the helices is significantly smaller than the pitch, this time scale is closely related to the time scale to complete a full turn of the helix, or equivalently, the rotation rate Ω along the helix. We compute the instantaneous rotation rate as follows:

$$\Omega(t) = \frac{V(t)}{\sqrt{P(t)^2 + R(t)^2}},$$

and report for each trajectory the average value $\overline{\Omega}$. In Fig. 4.7 D, we present our results as a function of the effective viscosity of the Ficoll and PAAm polymeric solutions. We find indeed that the rotation rate along the helix is the same for Newtonian Ficoll solutions and viscoelastic PAAm solutions and does not depend on the polymer concentration, see fig 4.7 D. In addition, for each concentration of polymeric solution, the distribution is narrow in both solutions, as can be seen from the small whiskers in fig 4.7 D, and in stark contrast with the wide distribution in swimming velocity in fig 4.7 A.

The rotation rate $\overline{\Omega}$ along the helical trajectory is, therefore, a motility invariant, with $\overline{\Omega} \approx 1.25$ Hz in all tested solutions. This result underlines the biological significance of the rotation rate $\overline{\Omega}$, compared to other motility parameters such as $\overline{V}$, $\overline{P}$, $\overline{R}$, or f, which are not invariant. Helical trajectories allow microalgae cells to survey and keep track of the light intensity in different directions [28, 207] and are central to the reorientation in response to light stimuli required for phototaxis [202, 203]. An invariant $\overline{\Omega}$ guarantees that cells retain the ability to scan the light distribution around them, regardless of the complex nature of their environment. How this invariance is achieved and its origin remains open questions. The helical swimming in *C. reinhardtii* cells originate from a force asymmetry between the flagella and the out-of-plane beating component of the flagella [113]. We hypothesize the existence of an active regulation mechanism for the asymmetric and out-of-plane beating component of the flagellar beat, supporting the invariance of $\overline{\Omega}$. In fact, in Newtonian solutions of increasing viscosities, the flagellar beating frequency decreases, see Fig. 4.3 A), which can only be compensated by an increase in the 3D beating component to keep $\overline{\Omega}$ constant. In viscoelastic solutions, the increase in viscoelasticity leads to surprising changes in the forward and backward velocities during the power and the recovery stroke, see Fig. 4.4, and the changes in the stress on the flagella lead to modulations in the flagellar deformations and swimming gait Qin *et al.* [45]. Despite these changes in swimming gait, the cells still maintain a constant $\overline{\Omega}$, which is, in fact, equal to the value measured for Newtonian solutions. Hence, the invariance of rotation rate $\overline{\Omega}$ requires complex modulation of the 3D beating gait that strongly depends on the beating frequency and the nature of the complex stress experienced in media of varying rheological properties; these modulations are therefore likely active in nature. What sets the value of the rotation rate $\overline{\Omega} \approx 1.25$ Hz, and how does a cell sense that it has completed a full rotation also remain open questions. The helical motion plays an important role in phototaxis, and it is therefore reasonable to look for an environmental origin to the value of $\overline{\Omega}$. The presence of a light source could provide an environmental signal to support a constant rotation rate. However, our experiments were performed under red light and in complete darkness to avoid any influence of phototactic response in the 3D trajectories of *C. Reinhardtii*. In the absence of environmental factors, our results could also point to a cellular mechanism allowing the cell to sense its own rotation.

4.3.4. CELL DIFFUSIVE BEHAVIOR IN NEWTONIAN & VISCOELASTIC FLUIDS

In the previous section, we quantified the effect of rheology on geometric trajectory parameters $\overline{P}$ and $\overline{V}$ and kinematic parameters $\overline{V}$, f, and $\overline{\Omega}$. These quantities are locally defined at a point along the trajectory and are derived from the motion of the cell. In the following, we quantify the effect of rheology on the long-term behavior of the cell and define new parameters characterizing the trajectories over long time scales. Over such long time scales, the motion of *C. Reinhardtii* is known to be diffusive in nature [92]. We characterize the diffusive behavior of cells by computing the reorientation time τ_p and persistence length L_p for each cell's trajectories in both Newtonian and viscoelastic fluids. The reorientation time τ_p represents the duration over which the travel direction of a cell no longer correlates with its initial travel direction. Related to τ_p, we compute the persistence length L_p, corresponding to the total distance the cell covers during the time interval τ_p, and over which the correlation in the swimming direction is lost.

Assuming that the correlation function of the swimming direction follows an exponential decay of the characteristic timescale τ_p, we can derive an expression for the mean squared displacement of the cell (MSD):

$$\mathrm{MSD}(\Delta t) = 2\langle V^2\rangle \Delta t \tau_p \left[1 - \frac{\tau_p}{\Delta t}\left(1 - e^{-\frac{\Delta t}{\tau_P}}\right)\right], \tag{4.1}$$

where ($\langle V^2\rangle$) is the mean square velocity. This derivation is equivalent to established definitions of the persistence length in polymer dynamics [208], see Appendix A.3 for more details. In our experiments, the mean square displacement (MSD) of the cell is directly deduced for each trajectory from the extracted position vector $\mathbf{X}(t)$, as $\mathrm{MSD}(\Delta t) = \langle|\mathbf{X}(\Delta t + t_\circ) - \mathbf{X}(t_\circ)|\rangle$, and τ_p can be readily deduced by fitting the model in equation 4.1 to our experimental data. The persistence length L_P is directly deduced from the reorientation time scale as:

$$L_p = \sqrt{\langle V^2\rangle}\tau_p. \tag{4.2}$$

Figure 4.8 presents the distributions of our measured τ_p and persistence length L_P for both Newtonian and viscoelastic fluids. For the Newtonian solutions, the average reorientation time remains constant, with a value of around 4s for all concentrations. The cells in viscoelastic media exhibit an average reorientation time that is higher than that of cells in Newtonian solutions of equivalent viscosity. Additionally, as the concentration of the viscoelastic solution increases, the reorientation time also increases, reaching a maximum of 10s for PAAm 320ppm with a viscosity (μ) of 2.6 mPa.s. This is 3-fold larger than in the Newtonian ficoll solution of equivalent viscosity. When considering persistence length (Fig. 4.8 B), we find that cells reorient more frequently in a Newtonian solution of increasing ficoll concentration, as demonstrated by the reduction in persistence length from approximately 500 μm to 100 μm as Ficoll concentration increases from 0 to 9% corresponding to η = 1mPa.s to η = 5mPa.s. As for viscoelastic solutions, the average persistence length varies between 250 μm and 400 μm for all concentrations, except for PAAm 560 ppm (η = 5mPa.s). Moreover, the persistence length in viscoelastic solutions is higher than in Newtonian solutions, corroborating the observation from 3D trajectories presented in Fig. 4.5.

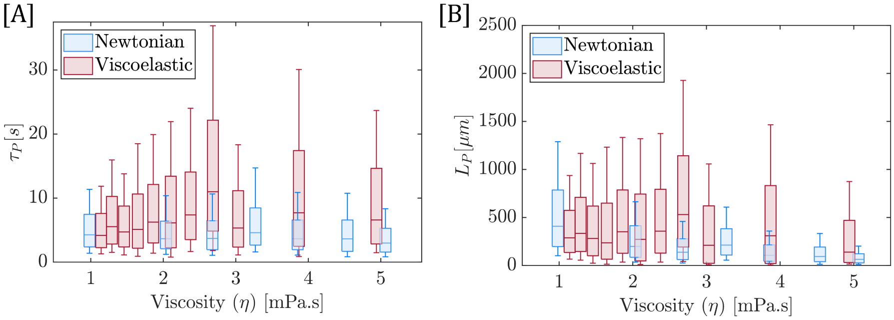

Figure 4.8: Box plots of [A] Reorientation time τ_P and [B] Persistence length L_P for three-dimensional trajectories swimming in Newtonian and viscoelastic fluids. The median value is represented by the central bar in each box, with the lower and upper bounds of the box indicating the 25th and 75th percentiles, respectively, forming the interquartile range. The top and bottom whiskers represent the 10th and 90th percentiles.

Our quantitative characterization of the long-term behavior of cell trajectories reveals a strong effect of fluid rheology on the diffusive behavior of cells. Our main result is the significant increase in reorientation time and associated increase in persistence length in viscoelastic solutions compared to Newtonian solutions of equivalent viscosities. The diffusive behavior of cells originates in the random walk-like run-and-tumble motion, where the tumbles are caused by the cell reorientations due to asynchronous flagellar beating [92]. The primary phenomenon that causes asynchrony is the phase slip of the trans flagellum [204]. The decrease in diffusivity observed in viscoelastic solutions suggests a strong effect of viscoelasticity in reducing the occurrence of phase slip and, consequently, in promoting flagellar synchrony. These results agree with our earlier observation that the slower swimming mode in Newtonian solutions is suppressed in viscoelastic solutions, see Fig. 4.6 and that elasticity supports synchronous flagellar beating.

4.4. SURFACE INTERACTIONS

This section presents our study of the surface interactions of *C. reinhardtii* cells in both Newtonian and viscoelastic fluids of varying polymer concentrations. Here, we consider only solutions with low effective viscosities of 1 mPa.s and 2 mPa.s. Previously, we found that, for these low polymeric concentrations, the trajectories maintain their orientations for longer times, as indicated by the high persistence length (see section 4.3.4). For high polymeric concentrations, cells frequently turn and swim at low velocities, making it challenging to isolate cell reorientation due to surface effects from the inherent cell motion. We, therefore, limit this study to two Newtonian solutions, namely Tris minimal and 4% Ficoll solutions, and two viscoelastic solutions of comparable viscosities, namely PAAm solutions at 40 ppm and 200 ppm. We use our three-dimensional microscope to investigate how rheology affects the scattering dynamics, residence time, and surface accumulation of cells.

4.4.1. NEAR-SURFACE SCATTERING

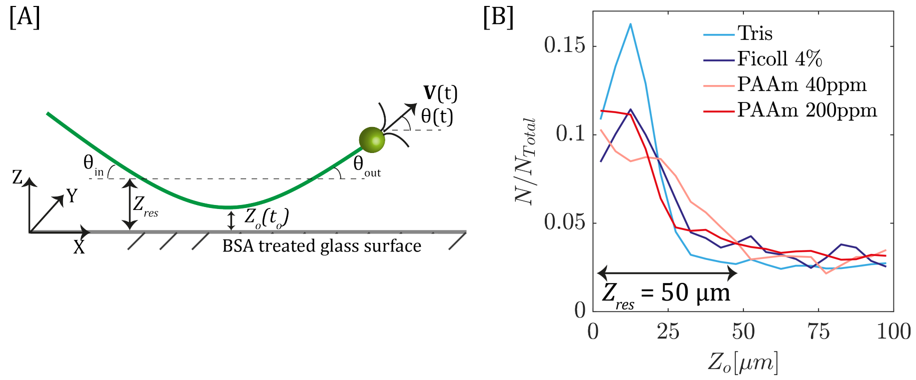

Figure 4.9: [A] Illustration of a cell surface interaction and the nomenclature used throughout this section. [B] The distributions of closest approach distance ($Z_\circ$) for all cell trajectories for both Newtonian (Tris & Ficoll 4%) and Viscoelastic (PAAm 40 ppm & 200 ppm) solutions.

First, we examine the scattering dynamics of motile *C. reinhardtii* cells in the near-surface region. For this, we identify a near-surface region characterized by a length scale Z_{res} determined as follows. For each trajectory, we identify the time $t_\circ$ when the cell is at its minimum distance to the surface and call this minimum distance $Z(t_\circ) = Z_\circ$ (see Fig. 4.9A). Fig. 4.9B represents the distribution of minimal approach distance $Z_\circ$ for all four solutions. For all solutions, the distribution increases significantly close to the surface, indicating that a significant number of cells approach and subsequently depart from the surface. Beyond a distance of 50 μm, the distribution is uniform, indicating that the surface has a limited effect beyond this distance. Therefore, we consider that the near-surface region extends to a distance of 50 μm from the surface, *i.e.*, $Z_{res} = 50\mu m$, and consider here only those trajectories for which the minimal approach distance is such that $Z_\circ \leq Z_{res}$. For these trajectories, we define $X_{2D}(t)$ as the distance traveled in the xy-plane parallel to the surface and present the trajectories in $(X_{2D}(t), Z(t))$ coordinates. Fig. 4.10 presents the distribution of these trajectories for the four solutions. We follow the same methodology as in our previous work on cell-surface scattering dynamics in a Newtonian medium [98] and re-center all trajectories around the position of minimal approach $X_{2D}(t_0)$.

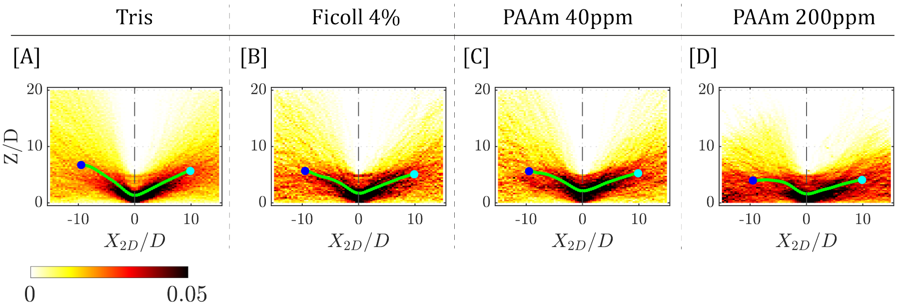

Figure 4.10: The distribution of cell trajectories in (X_{2D}, Z) coordinates centered at $X_{2D}(t_0)$ for different media. Green markers represent the average trajectory with cells moving from blue towards the cyan marker.

For Newtonian solutions, the addition of Ficoll results in shallower trajectories that remain on average closer to the surface, see Fig. 4.10B compared to A. Also, the cells approach and depart from the surface at shallower angles in the 4% Ficoll solution compared to the Tris medium. In viscoelastic solutions (PAAm 40 and 200 ppm), the increase of the polymeric concentration has a similar effect on the trajectories, see Fig. 4.10C and D. We compare the distribution of trajectories for solutions with similar viscosity, such as Tris vs. PAAm 40 (1 mPa.s) and Ficoll 4% vs. PAAm 200 ppm (2 mPa.s). In viscoelastic solutions, the average cell trajectories remain closer to the surface compared to the trajectories in the Newtonian solution, see Fig. 4.10A, C and Fig. 4.10B, D.

We further quantify how shallow the trajectories are and report the approach and departure angles. The approach angle θ_{in} and the departure angle θ_{out} correspond to the angle at which a cell enters and exits from the near-surface region ($Z = Z_{\text{res}}$), see Fig. 4.9. Figure 4.11 presents the distribution of θ_{in} and θ_{out}. In Tris medium, the median approach angle is 30°. With the addition of Ficoll, this decreases to a median angle of 24°. For PAAm at 40 ppm, the median approach angle is 27°, while at PAAm 200 ppm, it decreases to 20°. We find a similar decrease for the departure angles. In the Ficoll 4% and PAAm 200 ppm solutions, cells depart at smaller median angles, 20° and 18° respectively, compared to 24°, in the Tris medium. Both the approach and the departure angles are lower in the viscoelastic fluids compared to the Newtonian fluid of similar effective viscosity, see Fig. 4.11. These measurements of θ_{in} and θ_{out} confirm our observation from the trajectory distributions in Fig. 4.10 that cells remain closer to the surface in polymeric viscoelastic solutions compared to cells in Newtonian solutions.

We can directly characterize the effect of rheology on surface scattering by computing the expected value of departure angles $E(\theta_{\text{out}})$ conditional to the incoming angle θ_{in}. Fig. 4.11E & F shows that for the same incoming angle θ_{in}, cells in viscoelastic solutions scatter at a smaller departure angle θ_{out} compared to cells in the Newtonian medium of similar viscosity. This effect is stronger at the higher polymeric concentration, see Fig. 4.11E & F for cells in 4% Ficoll and PAAm 200 ppm. Our experimental results agree with previous numerical studies [182, 184], where increase in viscoelasitcity (Higher Weissenberg and Deborah number) resulted in shallower scattering angles. An increase in elastic properties promotes cell repulsion from the surface [184]. This elastic repulsion prevents cells from approaching the surface closely [184], thereby minimizing steric interactions. Instead, cells predominantly interact with the surface through hydrodynamic forces, causing them to scatter at shallower angles. Consequently, cells in viscoelastic solutions exhibit smaller scattering angles compared to those in Newtonian solutions, where closer approach leads to higher scattering angles due to steric interactions. The shallow scattering in viscoelastic solutions is a fundamental mechanism, leading directly to cells remaining in the near-surface region for longer time periods compare to cells in Newtonian media.

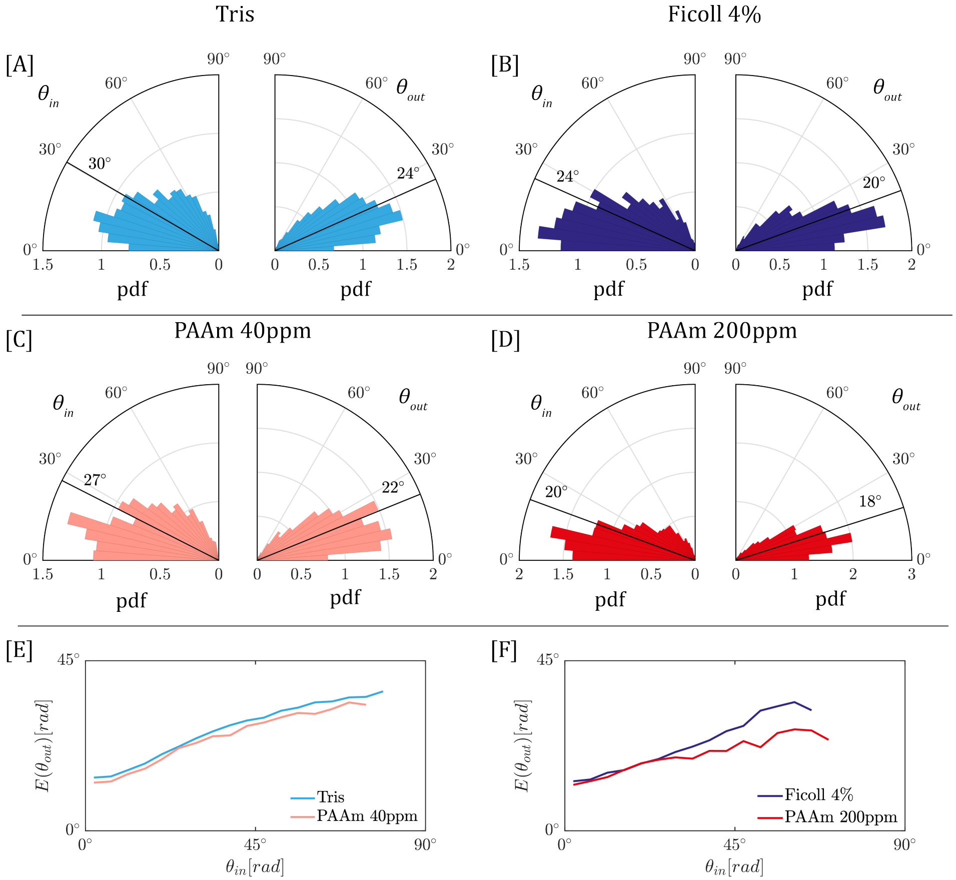

Figure 4.11: [A-D]The distributions of approach angle (θ_{in}) and departure angle (θ_{out}) for Newtonian and Viscoelastic fluids at different concentrations. Solid black lines represent the median value. [E-F] Expected value of θ_{out} for range of θ_{in} for solutions of 1 mPa.s(left) and 2 mPa.s viscosity(right).

4.4.2. RESIDENCE TIME & TRAJECTORY BEHAVIOR

surface-interactions can also be characterized by how long cells remain in the vicinity of the surface. We define the residence time t_r as the time spent by the cells within the near-surface region ($Z < 50\mu m$). Fig. 4.12 presents the distributions of residence time. In the Tris medium, the average residence time is 1.4s, indicating that prolonged trapping is rare and aligns with the deterministic departure mechanism as highlighted by earlier numerical and experimental research [143, 209]. We explored this mechanism in detail in our previous work on cell-surface scattering in a Newtonian medium [98]. In the 4% Ficoll solution, the cell residence time increases by 1.2 seconds compared to cells in the Tris medium. Cells in the viscoelastic solutions of PAAm 40 ppm and PAAm 200 ppm also exhibit longer residence times than in the Tris medium. When comparing solutions of similar viscosities, such as Tris versus PAAm 40 ppm and Ficoll 4% versus PAAm 200 ppm, cells in viscoelastic media have longer residence times than those in Newtonian media. This demonstrates the role of elasticity in increasing residence time and agrees with prior numerical [182] and analytical [172, 173] studies. It is worth noting, however, that Yazdi *et al.* [172, 173] reported instances where, based on cell orientation and distance to the surface, residence times could increase by an order of magnitude compared to swimming in Newtonian medium, leading to permanent entrapment. In our experiments, we observe no such instance of permanent entrapment. While some cells exhibited higher residence times, as seen in the distributions for PAAm 40 ppm and 200 ppm (Fig. 4.12C & D), the increase remained moderate.

We focus on the trajectories with longer residence times in the near-surface region for all different media. Through this examination, we identified two interaction types: cells that approach the surface and depart immediately, and others that exhibit spiral or hopping trajectories as illustrated in Fig. 4.13, where cells periodically move closer and away from the surface, leading to repeated surface interactions. For the Tris medium, 30% of the cell surface interactions show a hopping behavior. In the case of Ficoll 4%, PAAm 40 ppm, and PAAm 200 ppm, these percentages are 45%, 47%, and 58%, respectively. These spiral trajectories extend the overall duration cells spend in the near-surface region for Ficoll and PAAm solutions. In our previous work, we demonstrated that hopping trajectories were consistent with long-range hydrodynamic interactions with the surface [98]. The observed increase in hopping trajectories in both Ficoll and PAAm solutions implies that both viscosity and elasticity enhance this interaction. Our observation of spiral trajectories in viscoelastic media is in agreement with a previous numerical study on surface scattering in weakly viscoelastic fluids, which highlights the presence of spiral trajectories for puller-type swimmers [173]. However, while the numerical work did not indicate spiral trajectories in Newtonian fluids, we did observe them. This discrepancy could be due to the numerical study's assumption of a 2D swimmer, which influences hydrodynamic behaviors near a no-slip boundary.

4.4.3. SURFACE ACCUMULATION

In previous sections, we have characterized the scattering dynamics of puller-type *C. reinhardtii* cells in viscous and elastic solutions. A crucial question that remains to be investigated is whether the rheological properties of the medium influence the distribution of cells in the flow cell and, particularly, whether it leads to different degrees

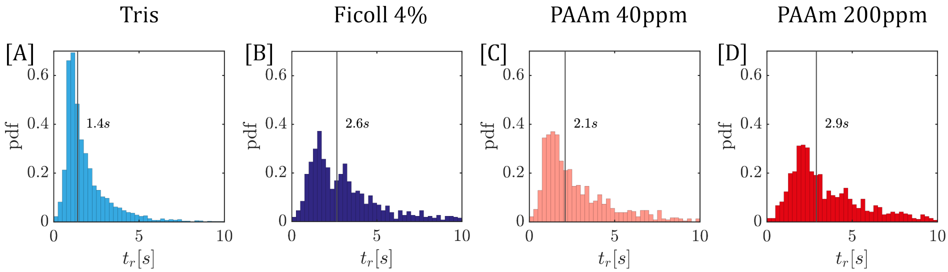

Figure 4.12: The distribution of residence time (t_r) for different solutions. Solid black lines represent the average value.

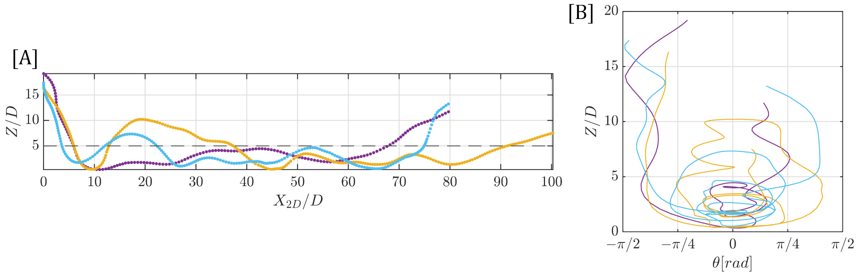

Figure 4.13: [A] Spiral trajectories in the near-surface region for PAAm concentration of 40 ppm. [B] Changes in cell orientation relative to the surface for trajectories shown in [A]. Negative θ values represent cells oriented to the surface, while positive represents orientation away from the surface.

of cell accumulation at the surface. We, therefore, use our experimental data to evaluate the distribution of cell density within our flow chamber and investigate how surface interactions in different media influence surface accumulation. For each solution, we computed the cell density. We first divided the total depth of the flow chamber into discrete bins, each spanning 20 μm. We then averaged the number of cells in each of these bins for the entire recording and divided this cell count by the volume of the respective bins. We normalize the cell density by the bulk density, which is defined as the average cell density in the middle of the flow chamber, specifically 500 μm away from the surfaces, a region least influenced by surface interactions. Fig. 4.14A presents the normalized cell density for all tested solutions.

For all media, we observe an increased concentration of cells near the surface. For both of the Newtonian media, accumulation near the surface decreases quickly. However, in viscoelastic media, cell density remains higher near the surface over a greater distance than Newtonian solutions. To characterize the extent of surface accumulation and determine how far into the fluid the influence of the surface extends, we calculate the penetration length. It is defined as $\int_0^{1000}(\rho(\mathrm{Z})-\rho(\mathrm{bulk}))/(\rho(0)-\rho(\mathrm{bulk}))$. For Newtonian fluids, the penetration length is approximately ~ $100\mu m$, similar to the one reported in [98]. For viscoelastic fluids, the penetration length increases to nearly ~ 200 μ m,. This increased penetration length in viscoelastic mediums demonstrates that elasticity increases cell accumulation near the surfaces for *C. reinhardtii* cells.

A recent experimental study showed that elasticity results in reduced surface accumulation for *Escherichia coli* bacteria [192]. This phenomenon arises due to a lift force generated by the rotating flagellum when swimming in a viscoelastic fluid, counteracting the hydrodynamic effects and thus reducing the surface accumulation for *E. Coli*. While *E. Coli* propels itself using a counter-rotating flagellum bundle, *C. reinhardtii* uses a breaststroke motion to swim. As a result, the lift forces attributed to the rotating flagellum in *E. Coli* would not be present for *C. reinhardtii* cells. Without such lift forces, the hydrodynamic interactions predominantly determine the surface accumulation [98]. Our observation of the surface accumulation in a viscoelastic medium indicates that the elasticity enhances these hydrodynamic interactions, leading to increased surface accumulation for *C. reinhardtii* cells. This increased surface accumulation can be explained by our prior results that, in viscoelastic solutions, cells depart at more shallow angles and spend a longer duration near the surfaces compared to a Newtonian solution.

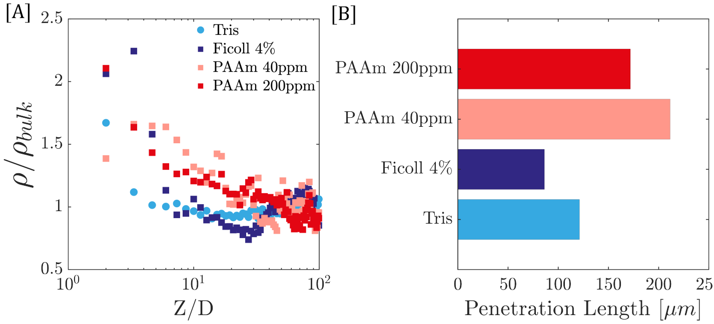

Figure 4.14: [A] Cell density distribution along the Z direction and [B] Penetration length for different fluid media.

4.5. CONCLUSION

In this study, we investigated the effects of non-Newtonian rheology on cell kinematics and surface interactions of *C. reinhardtii* cells. We used two media for our experiments: Ficoll400 solutions as Newtonian fluids of varying viscosities and Polyacrylamide (PAAm) solutions with viscoelastic properties. Our experiment included 2D and 3D tracking of *C. reinhardtii* cells. We used an inverted microscope for two-dimensional tracking to measure the beating frequency and velocities during power and recovery strokes. For 3D imaging, we used a multi-camera microscope that captured the microorganisms' three-dimensional behavior in an unconstrained environment. We then tracked the movement of cells in three dimensions using our in-house Lagrangian tracking algorithm.

Our study shows that *C. reinhardtii* cells swim with a higher beating frequency in viscoelastic solutions compared to those in Newtonian media of similar viscosities. This increase in beating frequency does not induce an increase in swimming speed.

Instead, the cells in viscoelastic fluids swim at lower speeds than those in Newtonian fluids of equivalent viscosities. Our measurements highlight the distinct impact of viscoelasticity on the velocities during power and recovery strokes. Specifically, an increase in backward velocities during the recovery stroke was observed in viscoelastic fluids, contributing to an overall lower swimming speed. These results are in agreement with the experimental work conducted by Qin *et al.* [45], providing further empirical support for their conclusions. We further investigated the influence of non-Newtonian rheology on the 3D kinematics of the *C. reinhardtii* cells. We found that the cell's velocity, radius, and pitch of the helical path are strongly influenced by the viscosity and elasticity of the surrounding medium. As the viscosity increased in Newtonian and viscoelastic solutions, cells adapted their swimming along a helical path with a smaller radius and pitch at low velocity. Cells in viscoelastic solutions swam with lower velocity, radius, and pitch values compared to cells in Newtonian solutions of equivalent viscosity.

We found that the distribution of swimming velocities and helical geometric parameters was rather broad for cells swimming in Newtonian media. These distributions were significantly broader in Newtonian compared to viscoelastic media. Close inspection of these distributions revealed bimodality for cells in Newtonian fluids, with a faster swimming mode, which arguably corresponds to cells swimming mostly with synchronized flagella, and a slower swimming mode, which corresponds to cells with a higher incidence of asynchronous tumble events. This bimodality disappears in viscoelastic media, and only the faster swimming mode remains, suggesting that viscoelasticity is responsible for reducing asynchrony between the flagella. These results are confirmed by a characterization of the long-term diffusive behavior of cells. We computed the persistence length of the cell trajectories, quantifying how long the cell maintains its direction. We found that the persistence length also depends significantly on the rheology. For viscoelastic solutions, the persistence length is higher than in Newtonian solutions, and therefore, cells in viscoelastic solutions display less diffusive dynamics than cells in Newtonian solutions. Our work also highlights how fluid properties can impact the directional changes and persistence of the cells' trajectory. The reorientation time of cells in viscoelastic fluids consistently exceeds that in Newtonian fluids of similar viscosity. This difference in reorientation time can be attributed to asynchronous flagellar beating, which is known to be responsible for the sharp turns exhibited by algae cells [92]. This asynchronous behavior is primarily driven by the phase slip of the trans flagellum [204]. While phase slips are generally considered random events [210], the difference in reorientation time between the two fluid types indicates that the elasticity of the medium reduces the asynchronous flagellar beating and promotes synchrony.

Despite the significant differences in the helical swimming of *C. reinhardtii* in the different media, the distribution of swimming parameters is consistent between all polymeric solutions in one surprising aspect. We found a very robust linear correlation between the swimming velocity and the pitch of the helix. This correlation is closely related to the angular velocity along the helix, which we found to be close to invariant and equal to 1.25 Hz in all solutions. This helical angular velocity is the rate at which algae cells scan their environment as they swim along their helical trajectory. To achieve this constant scanning frequency, cells likely tune the out-of-plane beating component of their flagella, especially when traversing tighter helices in more viscous and elastic conditions. Such a stable scanning rate is crucial for *C. reinhardtii*'s phototactic behaviors, aiding in efficiently locating light sources essential for their photosynthesis. In changing environments, maintaining this rate ensures a rapid response to stimuli.

Finally, we examined the surface interactions of cells in Newtonian and viscoelastic fluids. The surface interactions of the cells displayed differences in scattering dynamics between the Newtonian and non-Newtonian solutions. Notably, in viscoelastic media, the approach and departure angles were shallower, especially in high-concentration PAAm solutions, leading to cells remaining closer to the wall. This agrees with previous numerical studies [182, 184], which suggested that the increased elasticity resulted in cells departing at relatively shallow angles due to hydrodynamic interactions. The residence time of the cells near the surface was also affected by the properties of the fluid. In both Ficoll and PAAm solutions, we observed an increase in residence time compared to the Tris medium, demonstrating the impact of both viscosity and elasticity. We identified two types of cell-surface interactions, one where cells left immediately after approaching the surface and another where cells displayed spiral trajectories near the surface. The latter was more prevalent in viscoelastic solutions, increasing residence time. Although previous numerical studies reported the existence of these spirals in weakly viscoelastic fluids [173], our study revealed their presence even in Newtonian fluids.

We characterized the effect of the elasticity of the fluid on the accumulation of cells near surfaces. Cells in the viscoelastic fluids exhibit a higher cell density near the surface, which we quantified with a significant increase in the penetration length. This observation supports our earlier findings of an extended residence time and the presence of spiral trajectories in viscoelastic solutions. In viscoelastic media, the higher accumulation near surfaces could enhance cell-cell interactions, thus extending the duration for extracellular communication among algae cells, leading to biofilm formation at a much shortened time scale. For applications such as photobioreactors, it becomes essential to consider the cell scattering dynamics we have observed. Given that cells in these reactors swim in complex fluids, the strategic design of surface topologies is crucial. By doing so, excessive cell accumulation and, consequently, biofilm formation can be inhibited on the reactor walls.

5

IMPACT & OUTLOOK

"You can never know everything, and part of what you know is always wrong. Perhaps even the most important part. A portion of wisdom lies in knowing that. A portion of courage lies in going on anyway."

Lan Mandragoran in Winter's Heart, Robert Jordon

This dissertation introduces a new 3D imaging technique designed to deepen our understanding of microorganism motility in three dimensions. Using a novel multi-camera microscopy system introduced in Chapter 2, we have improved the tracking capabilities for microswimmers such as *C. reinhardtii*, achieving tracking at higher densities with more accuracy and precision compare to de-focused and holographic tracking methods. Our system has facilitated detailed analysis of their 3D trajectories and interactions. Chapter 3 and Chapter 4 demonstrate the application of our technology in understanding the dynamics of microswimmer interactions and the effects of fluid properties on their motility. We observed interesting scattering patterns and interaction dynamics critical for theoretical and practical implications in microbial ecology and biophysics. The following sections discuss the broader implications of our findings and future research possibilities.

5.1. SCIENTIFIC CONTRIBUTIONS AND IMPACT

This dissertation advances microorganism motility research by developing and implementing a multi-camera microscopy system for the three-dimensional tracking of microswimmers. This method enhances experimental research capabilities by providing detailed insights into the behaviors and interactions of microorganisms in a three-dimensional environment. Previously, research using multiple camera systems [110, 211] was restricted to macro scales due to technical constraints. This study adapts these methodologies for microscopic applications, enabling the exploration of microorganism dynamics. For instance, it can reveal the mechanisms behind the collective behavior of algae, contributing to advancements in algal biofuel production. Additionally, the new imaging technology can be used to investigate the chemotactic responses of bacteria to different nutrient gradients, providing a deeper understanding of microbial ecology. The ability to track interactions in three dimensions also aids in studying pathogen-host interactions, leading to novel antimicrobial strategies. Consequently, this work facilitates further studies into the taxis, collective behavior, and interactions of microorganisms, advancing microbiology, environmental science, and biotechnology.

This dissertation also introduces two innovative techniques that significantly enhance microscale research capabilities. The first is a volume-based calibration technique that uses projective geometry frameworks for microscale applications. This technique achieves high precision through linear computational approaches, simplifying the calibration process compared to traditional methods that require complex non-linear optimization [212, 213], hence computationally intensive. This process reduces computation time and resources, improving calibration and tracking applications across different scales. The second technique is the Lagrangian polynomial curve-fitting algorithm that converts discrete-time series data into continuous trajectories. This method facilitates accurate extraction of trajectory parameters, reducing potential errors and improving the reliability of trajectory analysis. However, selecting an inappropriate polynomial degree can lead to overfitting, which may introduce artificial oscillations (Runge's phenomenon), or underfitting, which might fail to capture essential dynamics of cell movements. Despite these limitations, this new tool benefits data analysis within this dissertation and serves as a resource for future research for 3D tracking studies.

Further, this dissertation provides a detailed analysis of the three-dimensional kinematics and interactions of microorganisms, specifically *C. reinhardtii*. This research overcomes the limitations of two-dimensional studies, offering a more accurate depiction of microorganism motility by precisely measuring parameters like swimming velocity, helical pitch and radius, and angular velocities. This 3D experimental data supports refining and enhancing analytical and numerical models for simulating microswimmer behaviors under different conditions.

A significant impact of this dissertation is its introduction of methods to quantify and analyze microorganism interactions in three dimensions. This study introduces metrics for analyzing cell interactions based on relative distance and incoming angle. These metrics help characterize cell behavior and set a foundation for future studies to validate or expand upon our experimental findings. The observed asymmetry in scattering behaviors and the avoidance of permanent bound states suggest that cell-cell interactions are influenced by individual cell characteristics and environmental factors, highlighting the need for further investigation into cell-cell interactions.

Additionally, applying this imaging technique to study the effects of non-Newtonian fluid dynamics on microorganism motility marks an advancement in understanding how fluid properties influence microorganism behavior. Observing how microorganisms adjust their motility in response to fluid rheology provides essential insights for biophysical and environmental sciences. This understanding is crucial for environmental monitoring and developing strategies to control and utilize microbial processes in wastewater treatment and bioremediation industries.

The discussion thus far has primarily focused on future research directions and the application of methods from this study to other areas. Another measure of impact is the societal relevance of research. This thesis addresses fundamental questions about microorganism motility and interactions and has a limited direct impact on society in the short term. However, its foundational contributions are crucial. By enhancing our understanding of microorganisms motility, this work informs future scientific efforts and aids in developing strategies to manage microbial activity in both environmental and clinical contexts. Potential applications of significant societal relevance might include optimizing bioreactor designs, improving wastewater treatment processes, or enhancing antimicrobial treatments by leveraging pathogen motility dynamics.

5.2. OUTLOOK AND FUTURE DIRECTIONS

Our study provides a foundation for understanding microorganism motility and behavior in three dimensions, but much remains to be explored. In this section, we outline potential future research directions.

5.2.1. FURTHER REFINEMENTS IN 3D TRACKING TECHNOLOGY

The 3D tracking system we developed represents a notable advancement in understanding the behaviors of microorganisms like *C. reinhardtii*. Although the current system provides valuable insights, there is still potential for further refinements and improvements to enhance its capabilities.

IMAGING OF SMALLER MICROORGANISMS

One of the primary limitations of the current 3D imaging system is its diffraction limit, which is 8 μm. When studying microorganisms smaller than this threshold, image overlap becomes a prevalent issue. Such overlaps make it challenging to determine whether microorganisms are truly in close proximity or merely appear overlapped due to the resolution constraints. Consequently, this ambiguity hinders accurate assessment of physical interactions between microorganisms, leaving many research questions regarding smaller organisms unexplored. One way to surpass this limitation is to replace the current lens in this imaging system. The system's resolution can be increased by introducing the objective lens with a focal length of 10 mm and a magnification of 2, compared to the current objective, which has a focal length of 30 mm and a magnification of 1.5. Another modification lies in adjusting the pinhole diameter to 3 mm. These modifications strike a better balance between resolution and depth of field for this setup. With these proposed modifications, the system's diffraction limit would be less than 2 μm. This would also ensure a maximum depth of field of 50 μm. The resulting system would be capable of imaging smaller microorganisms such as bacteria and spermatozoa and maintaining compatibility with 3D microscopy.

IMAGING AT HIGH DENSITIES

Successfully imaging and tracking microorganisms at high densities presents multiple challenges beyond our current system's capabilities. At such densities, microorganisms will likely have overlapping trajectories and exhibit complex multi-organism interactions. Enhancements in both tracking algorithms and imaging technology can help address these hurdles more effectively.

Improvement in Tracking:

On the computational side, while our current algorithms are adept at handling moderate densities, the complexity brought about by high densities necessitates more sophisticated methods. One such method involves using the Kalman filter [214], renowned for its efficiency in predicting and refining system states over time. This method could replace the polynomial fit during the time-resolved tracking step of our algorithm. By dynamically updating and predicting the trajectory of each microorganism, the Kalman filter can reduce errors caused by overlapping trajectories or sudden movements. Furthermore, machine learning and neural networks [215] can further refine the ability to discern individual trajectories amidst densely packed environments.

3D Fluorescence microscopy:

Highly dense particle suspension investigations are necessary to understand the collective behavior of microorganisms. However, particle tracking becomes infeasible when individual organisms cannot be differentiated separately, especially at high densities. Fluorescence microscopy [216] stands out as a promising technique to image suspensions at these densities. Fluorescence microscopy is an imaging technique that uses fluorescent dyes or genetically modified organisms to produce high-contrast images when exposed to specific wavelengths of light. By incorporating filters in front of the cameras that selectively allow light emitted by fluorescently tagged particles while blocking all other light, our 3D microscopy system can effectively reduce background noise. This selective imaging enhances the visibility of individual tagged particles within densely populated environments, making it feasible to track their dynamics and study collective behavior even at very high densities.

5.2.2. INFLUENCE OF EXTERNAL STIMULI

Understanding how microorganisms respond to external stimuli is paramount to grasping their ecological roles and physiological adaptations. Using the 3D microscopy system, microorganisms like *C. reinhardtii* under varying environmental conditions can be observed and analyzed. This system allows various flow chambers, which can be modified to study the effects of external stimuli.

LIGHT

Phototaxis, or the movement of an organism in response to light, is a well-documented behavior in many microorganisms [27, 31]. Adjusting factors like light intensity, direction, or wavelength enables us to study how these organisms navigate and adapt. These investigations can elucidate microorganisms' strategies in natural environments, such as seeking nutrient-dense areas or avoiding harmful UV radiation. The microalgae *C. reinhardtii* is known to display phototaxis under light wavelengths ranging from 420-500 nm [217]. Using our experimental setup, we conducted exploratory analyses on the phototactic response of the model microswimmer *C. reinhardtii* to two different wavelengths: 650nm (Red) and 500nm (Green) laser light.

In our experimental design, the light source's positioning ensured the incoming light rays aligned along the negative z-axis (Fig. 2.1). We analyzed our three-dimensional tracking data to determine the algae cells' orientation relative to these light rays. Specifically, the orientation angle, θ_ℓ, is calculated using $\theta_\ell = \cos^{-1}(\mathbf{T} \cdot -\mathbf{Z})$, where $\mathbf{T}$ represents the orientation vector of the cell at a different time step, and $\mathbf{Z}$ denotes the Z-axis direction.

Fig. 5.1 presents the distribution of θ_ℓ for all of the algae cells for all the time steps for both red and green wavelengths. There is a marked contrast in the microswimmer's population orientation between the red light (650 nm) and green light (500 nm). In the presence of red light, the orientation distribution peaks at $\theta_\ell = \pi/2$, suggesting the cells swim without any specific direction preference. This orientation matches the expected distribution for an isotropic system, as indicated by the solid blue lines in Fig. 5.1. Under green light exposure, however, the algae cells predominantly swim parallel or opposite to the light direction (shown by peaks around $\theta_\ell = 0$ and $\theta_\ell = \pi$) in Fig. 5.1. This exploratory analysis illustrates the impact of varying wavelengths on algae swimming. Future extensions of this study could consider cell distribution under specific light conditions.

TEMPERATURE

Temperature plays a pivotal role in influencing microbial motility [218]. By varying the ambient temperature, we can study alterations in the speed, trajectory, and overall behavior of microorganisms. Some species may exhibit heightened activity at elevated temperatures, while others might show optimal motility in cooler conditions. This research can also show how increasing global temperatures might affect ocean microbial

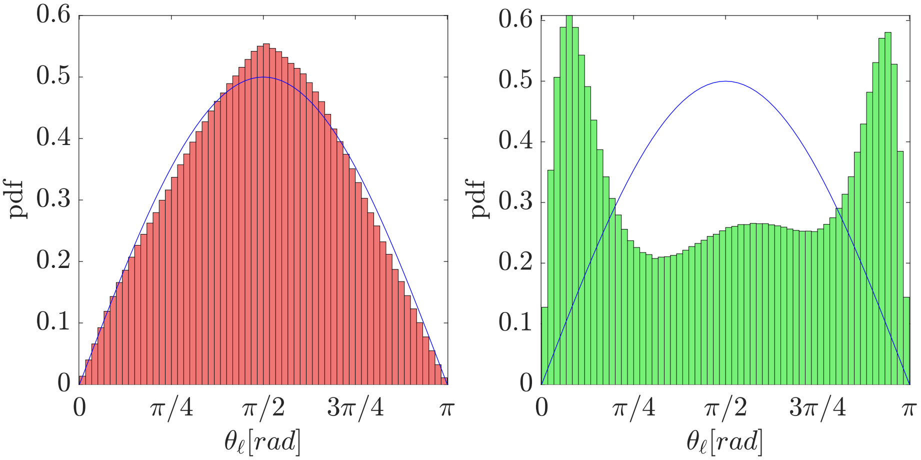

Figure 5.1: Comparison of the distributions of algae cell orientation in relation to light direction under red (left) and green (right) wavelengths. The solid blue line represents the theoretical distribution, given by $\sin(\theta)/2$, for the orientation angle of a particle moving randomly in three dimensions relative to the wall.

movements [219]. Our advanced 3D microscopy system offers a setup to study the microorganisms' thermal adaptations. In our group, we are already investigating the design of a specialized flow chamber for controlled temperature alterations to facilitate these observations. This chamber features an external bath, where the temperature is adjusted using water, and an internal reservoir for the microswimmers. One potential limitation of this setup is the possibility of uncontrolled background flows influencing microorganism motility. Nevertheless, we can model this influence and refine the flow chamber's design to minimize such disturbances.

SHEAR RATE

Microorganisms in natural habitats encounter a range of flow conditions, especially in aquatic environments. We can study how microorganisms cope with such conditions by introducing varying shear rates in our flow chamber. This will provide a deeper understanding of their behavior in natural water columns, where they navigate varying currents and turbulence. One such effort is already underway in our group where we aim to study the effect of shear rate on the three-dimensional motility of the cells by observing these cells under various shear stress conditions.

CHEMICAL GRADIENTS

Beyond the physical stimuli, chemical gradients, ranging from nutrient concentration to the presence of toxins, can influence microorganism behavior [22]. Chemotaxis, the directed motion of microorganisms along the gradient of a chemical substance, was one of the first forms of taxis investigated using 3D microscopy. Tracking microscopy was used to investigate bacterial chemotaxis [220]. Since then, this phenomenon has been explored extensively for various microorganisms and has provided important insights into biofilm formation [221, 222], quorum sensing [223], pathogenesis [224], and virulence [225]. Most of these studies concern the chemical pathways that trigger chemotactic responses. Few studies have explored the effect of chemotaxis on physiological roles [226] and its effect on population behavior [227]. Our 3D microscopy setup, when combined with custom flow chambers, can offer important insights into both physiological and population effects due to chemotaxis.

5.2.3. INVESTIGATING MICROORGANISM'S INTERACTIONS

Building on the insights obtained during our research on cell-cell interaction, several promising avenues emerge for a deeper understanding of microorganism interactions.

INCORPORATING STOCHASTICITY INTO THEORETICAL MODELS

One clear area of development lies in incorporating stochasticity into theoretical models to simulate microorganism motility to better represent biological complexities and variabilities. This could be achieved by either adding noise to swimmers' trajectories, considering the diffusive characteristics of these swimmers, or by simulating the swimmers with varying velocities, flagellar frequencies, and phases. Few efforts have been made to understand the run-and-tumble behavior of *C. reinhardtii* [228]. Integrating stochasticity into theoretical models and investigating its impact on interaction dynamics is essential for improving the models' predictive power, bridging the gap between theory and observed behaviors.

COLLECTIVE BEHAVIOR

Individual microorganism interactions, while important, represent only a small portion of what there is to understand about microbial ecosystems. These individual interactions underpin more complex, larger-scale collective behaviors such as bioconvection [117, 229], bacterial turbulence [118] and sperm aggregation [230]. Such collective behaviors influence survival strategies, where microorganisms perform coordinated action to inhibit competition [231]. Reproductive strategies, too, are intertwined with these collective behaviors. Clustering or swarming, for instance, might increase reproductive success by conserving the energy of the whole population [232].

Our advanced 3D microscopy system can be used to explore these collective dynamics experimentally. Its ability to accurately track multiple microorganisms allows for an understanding of how singular interactions scale up and shape group behaviors. For instance, how do short-range interactions compare with long-range hydrodynamic interactions in influencing group behavior? Can these long-range interactions induce large-scale patterns or steer the group in specific directions?

We have already taken the first step in answering these questions in this dissertation in chapter 3, where we explored the effect of cell-cell interaction on trajectory kinematics. The next step in this research is to investigate how these effects translate to the collective behavior of microswimmers. One difficulty we faced was isolating the effects of biological noise from interaction effects. Future efforts could focus on microswimmers with lower diffusion coefficients to minimize the impact of biological noise. We can better isolate and analyze the distinct effects of close-range and long-range interactions on collective behavior by utilizing microswimmers with lower diffusion coefficients. This could be achieved by studying these microswimmers at increasing densities and evaluating the relative effect of close and long-range interactions on their trajectory kinematics.

5.2.4. COMPLEX FLUID EXPLORATION

Our study on the motility of *C. reinhardtii* in viscoelastic fluids has pointed towards the adaptability and resilience of this microorganism in complex fluid environments. The findings offer insights into cellular behaviors and open doors to many research areas.

ROTATION SPEED AND PHOTOTAXIS

One of the important findings from our research was the adaptability of *C. reinhardtii* to modulate its rotation speed in both viscous and elastic environments. We hypothesized the existence of an active regulation mechanism for the asymmetric and out-of-plane beating component of the flagellar beat. Future studies could explore this hypothesis by measuring the out-of-plane beating component in both viscous and elastic environments, similar to the study of Cortese and Wan [113].

ELASTICITY AND ASYNCHRONOUS FLAGELLAR BEATING

The effects of fluid elasticity on the flagellar beating patterns of *C. reinhardtii* offer another rich avenue for exploration. Asynchronous beating patterns result in run and tumble behavior in *C. reinhardtii*. Future studies could focus on the following:

- How do varying degrees of elasticity influence the degree of asynchronicity in flagellar beats?
- What is the origin of this response? Is it hydrodynamic, or does the adaptability of swimming gait in viscoelastic environments result in reduced asynchrony?

REFERENCES

[1] I. Pepper, C. P. Gerba, T. Gentry, and R. M. Maier, *Environmental microbiology*. Academic press, 2011.

[2] E. Lauga and T. R. Powers, “The hydrodynamics of swimming microorganisms”, *Reports on progress in physics*, vol. 72, no. 9, p. 096 601, 2009.

[3] J. Elgeti, R. G. Winkler, and G. Gompper, “Physics of microswimmers—single particle motion and collective behavior: A review”, *Reports on progress in physics*, vol. 78, no. 5, p. 056 601, 2015.

[4] A. Jain *et al.*, “Bioenergy and bio-products from bio-waste and its associated modern circular economy: Current research trends, challenges, and future outlooks”, *Fuel*, vol. 307, p. 121 859, 2022.

[5] T. Mahmood, N. Hussain, A. Shahbaz, S. I. Mulla, H. M. Iqbal, and M. Bilal, “Sustainable production of biofuels from the algae-derived biomass”, *Bioprocess and Biosystems Engineering*, vol. 46, no. 8, pp. 1077–1097, 2023.

[6] I. S. Suh and C.-G. Lee, “Photobioreactor engineering: Design and performance”, *Biotechnology and bioprocess engineering*, vol. 8, pp. 313–321, 2003.

[7] V. Palma, M. S. Gutiérrez, O. Vargas, R. Parthasarathy, and P. Navarrete, “Methods to evaluate bacterial motility and its role in bacterial–host interactions”, *Microorganisms*, vol. 10, no. 3, p. 563, 2022.

[8] I. S. Shchelik, J. V. Molino, and K. Gademann, “Biohybrid microswimmers against bacterial infections”, *Acta Biomaterialia*, vol. 136, pp. 99–110, 2021.

[9] G. Yan, A. A. Solovev, G. Huang, J. Cui, and Y. Mei, “Soft microswimmers: Material capabilities and biomedical applications”, *Current Opinion in Colloid & Interface Science*, p. 101 609, 2022.

[10] R. M. Donlan and J. W. Costerton, “Biofilms: Survival mechanisms of clinically relevant microorganisms”, *Clinical microbiology reviews*, vol. 15, no. 2, pp. 167–193, 2002.

[11] E. Ralston and G. Swain, “Bioinspiration—the solution for biofouling control?”, *Bioinspiration & biomimetics*, vol. 4, no. 1, p. 015 007, 2009.

[12] R. Jacoby, M. Peukert, A. Succurro, A. Koprivova, and S. Kopriva, “The role of soil microorganisms in plant mineral nutrition—current knowledge and future directions”, *Frontiers in plant science*, vol. 8, p. 1617, 2017.

[13] E. L. Madsen, “Microorganisms and their roles in fundamental biogeochemical cycles”, *Current opinion in biotechnology*, vol. 22, no. 3, pp. 456–464, 2011.

[14] C. Evans *et al.*, “Potential climate change impacts on microbial distribution and carbon cycling in the australian southern ocean”, *Deep Sea Research Part II: Topical Studies in Oceanography*, vol. 58, no. 21-22, pp. 2150–2161, 2011.

[15] E. M. Purcell, “Life at low reynolds number”, *American journal of physics*, vol. 45, no. 1, pp. 3–11, 1977.

[16] S. Childress, *Mechanics of swimming and flying*, 2. Cambridge University Press, 1981.

[17] C. P. Ellington, “The aerodynamics of hovering insect flight. i. the quasi-steady analysis”, *Philosophical Transactions of the Royal Society of London. B, Biological Sciences*, vol. 305, no. 1122, pp. 1–15, 1984.

[18] E. Lauga, “Bacterial hydrodynamics”, *Annual Review of Fluid Mechanics*, vol. 48, pp. 105–130, 2016.

[19] T. Vladić and E. Petersson, “Artificially selected human sperm morphology after swim-up processing”, *Canadian journal of zoology*, vol. 90, no. 10, pp. 1207–1214, 2012.

[20] G. J. Amador, D. Wei, D. Tam, and M.-E. Aubin-Tam, “Fibrous flagellar hairs of chlamydomonas reinhardtii do not enhance swimming”, *Biophysical journal*, vol. 118, no. 12, pp. 2914–2925, 2020.

[21] C. Brennen and H. Winet, “Fluid mechanics of propulsion by cilia and flagella”, *Annual Review of Fluid Mechanics*, vol. 9, no. 1, pp. 339–398, 1977.

[22] H. C. Berg, *E. coli in Motion*. Springer New York, NY, 2004.

[23] L. Turner, W. S. Ryu, and H. C. Berg, “Real-time imaging of fluorescent flagellar filaments”, *Journal of bacteriology*, vol. 182, no. 10, pp. 2793–2801, 2000.

[24] U. Rüffer and W. Nultsch, “High-speed cinematographic analysis of the movement of chlamydomonas”, *Cell motility*, vol. 5, no. 3, pp. 251–263, 1985.

[25] T. Fenchel, “How dinoflagellates swim”, *Protist*, vol. 152, no. 4, pp. 329–338, 2001.

[26] L. Alvarez, B. M. Friedrich, G. Gompper, and U. B. Kaupp, “The computational sperm cell”, *Trends in cell biology*, vol. 24, no. 3, pp. 198–207, 2014.

[27] K. W. Foster *et al.*, “A rhodopsin is the functional photoreceptor for phototaxis in the unicellular eukaryote chlamydomonas”, *Nature*, vol. 311, no. 5988, pp. 756–759, 1984.

[28] K. Schaller, R. David, and R. Uhl, “How chlamydomonas keeps track of the light once it has reached the right phototactic orientation”, *Biophysical journal*, vol. 73, no. 3, pp. 1562–1572, 1997.

[29] H. Machemer and R. Braucker, “Gravireception and graviresponses in ciliates.”, *Acta protozoologica*, vol. 31, no. 4, pp. 185–214, 1992.

[30] A. Bren and M. Eisenbach, “How signals are heard during bacterial chemotaxis: Protein-protein interactions in sensory signal propagation”, *Journal of bacteriology*, vol. 182, no. 24, pp. 6865–6873, 2000.

[31] K. W. Foster and R. D. Smyth, “Light antennas in phototactic algae”, *Microbiological reviews*, vol. 44, no. 4, pp. 572–630, 1980.

[32] D. Saintillan and M. J. Shelley, “Emergence of coherent structures and large-scale flows in motile suspensions”, *Journal of the Royal Society Interface*, vol. 9, no. 68, pp. 571–585, 2012.

[33] T. Vicsek and A. Zafeiris, “Collective motion”, *Physics reports*, vol. 517, no. 3-4, pp. 71–140, 2012.

[34] W. Yin, Y. Wang, L. Liu, and J. He, “Biofilms: The microbial “protective clothing” in extreme environments”, *International journal of molecular sciences*, vol. 20, no. 14, p. 3423, 2019.

[35] L. H. Cisneros, J. O. Kessler, S. Ganguly, and R. E. Goldstein, “Dynamics of swimming bacteria: Transition to directional order at high concentration”, *Physical Review E*, vol. 83, no. 6, p. 061 907, 2011.

[36] H. H. Wensink *et al.*, “Meso-scale turbulence in living fluids”, *Proceedings of the national academy of sciences*, vol. 109, no. 36, pp. 14 308–14 313, 2012.

[37] L. Rothschild, “The activity of ram spermatozoa”, *Journal of Experimental Biology*, vol. 25, no. 3, pp. 219–226, 1948.

[38] A. Creppy, O. Praud, X. Druart, P. L. Kohnke, and F. Plouraboué, “Turbulence of swarming sperm”, *Physical Review E*, vol. 92, no. 3, p. 032 722, 2015.

[39] S. F. Schoeller, W. V. Holt, and E. E. Keaveny, “Collective dynamics of sperm cells”, *Philosophical Transactions of the Royal Society B*, vol. 375, no. 1807, p. 20 190 384, 2020.

[40] E. Lauga, “Propulsion in a viscoelastic fluid”, *Physics of Fluids*, vol. 19, no. 8, p. 083 104, 2007.

[41] ——, “Life at high deborah number”, *EPL (Europhysics Letters)*, vol. 86, no. 6, p. 64 001, 2009.

[42] D. Katz, R. Mills, and T. Pritchett, “The movement of human spermatozoa in cervical mucus”, *Reproduction*, vol. 53, no. 2, pp. 259–265, 1978.

[43] V. A. Martinez, J. Schwarz-Linek, M. Reufer, L. G. Wilson, A. N. Morozov, and W. C. Poon, “Flagellated bacterial motility in polymer solutions”, *Proceedings of the National Academy of Sciences*, vol. 111, no. 50, pp. 17 771–17 776, 2014.

[44] A. Patteson, A. Gopinath, M. Goulian, and P. Arratia, “Running and tumbling with e. coli in polymeric solutions”, *Scientific reports*, vol. 5, no. 1, pp. 1–11, 2015.

[45] B. Qin, A. Gopinath, J. Yang, J. P. Gollub, and P. E. Arratia, “Flagellar kinematics and swimming of algal cells in viscoelastic fluids”, *Scientific reports*, vol. 5, no. 1, pp. 1–7, 2015.

[46] C.-k. Tung *et al.*, “Fluid viscoelasticity promotes collective swimming of sperm”, *Scientific reports*, vol. 7, no. 1, pp. 1–9, 2017.

[47] S. Liu, S. Shankar, M. C. Marchetti, and Y. Wu, “Viscoelastic control of spatiotemporal order in bacterial active matter”, *Nature*, vol. 590, no. 7844, pp. 80–84, 2021.

[48] W. Liao and I. S. Aranson, “Viscoelasticity enhances collective motion of bacteria”, *PNAS nexus*, vol. 2, no. 9, pgad291, 2023.

[49] S. E. Spagnolie and P. T. Underhill, “Swimming in complex fluids”, *Annual Review of Condensed Matter Physics*, vol. 14, pp. 381–415, 2023.

[50] H. C. Berg, “How to track bacteria”, *Review of Scientific Instruments*, vol. 42, no. 6, pp. 868–871, 1971.

[51] M. Wu, J. W. Roberts, and M. Buckley, “Three-dimensional fluorescent particle tracking at micron-scale using a single camera”, *Experiments in Fluids*, vol. 38, no. 4, pp. 461–465, 2005.

[52] M. Wu, J. W. Roberts, S. Kim, D. L. Koch, and M. P. DeLisa, “Collective bacterial dynamics revealed using a three-dimensional population-scale defocused particle tracking technique”, *Applied and environmental microbiology*, vol. 72, no. 7, pp. 4987–4994, 2006.

[53] S. Coëtmellec, C. Buraga-Lefebvre, D. Lebrun, and C. Özkul, “Application of in-line digital holography to multiple plane velocimetry”, *Measurement Science and Technology*, vol. 12, no. 9, p. 1392, 2001.

[54] J. Sheng, E. Malkiel, J. Katz, J. Adolf, R. Belas, and A. R. Place, “Digital holographic microscopy reveals prey-induced changes in swimming behavior of predatory dinoflagellates”, *Proceedings of the National Academy of Sciences*, vol. 104, no. 44, pp. 17 512–17 517, 2007.

[55] J. Gao, D. R. Guildenbecher, P. L. Reu, and J. Chen, “Uncertainty characterization of particle depth measurement using digital in-line holography and the hybrid method”, *Optics express*, vol. 21, no. 22, pp. 26 432–26 449, 2013.

[56] M. Molaei and J. Sheng, “Imaging bacterial 3d motion using digital in-line holographic microscopy and correlation-based de-noising algorithm”, *Optics express*, vol. 22, no. 26, pp. 32 119–32 137, 2014.

[57] C. Cierpka and C. J. Kähler, “Particle imaging techniques for volumetric three-component (3d3c) velocity measurements in microfluidics”, *Journal of visualization*, vol. 15, no. 1, pp. 1–31, 2012.

[58] E. Lauga and R. E. Goldstein, “Dance of the microswimmers”, *Physics Today*, vol. 65, no. 9, pp. 30–35, 2012.

[59] T. Ishikawa and T. Pedley, “50-year history and perspective on biomechanics of swimming microorganisms: Part ii. collective behaviours”, *Journal of Biomechanics*, p. 111 706, 2023.

[60] D. L. Koch and G. Subramanian, “Collective hydrodynamics of swimming microorganisms: Living fluids”, *Annual Review of Fluid Mechanics*, vol. 43, pp. 637–659, 2011.

[61] K. Drescher, J. Dunkel, L. H. Cisneros, S. Ganguly, and R. E. Goldstein, “Fluid dynamics and noise in bacterial cell–cell and cell–surface scattering”, *Proceedings of the National Academy of Sciences*, vol. 108, no. 27, pp. 10 940–10 945, 2011.

[62] E. Lauga and R. E. Goldstein, “Microswimmers”, *Phys. Today*, vol. 65, no. 9, p. 30, 2012.

[63] N. Hill and R. Vincent, “A simple model and strategies for orientation in phototactic microorganisms”, *Journal of theoretical biology*, vol. 163, no. 2, pp. 223–235, 1993.

[64] K. Yoshimura, Y. Matsuo, and R. Kamiya, “Gravitaxis in chlamydomonas reinhardtii studied with novel mutants”, *Plant and cell physiology*, vol. 44, no. 10, pp. 1112–1118, 2003.

[65] U. Alon, M. G. Surette, N. Barkai, and S. Leibler, “Robustness in bacterial chemotaxis”, *Nature*, vol. 397, no. 6715, pp. 168–171, 1999.

[66] M. Eisenbach, “Sperm chemotaxis”, *Reviews of reproduction*, vol. 4, no. 1, pp. 56–66, 1999.

[67] G. Harkes, J. Dankert, and J. Feijen, “Bacterial migration along solid surfaces”, *Applied and environmental microbiology*, vol. 58, no. 5, pp. 1500–1505, 1992.

[68] C. Bechinger, R. Di Leonardo, H. Löwen, C. Reichhardt, G. Volpe, and G. Volpe, “Active particles in complex and crowded environments”, *Reviews of Modern Physics*, vol. 88, no. 4, p. 045 006, 2016.

[69] M. H. Huesemann, J. Van Wagenen, T. Miller, A. Chavis, S. Hobbs, and B. Crowe, “A screening model to predict microalgae biomass growth in photobioreactors and raceway ponds”, *Biotechnology and bioengineering*, vol. 110, no. 6, pp. 1583–1594, 2013.

[70] L. Pottier, J. Pruvost, J. Deremetz, J.-F. Cornet, J. Legrand, and C. Dussap, “A fully predictive model for one-dimensional light attenuation by chlamydomonas reinhardtii in a torus photobioreactor”, *Biotechnology and bioengineering*, vol. 91, no. 5, pp. 569–582, 2005.

[71] M. A. Constantino, M. Jabbarzadeh, H. C. Fu, and R. Bansil, “Helical and rod-shaped bacteria swim in helical trajectories with little additional propulsion from helical shape”, *Science Advances*, vol. 2, no. 11, e1601661, 2016.

[72] H. C. Crenshaw, C. N. Ciampaglio, and M. McHenry, “Analysis of the three-dimensional trajectories of organisms: Estimates of velocity, curvature and torsion from positional information”, *Journal of Experimental Biology*, vol. 203, no. 6, pp. 961–982, 2000.

[73] Rothschild, “Non-random distribution of bull spermatozoa in a drop of sperm suspension”, *Nature*, vol. 198, no. 488, p. 1221, 1963.

[74] M. E. H. FEINLEIB and G. M. CURRY, “The relationship between stimulus intensity and oriented phototactic response (topotaxis) in chlamydomonas”, *Physiologia Plantarum*, vol. 25, no. 3, pp. 346–352, 1971.

[75] K. C. Leptos, J. S. Guasto, J. P. Gollub, A. I. Pesci, and R. E. Goldstein, “Dynamics of enhanced tracer diffusion in suspensions of swimming eukaryotic microorganisms”, *Physical Review Letters*, vol. 103, no. 19, p. 198 103, 2009.

[76] V. Kantsler, J. Dunkel, M. Polin, and R. E. Goldstein, “Ciliary contact interactions dominate surface scattering of swimming eukaryotes”, *Proceedings of the National Academy of Sciences*, vol. 110, no. 4, pp. 1187–1192, 2013.

[77] T. Nakai, Y. Mouri, and T. Goto, “Analysis of the velocity correlation in the collective motion of bacteria”, *Journal of Aero Aqua Bio-mechanisms*, vol. 4, no. 1, pp. 32–36, 2015.

[78] M. T. Barry, R. Rusconi, J. S. Guasto, and R. Stocker, “Shear-induced orientational dynamics and spatial heterogeneity in suspensions of motile phytoplankton”, *Journal of The Royal Society Interface*, vol. 12, no. 112, p. 20 150 791, 2015.

[79] D. Jin, J. Kotar, E. Silvester, K. C. Leptos, and O. A. Croze, “Diurnal variations in the motility of populations of biflagellate microalgae”, *Biophysical journal*, vol. 119, no. 10, pp. 2055–2062, 2020.

[80] F. Liu, Y. Wu, and L. Zeng, “Swimming characteristics of chlamydomonas reinhardtii”, *Journal of Coastal Research*, vol. 104, no. SI, pp. 455–464, 2020.

[81] S. Coppola and V. Kantsler, “Green algae scatter off sharp viscosity gradients”, *Scientific reports*, vol. 11, no. 1, pp. 1–7, 2021.

[82] K. Taute, S. Gude, S. Tans, and T. Shimizu, “High-throughput 3d tracking of bacteria on a standard phase contrast microscope”, *Nature communications*, vol. 6, no. 1, pp. 1–9, 2015.

[83] A. J. Mathijssen, N. Figueroa-Morales, G. Junot, É. Clément, A. Lindner, and A. Zöttl, “Oscillatory surface rheotaxis of swimming e. coli bacteria”, *Nature communications*, vol. 10, no. 1, p. 3434, 2019.

[84] B. Liu, M. Gulino, M. Morse, J. X. Tang, T. R. Powers, and K. S. Breuer, “Helical motion of the cell body enhances caulobacter crescentus motility”, *Proceedings of the National Academy of Sciences*, vol. 111, no. 31, pp. 11 252–11 256, 2014.

[85] N. Giuliani, M. Rossi, G. Noselli, and A. DeSimone, “How euglena gracilis swims: Flow field reconstruction and analysis”, *Physical Review E*, vol. 103, no. 2, p. 023 102, 2021.

[86] T.-W. Su, L. Xue, and A. Ozcan, “High-throughput lensfree 3d tracking of human sperms reveals rare statistics of helical trajectories”, *Proceedings of the National Academy of Sciences*, vol. 109, no. 40, pp. 16 018–16 022, 2012.

[87] S. J. Lee, T. Go, and H. Byeon, “Three-dimensional swimming motility of microorganism in the near-wall region”, *Experiments in Fluids*, vol. 57, no. 2, pp. 1–10, 2016.

[88] F. C. Cheong *et al.*, “Rapid, high-throughput tracking of bacterial motility in 3d via phase-contrast holographic video microscopy”, *Biophysical journal*, vol. 108, no. 5, pp. 1248–1256, 2015.

[89] S. Bianchi, F. Saglimbeni, and R. Di Leonardo, “Holographic imaging reveals the mechanism of wall entrapment in swimming bacteria”, *Physical Review X*, vol. 7, no. 1, p. 011 010, 2017.

[90] S. A. Baba, S. Inomata, M. Ooya, Y. Mogami, and A. Izumi-Kurotani, “Three-dimensional recording and measurement of swimming paths of micro-organisms with two synchronized monochrome cameras”, *Review of scientific instruments*, vol. 62, no. 2, pp. 540–541, 1991.

[91] H. C. Crenshaw, “A new look at locomotion in microorganisms: Rotating and translating”, *American Zoologist*, vol. 36, no. 6, pp. 608–618, 1996.

[92] M. Polin, I. Tuval, K. Drescher, J. P. Gollub, and R. E. Goldstein, “Chlamydomonas swims with two “gears” in a eukaryotic version of run-and-tumble locomotion”, *Science*, vol. 325, no. 5939, pp. 487–490, 2009.

[93] K. Drescher, K. C. Leptos, and R. E. Goldstein, “How to track protists in three dimensions”, *Review of scientific instruments*, vol. 80, no. 1, p. 014 301, 2009.

[94] R. Thar, N. Blackburn, and M. Kühl, “A new system for three-dimensional tracking of motile microorganisms”, *Applied and Environmental Microbiology*, vol. 66, no. 5, pp. 2238–2242, 2000.

[95] M. Speidel, A. Jonáš, and E.-L. Florin, “Three-dimensional tracking of fluorescent nanoparticles with subnanometer precision by use of off-focus imaging”, *Optics letters*, vol. 28, no. 2, pp. 69–71, 2003.

[96] J. Sheng, E. Malkiel, and J. Katz, “Digital holographic microscope for measuring three-dimensional particle distributions and motions”, *Applied optics*, vol. 45, no. 16, pp. 3893–3901, 2006.

[97] G. E. Elsinga, F. Scarano, B. Wieneke, and B. W. van Oudheusden, “Tomographic particle image velocimetry”, *Experiments in fluids*, vol. 41, no. 6, pp. 933–947, 2006.

[98] A.-J. Buchner, K. Muller, J. Mehmood, and D. Tam, “Hopping trajectories due to long-range interactions determine surface accumulation of microalgae”, *Proceedings of the National Academy of Sciences*, vol. 118, no. 20, 2021.

[99] H. Kim, S. Große, G. E. Elsinga, and J. Westerweel, “Full 3d-3c velocity measurement inside a liquid immersion droplet”, *Experiments in fluids*, vol. 51, no. 2, pp. 395–405, 2011.

[100] H. Kim, J. Westerweel, and G. E. Elsinga, “Comparison of tomo-piv and 3d-ptv for microfluidic flows”, *Measurement Science and Technology*, vol. 24, no. 2, p. 024 007, 2012.

[101] R. Hartley and A. Zisserman, *Multiple view geometry in computer vision*. Cambridge university press, 2003.

[102] K. Muller, C. Hemelrijk, J. Westerweel, and D. Tam, “Calibration of multiple cameras for large-scale experiments using a freely moving calibration target”, *Experiments in Fluids*, vol. 61, no. 1, pp. 1–12, 2020.

[103] G. Quaranta, M.-E. Aubin-Tam, and D. Tam, “Hydrodynamics versus intracellular coupling in the synchronization of eukaryotic flagella”, *Physical review letters*, vol. 115, no. 23, p. 238 101, 2015.

[104] D. R. Mitchell, “Chlamydomonas flagella”, *Journal of Phycology*, vol. 36, no. 2, pp. 261–273, 2000.

[105] E. H. Harris, *The Chlamydomonas Sourcebook: Introduction to Chlamydomonas and Its Laboratory Use: Volume 1*. Academic press, 2009, vol. 1.

[106] K. Muller, “Tracking schooling fish in three dimensions: Experiments at the rotterdam zoo”, Ph.D. dissertation, Delft University of Technology, Gildeprint, Sep. 2023.

[107] P. Meer and I. Weiss, “Smoothed differentiation filters for images”, *Journal of Visual Communication and Image Representation*, vol. 3, no. 1, pp. 58–72, 1992.

[108] A. Attanasi *et al.*, “Greta-a novel global and recursive tracking algorithm in three dimensions”, *IEEE transactions on pattern analysis and machine intelligence*, vol. 37, no. 12, pp. 2451–2463, 2015.

[109] L. Adrian, R. J. Adrian, and J. Westerweel, *Particle image velocimetry*, 30. Cambridge university press, 2011.

[110] D. Schanz, S. Gesemann, and A. Schröder, “Shake-the-box: Lagrangian particle tracking at high particle image densities”, *Experiments in fluids*, vol. 57, no. 5, pp. 1–27, 2016.

[111] S. Kim and S. J. Lee, “Effect of particle number density in in-line digital holographic particle velocimetry”, *Experiments in fluids*, vol. 44, pp. 623–631, 2008.

[112] B. O’neill, *Elementary differential geometry*. Elsevier, 2006.

[113] D. Cortese and K. Y. Wan, “Control of helical navigation by three-dimensional flagellar beating”, *Physical Review Letters*, vol. 126, no. 8, p. 088 003, 2021.

[114] H. Kurtuldu, D. Tam, A. Hosoi, K. A. Johnson, and J. Gollub, “Flagellar waveform dynamics of freely swimming algal cells”, *Physical Review E*, vol. 88, no. 1, p. 013 015, 2013.

[115] A. Persat, H. A. Stone, and Z. Gitai, “The curved shape of caulobacter crescentus enhances surface colonization in flow”, *Nature Communications*, vol. 5, no. 1, p. 3824, 2014.

[116] L. A. Pratt and R. Kolter, “Genetic analysis of escherichia coli biofilm formation: Roles of flagella, motility, chemotaxis and type i pili”, *Molecular microbiology*, vol. 30, no. 2, pp. 285–293, 1998.

[117] M. Bees and N. Hill, “Wavelengths of bioconvection patterns”, *The Journal of Experimental Biology*, vol. 200, no. 10, pp. 1515–1526, 1997.

[118] J. Dunkel, S. Heidenreich, K. Drescher, H. H. Wensink, M. Bär, and R. E. Goldstein, “Fluid dynamics of bacterial turbulence”, *Physical review letters*, vol. 110, no. 22, p. 228 102, 2013.

[119] T. Ishikawa, M. Simmonds, and T. J. Pedley, “Hydrodynamic interaction of two swimming model micro-organisms”, *Journal of Fluid Mechanics*, vol. 568, pp. 119–160, 2006.

[120] T. Ishikawa, G. Sekiya, Y. Imai, and T. Yamaguchi, “Hydrodynamic interactions between two swimming bacteria”, *Biophysical journal*, vol. 93, no. 6, pp. 2217–2225, 2007.

[121] S. Ziegler, T. Scheel, M. Hubert, J. Harting, and A.-S. Smith, “Theoretical framework for pairwise microswimmer interactions”, *arXiv preprint arXiv:2102.05387*, 2021.

[122] C. Darveniza, T. Ishikawa, T. Pedley, and D. Brumley, “Pairwise scattering and bound states of spherical microorganisms”, *Physical Review Fluids*, vol. 7, no. 1, p. 013 104, 2022.

[123] I. O. Götze and G. Gompper, “Mesoscale simulations of hydrodynamic squirmer interactions”, *Physical Review E*, vol. 82, no. 4, p. 041 921, 2010.

[124] F. J. Schwarzendahl and M. G. Mazza, “Hydrodynamic interactions dominate the structure of active swimmers’ pair distribution functions”, *The Journal of Chemical Physics*, vol. 150, no. 18, p. 184 902, 2019.

[125] S. Belan and M. Kardar, “Pair dispersion in dilute suspension of active swimmers”, *The Journal of Chemical Physics*, vol. 150, no. 6, p. 064 907, 2019.

[126] C. Pooley, G. Alexander, and J. Yeomans, “Hydrodynamic interaction between two swimmers at low reynolds number”, *Physical review letters*, vol. 99, no. 22, p. 228 103, 2007.

[127] S. Chattopadhyay and X.-L. Wu, “The effect of long-range hydrodynamic interaction on the swimming of a single bacterium”, *Biophysical Journal*, vol. 96, no. 5, pp. 2023–2028, 2009.

[128] B. J. Walker, K. Ishimoto, and E. A. Gaffney, “Pairwise hydrodynamic interactions of synchronized spermatozoa”, *Physical Review Fluids*, vol. 4, no. 9, p. 093 101, 2019.

[129] R. Matas Navarro and I. Pagonabarraga, “Hydrodynamic interaction between two trapped swimming model micro-organisms”, *The European Physical Journal E*, vol. 33, no. 1, pp. 27–39, 2010.

[130] D. Giacché and T. Ishikawa, “Hydrodynamic interaction of two unsteady model microorganisms”, *Journal of theoretical biology*, vol. 267, no. 2, pp. 252–263, 2010.

[131] J. J. Molina, Y. Nakayama, and R. Yamamoto, “Hydrodynamic interactions of self-propelled swimmers”, *Soft Matter*, vol. 9, no. 19, pp. 4923–4936, 2013.

[132] M. Potomkin, V. Gyrya, I. Aranson, and L. Berlyand, “Collision of microswimmers in a viscous fluid”, *Physical Review E*, vol. 87, no. 5, p. 053 005, 2013.

[133] D. Papavassiliou and G. P. Alexander, “Exact solutions for hydrodynamic interactions of two squirming spheres”, *Journal of Fluid Mechanics*, vol. 813, pp. 618–646, 2017.

[134] M. Theers, E. Westphal, K. Qi, R. G. Winkler, and G. Gompper, “Clustering of microswimmers: Interplay of shape and hydrodynamics”, *Soft matter*, vol. 14, no. 42, pp. 8590–8603, 2018.

[135] J. R. Blake, "A spherical envelope approach to ciliary propulsion", *Journal of Fluid Mechanics*, vol. 46, no. 1, pp. 199–208, 1971.

[136] A. Najafi and R. Golestanian, "Simple swimmer at low reynolds number: Three linked spheres", *Physical Review E*, vol. 69, no. 6, p. 062 901, 2004.

[137] J. S. Guasto, K. A. Johnson, and J. P. Gollub, "Oscillatory flows induced by microorganisms swimming in two dimensions", *Physical review letters*, vol. 105, no. 16, p. 168 102, 2010.

[138] D. Wei, P. G. Dehnavi, M.-E. Aubin-Tam, and D. Tam, "Measurements of the unsteady flow field around beating cilia", *Journal of Fluid Mechanics*, vol. 915, 2021.

[139] Q. Liao, G. Subramanian, M. P. DeLisa, D. L. Koch, and M. Wu, "Pair velocity correlations among swimming escherichia coli bacteria are determined by force-quadrupole hydrodynamic interactions", *Physics of Fluids*, vol. 19, no. 6, p. 061 701, 2007.

[140] T. Ishikawa and M. Hota, "Interaction of two swimming paramecia", *Journal of Experimental Biology*, vol. 209, no. 22, pp. 4452–4463, 2006.

[141] P. T. Underhill and M. D. Graham, "Correlations and fluctuations of stress and velocity in suspensions of swimming microorganisms", *Physics of Fluids*, vol. 23, no. 12, p. 121 902, 2011.

[142] R. C. Veltkamp and W. Wesselink, "Modeling 3d curves of minimal energy", in *Computer Graphics Forum*, Wiley Online Library, vol. 14, 1995, pp. 97–110.

[143] E. Lushi, V. Kantsler, and R. E. Goldstein, "Scattering of biflagellate microswimmers from surfaces", *Physical Review E*, vol. 96, no. 2, p. 023 102, 2017.

[144] J. P. Hernandez-Ortiz, C. G. Stoltz, and M. D. Graham, "Transport and collective dynamics in suspensions of confined swimming particles", *Physical review letters*, vol. 95, no. 20, p. 204 501, 2005.

[145] J. P. Hernandez-Ortiz, P. T. Underhill, and M. D. Graham, "Dynamics of confined suspensions of swimming particles", *Journal of Physics: Condensed Matter*, vol. 21, no. 20, p. 204 107, 2009.

[146] M. S. Rizvi, A. Farutin, and C. Misbah, "Size and shape affect swimming of a triangular bead-spring microswimmer", *Physical Review E*, vol. 98, no. 4, p. 043 104, 2018.

[147] K. Drescher, R. E. Goldstein, N. Michel, M. Polin, and I. Tuval, "Direct measurement of the flow field around swimming microorganisms", *Physical Review Letters*, vol. 105, no. 16, p. 168 101, 2010.

[148] C. Villani *et al.*, *Optimal transport: old and new*. Springer, 2009, vol. 338.

[149] J. Lam, R. Chan, K. Lam, and J. Costerton, "Production of mucoid microcolonies by pseudomonas aeruginosa within infected lungs in cystic fibrosis", *Infection and immunity*, vol. 28, no. 2, pp. 546–556, 1980.

[150] R. L. Vogt and L. Dippold, “Escherichia coli o157: H7 outbreak associated with consumption of ground beef, june–july 2002”, *Public health reports*, vol. 120, no. 2, pp. 174–178, 2005.

[151] G. O’Toole, H. B. Kaplan, and R. Kolter, “Biofilm formation as microbial development”, *Annual Reviews in Microbiology*, vol. 54, no. 1, pp. 49–79, 2000.

[152] D. Katz, T. Bloom, and R. Bondurant, “Movement of bull spermatozoa in cervical mucus”, *Biology of reproduction*, vol. 25, no. 5, pp. 931–937, 1981.

[153] T. Hyakutake, H. Suzuki, and S. Yamamoto, “Effect of non-newtonian fluid properties on bovine sperm motility”, *Journal of biomechanics*, vol. 48, no. 12, pp. 2941–2947, 2015.

[154] K. Yahata *et al.*, “Gliding motility of plasmodium merozoites”, *Proceedings of the National Academy of Sciences*, vol. 118, no. 48, e2114442118, 2021.

[155] E. Errill, “Rheology of blood”, *Physiological reviews*, vol. 49, no. 4, pp. 863–888, 1969.

[156] S. Hwang, M. Litt, and W. Forsman, “Rheological properties of mucus”, *Rheologica Acta*, vol. 8, no. 4, pp. 438–448, 1969.

[157] J. N. Wilking, T. E. Angelini, A. Seminara, M. P. Brenner, and D. A. Weitz, “Biofilms as complex fluids”, *MRS bulletin*, vol. 36, no. 5, pp. 385–391, 2011.

[158] M. R. Raveshi, M. S. Abdul Halim, S. N. Agnihotri, M. K. O’Bryan, A. Neild, and R. Nosrati, “Curvature in the reproductive tract alters sperm–surface interactions”, *Nature communications*, vol. 12, no. 1, pp. 1–10, 2021.

[159] T. Qiu *et al.*, “Swimming by reciprocal motion at low reynolds number”, *Nature communications*, vol. 5, no. 1, p. 5119, 2014.

[160] E. Lauga, *The fluid dynamics of cell motility*. Cambridge University Press, 2020, vol. 62.

[161] T. Chaudhury, “On swimming in a visco-elastic liquid”, *Journal of Fluid Mechanics*, vol. 95, no. 1, pp. 189–197, 1979.

[162] G. R. Fulford, D. F. Katz, and R. L. Powell, “Swimming of spermatozoa in a linear viscoelastic fluid”, *Biorheology*, vol. 35, no. 4-5, pp. 295–309, 1998.

[163] H. C. Fu, T. R. Powers, and C. W. Wolgemuth, “Theory of swimming filaments in viscoelastic media”, *Physical review letters*, vol. 99, no. 25, p. 258 101, 2007.

[164] H. C. Fu, C. W. Wolgemuth, and T. R. Powers, “Swimming speeds of filaments in nonlinearly viscoelastic fluids”, *Physics of Fluids*, vol. 21, no. 3, p. 033 102, 2009.

[165] N. Balmforth, D. Coombs, and S. Pachmann, “Microelastohydrodynamics of swimming organisms near solid boundaries in complex fluids”, *Quarterly journal of mechanics and applied mathematics*, vol. 63, no. 3, pp. 267–294, 2010.

[166] O. S. Pak, L. Zhu, L. Brandt, and E. Lauga, “Micropropulsion and microrheology in complex fluids via symmetry breaking”, *Physics of fluids*, vol. 24, no. 10, p. 103 102, 2012.

[167] J. C. Chrispell, L. J. Fauci, and M. Shelley, “An actuated elastic sheet interacting with passive and active structures in a viscoelastic fluid”, *Physics of Fluids*, vol. 25, no. 1, e1002167, 2013.

[168] J. R. Vélez-Cordero and E. Lauga, “Waving transport and propulsion in a generalized newtonian fluid”, *Journal of Non-Newtonian Fluid Mechanics*, vol. 199, pp. 37–50, 2013.

[169] M. P. Curtis and E. A. Gaffney, “Three-sphere swimmer in a nonlinear viscoelastic medium”, *Physical Review E*, vol. 87, no. 4, p. 043 006, 2013.

[170] E. Lauga, “Locomotion in complex fluids: Integral theorems”, *Physics of Fluids*, vol. 26, no. 8, p. 081 902, 2014.

[171] M. De Corato, F. Greco, and P. Maffettone, “Locomotion of a microorganism in weakly viscoelastic liquids”, *Physical Review E*, vol. 92, no. 5, p. 053 008, 2015.

[172] S. Yazdi, A. M. Ardekani, and A. Borhan, “Locomotion of microorganisms near a no-slip boundary in a viscoelastic fluid”, *Physical review E*, vol. 90, no. 4, p. 043 002, 2014.

[173] S. Yazdi, A. M. Ardekani, and A. Borhan, “Swimming dynamics near a wall in a weakly elastic fluid”, *Journal of Nonlinear Science*, vol. 25, no. 5, pp. 1153–1167, 2015.

[174] G. J. Elfring and G. Goyal, “The effect of gait on swimming in viscoelastic fluids”, *Journal of Non-Newtonian Fluid Mechanics*, vol. 234, pp. 8–14, 2016.

[175] S. Yazdi and A. Borhan, “Effect of a planar interface on time-averaged locomotion of a spherical squirmer in a viscoelastic fluid”, *Physics of Fluids*, vol. 29, no. 9, p. 093 104, 2017.

[176] T. R. Ives and A. Morozov, “The mechanism of propulsion of a model microswimmer in a viscoelastic fluid next to a solid boundary”, *Physics of Fluids*, vol. 29, no. 12, p. 121 612, 2017.

[177] J. Teran, L. Fauci, and M. Shelley, “Viscoelastic fluid response can increase the speed and efficiency of a free swimmer”, *Physical review letters*, vol. 104, no. 3, p. 038 101, 2010.

[178] N. C. Keim, M. Garcia, and P. E. Arratia, “Fluid elasticity can enable propulsion at low reynolds number”, *Physics of Fluids*, vol. 24, no. 8, p. 081 703, 2012.

[179] L. Zhu, E. Lauga, and L. Brandt, “Self-propulsion in viscoelastic fluids: Pushers vs. pullers”, *Physics of fluids*, vol. 24, no. 5, p. 051 902, 2012.

[180] S. E. Spagnolie, B. Liu, and T. R. Powers, “Locomotion of helical bodies in viscoelastic fluids: Enhanced swimming at large helical amplitudes”, *Physical review letters*, vol. 111, no. 6, p. 068 101, 2013.

[181] T. D. Montenegro-Johnson, D. J. Smith, and D. Loghin, “Physics of rheologically enhanced propulsion: Different strokes in generalized stokes”, *Physics of Fluids*, vol. 25, no. 8, p. 081 903, 2013.

[182] G.-J. Li, A. Karimi, and A. M. Ardekani, “Effect of solid boundaries on swimming dynamics of microorganisms in a viscoelastic fluid”, *Rheologica acta*, vol. 53, no. 12, pp. 911–926, 2014.

[183] B. Thomases and R. D. Guy, “Mechanisms of elastic enhancement and hindrance for finite-length undulatory swimmers in viscoelastic fluids”, *Physical review letters*, vol. 113, no. 9, p. 098 102, 2014.

[184] K. Ishimoto and E. A. Gaffney, “Boundary element methods for particles and microswimmers in a linear viscoelastic fluid”, *Journal of Fluid Mechanics*, vol. 831, pp. 228–251, 2017.

[185] G. Li and A. M. Ardekani, “Near wall motion of undulatory swimmers in non-newtonian fluids”, *European Journal of Computational Mechanics*, vol. 26, no. 1-2, pp. 44–60, 2017.

[186] J. P. Binagia, A. Phoa, K. D. Housiadas, and E. S. Shaqfeh, “Swimming with swirl in a viscoelastic fluid”, *Journal of Fluid Mechanics*, vol. 900, 2020.

[187] K. D. Housiadas, J. P. Binagia, and E. S. Shaqfeh, “Squirmers with swirl at low weissenberg number”, *Journal of Fluid Mechanics*, vol. 911, 2021.

[188] X. Shen and P. E. Arratia, “Undulatory swimming in viscoelastic fluids”, *Physical review letters*, vol. 106, no. 20, p. 208 101, 2011.

[189] D. A. Gagnon, N. C. Keim, and P. E. Arratia, “Undulatory swimming in shear-thinning fluids: Experiments with caenorhabditis elegans”, *Journal of Fluid Mechanics*, vol. 758, 2014.

[190] W. R. Schneider and R. Doetsch, “Effect of viscosity on bacterial motility”, *Journal of bacteriology*, vol. 117, no. 2, pp. 696–701, 1974.

[191] C. Li, B. Qin, A. Gopinath, P. E. Arratia, B. Thomases, and R. D. Guy, “Flagellar swimming in viscoelastic fluids: Role of fluid elastic stress revealed by simulations based on experimental data”, *Journal of The Royal Society Interface*, vol. 14, no. 135, p. 20 170 289, 2017.

[192] D. Cao, M. Dvoriashyna, S. Liu, E. Lauga, and Y. Wu, “Reduced surface accumulation of swimming bacteria in viscoelastic polymer fluids”, *Proceedings of the National Academy of Sciences*, vol. 119, no. 45, e2212078119, 2022.

[193] Z. Qu and K. S. Breuer, “Effects of shear-thinning viscosity and viscoelastic stresses on flagellated bacteria motility”, *Physical Review Fluids*, vol. 5, no. 7, p. 073 103, 2020.

[194] K. Ishimoto, H. Gadêlha, E. A. Gaffney, D. J. Smith, and J. Kirkman-Brown, “Human sperm swimming in a high viscosity mucus analogue”, *Journal of theoretical biology*, vol. 446, pp. 1–10, 2018.

[195] A. Pommella, V. Preziosi, S. Caserta, J. M. Cooper, S. Guido, and M. Tassieri, “Using optical tweezers for the characterization of polyelectrolyte solutions with very low viscoelasticity”, *Langmuir*, vol. 29, no. 29, pp. 9224–9230, 2013.

[196] H. Liu *et al.*, “Rheological properties of xanthan gum and polyacrylamide mixture in inorganic salt solutions.”, *International Journal of Heat & Technology*, vol. 39, no. 4, 2021.

[197] E. Bazzani, C. Lauritano, O. Mangoni, F. Bolinesi, and M. Saggiomo, “Chlamydomonas responses to salinity stress and possible biotechnological exploitation”, *Journal of Marine Science and Engineering*, vol. 9, no. 11, p. 1242, 2021.

[198] M. T. Ghannam and M. N. Esmail, “Rheological properties of aqueous polyacrylamide solutions”, *Journal of applied polymer science*, vol. 69, no. 8, pp. 1587–1597, 1998.

[199] A. E. Koser, L. Pan, N. C. Keim, and P. E. Arratia, “Measuring material relaxation and creep recovery in a microfluidic device”, *Lab on a Chip*, vol. 13, no. 10, pp. 1850–1853, 2013.

[200] C. Brokaw, “Effects of increased viscosity on the movements of some invertebrate spermatozoa”, *Journal of Experimental Biology*, vol. 45, no. 1, pp. 113–139, 1966.

[201] L. Gheber, A. Korngreen, and Z. Priel, “Effect of viscosity on metachrony in mucus propelling cilia”, *Cell motility and the cytoskeleton*, vol. 39, no. 1, pp. 9–20, 1998.

[202] M. Rossi, G. Cicconofri, A. Beran, G. Noselli, and A. DeSimone, “Kinematics of flagellar swimming in euglena gracilis: Helical trajectories and flagellar shapes”, *Proceedings of the National Academy of Sciences*, vol. 114, no. 50, pp. 13 085–13 090, 2017.

[203] H. De Maleprade, F. Moisy, T. Ishikawa, and R. E. Goldstein, “Motility and phototaxis of gonium, the simplest differentiated colonial alga”, *Physical Review E*, vol. 101, no. 2, p. 022 416, 2020.

[204] K. Y. Wan, K. C. Leptos, and R. E. Goldstein, “Lag, lock, sync, slip: The many ‘phases’ of coupled flagella”, *Journal of the Royal Society Interface*, vol. 11, no. 94, p. 20 131 160, 2014.

[205] K. Y. Wan and R. E. Goldstein, “Coordinated beating of algal flagella is mediated by basal coupling”, *Proceedings of the National Academy of Sciences*, vol. 113, no. 20, E2784–E2793, 2016.

[206] H. Guo, Y. Man, K. Y. Wan, and E. Kanso, “Intracellular coupling modulates biflagellar synchrony”, *Journal of The Royal Society Interface*, vol. 18, no. 174, p. 20 200 660, 2021.

[207] R. R. Bennett and R. Golestanian, “A steering mechanism for phototaxis in chlamydomonas”, *Journal of The Royal Society Interface*, vol. 12, no. 104, p. 20 141 164, 2015.

[208] J.-Z. Zhang, X.-Y. Peng, S. Liu, B.-P. Jiang, S.-C. Ji, and X.-C. Shen, “The persistence length of semiflexible polymers in lattice monte carlo simulations”, *Polymers*, vol. 11, no. 2, p. 295, 2019.

[209] M. Contino, E. Lushi, I. Tuval, V. Kantsler, and M. Polin, “Microalgae scatter off solid surfaces by hydrodynamic and contact forces”, *Physical review letters*, vol. 115, no. 25, p. 258 102, 2015.

[210] R. E. Goldstein, M. Polin, and I. Tuval, “Noise and synchronization in pairs of beating eukaryotic flagella”, *Physical review letters*, vol. 103, no. 16, p. 168 103, 2009.

[211] H. Maas, A. Gruen, and D. Papantoniou, “Particle tracking velocimetry in three-dimensional flows”, *Experiments in fluids*, vol. 15, no. 2, pp. 133–146, 1993.

[212] S. M. Soloff, R. J. Adrian, and Z.-C. Liu, “Distortion compensation for generalized stereoscopic particle image velocimetry”, *Measurement science and technology*, vol. 8, no. 12, p. 1441, 1997.

[213] B. Wieneke, “Volume self-calibration for 3d particle image velocimetry”, *Experiments in fluids*, vol. 45, no. 4, pp. 549–556, 2008.

[214] G. F. Welch, “Kalman filter”, *Computer Vision: A Reference Guide*, pp. 1–3, 2020.

[215] M. Riekeles, J. Schirmack, and D. Schulze-Makuch, “Machine learning algorithms applied to identify microbial species by their motility”, *Life*, vol. 11, no. 1, p. 44, 2021.

[216] M. J. Sanderson, I. Smith, I. Parker, and M. D. Bootman, “Fluorescence microscopy”, *Cold Spring Harbor Protocols*, vol. 2014, no. 10, pdb–top071795, 2014.

[217] F. Crescitelli, T. James, J. Erickson, E. Loew, and W. McFarland, “The eyespot of chlamydomonas reinhardtii: A comparative microspectrophotometric study”, *Vision research*, vol. 32, no. 9, pp. 1593–1600, 1992.

[218] W. Schneider Jr and R. Doetsch, “Temperature effects on bacterial movement”, *Applied and environmental microbiology*, vol. 34, no. 6, pp. 695–700, 1977.

[219] K. K. Mullane, M. Nishiyama, T. Kurihara, and D. H. Bartlett, “Compounding deep sea physical impacts on marine microbial motility”, *Frontiers in Marine Science*, vol. 10, p. 859, 2023.

[220] H. C. Berg and D. A. Brown, “Chemotaxis in escherichia coli analysed by three-dimensional tracking”, *nature*, vol. 239, no. 5374, pp. 500–504, 1972.

[221] G. A. O’Toole and R. Kolter, “Flagellar and twitching motility are necessary for pseudomonas aeruginosa biofilm development”, *Molecular microbiology*, vol. 30, no. 2, pp. 295–304, 1998.

[222] P. L. Stelmack, M. R. Gray, and M. A. Pickard, “Bacterial adhesion to soil contaminants in the presence of surfactants”, *Applied and environmental microbiology*, vol. 65, no. 1, pp. 163–168, 1999.

[223] V. Sourjik and H. C. Berg, “Functional interactions between receptors in bacterial chemotaxis”, *Nature*, vol. 428, no. 6981, pp. 437–441, 2004.

[224] S. M. Williams, Y.-T. Chen, T. M. Andermann, J. E. Carter, D. J. McGee, and K. M. Ottemann, “Helicobacter pylori chemotaxis modulates inflammation and bacterium-gastric epithelium interactions in infected mice”, *Infection and immunity*, vol. 75, no. 8, pp. 3747–3757, 2007.

[225] E. Tamar, M. Koler, and A. Vaknin, “The role of motility and chemotaxis in the bacterial colonization of protected surfaces”, *Scientific reports*, vol. 6, no. 1, p. 19 616, 2016.

[226] A. M. Hein, F. Carrara, D. R. Brumley, R. Stocker, and S. A. Levin, "Natural search algorithms as a bridge between organisms, evolution, and ecology", *Proceedings of the National Academy of Sciences*, vol. 113, no. 34, pp. 9413–9420, 2016.

[227] M. Grognot and K. M. Taute, "A multiscale 3d chemotaxis assay reveals bacterial navigation mechanisms", *Communications biology*, vol. 4, no. 1, p. 669, 2021.

[228] R. R. Bennett and R. Golestanian, "Emergent run-and-tumble behavior in a simple model of chlamydomonas with intrinsic noise", *Physical review letters*, vol. 110, no. 14, p. 148 102, 2013.

[229] J. Kessler, "Functional patterns of swimming bacteria", *Mechanics and physiology of animal swimming*, 1994.

[230] D. M. Higginson and S. Pitnick, "Evolution of intra-ejaculate sperm interactions: Do sperm cooperate?", *Biological Reviews*, vol. 86, no. 1, pp. 249–270, 2011.

[231] D. A. Mavridou, D. Gonzalez, W. Kim, S. A. West, and K. R. Foster, "Bacteria use collective behavior to generate diverse combat strategies", *Current Biology*, vol. 28, no. 3, pp. 345–355, 2018.

[232] H. Trenchard and M. Perc, "Energy saving mechanisms, collective behavior and the variation range hypothesis in biological systems: A review", *Biosystems*, vol. 147, pp. 40–66, 2016.

[233] T. Speck, "Collective behavior of active brownian particles: From microscopic clustering to macroscopic phase separation", *The European Physical Journal Special Topics*, vol. 225, pp. 2287–2299, 2016.

[234] G. Gordon and R. Tibshirani, "Karush-kuhn-tucker conditions", *Optimization*, vol. 10, no. 725/36, p. 725, 2012.

[235] R. Cortez, L. Fauci, and A. Medovikov, "The method of regularized stokeslets in three dimensions: Analysis, validation, and application to helical swimming", *Physics of Fluids*, vol. 17, no. 3, p. 031 504, 2005.

A

SUPPLEMENTARY MATERIAL - CHAPTER 2

This appendix belongs to chapter 2.

A.1. CURVE FITTING ALGORITHM

Trajectory in the object domain is defined as a discrete vector function $\mathbf{X}_t$. where $t \in [0,\ 0.05,\ 0.1,\ 0.15, \ldots,\ t_N]$ and $\mathbf{X} = [X\ Y\ Z]^T$ are position values. We aim to find a continuous vector function $\mathbf{X}(t, \beta)$, where $t \in [0\ \ t_N]$ and β is a vector of coefficients. $\mathbf{X}(t, \beta)$ is a parameterized curve that can be obtained by minimizing the sum of least squares as follows:

$$\min_{\beta} \sum_{i=0}^{N} \left\| \mathbf{X}(t_i, \beta) - \mathbf{X}_{t_i} \right\|^2 \tag{A.1}$$

In matrix notation, this can be written as follow:

$$\min_{\beta_X, \beta_Y, \beta_Z} \sum_{i=0}^{N} \left\| \begin{bmatrix} X(t_i, \beta_X) \\ X(t_i, \beta_Y) \\ X(t_i, \beta_Z) \end{bmatrix} - \begin{bmatrix} X \\ Y \\ Z \end{bmatrix} \right\|^2 \tag{A.2}$$

Where $\beta_X, \beta_Y, \beta_Z$ are coefficients concerning X, Y and Z dimension. Equation A.2 shows that X, Y and Z components can be solved independently.

We can write the A.2 in the linear formulation as follows:

$$\begin{aligned} &\min_{\beta} \left\| A\beta - b \right\| \\ &\text{s.t.} \quad I\beta = d \end{aligned} \tag{A.3}$$

Where A is called the design matrix and I is the constraint matrix. From Karush-Kuhn-Tucker (KKT) conditions, the optimal value of β obeys:

$$\begin{bmatrix} 2A^TA & I^T \\ I & \mathbf{O} \end{bmatrix} \begin{bmatrix} \beta \\ z \end{bmatrix} = \begin{bmatrix} 2A^Tb \\ \mathbf{O} \end{bmatrix} \tag{A.4}$$

Where z is a Lagrangian multiplier. We aim to find the design and constraint matrices to solve the equation A.3.

$\mathbf{X}(t,\beta)$ is assumed to be a piecewise Legendre polynomial. For piece-wise polynomials, we first define the following sub-intervals based on kernel size l:

$$t_1 \le t_i \le t_l, \ \ t_l \le t_i \le t_{2l} \ \ \ldots \ \ t_{(n-2)l} \le t_i \le t_{(n-1)l}, \ \ t_{(n-1)l} \le t_i \le t_{nl}$$

Where n is the number of the sub-interval. In total, we have $n+1$ knots.

For simplicity, we will only focus on the X component for further discussion. Let $X(t_i,\beta_X)$ be a piece wise polynomial composed of $X_1(t_i,\beta_{X,1})$, $X_2(t_i,\beta_{X,2})$, $X_3(t_i,\beta_{X,3})$,..., $X_n(t_i,\beta_{X,n})$ where $X_n(t_i,\beta_{X,m})$ denotes the m^{th} spline, for $m = 1,2,\ldots,n$. The following conditions are imposed:

1. At the interior knots, adjacent splines are joined.
   $X_m(t_m,\beta_{X,m}) = X_{m+1}(t_m,\beta_{X,m+1})$, for $m = 1,2,\ldots,n-1$.

2. The first time derivatives matches at the interior knots.
   $X'_m(t_m,\beta_{X,m}) = X'_{m+1}(t_m,\beta_{X,m+1})$, for $m = 1,2,\ldots,n-1$.

3. The second time derivatives matches at the interior knots.
   $X''_m(t_m,\beta_{X,m}) = X''_{m+1}(t_m,\beta_{X,m+1})$, for $m = 1,2,\ldots,n-1$.

We represent each spline as a sum of Legendre polynomials of k^{th} order as follows:

$$X(t_i,\beta_X) = \begin{cases} \beta^0_{X,1}\mathscr{L}^0(t_i) + \beta^1_{X,1}\mathscr{L}^1(t_i) + \beta^2_{X,1}\mathscr{L}^2(t_i) + \ldots + \beta^k_{X,1}\mathscr{L}^k(t_i) & \text{if } t_1 \ge t_i \ge t_l \\ \beta^0_{X,2}\mathscr{L}^0(t_i) + \beta^1_{X,2}\mathscr{L}^1(t_i) + \beta^2_{X,2}\mathscr{L}^2(t_i) + \ldots + \beta^k_{X,2}\mathscr{L}^k(t_i) & \text{if } t_l \ge t_i \ge t_{2l} \\ \beta^0_{X,3}\mathscr{L}^0(t_i) + \beta^1_{X,3}\mathscr{L}^1(t_i) + \beta^2_{X,3}\mathscr{L}^2(t_i) + \ldots + \beta^k_{X,3}\mathscr{L}^k(t_i) & \text{if } t_{2l} \ge t_i \ge t_{3l} \end{cases} \tag{A.5}$$

Where as $\beta^k_{x,m}$ is the k^{th} order coefficient for the m^{th} spline. $\mathscr{L}^k(t_i)$ is k^{th} order Legendre polynomial as a function of t_i. Legendre polynomial up until 5^{th} order are listed in the table A.1:

Legendre polynomials are only orthogonal over the interval [-1, 1]. Thus for each sub-interval, t_i is first normalized between -1 and 1 as follows:

$$\tilde{t}_i = -1 + 2\left(\frac{t_i - t_m}{t_{m+1} - t_m}\right) \text{if } t_m \ge t_i \ge t_{m+1} \tag{A.6}$$

A design matrix A^1_x can be construed for first spline in equation A.5 as follows:

$$X_1(t_i,\beta_{X,1}) = \begin{bmatrix} \mathscr{L}^0(\tilde{t}_0) & \mathscr{L}^1(\tilde{t}_0) & \mathscr{L}^2(\tilde{t}_0) & \ldots & \mathscr{L}^k(\tilde{t}_0) \\ \mathscr{L}^0(\tilde{t}_1) & \mathscr{L}^1(\tilde{t}_1) & \mathscr{L}^2(\tilde{t}_1) & \ldots & \mathscr{L}^k(\tilde{t}_1) \\ \mathscr{L}^0(\tilde{t}_2) & \mathscr{L}^1(\tilde{t}_2) & \mathscr{L}^2(\tilde{t}_2) & \ldots & \mathscr{L}^k(\tilde{t}_2) \\ \vdots & \vdots & \vdots & \ddots & \vdots \\ \mathscr{L}^0(\tilde{t}_l) & \mathscr{L}^1(\tilde{t}_l) & \mathscr{L}^2(\tilde{t}_l) & \ldots & \mathscr{L}^k(\tilde{t}_l) \end{bmatrix} \begin{bmatrix} \beta^0_{X,1} \\ \beta^1_{X,1} \\ \beta^2_{X,1} \\ \vdots \\ \beta^k_{X,1} \end{bmatrix} \text{if } -1 \ge \tilde{t}_i \ge 1 \tag{A.7}$$

Label	Order	$\mathscr{L}^k(\tilde{t})$
$\mathscr{L}^0(\tilde{t})$	0	1
$\mathscr{L}^1(\tilde{t})$	1	$\tilde{t}$
$\mathscr{L}^2(\tilde{t})$	2	$\frac{1}{2}(3\tilde{t}^2 - 1)$
$\mathscr{L}^3(\tilde{t})$	3	$\frac{1}{2}(5\tilde{t}^3 - 3\tilde{t})$
$\mathscr{L}^4(\tilde{t})$	4	$\frac{1}{8}(35\tilde{t}^4 - 30\tilde{t}^2 + 3)$
$\mathscr{L}^5(\tilde{t})$	5	$\frac{1}{8}(63\tilde{t}^5 - 70\tilde{t}^3 + 15\tilde{t}$

Table A.1: Legendre Polynomials.

In its compact form, equation A.7 can be written as follows:

$$X_m(t_i, \beta_{X,m}) = A_X^m \beta_{X,m}^K \quad \text{if } -1 \geq \tilde{t}_i \geq 1 \tag{A.8}$$

Where A_X^m is design matrix for m^{th} spline and $\beta_{X,m}^K$ is a vector of coefficients for m^{th} spline for X dimension. Similarly, a design matrix for other splines can be derived, and equation A.5 takes the following form:

$$X(t_i, \beta_X) = \mathbf{A}_X \beta_X = \begin{bmatrix} A_X^1 & \mathbf{O} & \mathbf{O} \\ \mathbf{O} & A_X^2 & \mathbf{O} \\ \mathbf{O} & \mathbf{O} & A_X^3 \end{bmatrix} \begin{bmatrix} \beta_{X,1}^K \\ \beta_{X,2}^K \\ \beta_{X,3}^K \end{bmatrix} \tag{A.9}$$

Where A_X^1, A_X^2 and A_X^3 are design matrices for spline 1, 2, and 3 and $\mathbf{O}$ is zero matrix. Size of $\mathbf{O}$ is $l \times k$. Equation A.9 is written for only 3 splines, but it can be extended to m splines in a similar fashion.

We can calculate design matrices for Y and Z dimensions like the discussion above.

$$X(t_i, \beta_Y) = \mathbf{A}_Y \beta_Y = \begin{bmatrix} A_Y^1 & \mathbf{O} & \mathbf{O} \\ \mathbf{O} & A_Y^2 & \mathbf{O} \\ \mathbf{O} & \mathbf{O} & A_Y^3 \end{bmatrix} \begin{bmatrix} \beta_{Y,1}^K \\ \beta_{Y,2}^K \\ \beta_{Y,3}^K \end{bmatrix} \tag{A.10}$$

$$X(t_i, \beta_Z) = \mathbf{A}_Z \beta_Z = \begin{bmatrix} A_Z^1 & \mathbf{O} & \mathbf{O} \\ \mathbf{O} & A_Z^2 & \mathbf{O} \\ \mathbf{O} & \mathbf{O} & A_Z^3 \end{bmatrix} \begin{bmatrix} \beta_{Z,k}^K \\ \beta_{Z,k}^K \\ \beta_{Z,k}^K \end{bmatrix} \tag{A.11}$$

We can write a combined design matrix **A** and coefficient vector β to minimize objective functions in equation A.2.

$$\mathbf{A}\beta = \begin{bmatrix} A_X^1 & \mathbf{0} & \mathbf{0} & \mathbf{0} & \mathbf{0} & \mathbf{0} & \mathbf{0} & \mathbf{0} & \mathbf{0} \\ \mathbf{0} & A_X^2 & \mathbf{0} & \mathbf{0} & \mathbf{0} & \mathbf{0} & \mathbf{0} & \mathbf{0} & \mathbf{0} \\ \mathbf{0} & \mathbf{0} & A_X^3 & \mathbf{0} & \mathbf{0} & \mathbf{0} & \mathbf{0} & \mathbf{0} & \mathbf{0} \\ \mathbf{0} & \mathbf{0} & \mathbf{0} & A_Y^1 & \mathbf{0} & \mathbf{0} & \mathbf{0} & \mathbf{0} & \mathbf{0} \\ \mathbf{0} & \mathbf{0} & \mathbf{0} & \mathbf{0} & A_Y^2 & \mathbf{0} & \mathbf{0} & \mathbf{0} & \mathbf{0} \\ \mathbf{0} & \mathbf{0} & \mathbf{0} & \mathbf{0} & \mathbf{0} & A_Y^3 & \mathbf{0} & \mathbf{0} & \mathbf{0} \\ \mathbf{0} & \mathbf{0} & \mathbf{0} & \mathbf{0} & \mathbf{0} & \mathbf{0} & A_Z^1 & \mathbf{0} & \mathbf{0} \\ \mathbf{0} & \mathbf{0} & \mathbf{0} & \mathbf{0} & \mathbf{0} & \mathbf{0} & \mathbf{0} & A_Z^2 & \mathbf{0} \\ \mathbf{0} & \mathbf{0} & \mathbf{0} & \mathbf{0} & \mathbf{0} & \mathbf{0} & \mathbf{0} & \mathbf{0} & A_Z^3 \end{bmatrix} \begin{bmatrix} \beta_{X,k}^1 \\ \beta_{X,k}^2 \\ \beta_{X,k}^3 \\ \beta_{Y,k}^1 \\ \beta_{Y,k}^2 \\ \beta_{Y,k}^3 \\ \beta_{Z,k}^1 \\ \beta_{Z,k}^2 \\ \beta_{Z,k}^3 \end{bmatrix} \tag{A.12}$$

Let us now discuss how we formed the constraint matrix.

First constraint for first and second splines states that $X_1(l,\beta_1) = X_2(l,\beta_2)$. For a normalized time, each spline starts at $\tilde{t} = -1$, and the end is at $\tilde{t} = 1$.

Let $\mathscr{L}_{\mathbf{K}}(\tilde{t}_i) = \begin{bmatrix} \mathscr{L}^0(\tilde{t}_i) & \mathscr{L}^1(\tilde{t}_i) & \mathscr{L}^2(\tilde{t}_i) & \dots & \mathscr{L}^k(\tilde{t}_i) \end{bmatrix}$. The first condition can be written as follows:

$$\mathscr{L}_{\mathbf{K}}(1)\beta_{X,1}^K - \mathscr{L}_{\mathbf{K}}(-1)\beta_{X,2}^K = [\mathscr{L}_{\mathbf{K}}(1) \ -\mathscr{L}_{\mathbf{K}}(-1)] \begin{bmatrix} \beta_{X,1}^K \\ \beta_{X,2}^K \end{bmatrix} = 0 \tag{A.13}$$

For 3 splines, we can write the first constraint in matrix notation:

$$\begin{bmatrix} \mathscr{L}_{\mathbf{K}}(1) & -\mathscr{L}_{\mathbf{K}}(-1) & \mathbf{0} \\ \mathbf{0} & \mathscr{L}_{\mathbf{K}}(1) & -\mathscr{L}_{\mathbf{K}}(-1) \end{bmatrix} \begin{bmatrix} \beta_{X,1}^K \\ \beta_{X,2}^K \\ \beta_{X,3}^K \end{bmatrix} = 0 \tag{A.14}$$

Size of zero matrix **O** is 1 × k.

Similarly, we can define the first constraint for Y and Z components. The overall first constraint would take the following form:

$$\begin{bmatrix} \mathscr{L}_{\mathbf{K}}(1) & -\mathscr{L}_{\mathbf{K}}(-1) & \mathbf{0} & \mathbf{0} & \mathbf{0} & \mathbf{0} & \mathbf{0} & \mathbf{0} & \mathbf{0} \\ \mathbf{0} & \mathscr{L}_{\mathbf{K}}(1) & -\mathscr{L}_{\mathbf{K}}(-1) & \mathbf{0} & \mathbf{0} & \mathbf{0} & \mathbf{0} & \mathbf{0} & \mathbf{0} \\ \mathbf{0} & \mathbf{0} & \mathbf{0} & \mathscr{L}_{\mathbf{K}}(1) & -\mathscr{L}_{\mathbf{K}}(-1) & \mathbf{0} & \mathbf{0} & \mathbf{0} & \mathbf{0} \\ \mathbf{0} & \mathbf{0} & \mathbf{0} & \mathbf{0} & \mathscr{L}_{\mathbf{K}}(1) & -\mathscr{L}_{\mathbf{K}}(-1) & \mathbf{0} & \mathbf{0} & \mathbf{0} \\ \mathbf{0} & \mathbf{0} & \mathbf{0} & \mathbf{0} & \mathbf{0} & \mathbf{0} & \mathscr{L}_{\mathbf{K}}(1) & -\mathscr{L}_{\mathbf{K}}(-1) & \mathbf{0} \\ \mathbf{0} & \mathbf{0} & \mathbf{0} & \mathbf{0} & \mathbf{0} & \mathbf{0} & \mathbf{0} & \mathscr{L}_{\mathbf{K}}(1) & -\mathscr{L}_{\mathbf{K}}(\tilde{t}_{-1}) \end{bmatrix} \begin{bmatrix} \beta_{X,1}^K \\ \beta_{X,2}^K \\ \beta_{X,3}^K \\ \beta_{Y,1}^K \\ \beta_{Y,2}^K \\ \beta_{Y,3}^K \\ \beta_{Z,1}^K \\ \beta_{Z,2}^K \\ \beta_{Z,3}^K \end{bmatrix} = 0 \tag{A.15}$$

The second and third constraints deal with time derivatives. Chain rules are used to define derivatives with respect to t as follows:

$$X_m^{'}(t,\beta_{X,m}) = \frac{\mathrm{d}}{\mathrm{d}\tilde{t}}\left[\beta_{X,m}^0\mathscr{L}^0(t_i) + \beta_{X,m}^1\mathscr{L}^1(t_i) + \ldots + \beta_{X,m}^k\mathscr{L}^k(t_i)\right] \cdot \frac{\mathrm{d}\tilde{t}}{\mathrm{d}t} \tag{A.16}$$

From equation A.16 we can write an expression for $\mathscr{L}_{\mathbf{K}}^{'}(t)$:

$$\mathscr{L}_{\mathbf{K}}^{'}(\tilde{t}) = \frac{\mathrm{d}}{\mathrm{d}\tilde{t}}\left[\mathscr{L}_0(\tilde{t}) + \mathscr{L}_1(\tilde{t}) + \ldots + \mathscr{L}_k(\tilde{t})\right] \cdot \frac{\mathrm{d}\tilde{t}}{\mathrm{d}t} \tag{A.17}$$

For second-order time derivative, we can write:

$$\mathscr{L}''_{\mathbf{K}}(\tilde{t}) = \frac{\mathrm{d}^2}{\mathrm{d}\tilde{t}^2}\left[\mathscr{L}_0(\tilde{t}) + \mathscr{L}_1(\tilde{t}) + \ldots + \mathscr{L}_k(\tilde{t})\right] \cdot \left(\frac{\mathrm{d}\tilde{t}}{\mathrm{d}t}\right)^2 \tag{A.18}$$

We can do the same for the second and third constraints as we have constructed a matrix for the first constraint.

All of the constraints are written in the following form:

$$\mathbf{I}\beta = \begin{bmatrix}
\mathscr{L}_{\mathbf{K}}(1) & -\mathscr{L}_{\mathbf{K}}(-1) & \mathbf{0} & \mathbf{0} & \mathbf{0} & \mathbf{0} & \mathbf{0} & \mathbf{0} & \mathbf{0} \\
\mathbf{0} & \mathscr{L}_{\mathbf{K}}(1) & -\mathscr{L}_{\mathbf{K}}(-1) & \mathbf{0} & \mathbf{0} & \mathbf{0} & \mathbf{0} & \mathbf{0} & \mathbf{0} \\
\mathbf{0} & \mathbf{0} & \mathbf{0} & \mathscr{L}_{\mathbf{K}}(1) & -\mathscr{L}_{\mathbf{K}}(-1) & \mathbf{0} & \mathbf{0} & \mathbf{0} & \mathbf{0} \\
\mathbf{0} & \mathbf{0} & \mathbf{0} & \mathbf{0} & \mathscr{L}_{\mathbf{K}}(1) & -\mathscr{L}_{\mathbf{K}}(-1) & \mathbf{0} & \mathbf{0} & \mathbf{0} \\
\mathbf{0} & \mathbf{0} & \mathbf{0} & \mathbf{0} & \mathbf{0} & \mathbf{0} & \mathscr{L}_{\mathbf{K}}(1) & -\mathscr{L}_{\mathbf{K}}(-1) & \mathbf{0} \\
\mathbf{0} & \mathbf{0} & \mathbf{0} & \mathbf{0} & \mathbf{0} & \mathbf{0} & \mathbf{0} & \mathscr{L}_{\mathbf{K}}(1) & -\mathscr{L}_{\mathbf{K}}(\tilde{t}_{-1}) \\
\mathscr{L}'_{\mathbf{K}}(1) & -\mathscr{L}'_{\mathbf{K}}(-1) & \mathbf{0} & \mathbf{0} & \mathbf{0} & \mathbf{0} & \mathbf{0} & \mathbf{0} & \mathbf{0} \\
\mathbf{0} & \mathscr{L}'_{\mathbf{K}}(1) & -\mathscr{L}'_{\mathbf{K}}(-1) & \mathbf{0} & \mathbf{0} & \mathbf{0} & \mathbf{0} & \mathbf{0} & \mathbf{0} \\
\mathbf{0} & \mathbf{0} & \mathbf{0} & \mathscr{L}'_{\mathbf{K}}(1) & -\mathscr{L}'_{\mathbf{K}}(-1) & \mathbf{0} & \mathbf{0} & \mathbf{0} & \mathbf{0} \\
\mathbf{0} & \mathbf{0} & \mathbf{0} & \mathbf{0} & \mathscr{L}'_{\mathbf{K}}(1) & -\mathscr{L}'_{\mathbf{K}}(-1) & \mathbf{0} & \mathbf{0} & \mathbf{0} \\
\mathbf{0} & \mathbf{0} & \mathbf{0} & \mathbf{0} & \mathbf{0} & \mathbf{0} & \mathscr{L}'_{\mathbf{K}}(1) & -\mathscr{L}'_{\mathbf{K}}(-1) & \mathbf{0} \\
\mathbf{0} & \mathbf{0} & \mathbf{0} & \mathbf{0} & \mathbf{0} & \mathbf{0} & \mathbf{0} & \mathscr{L}'_{\mathbf{K}}(1) & -\mathscr{L}'_{\mathbf{K}}(\tilde{t}_{-1}) \\
\mathscr{L}''_{\mathbf{K}}(1) & -\mathscr{L}''_{\mathbf{K}}(-1) & \mathbf{0} & \mathbf{0} & \mathbf{0} & \mathbf{0} & \mathbf{0} & \mathbf{0} & \mathbf{0} \\
\mathbf{0} & \mathscr{L}''_{\mathbf{K}}(1) & -\mathscr{L}''_{\mathbf{K}}(-1) & \mathbf{0} & \mathbf{0} & \mathbf{0} & \mathbf{0} & \mathbf{0} & \mathbf{0} \\
\mathbf{0} & \mathbf{0} & \mathbf{0} & \mathscr{L}''_{\mathbf{K}}(1) & -\mathscr{L}''_{\mathbf{K}}(-1) & \mathbf{0} & \mathbf{0} & \mathbf{0} & \mathbf{0} \\
\mathbf{0} & \mathbf{0} & \mathbf{0} & \mathbf{0} & \mathscr{L}''_{\mathbf{K}}(1) & -\mathscr{L}''_{\mathbf{K}}(-1) & \mathbf{0} & \mathbf{0} & \mathbf{0} \\
\mathbf{0} & \mathbf{0} & \mathbf{0} & \mathbf{0} & \mathbf{0} & \mathbf{0} & \mathscr{L}''_{\mathbf{K}}(1) & -\mathscr{L}''_{\mathbf{K}}(-1) & \mathbf{0} \\
\mathbf{0} & \mathbf{0} & \mathbf{0} & \mathbf{0} & \mathbf{0} & \mathbf{0} & \mathbf{0} & \mathscr{L}''_{\mathbf{K}}(1) & -\mathscr{L}''_{\mathbf{K}}(\tilde{t}_{-1})
\end{bmatrix}
\begin{bmatrix}
\beta^K_{X,1} \\ \beta^K_{X,2} \\ \beta^K_{X,3} \\ \beta^K_{Y,1} \\ \beta^K_{Y,2} \\ \beta^K_{Y,3} \\ \beta^K_{Z,1} \\ \beta^K_{Z,2} \\ \beta^K_{Z,3}
\end{bmatrix} = 0 \tag{A.19}$$

As discussed above, the KKT condition is used to solve for β after the design and constraint matrix are computed. For our case b in equation A.4 takes the form of $[X_i \;\; Y_i \;\; Z_i]^T$, while d is zero column vector. Solution vector β is computed as follows:

$$\begin{bmatrix} \beta \\ z \end{bmatrix} = \begin{bmatrix} 2A^T A & I^T \\ I & \mathbf{0} \end{bmatrix}^{-1} \begin{bmatrix} 2A^T\mathbf{X} \\ \mathbf{0} \end{bmatrix} \tag{A.20}$$

A.2. BACKGROUND FLOW

A.2.1. TOMO-PIV RECONSTRUCTION

Experiments were conducted using flow chambers of different sizes ranging from 8mm to 12mm in diameter to characterize the background flow inside the reservoir. Potter's hollow spherical particles were used as passive tracers, and recording was performed using four imager sCMOS cameras at a frame rate of 20 fps for 1 minute. The Lavision Tomo-PIV toolbox was utilized to reconstruct the flow fields, as depicted in Fig. A.1.

A.2.2. COMSOL SIMULATIONS

COMSOL Multiphysics software was used to conduct the simulations. Fig. A.2 illustrates the geometry and mesh utilized for the simulation. The gravity vector was aligned with the negative Y-axis, consistent with the experimental setup. In addition, a small

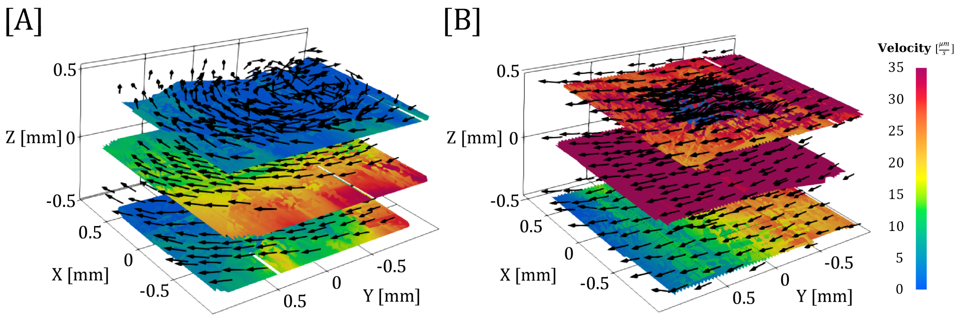

Figure A.1: Background flow for [A] 8mm and [B] 10mm diameter flow chambers.

temperature difference of 1 $^\circ C$ was introduced on the inside left wall of the flow chamber (see Fig. A.2 A).

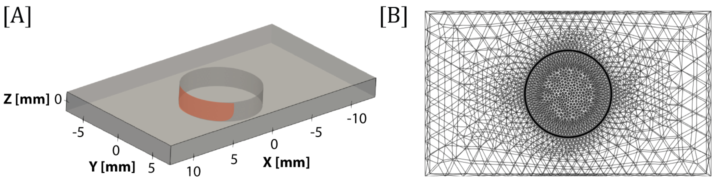

Figure A.2: [A] Geometry representing the flow chamber with an 8mm diameter reservoir. The red area indicates the wall where the temperature was increased by 1 $^\circ C$ compared to the rest of the flow chamber. [B] Mesh for the simulation.

Fig. A.3A presents the simulation results in terms of the vector field across the entire flow chamber. Additionally, we display the simulated flow field corresponding to the image volume used in our tomo-PIV experiments. The simulated results qualitatively match our experimental results, suggesting that the observed background flow in the experiments is attributed to the temperature difference of 1 $^\circ C$.

A.2.3. ALGAE CELL DRIFT

Fig. A.4 illustrates the drifting of algae cells within the background flow with the velocity of 10 μm/s. The flow pattern of drifting cells is the same as observed via simulations and experiments using passive particles.

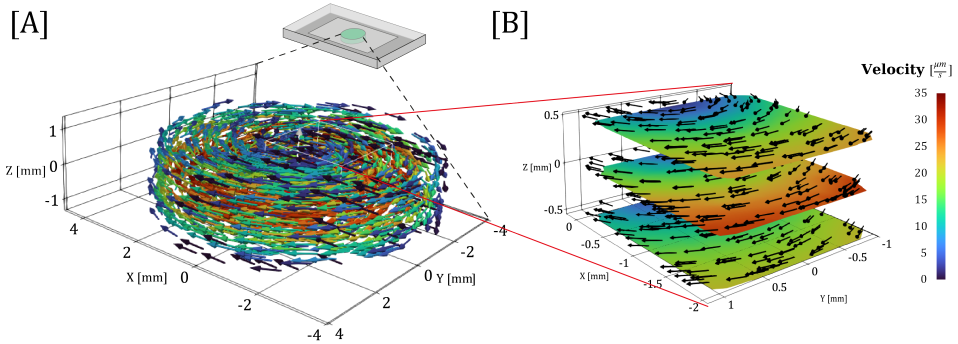

Figure A.3: [A] Vector field representing simulated background flow across the flow chamber for an 8mm diameter reservoir. [B] Simulated background flow at the same location as the passive tracer particles.

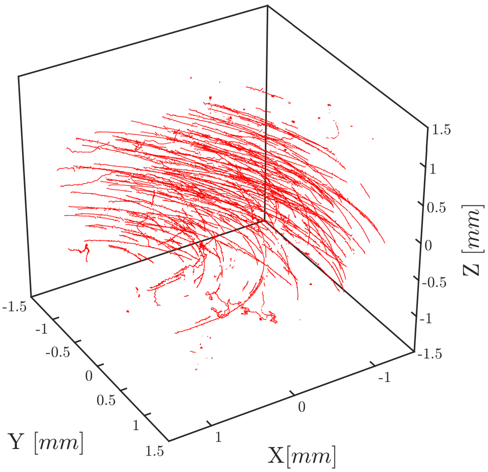

Figure A.4: Algae cells drifting with the background flow.

A.3. PERSISTENCE LENGTH AND DIFFUSION COEFFICIENTS

Persistence length is a key concept in polymer physics and plays an essential role in the modeling and analysis of polymer chains. It measures the chain's rigidity or flexibility and describes the length scale over which correlations in the direction of the tangent are lost [208]. This quantity is especially useful in worm-like chain models for describing the behavior of rigid and semiflexible polymers.

For a polymer chain of length L and end-to-end distance E (see Figure A.5A), the autocorrelation of tangent vectors relate to the persistence length as follows:

$$\langle \mathbf{T}(s) \cdot \mathbf{T}(s') \rangle = e^{-\frac{|s-s'|}{L_P}}. \tag{A.21}$$

Here, $\mathbf{T}(s)$ represents the tangent vector at position s along the chain, and $\langle \cdot \rangle$ denotes an ensemble average.

The persistence length can be computed by considering the mean square of the end-to-end vector **E** [208]. Specifically, we have:

$$\langle E^2\rangle = \langle \mathbf{E}\cdot\mathbf{E}\rangle = \langle \int_0^L \mathbf{T}(s)ds \cdot \int_0^L \mathbf{T}(s')ds'\rangle. \tag{A.22}$$

Substituting Equation A.21 into the above equation and integrating yields:

$$\langle E^2\rangle = 2L_P L\left\{1-\frac{L_P}{L}\left[1-e^{\left(-\frac{L}{L_P}\right)}\right]\right\}, \tag{A.23}$$

Where L is the length of the polymer chain, this expression gives a relationship between **E**, L, and L_P, which can be used to calculate the persistence length of the chain.

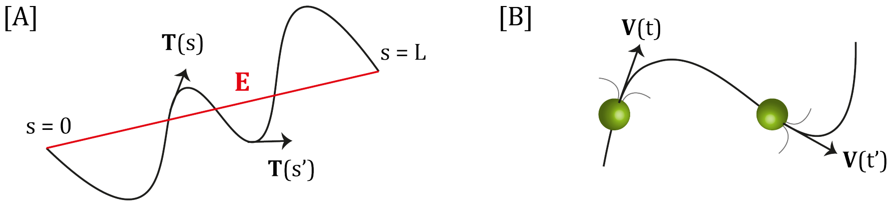

Figure A.5: [A] An illustration of the worm like chain of length L with unit tangent vectors (**T**) at different location along the chain. [B] An algae cell moves along a three-dimensional curve with velocity **V** at different time steps.

Cell trajectory is similar to the polymer chain, and we can use the same formulation to define the persistence length of a cell trajectory. To determine the persistence length of a cell trajectory, we use the decay of the auto-correlation function of velocity to compute the reorientation time τ_P, which is the time the cell has traveled on a straight path before taking a sharp turn. From reorientation time, persistence length can be calculated by $L_P = \sqrt{\langle V^2\rangle}\tau_P$, where $\langle V^2\rangle$ is the cell mean square velocity.

For a cell trajectory as displayed in Figure A.5B, the decay of the auto-correlation function of velocity is described by:

$$\langle \mathbf{V}(t)\cdot\mathbf{V}(t')\rangle = \langle V^2\rangle e^{\left(-\frac{t-t'}{\tau_P}\right)}, \tag{A.24}$$

where $\langle V^2\rangle$ is the cell mean square velocity.

Mean square displacement (MSD) can be defined analogously to mean square end-to-end vector distance for the worm-like chain as follows:

$$\mathrm{MSD}(\Delta t) = \langle \int_0^{\Delta t} \mathbf{V}(t)dt \cdot \int_0^{\Delta t} \mathbf{V}(t')dt'\rangle. \tag{A.25}$$

This equation can be solved by using Eq. A.24, resulting in the following relationship:

$$\mathrm{MSD}(\Delta t) = 2\langle V^2\rangle \Delta t \tau_P\left[1-\frac{\tau_P}{\Delta t}\left(1-e^{-\frac{\Delta t}{\tau_P}}\right)\right] \tag{A.26}$$

It is important to note that Eq. A.26 takes into account both the ballistic and diffusive behavior of the cell trajectory. Specifically, for short time scales where $t \ll \tau_P$, the motion is ballistic, and the mean square displacement is well approximated by $\langle V^2 \rangle \Delta t^2$. In contrast, the motion becomes diffusive for long time scales where $t \gg \tau_P$, and the mean square displacement is approximated by $\langle V^2 \rangle \Delta t$. Furthermore, in the diffusive regime, the mean square displacement is related to the translational diffusion coefficient D_T by $\mathrm{MSD}(\Delta t) = 6D_T(\Delta t)$. By taking the limit of Eq. A.26 for $t \gg \tau_P$, we can compute the translational diffusion coefficient as $D_T = \frac{L_P^2}{3\tau_P}$. In addition, for active Brownian particles, the reorientation time τ_P is directly related to the rotational diffusion coefficient D_R through the relationship $D_R = 1/(2\tau_P)$ [233]. Therefore, if the reorientation time (τ_P) is known, the persistence length, translational, and rotational diffusion coefficients can be easily computed.

The trajectory data obtained from our experiments consisted of individual tracks with varying lengths. We have two approaches to determine the reorientation time (τ_P) from $\mathrm{MSD}(\Delta t)$ and $\langle V^2 \rangle$. First, we can use Eq. A.26 for each long trajectory individually to obtain its τ_P. This method results in a distribution of trajectory parameters for all of the trajectories. Alternatively, we can concatenate all the individual tracks to create a single long trajectory, which we can then use to estimate the average τ_P for the whole population. In this thesis, we used both methods to calculate the parameters. However, we only considered the tracks at least 200 μm away from the surfaces to acquire the bulk statistics. Here we also provide details of our algorithm to obtain a single long trajectory from the individual tracks.

Let $\mathbf{P}_A(t)$ and $\mathbf{V}_A(t)$ be the position and velocity of track A, respectively. Let $\mathbf{P}_B(t)$ and $\mathbf{V}_B(t)$ be the position and velocity of track B, respectively. To join track B with track A, we first calculate the position of the last point in track A, denoted as $\mathbf{P}_A(t_L)$, plus the displacement of that point due to its velocity over a given time step Δt, which is 0.05 seconds in our case. This gives us the position value $\mathbf{X}_A$:

$$\mathbf{X}_A = \mathbf{P}_A(t_L) + \mathbf{V}_A(t_L)\Delta t$$

We then determine the unit vectors in the direction of the velocity vectors of tracks A and B, denoted as $\hat{\mathbf{U}}_A(t_L)$ and $\hat{\mathbf{U}}_B(t_1)$, respectively:

$$\hat{\mathbf{U}}_A(t_L) = \frac{\mathbf{V}_A(t_L)}{\|\mathbf{V}_A(t_L)\|}$$
$$\hat{\mathbf{U}}_B(t_1) = \frac{\mathbf{V}_B(t_1)}{\|\mathbf{V}_B(t_1)\|}$$

Using Rodrigues' rotation formula, we compute the rotation matrix R that rotates $\hat{\mathbf{U}}_B(t_1)$ onto $\hat{\mathbf{U}}_A(t_L)$. To do this, we first compute the vector $\mathbf{V}$ that is perpendicular to both $\hat{\mathbf{U}}_A(t_L)$ and $\hat{\mathbf{U}}_B(t_1)$, and whose magnitude is equal to $|\hat{\mathbf{U}}_A(t_L)||\hat{\mathbf{U}}_B(t_1)|\sin(\theta)$, where θ is the angle between the two vectors. The skew-symmetric matrix associated with $\mathbf{V}$ is then denoted as $\mathbf{S}$:

$$\mathbf{S} = \begin{bmatrix} 0 & -V_3 & V_2 \\ V_3 & 0 & -V_1 \\ -V_2 & V_1 & 0 \end{bmatrix}$$

Using **V** and **S**, we can compute the rotation matrix R:

$$\mathbf{R} = \mathbf{I} + \sin(\theta)\mathbf{S} + (1 - \cos(\theta))\mathbf{S}^2$$

where **I** is the 3×3 identity matrix. With the rotation matrix **R** known, we can then translate the position and velocity of track B to align with the end point of track A:

$$\mathbf{P}_{B'}(t) = \mathbf{R}(\mathbf{P}_B(t) - \mathbf{P}_B(t_1)) + \mathbf{X}_A$$
$$\mathbf{V}_{B'} = \mathbf{R}\mathbf{V}_B$$

Finally, we concatenate the transformed position and velocities of track B with track A to acquire joined trajectory:

$$\mathbf{P}_{A,B} = \begin{bmatrix} \mathbf{P}_A & \mathbf{P}_{B'} \end{bmatrix}$$
$$\mathbf{V}_{A,B} = \begin{bmatrix} \mathbf{V}_A & \mathbf{V}_{B'} \end{bmatrix}$$

To obtain a complete trajectory, we repeated the procedure mentioned above for all the individual trajectories and concatenated them. Figure A.6 shows the resulting long trajectory. We computed the mean square displacement MSD(Δt) and the mean square velocity $\langle V^2 \rangle$ using this trajectory. To determine the reorientation time τ_P, we performed a linear least squares fit of the form described in Equation A.26 (see Fig 2.25). Once we obtained the reorientation time, we calculated the persistence length and the diffusion coefficients using the equations above.

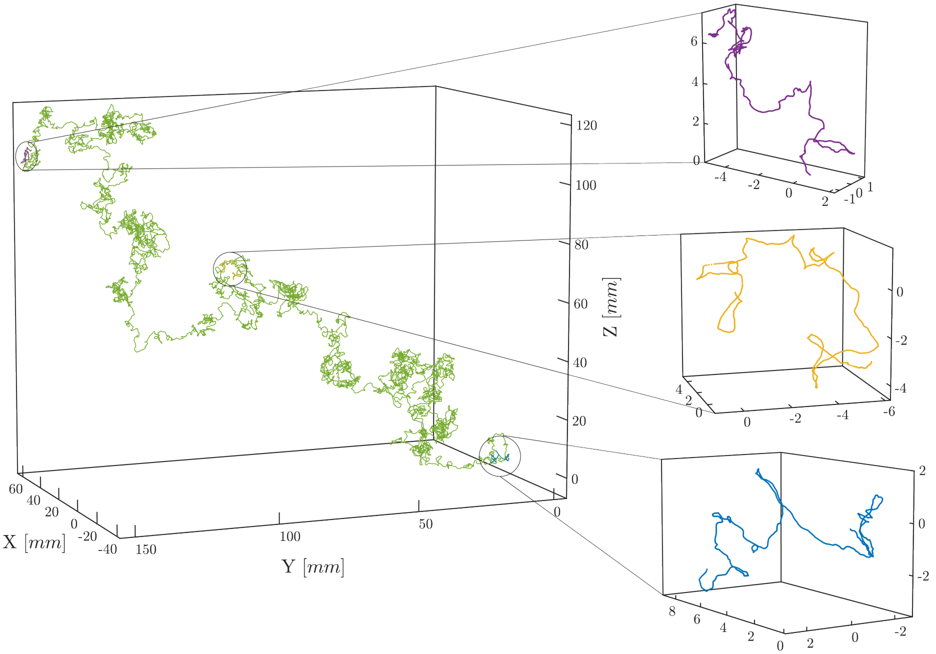

Figure A.6: Concatenated trajectory for 6667 individual tracks for the concentration of 5×10^4 cells/ml. Insets show different trajectory locations. The total track length for all of the insets is 5 minutes.

B

SUPPLEMENTARY MATERIAL - CHAPTER 3

This appendix belongs to chapter 3.

B.1. CORRECTION PROCEDURE FOR TRAJECTORY SWITCHING IN CELL TRACKING

In this appendix, we provide a comprehensive description of the trajectory switching problem observed during the cell tracking process and elaborate on the correction procedure implemented to rectify this issue. The problem is primarily identified through manual inspection focused on cell pairs with a minimum three-dimensional distance of less than 30 μm, where cell images are likely to overlap. The primary consequence of this cell overlap is an uncertainty in cell tracking, leading to a phenomenon we term as *trajectory switching*. This is where trajectories are mistakenly assigned to the wrong cells.

Fig. B.1 A exhibits the three-dimensional positions of one such pair of cells. For this pair, the minimum distance between the cells is 15 μm. At first glance, the trajectories suggest a head-to-head steric interaction, where the cells collide and then proceed in opposite directions. To delve deeper, we consider the velocities of these cells, represented as a color marker on Fig. B.1 B. Prior to the cell interaction, the velocity of track a was approximately 100 μm/s, whereas the velocity of track b was approximately 150 μm/s. However, after the interaction, a sudden velocity change is observed, with track a increasing to about 150 μm/s and track b decreasing. This irregularity is the first hint that a trajectory switch might have occurred during the passing event.

To further investigate, we re-projected the three-dimensional positions onto the camera plane and produced a video sequence of the entire interaction. Fig. B.1 C presents the positions of the cells and their re-projected positions from $t = -0.25s$ to $t = 0.25s$. Initially, track a (depicted by a green dot) is above track b (depicted by a red dot). As the cells approach each other, the green dot starts shifting towards the lower cell, signifying a possible switch in trajectory.

To provide a clearer perspective, we display only the cell images in Fig. B.1 D. Here, two distinct algae images can be seen in all camera views, except for camera 3, where the images overlap between time steps $t = -0.20$ to $t = 0$s. We assigned labels (i) and (ii) to the algae, independent of the labels a and b, as at this juncture we are uncertain about the precise algae-track correlation. Alga (i) moves from right to left in all camera frames, while alga (ii) moves from left to right. Importantly, cell (i) passes over cell (ii) in all camera views.

Now, by consolidating information from Fig. B.1 C and D, it becomes apparent that before the passing event, cell (i) correlates with track a and cell (ii) with track b. However, post the event, a switch in trajectory assignment is observed, resulting in wrong allocation of the tracks to the cells. This analysis underscores the necessity for a corrective procedure to resolve such trajectory switching.

We now consider the underlying cause of trajectory switching. Fig. B.2 illustrates the output from the object detection step, displaying conics and midpoints for the pair of cells under consideration. Apart from camera 3, both cells are accurately detected from time steps $t = -0.25s$ to $t = -0.05$s. This situation parallels the one depicted in Fig. 3.2A, where the tracking algorithm functioned correctly, thereby preventing trajectory switching. The crucial difference between these two instances lies in the duration of overlap between the cells. A close examination of the images from camera 2 and 3 in Fig. B.2 reveals that the cell overlap commences 5 frames before the closest approach. This duration exceeds that observed in Fig. 3.2A, where the overlap began just 2 frames prior. A prolonged overlap period increases the likelihood of both cells meeting the appending conditions related to the re-projection error. The trajectory switching observed in this scenario can be traced back to an implementation detail linked to the re-projection error. The algorithm is designed to prioritize appending the track that is longer when two cells satisfy the re-projection conditions. This preference, derived from the algorithm's objective to generate longer trajectories, can occasionally lead to trajectory switching, as demonstrated in the scenario discussed here.

The switched trajectory pairs are rectified using the same iterative optimization algorithm. However, this time we adjust the optimization criterion by decreasing the tolerance for re-projection error. This adjustment is performed exclusively for switched pairs.

Fig. B.3 A illustrates the corrected three-dimensional positions of the previously discussed switched pair, with the minimum distance between trajectories now measured at 25 μm. The velocity plot in Fig. B.3 B further demonstrates the effectiveness of the correction process as the velocities of both trajectories maintain consistency throughout the entire passing event. Moreover, we also present the reprojected positions on the camera images in Fig. B.3 C. With the trajectory switching error rectified, both the green and red reprojected trajectories accurately follow their respective cell paths.

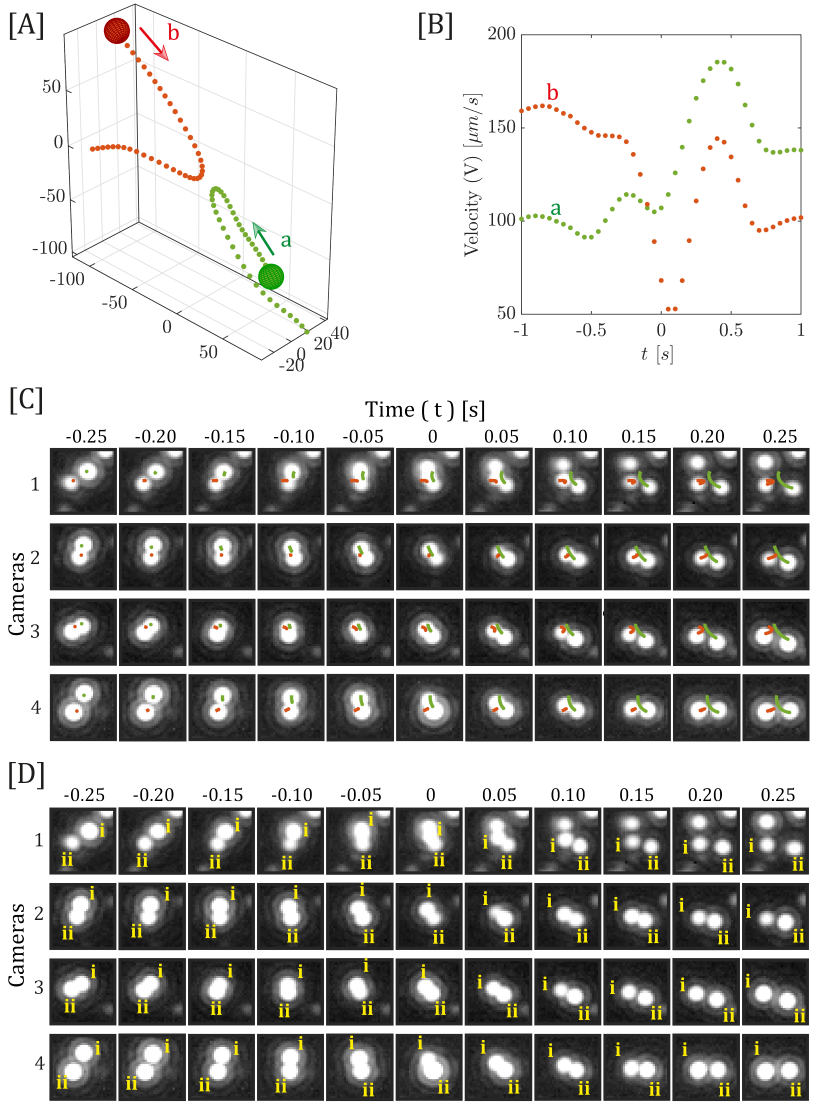

Figure B.1: [A] Three-dimensional positions of a pair of cells (tracks a and b) demonstrating a potential steric interaction. The minimum distance between the cells is 15 μm. [B] Velocities of the cells shown with color markers representing each track. [C] Re-projected positions of cells on the camera plane from $t = -0.25s$ to $t = 0.25s$. As the cells approach each other, track a (green dot) appears to shift towards the lower cell (track b, red dot), indicating a potential trajectory switch. [D] Cell images in all camera views, except for camera 3, where the images overlap from time steps $t = -0.20s$ to $t = 0$s. Two distinct algae images can be observed, labeled as (i) and (ii). Cell (i) moves from right to left and cell (ii) moves from left to right in all camera frames. Cell (i) is seen to pass over cell (ii) in all camera views.

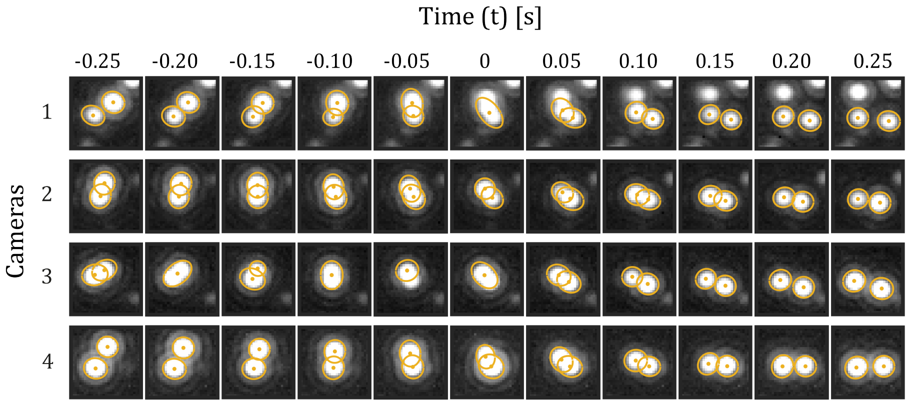

Figure B.2: Conics and midpoints obtained via the peak-finding algorithm during the object detection step of cell tracking for the pair of cells where trajectory switching occurred.

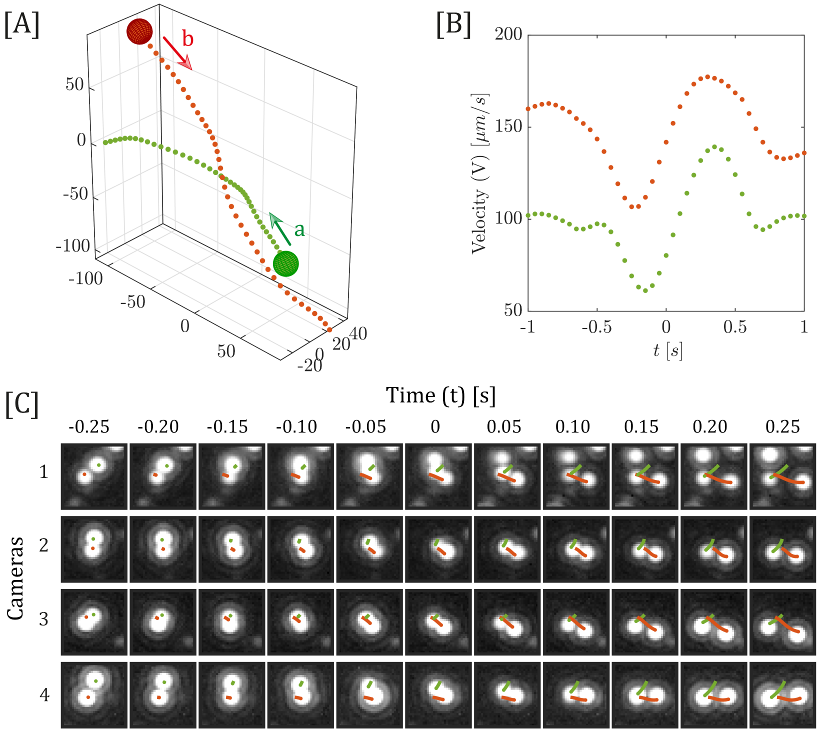

Figure B.3: [A] Three-dimensional positions of the corrected trajectories. [B] Velocities of both of the corrected trajectories. [C] Reprojected position of corrected positions on the camera images. Green and red solid lines display the re-projected track for successive time steps.

B.2. ENERGY MINIMIZING CURVE FITTING

The objective function of our minimization problem combines least square and stretch energy:

$$\min_{\beta} \sum_{i=0}^{N} \left|\mathbf{X}(t_i,\beta) - \mathbf{X}_i\right|^2 + \gamma \int_0^N \left|\mathbf{X}^{'}(t_i,\beta)\right|^2 dt$$

Representation of $\chi(t,\beta)$ is performed via a piecewise Legendre polynomial. The Hessian matrix (H_s) for the objective function from equation 3.3 is calculated analytically. Karush-Kuhn-Tucker (KKT) conditions [234] are employed to find the β parameters which minimize the objective function.

$$\begin{bmatrix} \beta \\ z \end{bmatrix} = \begin{bmatrix} 2A^T A + H_s & I^T \\ I & \mathbf{O} \end{bmatrix}^{-1} \begin{bmatrix} 2A^T \mathbf{X} \\ \mathbf{O} \end{bmatrix} \tag{B.1}$$

Here, A is the design matrix for the least square fit, I is the constraint matrix, $\mathbf{X}$ is a column vector of the positions of the swimmers and z is the Lagrange multiplier.

Details about the calculation of the design matrix, and the constraint matrix, as well as the specifics of the optimization problem setup are provided in appendix A.1.

B.3. SPRING BEAD MODEL

B.3.1. MODEL OUTLINE

In this model, each *C. reinhardtii* cell is represented as a three-bead connected system, as depicted in Fig. B.4. The swimmer moves in a specific direction denoted by $\hat{\mathbf{n}}$, which is computed by normalizing $\mathbf{n} = (\mathbf{X}_L + \mathbf{X}_R)/2 - \mathbf{X}_B$, where $\mathbf{X}_L$, $\mathbf{X}_R$, and $\mathbf{X}_B$ are the locations of the left, right, and the body beads, respectively. The propulsion force $\mathbf{F}^f$ acts only on the left and right beads in the direction of $\hat{\mathbf{n}}$. In response, these beads exert equal and opposite forces $-\mathbf{F}^f$ on the fluid. The beads are connected by springs, where the length of the spring between the left and right bead, denoted as ℓ_{RL}, depends on the angle φ between the springs **BR** and **LB** that connect the body to the right and left beads, respectively. The springs **BR** and **LB** are of equal length ℓ_F.

The equation of motion for each bead is determined by considering the zero-force condition:

$$\mathbf{F}^c_{\mathrm{k}} + \delta_{\mathrm{k},(L,R)} \mathbf{F}^f_{\mathrm{k}} + \mathbf{F}^h_{\mathrm{k}} = 0 \tag{B.2}$$

where $\mathrm{k} = \{\mathrm{B: Body},\ \mathrm{L: Left},\ \mathrm{R: Right}\}$ represents the bead type. In this equation, δ is the Kronecker delta function for the left and right flagellar force $\mathbf{F}^f_j$, $\mathbf{F}^h_{\mathrm{k}}$ is the hydrodynamic drag force, and $\mathbf{F}^c_{\mathrm{k}}$ is the spring force acting on each bead. We only consider hydrodynamic interactions for our simulations so no collision force is considered for this force balance.

The hydrodynamic drag force on a bead is given by:

$$\mathbf{F}^h_{\mathrm{k}} = -6\pi\eta a_{\mathrm{k}} (\mathbf{V}_{\mathrm{k}} - \mathbf{U}_{\mathrm{k}}) \tag{B.3}$$

Here, a_{k} represents the radii of the bead, which is set to 5 μm for the Body bead and 2.5 μm for the Left and Right beads. The variable η is the water's viscosity, $\mathbf{V}_{\mathrm{k}} = \mathrm{d}\mathbf{X}_{\mathrm{k}}/\mathrm{d}t$ is the

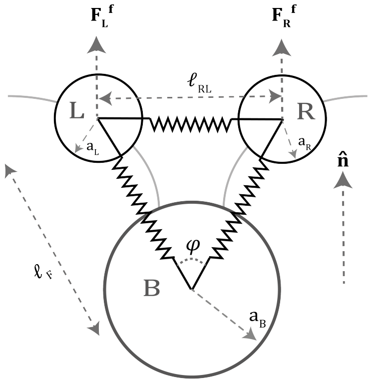

Figure B.4: A schematic of the three-bead swimmer model of a *C. reinhardtii* cell. Each cell is represented by three beads: B (Body), L (Left), and R (Right), with radius a_B, a_L, and a_R, respectively. The swimmer's movement direction $\hat{\mathbf{n}}$ is determined by the relative positions of the beads. The propulsion force $\mathbf{F}^f$ is exerted on the left and right beads in the direction of $\hat{\mathbf{n}}$. The beads are interconnected by springs, with ℓ_{RL} depicting the spring length between the left and right beads, dependent on the angle φ between the springs **BR** and **LB**. The springs **BR** and **LB** are of equal length ℓ_F.

velocity of bead k, and $\mathbf{U}_\mathrm{k}$ is the velocity of the fluid at the location of the k-th bead of swimmer. By combining Eq. B.2 and B.3, we obtain the equation for bead position:

$$\frac{\mathrm{d}\mathbf{X}_\mathrm{k}}{\mathrm{d}t} = \mathbf{U}_\mathrm{k} + \frac{1}{6\pi\eta a_\mathrm{k}}\left(\mathbf{F}_\mathrm{k}^c + \delta_{\mathrm{k},(L,R)}\mathbf{F}_\mathrm{k}^f\right) \tag{B.4}$$

In this equation, $\mathbf{F}_\mathrm{k}^f$ is the propulsion force acting on the left and right bead, which is dependent upon the desired cell velocity ($\mathbf{V}$). The fluid velocity at the bead location, denoted as ($\mathbf{U}_\mathrm{k}$), is zero for a single swimmer, as the swimmer's own movement primarily influences the surrounding fluid dynamics. However, in simulations involving interactions between pairs of swimmers, $\mathbf{U}_\mathrm{k}$ is determined by computing the velocity of the fluid at the bead location due to the other swimmer. The spring forces $\mathbf{F}^c$ are calculated using the Finitely Extensible Nonlinear Elastic (FENE) spring model, and the methodology to compute these forces along with the velocity due to swimmer movement is discussed below:

Spring Force Calculation:

The force exerted by the springs in our model is determined using the Finitely Extensible Nonlinear Elastic (FENE) spring model [145]:

$$\mathbf{F}^c = h\mathbf{Q}\frac{1-\frac{\ell}{|\mathbf{Q}|}}{1-\left[\frac{|\mathbf{Q}|-\ell}{\ell_m-\ell}\right]^2} \tag{B.5}$$

In this equation, h represents the spring constant, $\mathbf{Q}$ is the vector connecting one bead to the next, ℓ denotes the length of the spring, and ℓ_m is the maximum spring extension that can be accommodated. The terms h and ℓ_m are variables intrinsic to the model, while ℓ specifies the spring lengths, denoting ℓ_F for the **LB** and **BR** springs, and ℓ_{RL} for the **RL** spring. In our simulations, we have set $h = f^f / 0.1\ell$ and $\ell_m = 1.15\ell$, values that are consistent with those used in the previous study [145].

The connector vectors for each spring are defined as follows:

$$\mathbf{Q}_{LB} = \mathbf{X}_B - \mathbf{X}_L \tag{B.6}$$

$$\mathbf{Q}_{RL} = \mathbf{X}_L - \mathbf{X}_R \tag{B.7}$$

$$\mathbf{Q}_{BR} = \mathbf{X}_R - \mathbf{X}_B \tag{B.8}$$

These values are then used to calculate the spring force for each spring, **BR**, **LB** and **RL** according to Equation B.5. Finally, the spring force on each bead is calculated as follows:

$$\mathbf{F}^c_B = \mathbf{F}^c_{BR} - \mathbf{F}^c_{LB} \tag{B.9}$$

$$\mathbf{F}^c_L = \mathbf{F}^c_{LB} - \mathbf{F}^c_{RL} \tag{B.10}$$

$$\mathbf{F}^c_R = \mathbf{F}^c_{RL} - \mathbf{F}^c_{BR} \tag{B.11}$$

Fluid Velocity Calculations:
At any location **X** in the fluid, the fluid velocity is determined by the sum of bead point forces and flagellar propulsion forces. This can be expressed as follows:

$$\mathbf{U}(\mathbf{X}) = \sum_{\mathrm{k}\in\{B,L,R\}} \mathbf{G}_{a_\mathrm{k}}(\mathbf{X}, \mathbf{X}_\mathrm{k}) \cdot \left(-\mathbf{F}^h_\mathrm{k} - \delta_{\mathrm{k},(L,R)} \mathbf{F}^f_\mathrm{k}\right) \tag{B.12}$$

Considering force balance, Equation B.12 can be simplified to:

$$\mathbf{U}(\mathbf{X}) = \sum_{\mathrm{k}\in\{B,L,R\}} \mathbf{G}_{a_\mathrm{k}}(\mathbf{X}, \mathbf{X}_\mathrm{k}) \cdot \mathbf{F}^c_\mathrm{k} \tag{B.13}$$

In Equation B.13, $\mathbf{G}_{a_\mathrm{k}}(\mathbf{X}, \mathbf{X}_\mathrm{k})$ represents the regularized stokeslet [235]:

$$\mathbf{G}_{a_\mathrm{k}}(\mathbf{X}, \mathbf{X}_\mathrm{k}) = \frac{1}{8\pi}\left[\frac{r^2 + 2a_\mathrm{k}^2}{\left(r^2 + a_\mathrm{k}^2\right)^{3/2}}\mathbf{I} + \frac{(\mathbf{X} - \mathbf{X}_\mathrm{k})(\mathbf{X} - \mathbf{X}_\mathrm{k})^T}{\left(r^2 + a_\mathrm{k}^2\right)^{3/2}}\right] \tag{B.14}$$

while $r = \|\mathbf{X} - \mathbf{X}_\mathrm{k}\|$.

The swimmer's motion is simulated by integrating Eq. B.4, where the swimmer's velocity is contingent upon the flagellar force, denoted as $\mathbf{F}^f$. By applying Stokes' law, $F = 6\pi\eta a V$, the flagellar force can be computed using predetermined velocity and the bead's radius values. For instance, for the velocity of $100\mu m$/s and the total bead radius of $10\mu m$; the required flagellar force is 20 pN. Additionally, we set the ℓ_F to be $16\mu m$ and the angle φ between springs **BR** and **LB** to be 120°. The simulation results, including the generated flow field, are depicted in Fig. B.5, showing the fluid streamlines at several time intervals.

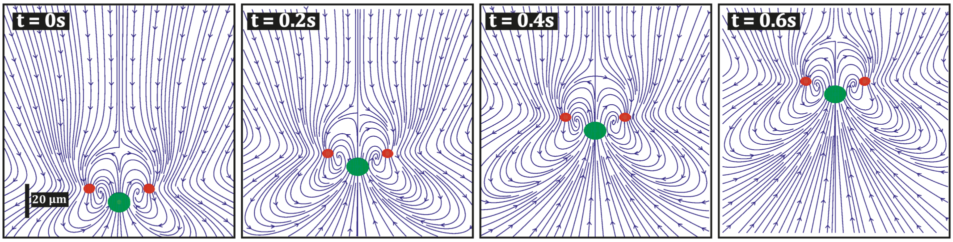

Figure B.5: Fluid streamlines for to the *C. reinhardtii* spring-bead model at different time steps, depicted in the plane of the beads.

B.3.2. MODEL VALIDATION

To validate our model, we initially configure it to generate the flow field of a single swimmer, as visualized in Fig. B.6 A. This flow field exhibits qualitative similarities with those models in prior studies [143, 147]. We set the simulation parameters for a more rigorous quantitative comparison to compare our swimmer flow field with the one presented in Drescher *et al.* [147]. In the scenario where $f^f = 4$ pN, $a_B = 5\mu m$, $\ell_F = 16\mu m$, and $\varphi = 120°$, there is a good agreement between the two models, as demonstrated in Fig. B.6 B.

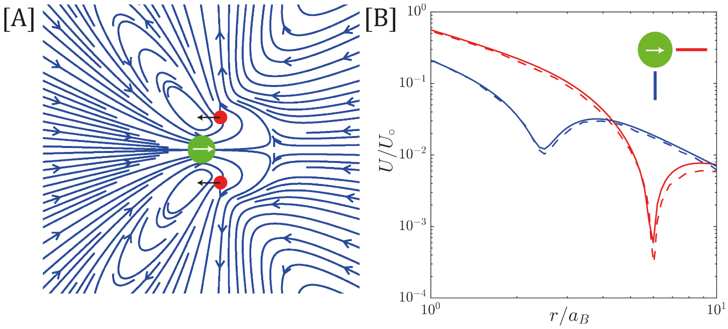

Figure B.6: Flow field of C. reinhardtii. [A] Streamlines of the azimuthally averaged flow field of the 3-bead swimmer model. [B] Magnitude of the flow field U normalized by $U_\circ = 100\mu m/s$ in two directions (represented by different colors solid lines in the inset), with results from Drescher *et al.* [147] (dashed lines).

B.3.3. PAIRWISE SIMULATIONS

We described the coordinate system (Fig. 3.5) and the initialization setup for pairwise simulation in section 3.2.5. Here, we discuss these simulations in detail.

For each of the pairwise simulation, we initialize their positions, velocities, and directions of motion at $t = 0$. Swimmer "a" is positioned at $r_a = 200$ µm, $\theta_a = \pi$, and $\phi_a = 0$, moving in the positive Z-direction with a velocity of V_a (see Fig. B.7 a). The starting coordinates of swimmer "b", r_b, θ_b, and ϕ_b, are chosen within specific ranges:

r_b from 180 μm to 220 μm, θ_b from 0 to π, and ϕ_b from 0 to $\pi/4$. This is depicted in Fig. B.7A by spheres of blue to pink color. The direction of motion for swimmer "b" is adjusted by varying $\mathbf{V}_b$ as shown in Fig. B.7B for two of the starting position of swimmer "b". The propulsion force for each swimmer is adjusted to achieve specific velocities: swimmer "a" moves at $V_a = 100\mu\text{m/s}$, and swimmer "b" at $V_b = 112\mu\text{m/s}$.

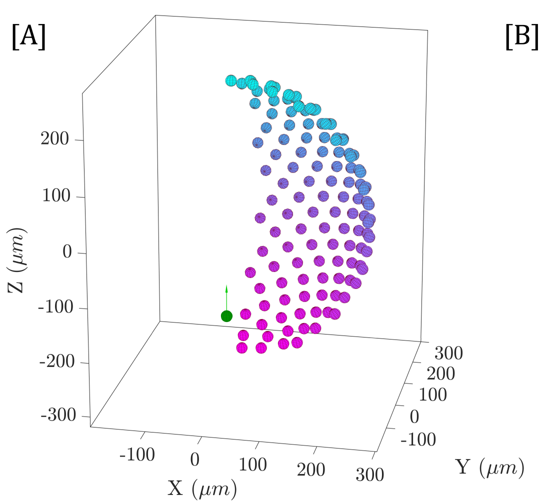

Figure B.7: Pair-wise Simulation setup illustrating the initial positions of two swimmers. [A] Swimmer "a" is denoted by a green sphere and travels in the Positive Z direction, while the starting positions of swimmer "b" are depicted by spheres of color gradient from blue to pink, indicating the difference in initial r_b from 180 to 220 μm, ϕ_b from 0 to $\pi/4$ and θ_b from -π to π [B] Swimmer "a" and two of the starting position of swimmer "b". The direction vectors of swimmer "b", indicated by color-coded arrows, represent the initial direction $\mathbf{V}_b$, with each color denoting a distinct minimum approach distance ranging from 10 μm to 100 μm.

B

The movement of each bead of the swimmers is governed by Eq. B.4, which states:

$$\frac{\mathrm{d}\mathbf{X}_\mathrm{k}}{\mathrm{d}t} = \mathbf{U}_\mathrm{k} + \frac{1}{6\pi\eta a_\mathrm{k}}\left(\mathbf{F}^c_\mathrm{k} + \delta_{\mathrm{k},(L,R)}\mathbf{F}^f_\mathrm{k}\right)$$

The fluid velocity $\mathbf{U}_\mathrm{k}$ at the location of each k-th bead is calculated as follows:

$$\mathbf{U}_\mathrm{k} = \sum_{\mathrm{j}\in\{B,L,R\}} \mathbf{G}_\mathrm{j}(\mathbf{X}_\mathrm{k}, \mathbf{X}'_\mathrm{j}) \cdot \mathbf{F}^{c'}_\mathrm{j} \tag{B.15}$$

This calculation includes contributions from all beads (B, L, R) of the other swimmer, denoted by their positions ($\mathbf{X}'$) and the forces acting on them ($\mathbf{F}^{c'}$).

In our simulations, we initialize the swimmer's positions, their velocity and their direction of motion. The movement of both swimmers is then simulated using Eq. B.4, which updates each bead's position based on the forces acting on them and their velocity. The propulsion force, $\mathbf{F}^f_\mathrm{k}$, drives both swimmers at velocities $V_a = 100\mu m/s$ and $V_b = 112\mu m/s$, respectively. We calculate spring forces ($\mathbf{F}^c_\mathrm{k}$) using the FENE model, as described previously. The hydrodynamic interactions are considered by calculating the fluid velocity at each bead's location ($\mathbf{U}_k$) in each time step, incorporating the influence of the adjacent swimmer's beads, as outlined in Eq. B.15.

B.4. SCATTERING ANGLE

The scattering angle, denoted as α, quantifies the deviation in the path of cell trajectories as two cells pass each other. To compute the scattering angle, we analyze the trajectory of each cell in a series of time intervals around the point of their closest approach. The closest approach is defined as the time step $t = 0$. The trajectory is divided into several intervals before and after this closest approach point using a sliding window approach, as illustrated in Fig. B.8.

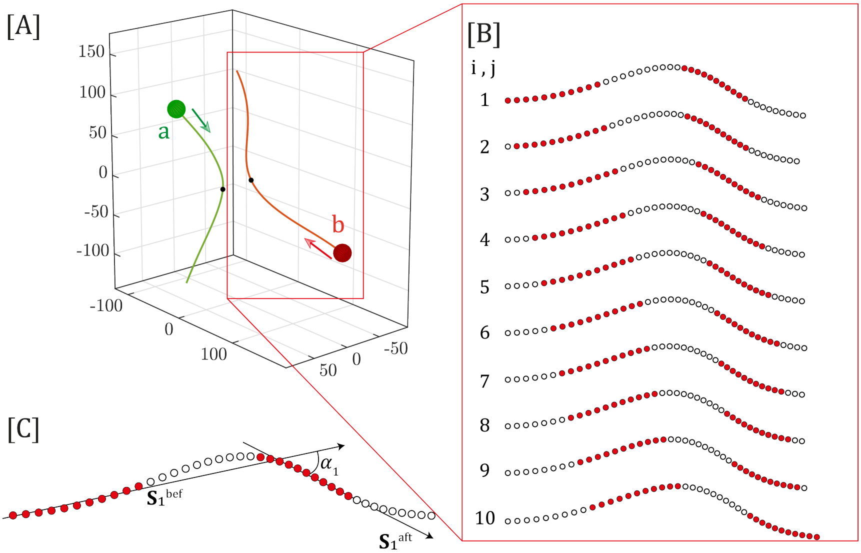

Figure B.8: The computation of the scattering angle (α). [A] Three-dimensional trajectories of a pair of cells approaching each other at a minimum distance (d_{min}) of 20.8 μm. [B] Illustrations of the division of one of the trajectories into half-second intervals using a sliding window. The red dots denote the positional values at each selected window both before (i) and after (j) the minimum distance point. Each i and j varies from 1 to 10, representing each window. [C] A schematic of the calculation of the scattering angle for one of the intervals. $S_{\mathrm{bef},1}$ and $S_{\mathrm{aft},1}$ are the line segments fitted on points corresponding to the 1st trajectory interval. α_1 is the angle between $\mathbf{S}_i^{\mathrm{bef}}$ and $\mathbf{S}_i^{\mathrm{aft}}$. Similarly, α_2 to α_{10} are computed, and the mean value of these angles corresponds to the scattering angle α for the respective trajectory.

For the intervals before the closest approach, denoted as bef, the time t is defined in a range of $t \in [-1, 0]$ s. Similarly, for the interval after the closest approach, labeled aft, the time t encompasses $[0, 1]$s. Each interval is of half-second length, as indicated by the red circles in Fig. B.8 B. For the bef part of the trajectory, we define the index i to denote specific intervals within this phase. Conversely, for the aft part, the index j is used to similarly denote specific intervals following the closest approach.

For each interval before and after the closest approach, we fit a parameterized line segment using a linear least squares approximation on $\mathbf{X}(t)$:

$$\underset{\mathbf{A},\mathbf{B}}{\arg\min} \sum_{t=1}^{N} |\mathbf{X}(t) - \mathbf{S}(t)|^2 \quad \text{where} \quad \mathbf{S} = \mathbf{A} + t\mathbf{B} = \begin{bmatrix} A_X \\ A_Y \\ A_Z \end{bmatrix} + t \begin{bmatrix} B_X \\ B_Y \\ B_Z \end{bmatrix} \tag{B.16}$$

With these line segments, the scattering angle is computed as the average angle between direction vectors $\mathbf{B}$ of corresponding pairs of line segments:

$$\alpha = \frac{1}{10} \sum_{i=j=1}^{10} \cos^{-1}\left(\frac{\mathbf{B}_i^{\text{bef}} \cdot \mathbf{B}_j^{\text{aft}}}{\left|\mathbf{B}_i^{\text{bef}}\right| \left|\mathbf{B}_j^{\text{aft}}\right|} \right) \tag{B.17}$$

Here, $\mathbf{B}_i^{\text{bef}}$ and $\mathbf{B}_j^{\text{aft}}$ represent the direction vectors for line segments before and after the minimum approach distance.

ACKNOWLEDGEMENTS

"Journey before destination" they say. Yet, destinations are seldom reached without companions. Now that I have finally arrived at my destination (though it is just one of many in this journey of life, and probably the hardest one to reach so far..), I was rarely alone along the way. I am grateful to all the people who accompanied me, whether for a short time or for the long haul. I would like to take this opportunity to express my appreciation to those who have been part of this journey.

First, to my promoter and daily advisor, Daniel. When I received the offer for this Ph.D., I was thinking of going back to Pakistan, and whatever followed is only because you took a chance on me. From taking the 'Advanced Fluid Dynamics' course to setting up the lab and experiments, and figuring out all the small problems along the way, it has been a great honor working with you throughout these years. I have learned so much from you, ranging from critical thinking to academic writing, that has shaped me into, I hope, a better scientist. There have been many ups and downs, but your support over these last couple of years has gone far beyond what one could expect from a supervisor. I will always be indebted to you. I would also like to thank my co-promoter, John. When I joined this lab, you were finishing your postdoc, and you helped me settle in, taught me everything about the 3D tracking code and the microscopy setup, and were always available whenever I needed assistance. I am really grateful for that. Also, thank you for being there whenever I needed an ear; not just to rant, but to bounce ideas off of. Our discussions were never boring, probably why our meetings always ran over time!. I want to also thank my committee members Prof. Johan Padding, Prof. Valeria Garbin, Dr. Hermes Gadelha, Dr. Guillermo Amador and Dr. Gerrit Elsinga for taking the time to review this thesis and being part of my defence ceremony.

I want to extend my heartfelt thanks to the members of Daniel's lab. Koen, this work would not have been possible without, first, your pioneering M.Sc. thesis on algae tracking and, second, your incredible 3D tracking code. I am still in awe that you managed to complete that code on your own during your Ph.D., and it was just one chapter of your thesis. This speaks volumes about your intelligence and acumen, which proved invaluable whenever I faced issues with experiments or analysis. I also enjoyed our time together outside the lab. Parviz, without you working alongside me when COVID hit, I am sure it would have been excruciatingly painful. They say that bonds formed over shared misery are unbreakable, and I hope ours remains the same. Bob, you joined a year after me, and our shared 'mutual' habit was a great comfort during those 10-hour, five-day experiments. Also, because of you, I got to learn about 3D printing, which helped greatly with the imaging setup. I have also always enjoyed our time outside the lab, discussing world events and Dutch politics. Sowmya, you were a wonderful addition to our team. Your help with autoclaving and solution making greatly reduced my stress. and, of course, our discussions are always a pleasure. Also, to master students I worked with during this Ph.D, Stefan and Anand, thank you for giving me the opportunity to learn from you. Without your work, this thesis would be unfinished.

During these years, I have had the support of wonderful colleagues who have made this journey as manageable as possible. I want to express my gratitude to Edwin for all your help in resolving issues with the imaging system and DaVis, and for never getting annoyed at me despite how often I bothered you about restarting the servers. Jasper, I am incredibly thankful for your amazing expertise with machining tools; without it, I don't know how I could have ever built this amazing machine. Caroline, I am grateful for your assistance when I first joined the lab, you helped me greatly in settling in and later in figuring out contract issues and all the other small things that made navigating this job much easier. I would also like to thank Dr. Mathieu Pourque; your amazing attitude and resourcefulness in providing computational resources were instrumental to this work.

I have been fortunate to share the Fluids Lab with many wonderful colleagues and friends over the years: Abhinash, Abirath, Amitosh, Esra, Haoyu, Jesse, Lina, Luuk, Lyke, Nicola, Sudarshan, Tea, Udhav, Willian, Wout, Wouter, Yavuz and others. Hopefully, I have managed to get all your names right this time :). It has been a true pleasure to know you and enjoy your company throughout this time. From engaging discussions at the coffee table to drinks and sharing cakes, I truly cherish the experiences we have shared together.

I am incredibly grateful for the amazing friends I have made along the way during these years. Amantrita and Krishti, thank you for always being there, listening to my endless complaints, and providing unwavering support. Our countless dinners together, parties, and hangouts have created memories that will stay with me for a long time. Robin, your energy and enthusiasm have always made spending time with you a joy. Ankur, your help both in the lab and beyond has been invaluable. Tariq, thank you for organizing so many great hangouts at your place and for always being available whenever I needed your company.

In the past year, I started a new job and had the chance to meet some wonderful people. First, Sherwin and Sara, thank you for giving me the opportunity to work with this amazing team and for believing in me that I would one day finish this Ph.D. Chrysa and Panos, thank you for bringing much-needed laughter to our 'meetings' and for being the awesome people you are.

A special thanks to my friends from the Pakistani community, who provided me with a sense of home away from home. Saad and Hassam bhai, thank you for warmly welcoming me when I first arrived in the Netherlands, offering incredible help and delicious food that made those first few months so much easier to navigate. I have appreciated your constant support and availability whenever I had any questions. Harris, Samad and Muneeb, thank you for all the amazing meals, fun hangouts, and game nights. You truly made these years more enjoyable, and I hope we continue to do so in the years ahead.

To my friends back home, even from miles away, your unwavering support and encouragement have meant the world to me. Shoaib, you were the first person to encourage me to pursue a Ph.D., and now that I am at the finish line, I can not thank you enough, not just for that advice, but for always being like a big brother to me. Hammad, who would have thought how far we would come since we first met? From teaching me how to play table tennis to helping me communicate more effectively, your

friendship has been instrumental in shaping who I am today. Mohsin, thank you for being a constant source of guidance throughout the years. Itrat, our long calls and conversations truly brought joy to these past few years. Without them, it would have been far less exciting, and I can not thank you enough for always being there whenever I needed you. Maryam, thank you for always answering my calls and patiently listening to me talk for hours. Your incredible meals and the amazing recipes you have shared have been a true gift, ones I am still trying to master. Rafay, I am incredibly grateful for your valuable insights and all the free ‘therapy sessions’, your support has been truly meaningful. Ittefaq, thank you for being such a joy to be around and for your incredible advice on academic writing and everything else.

I left my family back in Pakistan eight years ago to pursue my master’s, and starting this Ph.D. has been as challenging as I imagined it would be without them by my side. Their unconditional love, belief in me, and encouragement have been my greatest pillars of strength throughout this journey. So, I would like to express these final words of gratitude to them. Raheel, thank you for always offering wise advice when I needed it most and for being the person I can always lean on. Sherjeel, your humor and support have been a constant source of joy, and knowing you are there has always given me strength. Azqa, thank you for always being there for me through it all. To my brothers, Ubaid and Asad, your support and encouragement have meant the world to me. And to my sister Zainab, thank you for your kindness, motivation, and mischievousness that never fails to lift my spirits. Finally, to my mother, it feels strange to simply say ‘thank you’, those words seem too small to express my deep gratitude. Thank you for your courage throughout all these years, for taking the steps that set me on this path, and for your unwavering love and support. I owe everything to you.

Junaid Mehmood
October 15, 2024

LIST OF PUBLICATIONS

JOURNAL ARTICLES

5. **Mehmood,J.**, Muller, K., Buchner, A. J., & Tam, D. (2024). Kinematics & surface interactions of Chlamydomonas Reinhardtii in complex fluids, Journal of the Royal Society Interface. [In Preparation]

4. **Mehmood,J.**, Muller, K., & Tam, D. (2024). Pair-wise interactions of Chlamydomonas Reinhardtii", Physical Review Fluids. [In Preparation]

3. **Mehmood,J.**, Muller, K., Kumar, S., Buchner, A. J., & Tam, D. (2024). Three dimensional tracking of microswimmers, Experiments in Fluids. [Submitted]

2. Buchner, A. J., Muller, K., **Mehmood, J.**, & Tam, D. (2021). Hopping trajectories due to long-range interactions determine surface accumulation of microalgae. Proceedings of the National Academy of Sciences, 118(20).

1. Mahajan, V. V., **Mehmood, J**., El Hasadi, Y. M., & Padding, J. T. (2019). Fluid medium effect on stresses in suspensions of high-inertia rod-like particles. Chemical Engineering Science: X, 3, 100030.

CONFERENCE PROCEEDINGS

3. **Mehmood, J.**, Muller, K., Buchner, A. J., & Tam, D. (2021). Pair-wise interactions between Chlamydomonas Reinhardtii: A numerical and experimental study. In APS Division of Fluid Dynamics Meeting Abstracts (pp. Q05-009).

2. **Mehmood, J**., Muller, K., Buchner, A. J., & Tam, D. (2020). Experimental investigation of pair-wise interactions between Chlamydomonas reinhardtii. In APS Division of Fluid Dynamics Meeting Abstracts (pp. E06-048).

1. Fitzgerald, B., **Mehmood, J.**, Mahajan, V., & Padding, J. (2018). Stress Tensor Measurements of Sheared Packings of Non-Spherical Particles. In APS March Meeting Abstracts (Vol. 2018, pp. K48-009).

Curriculum Vitæ

Junaid Mehmood

1994	Born in Vehari, Pakistan.

Education

2010–2014	Bachelors in Chemical Engineering University of Engineering & Technology, Lahore, Pakistan
2016–2018	Masters in Process Engineering Delft University of Technology, Delft, The Netherlands
2018–2024	Doctor of Philosophy, Biophysics Delft University of Technology, Delft, The Netherlands

Professional Experience

2014–2015	Process Engineer Fauji Fertilizer Comoany limited, Pakistan
2015–2016	Operations Engineer Oil & Gas Development Company, Pakistan
2023–	Data Scientist & Process Technologist Danone Research & Innovation, The Netherlands

Awards

2015	Gold Medalist, UET Lahore, Pakistan
2016	Awarded the JvEffen Excellence Scholarship (€55,000)
2018	Honours Certificate, Master’s Program